Fracture Studies from Amplitude versus Offset and Azimuth and Vertical Seismic Profile data

Isabel Varela

Thesis submitted in fulfilment of
the requirements for the degree of
Doctor of Philosophy

School of GeoSciences
University of Edinburgh

2009

Declaration

I hereby declare that this thesis has been composed by myself and that the work described is entirely my own unless explicitly stated in the text.

Isabel Varela

Software used for this thesis:
This thesis was written using LaTeX and the references and citations were produced by BibTeX. Most diagrams including seismograms were produced with the Matlab. Other softwares used include Rock Unix, Seismic Unix and Aniseis. All other calculations were done by Matlab, shell scripts and Fortran programs which were written by myself.

Abstract

In this thesis I address the problem of determining fracture properties of subsurface rocks from geophysical surface seismic and vertical seismic profile (VSP) data.

In the first part of this thesis I perform multi-attribute analysis, including frequency content, amplitude, travel time and angle of rotation studies on field VSP data from two different carbonate fields, both containing time-lapse surveys. I compare the findings to independent data available in the region and find that the interpreted fracture orientations from the attribute analyses correlate with independent fracture studies in the area, the principal axis of major faults, or the maximum horizontal stress of the area studied. Although I show the existence of these correlations, due to the limited knowledge of the rock properties, these correlations are only qualitative. A more robust inversion of fracture properties requires more knowledge of the physical properties of the medium and forward modelling of the seismic response. A rock physics theory would be required to model the elastic response of the fractured rock; hence a more quantitative fracture characterisation is necessary. In the second part of this thesis I address this need by developing and testing a method for fracture density inversion.

Linearised approximations are commonly used in azimuthal amplitude versus offset (AVO) analysis. However, these approximations perform poorly at large angles of incidence where the effect of fractures is more significant. The method proposed here uses a model based approach that does not use these approximations but calculates the exact azimuthal AVO response based on prior knowledge of the elastic constants of the medium, assumed to be known, and a range of fracture densities. A rock physics theory is used for modelling the elastic constants of the fractured rock. I then create a linearized relationship for a specific model that separates the effect due to fracture density from the modelled AVOZ responses. This separation is key to the method, as

it provides both a new set of orthogonal basis functions that can be used to express the AVOZ response of field data, and a set of coefficients that are related to fracture density. In general, the inversion is based on these coefficients. The coefficient or coefficients which present the highest correlation with fracture density must be determined on a case by case basis, as they will vary depending on the contrast between the elastic constants across the boundary of interest.

I develop and test the method on synthetic surface seismic data and then apply it to seismic data acquired from a laboratory-scale physical geological model. Due to the prior knowledge of the rock properties and structure of the physical geological model, I am able to corroborate that the inverted fracture density from the seismic data matches that of the physical model within the error. I compare the inversion for two different levels of uncertainty in the velocities and densities of the modelled reflection coefficients and show that the inversion results are more precise and accurate when there is less uncertainty in the rock properties of the modelled reflection coefficients. In both the synthetic and physical geological model studies I find that the inversion is optimal for a certain range of offsets/angles of incidence. This means that the optimal range for inversion must be found on a case by case basis, as it depends on the behaviour of the data.

Finally, as the inversion relies on the input modelled azimuthal AVO curves, a careful choice of the input rock properties is essential for the inversion process. The inverted fracture density values will only be valid if the rock properties of the field data fall within the range of the modelled ones. This is a limitation of the method, as adequate knowledge of the rock properties is not always available.

Acknowledgements

I am most grateful to Xiang-Yang Li, Enru Liu, Mark Chapman and Ian Main for taking me into the PhD program at the EAP, for their trust, support and guidance, and for constantly reviewing the progress of this thesis. In particular, I would like to thank Xiang-Yang for always keeping the big picture of this project in mind; Enru, whose vast work on fractures has been an inspiration and forms the backbone motivation for this thesis; Ian, whose work involving principal component analysis in seismology gave way to stimulating discussions on the method I develop; and Mark, from whose knowledge on poroelasticity I have been lucky to tap on, and whose insight at every crucial moment of this thesis has been invaluable.

I am very grateful to the sponsors of the Edinburgh Anisotropy Project and (EAP) the British University Funding Initiative (BUFI) for the funding that supported my studies in Edinburgh.

Furthermore, I would like to thank all the companies that provided the data used in this thesis. Thanks to PDO and Shell for the Omani data, Lawrence Berkely Lab for the Weyburn data, CNPC for the physical modelling data and Total for the well log data. Specially, I would like to thank Sonja Maultzsch and the Geoscience Research Center of Total for suggesting the line of research developed in this thesis.

I am in great debt to all those that contributed to this work through fruitful discussions. Here I would like to specifically thank Mosab Nasser, Andrea Grandi, Igor Escobar and David Booth. In addition, I would like to thank David Booth for numerous revisions of this document. The computer support team at the BGS which includes Brian Bainbridge, Ruth Addinal, Jane Robertson and Steve Love was of great help throughout the years.

My officemates Jinghua Z., Zhongping Q., Adam W., Anish V., Martin E., Heather N., Yungui X., Tieqiang Z., and Chuntao Z. were always available for consultations and made the days in the office an entertaining endeavor.

A heartful thanks to my family whose support I could not have done without, and to Marek whose encouragement in the last year was essential.

Para Nydia Elisa

Contents

List of Tables

List of Figures

Notations and Conventions

Symbol	Meaning	Unit
V_p	velocity of compressional wave	Km/s
V_s	velocity of shear wave	Km/s
ρ	density	gr/cc
C_i	Coefficient i	
F_i	Function i	
3C	3-component geophone	
2C	2-component geophone	
AVO	Amplitude versus offset	
AVOZ	Amplitude versus offset and azimuth	
CMP	Common mid-point gather	
SVD	Singular value decomposition	
HTI	Transverse isotropy with a horizontal axis of symmetry	
VTI	Transverse isotropy with a vertical axis of symmetry	
VSP	Vertical seismic profile	
WAR VSP	Walk-around VSP	
WAW VSP	Walk-away VSP	

Chapter 1

Introduction

1.1 Rationale and outline

Seismic fracture characterization has become a topic of increased interest in geophysical exploration, as fractures are known to facilitate the movement of fluids -and thus the production of hydrocarbons- by increasing porosity and permeability. However, the complex relationship between rock properties and the seismic signal complicates their study. The goal of my thesis is to develop and improve techniques for fracture studies from seismic data.

The drive for energy has led to development of new technologies for maximisation of hydrocarbon production from existing reservoirs, and exploration for new fields; increasing permeability by mechanically fracturing reservoirs has been one of them. The same energy needs have led to exploration of unconventional reservoirs such as tight gas sands, which by nature have very low porosity and permeability, so that fractures provide the only way for extraction (Tsvankin and Lynn, 1999, Sayers, 2007). For environmental purposes, the possibility of CO_2 sequestration in subsurface rocks has gained much attention in recent years. Fractures here play a double role, as they may provide more space for storage, but depending on the structure of the trap they can also be the cause of leakage. Amongst the indirect methods in geophysics, seismics may be the one with the highest potential for detecting fractures, due to its resolution and penetration.

It is because of this that an understanding of the effect of fractures on wave propagation is highly desirable.

Traditional methods for fracture characterisation have relied on simplified notions - which are often little more than rules of thumb- that aim to extract fracture information from seismic data. For example, a common practice is to fit an ellipse to the azimuthal variations of seismic attributes to obtain fracture properties, which is often done without any forward modelling or theoretical justification. In the first part of this thesis I analyse data sets from two different fields for fracture properties by fitting an ellipse to various seismic attributes. However, this approach does not involve any forward modelling of the seismic signal and thus remains only a qualitative analysis. A quantitative study requires a degree of knowledge of the rock properties that would allow for forward modelling of the seismic signal, so that an inversion method can be applied. In the second part of this thesis I develop a method for quantitative fracture characterisation from seismic data. For this end, the use of effective medium theories (explained below) are necessary to model the response of the fractured rock.

When a rock is subject to stress a deformation (or strain) in the rock will occur. If the deformation caused by the stress disappears after the stress is released the rock presents an elastic behaviour. If some deformation is retained, the rock presents what is termed an anelastic deformation, energy is dissipated depending on the properties of the rock, and attenuation occurs. Real rocks present anelastic deformations. When a seismic wave propagates through a medium it exerts a small amount of stress on the medium. Hence, measurements of attenuation from seismic data have the potential to provide information on the anelastic properties of the rock.

Poroelastic theories study the elastic response of a porous medium (rock) depending on the structure (shape of pores and connectivity between them) and saturation (types and quantity of fluids) of the pore space. These theories are also called effective medium theories, as they aim to obtain physical properties of

the composite medium (including rock matrix and the fillings of its pore space) in the case where the length of the propagating wave is much larger than the size of the heterogeneities in the rock. Because the length of fractures that play an important role in fluid flow of reservoirs is usually small compared to the seismic wavelengths, we can represent a fractured rock by an anisotropic effective medium (Sayers, 2007). The classical example for these theories is the Gassmann (1951) low frequency theory, which calculates the bulk modulus of a rock given the porosity, the bulk moduli of the matrix, the rock frame, and the infill fluid. Gassmann's theory is widely used for fluid substitution even though it has a set of assumptions which are rarely met in full in real conditions (Smith et al., 2003, Wang, 2000). An extension of Gassmann's theory to higher frequencies is presented by Biot (1956), who takes into account the viscosity of the fluids, and amongst other findings proves that the viscoelastic effect depends on the frequency used, a phenomenon known as dispersion. Experimental data have shown that the Gassmann theory works particularly well for high porosity sandstones but breaks down for measurements in rocks subject to high effective pressures, particularly in carbonates (Wang, 2000, Adam et al., 2006).

Another group of models were developed in response to the mismatch between Gassmann-Biot models and the experimental data. These models take into account two additional factors, (1) the movement of fluids at the grain scale in directions that are not necessarily those of the propagating wave, and (2) the presence of crack-like pores that may close at high effective pressures. These models are known as squirt flow models as they consider that when the crack-like pores are subject to stress they will close, moving the fluid towards the stiffer (more circular) pores (Mavko and Jizba, 1991, Dvorkin et al., 1995). Though squirt flow theories introduce the concept of crack-like pores, these cracks are randomly oriented so that anisotropic effects can not be modelled. A similar limitation occurs with the inclusion models, which consider the pore space to be composed of ellipsoids with different aspect ratios (Kuster and Toksöz, 1974, Endres and Knight, 1997, Berryman, 1980, Mavko et al., 1999).

Fractures have traditionally been modelled as the composite effect of small aligned cracks (Hudson, 1980, Hudson, 1981, Liu et al., 2000, Marrett et al., 2007). One of the most popular models for calculating the effect of aligned cracks on the elastic constants of the composite rock was developed by Hudson (1981). Hudson's model considers cracks that can be empty or fluid-filled, but allows only for a small concentration of isolated cracks. Hudson et al. (1996) extend the model to allow for a porosity due to small spherical pores (equant porosity), separate from that caused by the cracks, and consider fluid flow between the pores and the cracks. A complication of these theories is that the long wavelength seismic response of numerous small aligned compliant cracks is the same as that for a small number of large stiff cracks (Sayers, 2007). Chapman (2003) presents a model containing likewise randomly oriented small cracks in the presence of equant porosity, but additionally introduces a set of larger meso-scale aligned cracks. Chapman (2003) argues that these large cracks have the effect of bringing the dispersion curve within the seismic frequency band; in theory, the size of the large cracks can be determined by inversion (Maultzsch et al., 2003).

Even though theories have been developed for modelling the effect of cracks from wave propagation, we are usually confronted with the inverse problem: we would like to get the properties of the rocks from the seismic data by measuring their deformation or seismic signal (for example, the reflection coefficient). Anisotropic studies using seismic data attempt to extract fracture information. Studies with calibrated measurements have shown that the seismic waves are sensitive to the presence of fractures in the propagating medium (Corrigan et al., 1996). The two most desired properties to be obtained are fracture orientation and fracture density, as they provide the direction in which the fluid flows with ease and the intensity of the fracturing. However, quantitative studies of fractures from seismic data that make direct use of rock physics models used to estimate their response are rare (Tsvankin and Lynn, 1999, Marrett et al., 2007). In this dissertation I propose a method that meets this criterion.

The complex non-linear relationship between the rock properties - including those of the fractures- and the seismic signal have led to the use of linearised approximations to model the seismic signal and to invert for rock properties. But these approximations tend to lose accuracy at large angles of incidence, coinciding with where the effect due to fractures appears. At near offsets (or steep angles of incidence) the dominant factors in the reflection coefficient are the velocities and densities of rocks on both sides of the interface (Aki and Richards, 1980), while in the middle-range of angles of incidence, Poisson's ratio -or Vp/Vs- is the dominant factor. Fracture properties dominate the signal in the range of angles of incidence where most approximations lose accuracy, and thus fail to provide a means for fracture detection and study.

Within the last five years, several studies have searched for optimal linear relationships between certain rock properties and the seismic signal. Reid et al. (2003), Causse and Hokstad (2005) and Causse et al. (2007a) developed a technique for fluid discrimination with a novel approach that formulates the AVO response in terms of optimal basis functions obtained via singular value decomposition (SVD). It is encouraging that Causse et al. (2007b) have successfully implemented this technique in a field data study. However these studies have been undertaken only for AVO at a fixed azimuth.

In my work I develop a method for quantitative fracture characterisation from seismic data by establishing a linear relationship between the fracture properties and the seismic signal. I base my method on the Causse and Hokstad (2005) approach, and modify it to allow for variation with azimuth and use it for fracture characterisation instead of fluid discrimination. The method I propose uses a model-based approach that calculates the exact AVOZ response based on prior knowledge of the elastic constants of the medium, assumed to be known, and a range of fracture densities. A rock physics theory is used for modelling the elastic constants of the fractured rock. I then create a linearized relationship for a specific model that separates the effect due to fracture density from the modelled AVOZ

responses. This separation provides both a new set of orthogonal basis functions that can be used to write the azimuthal AVO (AVOZ) response of field data, and a set of coefficients that are related to fracture density. In general, the inversion is based on these coefficients.

As the inversion relies on the input modelled azimuthal AVO curves, a careful choice of the model parameters (rock properties) is essential for the inversion process. The inverted fracture density values will only be valid if the rock properties of the field data fall within the range of the modelled ones. This is a limitation of the method, as adequate knowledge of the rock properties is not always available.

In this thesis I confront the inversion problem (see Figure 1.1) that uses surface seismic, well logs and vertical seismic profiles to calculate the fracture properties of subsurface rocks. The rationale discussed above is outlined in Figure 1.2.

My results demonstrate that for a reliable interpretation of seismic data in terms of fracture properties, independent measurements must be used to calibrate the results. I expose the need for using effective medium theories that model the elastic properties of the fractured rock as imperative for a quantitative study. This thesis demonstrates that a quantitative inversion method for fracture characterisation can work successfully on seismic data given prior knowledge of the rock properties. Furthermore, I show that a model-based linear relationship between fracture properties and the seismic signal can be established on a case-by-case basis and be used for a quantitative inversion.

I begin my thesis by introducing basic anisotropy terminology and reviewing some relevant effective medium theories used to model the effect of cracks and fractures in the subsurface. I then discuss methods for fracture characterisation using P-wave data, with an emphasis on amplitude variations with azimuth and offset.

In chapters 3 and 4 I work on field 3D VSP data acquired over two different carbonate fields. In Chapter 3 I study the fracture network of a hydrocarbon

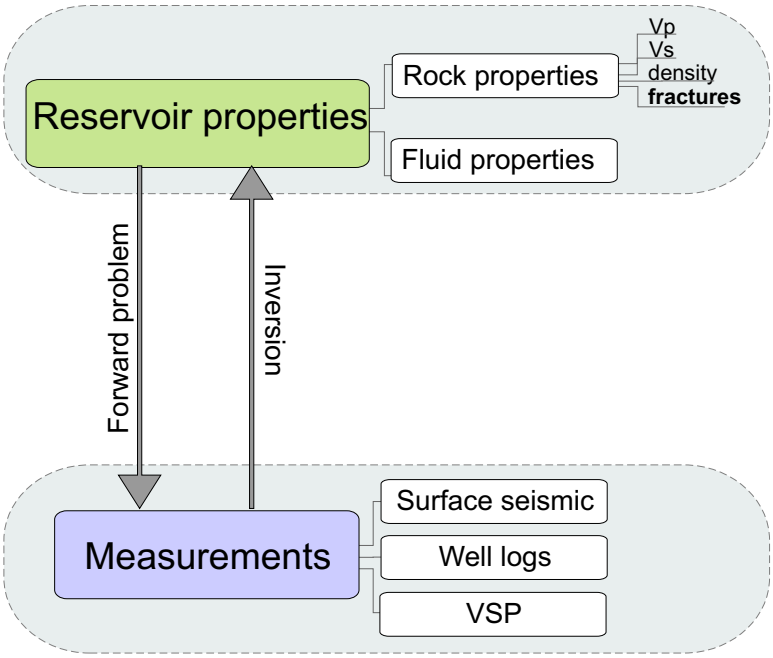

Figure 1.1: Forward and inverse problem for fracture studies in geophysics.

field in Oman, using various geophysical techniques, including attenuation. The acquisition configuration of the data -which consists of walk-around time-lapse VSP's- is almost ideal. On the down side, these are land seismic data with significant noise levels.

Chapter 4 consists of a case study on fractures from the Weyburn field in Canada. I use a compilation of azimuthal analysis techniques on a data set consisting of a 3D-3C (three dimension, three component) time-lapse VSP.

In Chapter 5 I introduce and develop a method for quantitative fracture characterization using a linearised relationship between the seismic signal and the properties of the fractures. I build the relationship by modelling the seismic response for a range of fracture densities and then calculating singular value decomposition on the modelled curves. Furthermore, I apply this model- and statistically-based method to a synthetic data set.

In Chapter 6 I apply the method presented in Chapter 5 to seismic data acquired from a laboratory-scale physical geological model, where the prior knowledge of the fracture network allows me to validate the method in a more realistic setting.

Finally in Chapter 7 I summarise the work presented and discuss the findings from the field studies, the method developed, its potential and limitations. Figure 1.3 summarises the thesis contents per chapter as explained above.

1.2 Data Sets

All data sets used in this dissertation were previously acquired by organizations and companies that are collaborators with the Edinburgh Anisotropy Project (EAP), and I am grateful for their generosity in making them available for my work. However, this also means that their acquisition parameters were not tailored to my project, and thus may not be optimal for application of our techniques; a common situation in geophysical exploration research. The data sets used are as follows,

Weyburn data The 3D time-lapse VSP data set was acquired by a consortium of companies and research institutions from 2004 to 2005. They were provided to EAP by Lawrence Berkley Laboratories.

Oman data This data set was acquired during several years, from 2002 through 2005, by PDO (the state oil company of Oman) in partnership with Shell. It consists of three walk-around VSP's around three wells over a fractured carbonate field.

Well log data The well log data used for building a rock model in Chapter 5 were acquired by TOTAL from a gas reservoir.

Physical modelling data This is a data set acquired by the CNPC Geophysical Key Laboratory at the China University of Petroleum in Beijing.

Both VSP data sets, from the Weyburn field and Oman, were acquired on land over fractured carbonates. Additionally, both include time-lapse measurements at different stages of either CO_2 (Weyburn) or steam injection (Omani field).

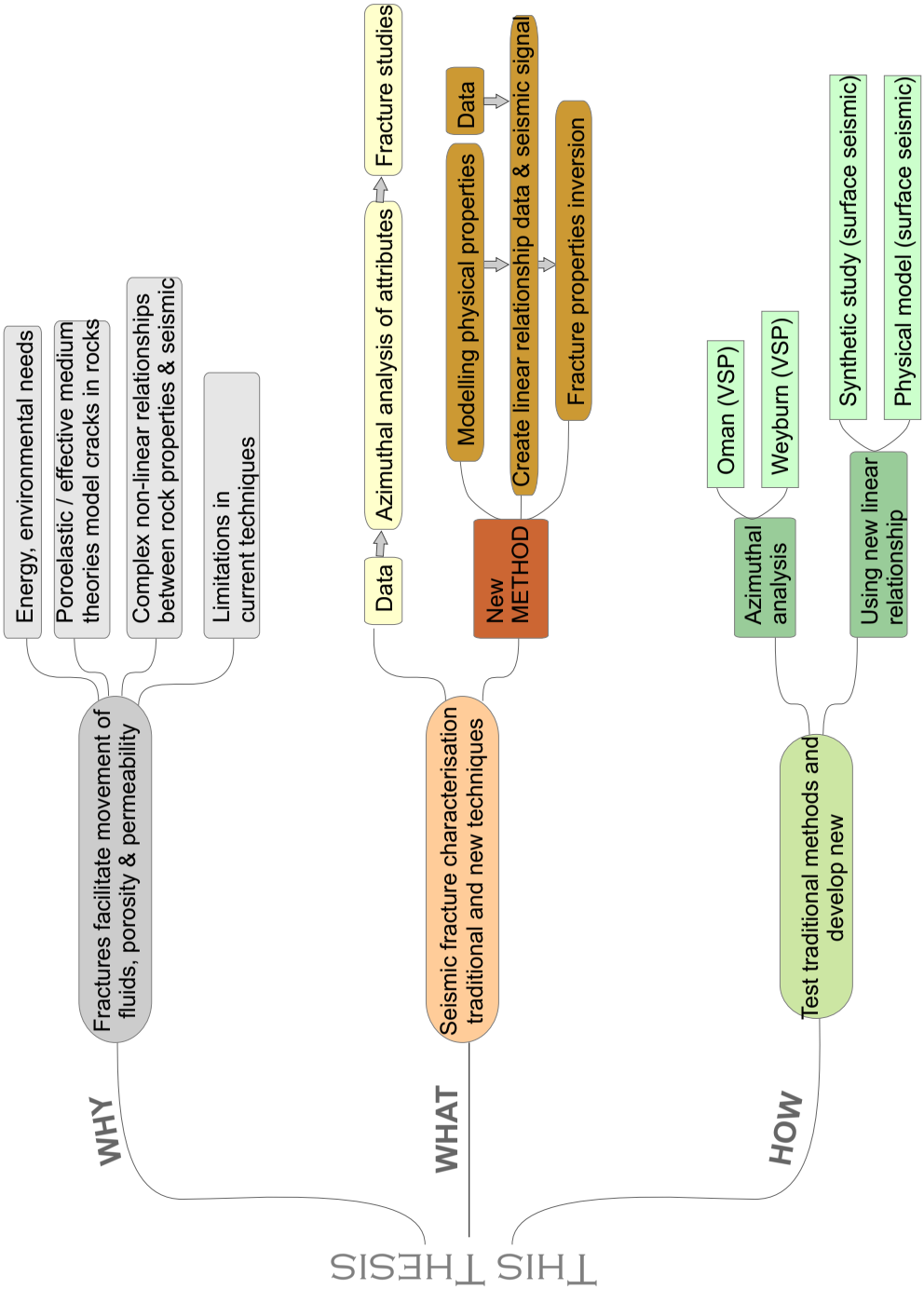

Figure 1.2: Chart sketching the "why, what and how" of this thesis.

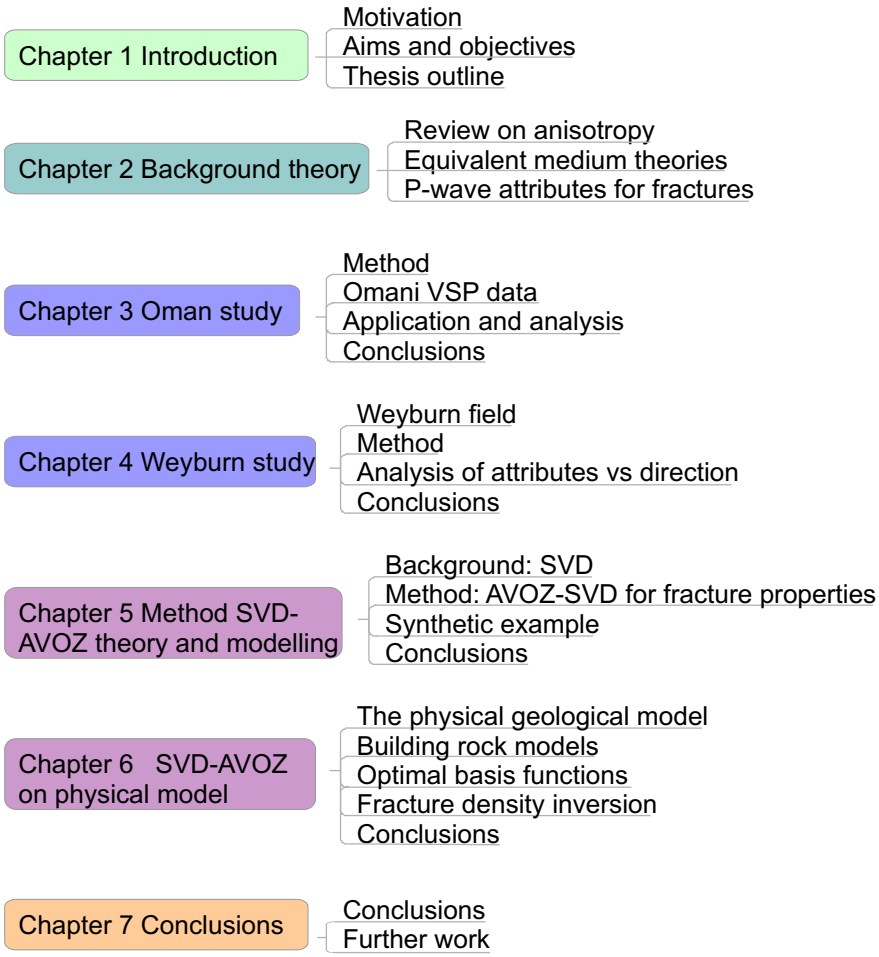

Figure 1.3: Chart of thesis contents by chapters.

The producing reservoir in both cases is located below the deepest geophone in the well.

The Weyburn data set was selected for fracture studies as it has a vast surface and depth coverage, with 247 surface source locations and 80 3C receivers in depth. However, due to the distribution of the sources the azimuthal coverage is not uniform. The Omani data have an acquisition design that is almost ideal for azimuthal studies, as the sources are arranged at a constant spacing in a circle around each well. Yet, there are gaps in the acquisition at certain azimuths in each well. The challenge of working with the Omani data comes from the recorded noise. To minimise the random noise, every trace in the survey acquired in 2002 is the average of recordings of three shots in the same location. For the surveys acquired in 2004 and 2005 the number of shots per shot location was increased to 10.

The laboratory-scale physical geological model data was built for fracture studies by CNPC. I chose it to test the fracture inversion method as it provides data acquired with surface seismic techniques over a model with good understanding of its structure and physical properties.

Throughout this document the locations and field names of some of these data sets may not be specified; if so, it is by request of their providers.

Chapter 2

Theoretical Framework

In this chapter I introduce basic concepts used throughout this thesis. I start by presenting the anisotropy terminology adopted in the following chapters. In the second section I review relevant effective medium theories used to represent a rock when the size of the heterogeneities is much smaller than the wavelength. This is pertinent as in Chapters 5 and 6 I make use of an effective medium model to describe fractured rocks. In Chapters 3 and 4 I use various seismic attributes for fracture studies. For comparison, in the last section of the present chapter I review common seismic attributes used for fracture characterisation.

2.1 Review of Anisotropy

2.1.1 Physical basis

Elastic wave propagation is fundamentally based on the theory of elasticity, where the stress σ_{ik} and strain ε_{ik} tensors are linked together by an equation of state for a given medium. In a linear elastic material this relationship is given by the generalized Hooke's law (Schön, 1998),

$$\sigma_{ij} = C_{ijkl}\varepsilon_{kl} \tag{2.1}$$

where C_{ijkl} is the elastic stiffness tensor containing 81 components. If the strain is expressed in terms of the stresses we then have,

$$\varepsilon_{ij} = S_{ijkl}\sigma_{kl} \tag{2.2}$$

where S_{ijkl} is the tensor of elastic compliances and $S^{-1} = C$. Both S_{ijkl} and C_{ijkl} are rank four elastic tensors, however not all of their 81 components are independent. The symmetry of stresses, which implies that $C_{ijkl} = C_{jikl} = C_{ijlk} = C_{jilk}$, brings the number of independent elastic constants to 36. In addition, the existence of a unique strain energy potential (which requires that $C_{ijkl} = C_{klij}$) further reduces the number of independent elastic constants to 21, which is the maximum number any material can have. Further reductions are possible depending on the symmetry of the material; an isotropic material (with the highest symmetry) can be fully characterized with just two independent elastic constants. A medium with triclinic symmetry (lowest symmetry) requires all 21 constants. Table 2.1 lists the number of independent elastic constants required to fully characterise different symmetry systems.

Symmetry	N
Triclinic	21
Orthorhombic	9
Trigonal	6
Hexagonal (transversely isotropic)	5
Cubic	3
Isotropic	2

Table 2.1: Number of independent elastic constants per symmetry system. (Modified from Schön, 1998)

It is standard practice to use an abbreviated notation for the subscripts of the elastic, strain and stress tensors. This index transformation is done on the pair of subscripts ij and kl as shown in Table 2.2,

ij or kl	I or J
11	1
22	2
33	3
23,32	4
13,31	5
12,21	6

Table 2.2: Index transformation for elastic, stress and strain tensors

2.1.2 Symmetry systems

The different symmetry systems are defined by their elastic tensor as follows (Mavko et al., 1999),

Isotropic (two independent constants)

$$C_{ij} = \begin{pmatrix} c_{11} & c_{12} & c_{12} & 0 & 0 & 0 \\ c_{12} & c_{11} & c_{12} & 0 & 0 & 0 \\ c_{12} & c_{12} & c_{11} & 0 & 0 & 0 \\ 0 & 0 & 0 & c_{44} & 0 & 0 \\ 0 & 0 & 0 & 0 & c_{44} & 0 \\ 0 & 0 & 0 & 0 & 0 & c_{44} \end{pmatrix}, c_{12} = c_{11} - 2c_{44} \tag{2.3}$$

In the isotropic case the elastic constants are related to the Lamé parameters with $c_{12} = \lambda$, $c_{44} = \mu$ and $c_{11} = \lambda + 2\mu$.

Cubic (three independent constants)

$$C_{ij} = \begin{pmatrix} c_{11} & c_{12} & c_{12} & 0 & 0 & 0 \\ c_{12} & c_{11} & c_{12} & 0 & 0 & 0 \\ c_{12} & c_{12} & c_{11} & 0 & 0 & 0 \\ 0 & 0 & 0 & c_{44} & 0 & 0 \\ 0 & 0 & 0 & 0 & c_{44} & 0 \\ 0 & 0 & 0 & 0 & 0 & c_{44} \end{pmatrix} \tag{2.4}$$

Hexagonal or Transversely isotropic (five independent constants)

$$C_{ij} = \begin{pmatrix} c_{11} & c_{12} & c_{13} & 0 & 0 & 0 \\ c_{12} & c_{11} & c_{13} & 0 & 0 & 0 \\ c_{13} & c_{13} & c_{33} & 0 & 0 & 0 \\ 0 & 0 & 0 & c_{44} & 0 & 0 \\ 0 & 0 & 0 & 0 & c_{44} & 0 \\ 0 & 0 & 0 & 0 & 0 & c_{66} \end{pmatrix}, c_{66} = (c_{11} - c_{12}) \tag{2.5}$$

Orthorhombic (nine independent constants)

$$C_{ij} = \begin{pmatrix} c_{11} & c_{12} & c_{13} & 0 & 0 & 0 \\ c_{12} & c_{22} & c_{13} & 0 & 0 & 0 \\ c_{13} & c_{13} & c_{33} & 0 & 0 & 0 \\ 0 & 0 & 0 & c_{44} & 0 & 0 \\ 0 & 0 & 0 & 0 & c_{44} & 0 \\ 0 & 0 & 0 & 0 & 0 & c_{66} \end{pmatrix} \tag{2.6}$$

The structure of the elastic tensor C_{ij}, of each of these symmetries is further illustrated in Figure 2.1 by colour coding the elements of the elastic tensor with the same value.

In this thesis I work with isotropic, hexagonal or transversely isotropic (TI) and orthorhombic symmetries. It can be shown that a material with vertically aligned fractures has a TI symmetry with a horizontal axis of symmetry (abbreviated as HTI). Furthermore, depending on the length and spatial distribution of fractures a fractured medium can show an orthorhombic symmetry. Shales are known for having a TI symmetry with a vertical axis of symmetry (VTI).

For anisotropic materials with TI and orthorhombic symmetry, there are equations relating the density and elastic constants of the material to velocities of the different wave modes (see Mavko et al., 1999, page 22-24).

In materials with TI symmetry and weak elastic anisotropy (explained below), Thomsen (1986) introduced a notation system that has become widely used, as it

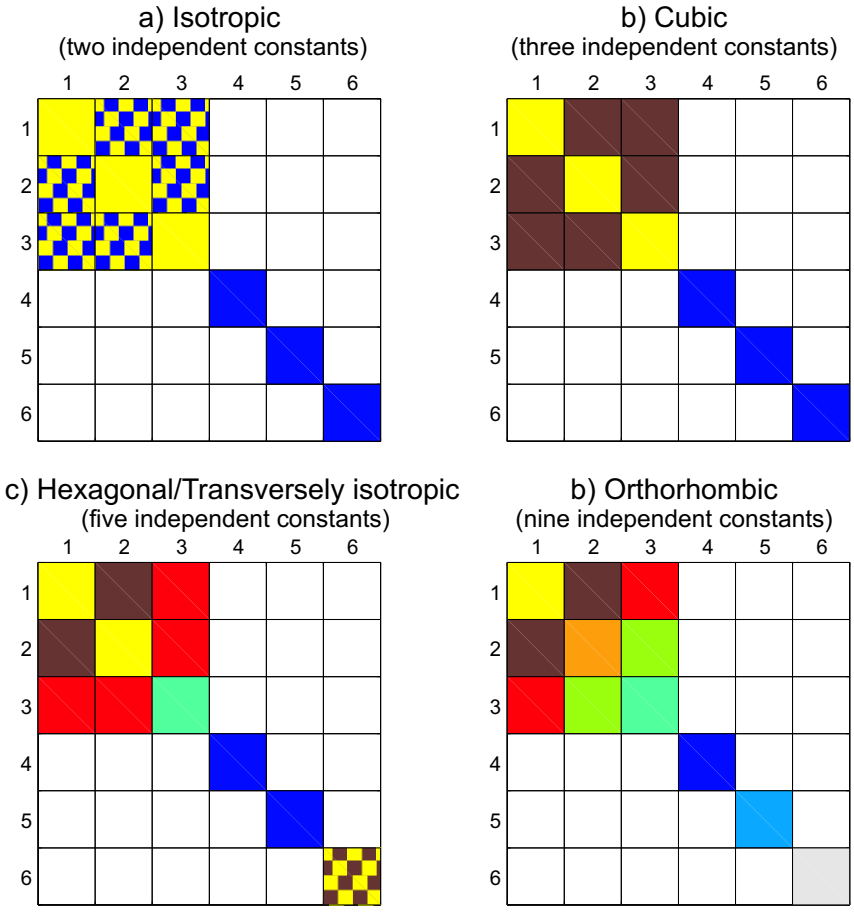

Figure 2.1: Symmetry systems, a)Isotropic, b)Cubic, c)Transversely Isotropic and d)Orthorhombic.

simplifies the equations of velocities of the P- S_V and S_H waves. Thomsen's notation consists of regrouping the elastic constants into three anisotropic parameters (ε, γ and δ) and calculating the P- and S-wave velocities along the symmetry axis. His notation consists of,

$$\begin{aligned} \alpha &= \sqrt{c_{33}/\rho} \\ \beta &= \sqrt{c_{44}/\rho} \\ \varepsilon &= \frac{c_{11} - c_{33}}{2c_{33}} \\ \gamma &= \frac{c_{66} - c_{44}}{2c_{44}} \\ \delta &= \frac{(c_{13} + c_{44})^2 - (c_{33} - c_{44})^2}{2c_{33}(c_{33} - c_{44})} \end{aligned} \tag{2.7}$$

where α and β are the P- and S-wave velocities along the symmetry axis. Thomsen's assumption of weak elastic anisotropy requires that $\varepsilon, \gamma, \delta \ll 1$.

An important observation about the stress-strain relations is that rocks are not ideally elastic materials. The reaction to stresses will also depend on the velocity and history of deformation. This deviation in the requirements of Hooke's law causes two phenomena (Schön, 1998): 1) energy absorption by the material, and 2) differences between dynamic and statically determined elastic moduli.

2.1.3 Fractures

Fractures are planar discontinuities in rocks (Sheriff, 2002) which may significantly affect the permeability of a rock. Their particular effect on the permeability varies depending on whether they are open (increasing permeability) or sealed (decreasing formation permeability). Fractures can form through naturally occurring processes such as folding, faulting, dissecation, cooling, etc.; or they can be induced by subjecting the host rock to high fluid pressure in the borehole, known as hydraulic fracturing (Sheriff, 2002). A set of naturally occurring frac-

tures are shown in Figure 2.2. Furthermore, Figure 2.2b) shows how fracturing can become a conduit for escaping gases to reach the surface.

(a) Basaltic tubes (b) Escaping gases through fractures

Figure 2.2: Outcrops of fractured rocks in Milos island, Greece. a) Shows an excellent example of basaltic tubes, b) Gases are escaping to the surface through the fractured rock.

Crack density

In geophysics cracks are often modelled as a disc or 'penny' shape. Crack -or fracture- density is then defined as (Barton, 2006):

$$e = \frac{Na^3}{V} \tag{2.8}$$

where a is the crack radius, and N is the number of such cracks in a volume V. Crack density is often in the range of 0.01 to 0.05 throughout different geologic and tectonic settings (Leary et al., 1990). Barton (2006) provides the parameters for microcracks, fractures and minor faults so that they have an average crack density of 0.01 (see table 2.3).

Crack denomination	a	N	V
Microcracks	$100\mu m$	10^7	$10cm^3$
Fractures	$1m$	10	$10m^3$
Minor fault	$100m$	10	$1Km^3$

Table 2.3: Parameters for microcracks, fractures and minor faults with a crack density of 0.01. a is crack radius, and N is the number of cracks in volume V.

Crack density is often used for fracture characterisation, as it may be an indicator of the pore space connectivity even though it is independent of the fracture size.

2.2 Equivalent Medium Theories

The common interest in rock physics is to fully characterise the physical properties of rocks. The difficulty lies in the heterogeneous nature of rocks; Schön (1998) lists the following factors as the main drivers in determining rock properties:

Properties of components and volume fractions: mineral composition, porosity and saturation.

Internal geometry (texture and structure): size and shape of grains, arrangement of grains, internal surfaces.

Bonding properties: effects at grain boundaries and interfaces, cementation.

Thermodynamic conditions: pressure, temperature and stress fields.

Despite the diverse nature of these parameters, many theories have been developed to calculate the effective physical properties of the rocks from the properties of its constituents. These so-called effective medium theories calculate the physical properties of the rock at a scale (wavelength) that is much larger than the

scale/size of the grains. I classify these theories based on their conceptual basis in a modification to Schön's (1998) classification as follows,

- Parallel sheets: segregation of different elements into parallel sheets.
- Connected porosity, no specific pore geometry: fluid pressure equilibrium in pores.
- Geometrical inclusion models: isolated ellipsoidal pores of different aspect ratios.
- Fractures: modelling of cracks and fractures as linear slip interfaces, planes of cracks or contacts.

Figure 2.3 shows a classification of relevant effective medium theories based on these criteria. In the following sections I review the main aspects of these theories. It must be noted that the summary I present below is not exhaustive; the purpose is to provide a theoretical basis for the studies of fractures, not a detailed review of these numerous effective medium models.

2.2.1 Parallel sheets

These theories use spatial (volumetric) averaging of the properties of the constituents of the medium to calculate estimates of the composite. Here the assumption is that the individual rock components are isotropic and arranged separately as sheets. The elastic wave is oriented either perpendicular or parallel to the planes of sheets. Voigt and Reuss calculate the shear and bulk modulus for the composite rock under homogeneous stress (Voigt average) and homogeneous strain (Reuss average) conditions (Mavko et al., 1999). These two averages are widely used in rock physics as they provide upper (Voigt) and lower (Reuss) bounds for the elastic constants of a rock with the volumetric partitioning of the

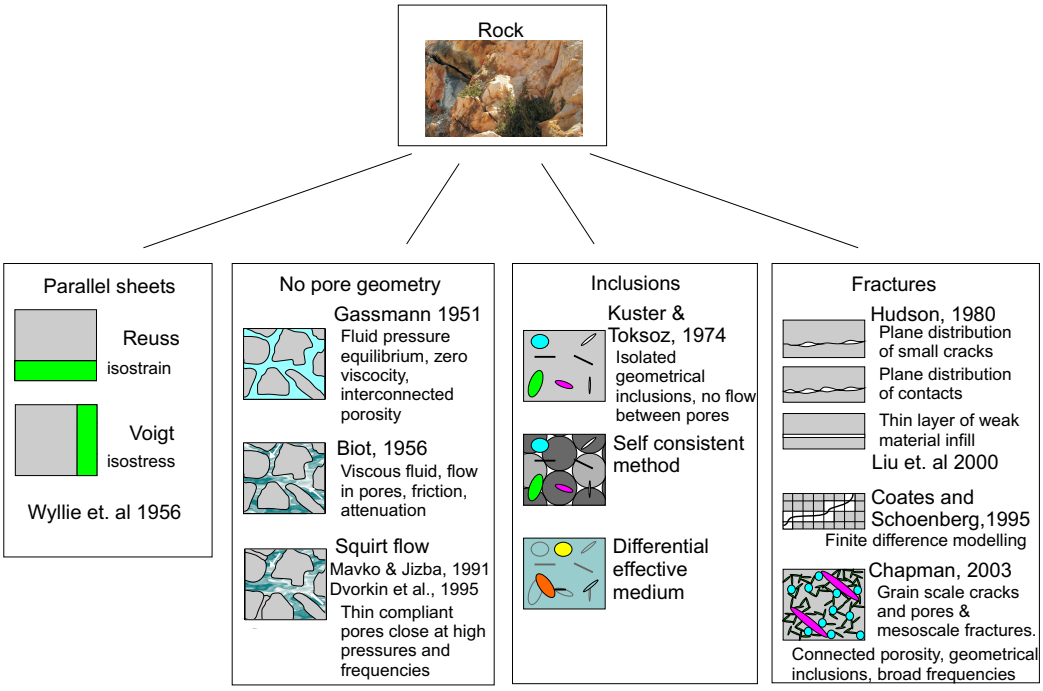

Figure 2.3: Classification of effective medium theories (modified from Schön, 1998).

elements considered. The Voigt effective elastic modulus of a composite is then,

$$M_V = \sum_{i=1}^{N} f_i M_i \tag{2.9}$$

and the Reuss is,

$$\frac{1}{M_R} = \sum_{i=1}^{N} \frac{f_i}{M_i} \tag{2.10}$$

where M_i is the modulus of the the individual element i, and f_i is the volumetric fraction of that element.

Others have used the same conceptual model with added modifications. The well known time-average equation of Wyllie is a good example, as well as the Hill average, which is the arithmetic mean of the Voigt and Reuss bounds. Additionally, Nur (1991) uses experimental data in conjunction with the parallel sheet models to develop the critical porosity model.

2.2.2 No pore geometry

Gassmann

Probably the best known example of effective medium theories that are independent of pore geometry is that developed by Gassmann (1951). Gassmann (1951) calculates the compressional or bulk modulus of a saturated rock based on the modulus of the matrix material (K_o), that of the fluid in the pores (K_{fl}), the porosity (φ) and the modulus of the dry frame (K_{dry}). This relationship is as follows,

$$K_{sat} = K_{dry} + \frac{(1 - \frac{K_{dry}}{K_o})^2}{\frac{\varphi}{K_{fl}} + \frac{(1-\varphi)}{K_o} - \frac{K_{dry}}{K_o^2}} \tag{2.11}$$

The dry-frame bulk modulus was a new concept introduced by Gassmann; it consists of the bulk modulus of the mineral frame with low amount of humidity or the irreducible water saturation.

Gassmann's theory assumptions (Wang, 2001) are that,

1. The rock (matrix and frame) is homogeneous and isotropic on a macroscopic scale
2. All pores are interconnected or in communication
3. The fluid in the pores is frictionless and moveable
4. The system (rock-fluids) is closed
5. The pore fluids do not interact with the matrix
6. The relative motion between rock and fluid is negligible compared to the movement of the composite when excited by a wave

The first assumption that the rock is homogeneous and isotropic implies that all grains have the same bulk modulus. This assumption is violated if the mineral matrix is composed of elements with a large contrast in the elastic stiffness or if

it is composed of minerals with a preferred anisotropic orientation (Smith et al., 2003).

The second assumption requires that all pores must be interconnected, it is worth mentioning that this is regardless of the shape of the pore. This assumption is to allow the fluid to equilibrate within the time frame of half a wave period. For seismic waves, this criterion will be met only by unconsolidated sands (Wang, 2000). Furthermore, in low porosity rocks, or rocks with poor pore connectivity such as carbonates, this assumption will be strained (Smith et al., 2003). Adam et al. (2006) show that for carbonates with compliant pores or microcracks, laboratory measurements of brine saturated bulk modulus at seismic frequencies (and high differential pressures) don't match those predicted by Gassmann's theory. The third assumption requires the fluid to have zero viscosity, again so that the pore fluid can fully equilibrate (Wang, 2000).

It is often erroneously stated that one of Gassmann's assumptions is that the saturated and dry frame shear moduli are equal. As Berryman (1999) emphasises, this is a result of Gassmann's equation, not an assumption. Since the shear modulus of fluids is zero, it is then reasonable to expect that the shear modulus of the dry and saturated rock are equal. The fifth assumption is that there is no interaction between the fluids and the rock frame. However, in a reservoir (especially carbonates) when substituting a gas for a brine, due to the nature of the new fluid (viscosity, pressure, temperature, etc) an interaction between the fluid and the matrix is likely to occur which can change the properties of the matrix (Adam et al., 2006). Laboratory measurements in carbonates have shown that the shear modulus of the brine saturated rock is weaker (by $\sim 20\%$) than the dry frame modulus at seismic frequencies (Adam et al., 2006).

The sixth assumption limits Gassmann's formulation to frequencies that are low enough so that differences in pore pressure caused by external stresses (passing of wave) have time to equilibrate (Mavko and Jizba, 1991).

Despite the caveats of special cases that violate Gassmann's assumptions (discussed above), equation 2.11 is used extensively in the oil industry to model different fluid scenarios that might generate a seismic anomaly, as it works particularly well for high porosity sandstones. When substituting brine for gas or oil in a sandstone, the bulk density should always decrease and the shear velocity should always increase (Smith et al., 2003). This is due to the dependence of the shear velocity on the inverse of the bulk density. Smith et al. (2003) and Wang (2000) thoroughly discuss the assumptions, workflow, applicability and limitations of Gassmann's theory for fluid substitution, with descriptions on how to obtain the different fluid and rock properties required.

Gassmann's equation has been hard to verify in the laboratory due to the low frequency assumption. A core is required to have a length of at least half the wavelength to be measured in the laboratory, and at low (seismic) frequencies this would yield unfeasibly large cores. Adam et al. (2006) overcome this by using a strain-stress method in core samples of standard size (diameter and height $\sim$3.5cm). The measured strains are converted to the Young modulus and Poisson's ratio, and these in turn are converted to shear and bulk modulus.

Brown and Korringa (1975) extend Gassmann's theory for microscopically heterogeneous materials, and lift the restriction that all pores be interconected. By doing this they add an extra effective compressibility modulus to the equation as follows,

$$(K_{sat} - K_o)^{-1} = (K_{dry} - K_o)^{-1} + [(K_{fl} - K_\varphi \varphi)]^{-1} \tag{2.12}$$

For homogeneous materials $K_o = K_\varphi$. They treat all fluid inclusions that are not interconected as part of the volume of the solid material. Although K_φ has a physical definition (as the fractional volume change of the porous space as a function of pore pressure when the differential pressure is kept constant), obtaining its value may be a limitation on the applicability of equation 2.12.

Biot

Biot (1956) derived formulae for the velocities of P- and S-waves as a function of frequency for a poroelastic material, in terms of the dry rock properties and the saturating viscous fluid. In the low frequency limit Biot's theory reduces to Gassmann's calculations. However, in contrast to Gassmann, Biot introduced fluid viscosity and permeability of the frame into his model, and allowed fluid movement between connected pores. This movement generates energy losses from viscous friction, and thus provides a model for attenuation.

One of the main outcomes of the Biot theory is that there exist two compressional waves, the first being the normal P-body wave, and the second being a lower frequency highly attenuated diffusion wave that has a propagation analogous to that of heat conduction. Geertsma and Smit (1961) calculate the velocities and attenuation for the first and second waves at the limits of zero frequency (which reduces to the Gassmann equations) and infinite frequency. They show that the second wave of Biot attenuates rapidly with distance, so it is not expected to be recorded in seismic surveys. They also show that a wave of the second kind is created at an interface between two porous solids saturated with different fluids.

The second major outcome of Biot's theory is that wave velocities are shown to be frequency dependent. He shows that there is a characteristic frequency which divides the wave behaviour in two distinct ranges. This characteristic frequency depends on the viscocity (η) and density (ρ_{fl}) of the fluid, and the permeability (κ) and porosity (φ) as follows,

$$f_c = \frac{\varphi \eta}{2\pi \rho_{fl} k} \tag{2.13}$$

At low frequencies the wave is dominated by laminar drag against the solid. At high frequencies the effects of fluid inertia control the wave behaviour (Biot, 1956). Mavko et al. (1999) interpret f_c to be the frequency where the viscous forces acting on the fluid (at low frequencies) equal the inertial forces (at higher frequencies).

Squirt flow

Nevertheless, it has been shown that seismic velocities measured in the laboratory at ultrasonic frequencies are often faster than those predicted by either Gassmann or Biot (Mavko and Jizba, 1991). This mismatch increases with frequency and viscosity and decreases with effective pressure. Mavko and Jizba (1991) propose a model that, unlike the Gassmann formulation, allows for local grain-scale flow, which they argue is the reason for the disagreement between the measurements at high frequencies and Gassmmann or Biot's predictions.

Mavko and Jizba (1991) explain that when a load is applied to a rock at low frequencies the fluid can move between the pores easily. However, at high frequencies due to the viscous effects pressure builds up in the thinner pores and they become isolated from the local flow. This effect makes the thinner pores stiffer at higher frequencies, increasing the bulk modulus of the frame. In their model, Mavko and Jizba (1991) calculate these unrelaxed saturated moduli K_{uf} and μ_{uf} with the following equations,

$$\begin{aligned} \frac{1}{K_{uf}} &\approx \frac{1}{K_{dry-hiP}} + \left(\frac{1}{K_{fl}} - \frac{1}{K_o}\right)\varphi_{soft} \\ \left(\frac{1}{\mu_{uf}} - \frac{1}{\mu_{dry}}\right) &= \frac{4}{15}\left(\frac{1}{K_{uf}} - \frac{1}{K_{dry}}\right) \end{aligned} \tag{2.14}$$

where $K_{dry-hiP}$ is the effective bulk modulus at high pressure and φ_{soft} is the soft porosity, or compliant porosity that closes at high pressures.

The main outcomes of Mavko and Jizba's model are 1)they calculate the saturated unrelaxed frame modulus based on K_{dry}, K_o, K_{fl} (as in Gassmann), plus $\phi(p)$ and $K_{dry}(p)$, where p is pressure. 2)They find that the change between the unrelaxed saturated shear modulus and the dry shear modulus is proportional to the change in the bulk moduli, which suggests that they are caused by the same effect, as shown in equation 2.14 (Mavko and Jizba, 1991).

They do these calculations for high and low frequency limits, with the low frequency being the same result as Gassmann. They do not consider a range of

frequencies as these would involve making assumptions on the pore shape.

The main assumptions of their model are that (Mavko and Jizba, 1991): 1) the grains and matrix are homogeneous and isotropic; 2) the pore space that is unrelaxed at high frequencies is the same one that closes at high confining pressures; 3) the compressibility of the stiff pores at any pressure is the same compressibility of the whole composite at high pressures; 4) stiff pores conserve their volume, whereas soft pores close under compression.

Dvorkin et al. (1995) extend the squirt flow model to calculate velocities and attenuation as a function of frequency. In the low frequency limit their calculations are equal to those provided by Gassmann. However, in the high frequency limit their velocities can be significantly higher than those of Biot's theory.

2.2.3 Inclusion models

In contrast to the rock models provided in the previous section, where the background is an empty (or fluid filled) space, and the space is filled with grains, in this section the problem is posed starting from a solid matrix where geometrical inclusions are introduced in the background solid. The shape of these inclusions can vary between spheres, ellipsoids or needles, and they can be filled with gases, fluids, solid materials or remain empty.

Kuster and Toksöz (1974) calculate the elastic moduli of a two phase composite given the concentration, shape and properties of both the inclusion material and the background matrix. They show that low aspect ratio (thin) inclusions have a larger effect on the velocity of the composite than those with high aspect ratio (spherical). Furthermore, they show that a small concentration of thin inclusions can change the velocity of the medium by up to 10%.

Kuster and Toksöz's (1974) expressions for the effective moduli K^*_{KT} and μ^*_{KT}

are generalised as follows (Mavko et al., 1999),

$$\begin{aligned}(K^*_{KT} - K_m)\frac{(K_m + \frac{4}{3}\mu_m)}{(K^*_{KT} + \frac{4}{3}\mu_m)} &= \sum_{N}^{i=1}(K_i - K_m)P^{mi} \\ (\mu^*_{KT} - \mu_m)\frac{(\mu_m + \psi_m)}{(\mu^*_{KT} + \mu_m)} &= \sum_{N}^{i=1}(\mu_i - \mu_m)Q^{mi} \end{aligned} \tag{2.15}$$

where x_i is the volumetric concentration of inclusions of type i in a background with moduli K_m and μ_m, and $\psi = \frac{\mu}{6}\frac{9K+8\mu}{K+2\mu}$. The coefficients P^{mi} and Q^{mi} contain the effect of an inclusion of type i in a background m. For an explicit form of coefficients P^{mi} and Q^{mi} see Mavko et al. (1999). The dry elastic moduli are calculated by setting the moduli of the inclusions to zero.

A limitation of the Kuster and Toksöz (1974) model is that it only allows for a low concentration of inclusions, which are randomly placed, isolated and do not interact with each other. Because the inclusions are isolated from one another, there is no flow of pore fluids between them. The Kuster and Toksöz (1974) model thus simulates high frequency data such as those measured in the laboratories (Mavko et al., 1999).

Other approaches, such as the self consistent (SC) method and the differential effective medium method (DEM), have been developed by others to allow for a higher concentration of inclusions (Mavko et al., 1999). The DEM method consists of starting with a 100% concentration of one material and incrementally adding a small concentration of the second material, such that the new background material becomes the effective modulus of the previous step until the final desired concentration of the inclusions is reached.

In the self consistent approach all the components of the materials (including the solid parts) are introduced with specification of their shape, moduli and concentration into an unknown background. These background effective moduli can then be solved for iteratively, yielding the effective moduli of the composite. Berryman (1980) presents the following equations for N phases of concentrations

x_i (Mavko et al., 1999),

$$\begin{aligned} \sum_{i=1}^{N} x_i(K_i - K^*_{SC})P^{*i} &= 0 \\ \sum_{i=1}^{N} x_i(\mu_i - \mu^*_{SC})Q^{*i} &= 0 \end{aligned} \tag{2.16}$$

In contrast to Gassmann, Biot and the squirt flow models discussed above, the inclusion models specify the exact shape of the inclusions with idealised ellipsoidal geometries of varying aspect ratio. Thus, the effect of flat crack-like pores can be calculated using low aspect ratios. However, because the inclusions are placed randomly (with no specific orientation) anisotropic effects due to the alignment of cracks can not be modelled with these techniques.

Endres and Knight (1997) consider fluid pressure communication between the inclusions, in contrast to the inclusion models discussed above, where there is no communication between inclusions. Thus, Endres and Knight (1997) are able to obtain the elastic response of the composite rock at different frequencies and for different pore shapes, with the low frequencies corresponding to complete pressure communication. They find two major outcomes of these considerations: 1) they show the equivalence between the Biot-Gassmann theory and inclusion models (when only spherical pores are used), 2) they show the dependence of the elastic moduli on fluid pressure communication and pore geometry.

2.2.4 Fractures

Linear slip

Schoenberg (1980) models fractures as imperfectly bonded interfaces between two elastic media. At these interfaces or surfaces, the stresses caused by the passing of a seismic wave are continuous. However, the displacement is not continuous, and slip occurs.

The small displacement is linearly dependent on the stress. For viscoelastic materials this dependence is complex and varies with the frequency of the wave. Schoenberg (1980) proposes a linear relationship between the displacement Δu and the stress σ which are linked by the fracture compliance Z,

$$\Delta u = Z\sigma.n \tag{2.17}$$

where **n** is a unit vector normal to the fracture. Schoenberg (1980) shows that the compliance matrix of the fracture can be represented with just two independent compliances (the normal and tangential fracture compliances), which are arranged in the diagonal of the compliance matrix.

Coates and Schoenberg (1995) do finite difference modelling of faults and fractures by regarding them as linear slip interfaces based on the theory of Schoenberg (1980). They calculate the compliance of a rotationaly symmetric fracture as,

$$s_f = \frac{1}{L}\begin{pmatrix} 0 & 0 & 0 & 0 & 0 & 0 \\ 0 & 0 & 0 & 0 & 0 & 0 \\ 0 & 0 & Z_N & 0 & 0 & 0 \\ 0 & 0 & 0 & Z_T & 0 & 0 \\ 0 & 0 & 0 & 0 & Z_T & 0 \\ 0 & 0 & 0 & 0 & 0 & 0 \end{pmatrix} \tag{2.18}$$

where Z_N and Z_T are the normal and tangential fracture compliances respectively. Coates and Schoenberg (1995) write the effective compliance of the cell as the sum of the compliance of the background rock s_b and that caused by the fracture s_f,

$$s = s_b + s_f \tag{2.19}$$

where $c = s^{-1}$. Coates and Schoenberg (1995) then write the elastic constants of the rock in terms of the stiffness tensor of the background rock and the compliance

due to the fracture as,

$$c = s^{-1} = [(I + s_f s_b^{-1})s_b]^{-1} = c_b(I + s_f c_b)^{-1} \tag{2.20}$$

In the Coates and Schoenberg (1995) model, the properties of every cell intersected by the fracture plane is replaced by the effective medium properties of the background rock and the fracture compliance. Within each cell, if the length of the fracture is Δl then Coates and Schoenberg (1995) propose that the elastic constants of the rectangular region with area Δlh are proportional to h such that,

$$c_{ij} = h\tilde{c}_{ij} \tag{2.21}$$

where $\tilde{c}_{ij}$ has units of $stress/length$ and h can be written as $h = \frac{\Delta A}{\Delta l}$, with ΔA being the area of the cell. Furthermore they define L as $\frac{\Delta l}{\Delta A}$.

By substituting equation 2.18 into equation 2.20 they calculate the elastic constants of the effective medium for each cell that is intersected by the fracture plane in terms of the stiffness tensor of the background rock, the normal and tangential compliances of the fracture, and the length L.

Planes of cracks or welds

Liu et al. (2000) investigate the effect of aligned cracks or fractures on seismic wave propagation. They present three models that represent the state of a fracture at different stages of its development: 1) small and isolated areas of slip or cracks distributed on a plane; 2) areas of contacts distributed on a plane; 3) a thin layer in between two parallel sheets filled with a weak material. It is expected that the fracture evolves progressively from model 2 to 1 as the rock is subject to compressive stresses and the contact area between the two surfaces involved increases. Model 3 is commonly used for representing fractures caused by hydraulic fracturing (Liu et al., 2000).

Liu et al. (2000) calculate analytic expressions for the fracture compliance and the elastic constants of the fractured rock for the three models mentioned above. In their work, they model a fracture as a cluster of small cracks (or contacts), a fault is regarded as a cluster of fractures. A practical outcome of their study is that they find the fracture compliances to be related to physical parameters describing the microstructure of the fractures. For all models the fracture compliance will depend on the Lamé constants (λ and μ) of the unfractured rock, the fracture radius a_f and the parameters U_{33} and U_{11}, which capture the response of a single crack to shear tension and traction. U_{33} and U_{11} will change depending on the properties of the material filling the cracks or fracture. Hudson (1981), Hudson (1988) and Hudson et al. (1996) give explicit forms of U_{33} and U_{11} considering fluid filled cracks, partially saturated cracks, and fluid flow between pores and cracks respectively.

Additionally, for model 1 the fracture compliance S^{-1} is a function of $\gamma_c, a_c, \alpha, \beta$ and ϵ, where γ_c is the number of elementary cracks per unit area, a_c is the average radius of a crack, α and β are the P and S wave velocities of the unfractured rock, and ϵ is the crack density. For model 2 additional parameters govern the fracture compliance such that $S^{-1}(\gamma_w, b, e_f, a_f)$, where γ_w is the number of contacts per unit area, b is the average radius of the contacts (welded regions), e_f is the density of contacts on a fracture, and a_f is the mean fracture radius.

In model 3 parameters corresponding to the infill material, such as the Lamé constants for the fluid μ_f, λ_f, and the fluid viscosity η_f come into play. The other governing parameters for the fracture compliance of model 3 are the average fracture aperture d, the porosity of the fractured material ϕ, the frequency w and the fracture density ϵ_f, such that $S^{-1} = S^{-1}(\mu_f, \lambda_f, \eta_f, d, \phi, w, \epsilon_f)$.

Liu et al. (2000) show that through the fracture compliances it is possible to estimate the infill of the cracks or fractures. More specifically, the ratio of the normal to shear compliances is used as an indicator, with $Z_N/Z_T \approx 1$ for dry cracks, and $Z_N/Z_T \approx 0$ for liquid filled cracks. Lubbe et al. (2008) measured

fracture normal and shear compliances in the laboratory for rocks with dry and fluid (honey) filled fractures. Lubbe et al. (2008) use a relationship from the linear slip theory that relates the fracture compliances to the acoustic impedance of the unfractured rock and the reflection coefficient of the fractured interface. The ratio of their measurements agree with Liu et al. (2000) for dry cracks, yet for fluid filled cracks they suggest that a ratio of $Z_N/Z_T \approx 0.5$ is more appropriate.

When fractures are not completely aligned, Liu et al. (2000) propose separating them into different aligned fracture sets, calculating their compliances and then adding the resulting fracture compliances. The total fracture density is the sum of the individual ones, and the average polarisation is weighted by the fracture density such that,

$$\epsilon_{total} = \epsilon_1 + \epsilon_2, \tag{2.22}$$

and,

$$\varphi_{average} \approx \frac{\epsilon_1\varphi_1 + \epsilon_2\varphi_2}{\epsilon_1 + \epsilon_2}, \tag{2.23}$$

where ϵ_1 and ϵ_2 correspond to the individual fracture densities and φ_1 and φ_2 to the polarisation of each fracture set.

In their study Liu et al. (2000) assume that for model 1 the crack density is very small ($\epsilon_c \ll 1$) and for model 2 that the density of contacts is very small ($\epsilon_w \ll 1$). Theoretically, in the region where these two models meet, these conditions are not met and neither model is valid. The weak assumption is that ϵ takes values up to 0.1. Nevertheless, Liu et al. (2000) show that it is possible to apply their work using models 1 and 2 for fracture densities greater than 0.1.

Cracks, pores and meso-scale fractures

Chapman et al. (2002) develop a poroelastic model with varying frequency for a pore space consisting of two types of pores: spherical pores and small aspect ratio cracks randomly oriented. Their model is consistent with the Gassmann theory at low frequencies and predicts the slow P-wave derived by Biot (1956).

Chapman et. al.'s (2002) model is also in agreement with the model of Endres and Knight (1997), with the additional consideration of allowing for macroscopic flow at high frequencies. A new parameter introduced by Chapman et al. (2002) is the timescale relaxation parameter τ, which will mark the low and high frequency ranges. Chapman et. al.'s (2002) main outcome is that they show the dependence of the elastic properties on the permeability of the rock, effective pressure, viscosity of the fluid and frequency of the measurement.

Chapman (2003) expands on Chapman et al. (2002) by introducing movements of fluids at two different scales, the grain scale (squirt flow) and the fracture scale. To this end, he considers the presence of another set of cracks in the model, which are aligned and larger in size (meso-scale cracks). In the presence of large fractures the main outcomes of Chapman (2003) are that 1) frequency dependent anisotropy of the P-wave velocity, S-wave velocity and attenuation can occur in the seismic frequency band, 2) the magnitude of this variation will depend on the equant porosity (porosity due to the small spherical pores). This is due to the fact that as the equant porosity increases the fluid from the cracks or fractures are able to flow into the circular pores making the crack-like pores more compliant. 3) At low frequencies (i.e. 40Hz) the shape of the P-wave anisotropy presents a $\cos 2\theta$ behaviour, whereas at high frequencies (i.e. 1KHz) it exhibits a $\cos 4\theta$ form, where θ is the azimuthal angle.

Chapman (2003) shows that the effective elastic stiffness of the rock can be written as,

$$C = C_0 + \phi C_1 + \varepsilon_2 C_2 + \varepsilon_f C_f \tag{2.24}$$

where ϕ is the porosity, ε_2 and ε_f are the crack and fracture density, and C_1, C_2, and C_3 are the elastic stiffnesses due to the effect of the porosity, cracks and fractures. There are two time-scale parameters in Chapman (2003), which affect the elastic stiffnesses depending on the relationship between the size of cracks and fractures. The time scale parameters τ_f and τ_m are related by,

$$\tau_f = \left(\frac{a_f}{a_m}\right) \tau_m \tag{2.25}$$

where τ_f is related to the flow due to the larger fractures and τ_m is related to the microstructural squirt flow. a_f is the fracture radius and a_m is the size of the pores and microcracks. The dependence on frequency is dictated by two terms: $(1 + iw\tau_f)^{-1}$ and $[(1 + iw\gamma\tau_m)/(1 + iw\tau_m)]$. The first is related to fluid flow between fractures and pores, and the second is related to flow at the grain scale between cracks and pores (Liu et al., 2007).

Fracture compliance and seismic data

A common procedure in evaluating the effect of fractures in the seismic data involves reservoir modelling. As Worthington (2008) mentions, even if a unique answer is not expected, seismic data can constrain the range of suitable reservoir models. The general approach involves calculating anisotropy from borehole, VSP and surface seismic data. This information is then used to create multiple realizations of a fractured reservoir model from which synthetic seismic data can be generated. The resulting synthetic seismic is then compared to the measured seismic and mismatching results lead to disregarding the reservoir model and updating the reservoir grid for a better match.

If the maximum fracture compliance of a set of fractures can be estimated, this can be used in the reservoir model, and the maximum anisotropic effect in the seismic can be obtained (Worthington, 2008). It would then be possible to evaluate the characteristics of the fractures that will be detected with the seismic data. The presence of fluids in the cracks will make the cracks stiffer. Furthermore as the frequency of the measurement increases the fractures will become stiffer as the fluids in the crack will not have enough time to equilibrate. Worthington (2008) calculates the maximum normal compliance Z_n of a dry circular fracture with a simple equation that depends on the radius of the crack, Poisson's ratio and Young modulus of the rock matrix (uncracked). The fracture will close when the stress normal to the fracture equals b/Z_n, where b is the fracture width (Worthington, 2008). Given the crack aspect ratio, V_p, V_s and density of the

matrix, it can then be calculated whether at reservoir depths the cracks will be open or closed.

At well locations fracture compliances can be estimated from wireline logs and VSP data. Yet, as Worthington (2007) emphasises, there are not enough measurements of fracture compliance of subsurface rocks that can be used to reliably model the seismic response. The scarcity of these measurements is due to the difficulty in separating the effect of fractures from that of the rock matrix (Worthington, 2007). Lubbe and Worthington (2006) calculate fracture compliance from field measurements (cross-hole and sonic data), and compare them to compliances of fractures at the same location resulting from core measurements. They find that the compliances from field measurements are an order of magnitude higher than those from the cores. Lubbe and Worthington's (2006) work highlights the differences between fracture compliances obtained from measurements at different scales. Worthington (2008) presents a compilation of fracture compliances from field measurements, and Worthington (2007) emphasises three points, 1) the fracture compliance seems to increase as the size of the fractures increases, 2) there are very few measurements to build a robust relationship between the fracture size and fracture compliance, and 3) the need for such a scaling relationship, that would allow modelling of the fracture compliance based on field measurements and empirical relationships and not solely on theoretical estimates as is the current practice.

Limitations of effective medium theories

It is worth mentioning that some of the assumptions common to effective medium theories may not be exhibited by naturally occurring fractures. Marrett et al. (2007) discuss these assumptions and common problems found in studies of fractures using geophysical methods. They emphasise that fractures in the subsurface are not found equally spaced, but tend to be distributed in clusters, specially for the case of large fractures. A few large interconnected fractures will then in-

crease the permeability of the rock significantly compared to the same number of large but isolated fractures. In addition they demonstrate that the size of fractures varies following a power law distribution, so the assumption of a single fracture size is unrealistic. They also show that open fractures, contrary to what is commonly assumed in geophysical analysis, are not necessarily parallel to the maximum horizontal stress. Precipitation of cement during or immediately after the formation of the fractures can make them stiffer and more resistant to closing under high pressures, or can completely seal the fracture. Marrett et al. (2007) also elaborate on the common assumption of a single set of aligned fractures. They mention that rocks may have many sets of open fractures, and within each set fractures are not always parallel. They explain this by isotropic loading which may lead to the generation of randomly orthogonal fracture sets, or by the perturbation of the stress field due to the presence of large faults. Furthermore, in the presence of an orthogonal set of fractures the resulting anisotropy may be less than that from each individual fracture set (Marrett et al., 2007).

2.3 P-wave attributes for fracture studies

Although shear wave splitting (birefringence of S-wave) has proved to be a useful tool in seismic fracture characterisation (Mueller, 1992, Crampin, 1985) there are various reasons for the continued use of P-wave data to this end. Tsvankin and Lynn (1999) list the following advantages for using P-wave data, 1) lower cost of P-wave acquisition compared to surveys for acquiring S-waves, 2) usually higher data quality of P-waves compared to S-waves, 3) development of recent azimuthal techniques on P-wave data for obtaining principal directions and magnitude of anisotropy. To this list I add that the industry has a large history of acquiring P-wave seismic data (Corrigan et al., 1996) and thus the availability of P-wave data for research purposes is higher than that of S-wave surveys, as shown in the data examples of this thesis.

2.3.1 Travel time

Differences in travel time with azimuth have been used to determine fracture orientations (Li, 1999). Li (1999) develops a method for detection of the fracture orientation using differences in travel time to the bottom of the fractured layer using two sets of orthogonal 2D seismic lines that intersect at one point. For an HTI medium Li (1999) obtains a simple analytical expression for the travel time difference in a direction perpendicular and parallel to the fractures,

$$\Delta t(\phi, x) = (t_{\perp} - t_{\parallel}) cos2\phi = B_0(x, \epsilon, \delta) cos2\phi \tag{2.26}$$

where x is offset, ϕ is the azimuthal angle of the line with respect to the fracture strike, $t_{\perp}$ and $t_{\parallel}$ are the travel times in directions perpendicular and parallel to the fractures respectively, and $B_0(x, \epsilon, \delta)$ is independent of azimuth and depends on Thomsen's parameters ϵ and δ (see Li, 1999 for an explicit form of B_0). Although the method was developed for an acquisition geometry with certain restrictions, in general travel time differences can be used to detect fracture orientations if a wide range of azimuths and large offsets are available. Additionally, as Li (1999) concludes, offset to depth ratios to the bottom of the fractured layer are required to be greater or equal to 1 (up to 1.5), for a reliable quantification of the moveout difference.

2.3.2 Velocities

Grechka and Tsvankin (1998) derive analytical expressions for the normal move-out velocity in VTI and orthorhombic media. In general they find that this velocity follows an ellipse in the horizontal plane depending on the properties of the medium. For a fractured reservoir presenting an orthorhombic symmetry, the symmetry planes could be inverted following Grechka and Tsvankin (1998).

Corrigan et al. (1996) analyse seismic data and find azimuthal variations in the P-wave velocities on 3D surface seismic due to the presence of fractures in the

reservoir of their study. The direction of maximum velocity obtained from normal move-out (NMO) is consistent with well log and VSP data as that of the fracture plane. Corrigan et al. (1996) use a normal moveout equation that accounts for azimuthal anisotropy; so that it will depend on the travel time at zero offset, the offset, velocity ellipticity, shot-receiver azimuth, and fracture azimuth.

Crampin et al. (1980) use velocity anisotropy to map cracks in limestone at three different sites. They show that the same crack density and orientation can display different azimuthal variations depending on the saturating fluids of the cracks.

In a recent study, Wilson et al. (2009) extend the two term AVO approximation of Smith and Gidlow (1987) for the isotropic case to include frequency dependence. The resulting relationship would then allow inversion for the P-wave velocity dispersion properties that are often associated with hydrocarbons (Wilson et al., 2009).

2.3.3 Amplitudes

Analysis of amplitudes from reflection data are often favoured over velocity analysis for fracture characterisation, as they have a higher vertical resolution and are more sensitive to the properties of the reservoir (Sayers, 2007). The use of amplitude analysis versus offset (AVO) as a means for studies of rock properties started with the work of Ostrander (1984). In current exploration geophysics it is now a routine procedure.

The reflection and transmission coefficients of an incident plane at an interface between two isotropic media are given analytically by Zoeppritz (1919) (Mavko et al., 1999). A practical form of these equations using matrix notation is given by Aki and Richards (1980). Yet even when both media are isotropic, the algebraic complexity of the relationship between the physical parameters and the reflection coefficient (at an incidence angle different from the vertical zero offset) has led

to the inversion of physical properties to be based on linearised approximations. Commonly used approximations for isotropic media include those given by Shuey (1985), Smith and Gidlow (1987) and Hilterman (1989).

For anisotropic media the numerical complexity also obscures any insight into the effect of the physical properties in the AVO signal (Rüger, 2001). Rüger (1995) derives approximate equations for the P-wave reflection coefficient in VTI and HTI symmetries at the symmetry planes. Rüger (1996) extends the work of Rüger (1995) to arbitrary azimuths in HTI and orthorhombic media. Rüger's approximation of the reflection coefficients for an arbitrary azimuth (ϕ) and incidence angle (θ) in HTI media is as follows,

$$R_P(\theta,\phi) = \frac{1}{2}\frac{\Delta Z}{\bar{Z}} + \frac{1}{2}\left\{\frac{\Delta\alpha}{\bar{\alpha}} - \left(\frac{2\bar{\beta}}{\bar{\alpha}}\right)^2\frac{\Delta G}{\bar{G}} + \left[\Delta\delta^{(V)} + 2\left(\frac{2\bar{\beta}}{\bar{\alpha}}\right)^2\Delta\gamma\right]\cos^2(\phi)\right\}\sin^2(\theta) + \frac{1}{2}\left\{\frac{\Delta\alpha}{\bar{\alpha}} + \Delta\epsilon^{(V)}\cos^4(\phi) + \Delta\delta^{(V)}\sin^2(\phi)\cos^2(\phi)\right\}\sin^2(\theta)\cos^2(\theta) \tag{2.27}$$

where α and β are the P-wave and $S-$wave velocities respectively, Z is the $P-$wave impedance $Z = \alpha\rho$, and G is the vertical shear modulus, $G = \beta^2\rho$. The average of the properties from above and below the interface is denoted with a line over the variable such that $\bar{\alpha} = \alpha_2 - \alpha_1$, and the difference is denoted by $\Delta\alpha = \alpha_2 - \alpha_1$. γ is the anisotropic parameter defined by Thomsen, and $\epsilon^{(V)}$ and $\delta^{(V)}$ are anisotropic parameters defined for HTI media by Rüger (1996).

At small angles of incidence the second term of equation 2.27 (AVO gradient B) describes the AVO behaviour (Rüger, 2001). If the symmetry axis is unknown, the AVO gradient can be expressed in terms of an observed azimuth ϕ_k as follows (Rüger, 2001),

$$B(\phi_k) = B^{iso} + B^{ani}\cos^2(\phi_k - \phi_{sym}) \quad (2.28)$$

$$B^{iso} = 1/2\left[\frac{\Delta\alpha}{\bar{\alpha}} - \left(\frac{2\bar{\beta}}{\bar{\alpha}}\right)^2 \frac{\Delta G}{\bar{G}}\right] \quad (2.29)$$

$$B^{ani} = 1/2\left[\Delta\delta^{(V)} + 2\left(\frac{2\bar{\beta}}{\bar{\alpha}}\right)^2 \Delta\gamma\right] \quad (2.30)$$

where B^{iso} is the azimuthally invariant part of the gradient, and B^{ani} is the azimuthally anisotropic part of the gradient.

At large angles of incidence, greater than 20°, both the AVO gradient and the higher angle term will affect the reflection coefficient (Rüger, 2001). At azimuthal angles close to the symmetry axis the effect of the parameter $\epsilon^{(V)}$ becomes important. At azimuthal angles close to the isotropy plane the parameter $\delta^{(V)}$ has a larger influence (Rüger, 2001).

Rüger's (1996) approximation has become widely used in azimuthal AVO studies to detect anomalies as it provides a qualitative way of analysis. However, it fails for a quantitative study at interfaces with a large contrast in the elastic parameters and strong anisotropy (Rüger, 1996).

Other linearised approximations to the azimuthal AVO signal include those of Haugen and Ursin (1996), Teng and Mavko (1996) and Vavryčuk and Pšenčík (1998). Haugen and Ursin (1996) consider a VTI medium (caused by shales) overlying an HTI medium resulting from a fractured sandstone, and derive an analytic approximation for the case of weak contrasts at the interface and weak anisotropy. For the VTI medium they use Thomsen's style parameters, whereas for the HTI medium they use parameters from an effective medium theory.

Teng and Mavko (1996) interpolate expressions for P-wave reflectivity at the symmetry planes and obtain an analytic expression for the reflectivity varying with azimuth and offset. For HTI media, they use the theory from Hudson (1980) to calculate the elastic moduli as a function of the background rock moduli, the crack density, crack orientation, aspect ratio and the material filling the cracks.

They then express the $P-$wave reflectivity for near offsets at the symmetry plane and perpendicular to the fractures in terms of the parameters used by Hudson (1980). They find that the $P-$wave azimuthal variation is proportional to the crack density, and the saturating fluid.

Vavryčuk and Pšenčík (1998) derive approximations for $P-$wave reflection coefficients for anisotropic media of arbitrary symmetry. They introduce a different set of parameters which are a linearised form of Thomsen's parameters for weak anisotropy.

2.3.4 Attenuation

Traditional methods for studying fractures from P-waves include travel time and amplitude analysis. In recent years there has been an increased interest in attenuation analysis, as it has been shown to be sensitive to fractures and to the different fluids encountered in the pore space. However, measuring attenuation directly from seismic data has proven to be a difficult task and is thus seldom used in common practice.

Attenuation is known as the loss in energy or amplitude due to the physical properties of the transmitting media. The attenuation mechanisms are usually a combination of various effects, such as spherical divergence, which accounts for the decrease in energy per unit area of wavefront with distance, absorption or conversion of energy into heat, and loss of energy at interfaces by reflection, mode conversion and scattering (Sheriff, 2002).

In a homogeneous medium (no loss by reflections or scattering) the amplitudes A at two distances x_1 and x_2 from the seismic source are described by (Schön, 1998),

$$A(x_2) = A(x_1) \left(\frac{x_1}{x_2} \right)^n e^{\alpha(x_2 - x_1)} \tag{2.31}$$

where the term $\left(\frac{x_1}{x_2}\right)^n$ describes the amplitude decrease by geometrical divergence.

The term $e^{\alpha(x_2-x_1)}$ contains the decrease caused by attenuation, where α is the attenuation coefficient. For a plane wave, $n = 0$, and α can be solved by,

$$\alpha = \frac{1}{x_2 - x_1} \ln[\frac{A(x_1)}{A(x_2)}] \tag{2.32}$$

If the distance equals one wave cycle the attenuation coefficient would then be $\alpha = \frac{1}{\lambda} \ln \left[\frac{A(x)}{A(x+\lambda)}\right]$, and the logarithmic decrement after one wave cycle is then, $\delta = \ln \left[\frac{A(x)}{A(x+\lambda)}\right] = \alpha\lambda = \alpha\frac{v}{f}$, where v is the velocity and f the frequency of the propagating wave (Schön, 1998).

A more common measure of the subsurface absorption is given by the specific attenuation factor Q, which is the fractional loss of energy in one wave cycle and is regarded as an intrinsic property of the rock. Various definitions of Q can be found in the literatuere (Mavko et al., 1999, Schön, 1998, Johnston and Toksöz, 1981). Q is related to the attenuation coefficient α and the logarithmic decrement δ by (Schön, 1998),

$$Q^{-1} = \frac{\delta}{\pi} = \alpha\frac{v}{\pi f} \tag{2.33}$$

Dasios et al. (2001) explain that as seismic waves travel through the earth part of the energy is converted to heat due to the anelastic behaviour of the rocks. This loss in energy (or absorption of energy), known as anelastic attenuation, will depend on the composition of the rock, including its saturating fluids, the temperature and pressure conditions to which they are subject and the frequency of the traveling waves. Schön (1998) lists the following as the main mechanisms causing intrinsic attenuation,

Matrix anelasticity: energy dissipation due to friction at grain boundaries and crack surfaces.

Fluid mechanisms: loss due to a) shear motion at the boundary between fluids and pores or cracks, b) differences in relative particle motion between fluids and the rock frame, c) squirt-flow phenomena and d) effect of gas bubbles moving due to differences in densities with other fluids.

Scattering from small grains

The effect of attenuation due to varying pore fluids has been studied by Klimentos (1995). He calculates P- and S-wave attenuation from sonic waveforms for sandstones saturated with water, oil, gas and gas-condensate and finds that attenuation of P-waves is higher in gas and gas-condensates than in either oil or water saturated sandstones. He also observes that attenuation of S-waves is not dependent on pore fluids. In gas and gas-condensates sandstones P-wave attenuation is higher than S-wave attenuation. MacBeth (1999) suggests that at seismic frequencies one of the main attenuation mechanisms in porous saturated rocks is the local viscous intracrack flow. Attenuation has thus the potential to serve as a fluid indicator.

Dasgupta and Clark (1998) present a method, based on the traditional spectral ratio method (Tonn, 1991), for calculating Q from surface seismic data on CMP gathers. For sedimentary rocks Q values range between 10 and 450, with lower values corresponding to higher attenuation (Dasgupta and Clark, 1998, Schön, 1998). For igneous and metamorphic rocks the values are generally higher, from 100 up to 1000 (Dasgupta and Clark, 1998). Furthermore, Q has been recorded to decrease by $\approx 20\%$ in the presence of gas for saturations as low as $30\% - 40\%$ (Dasgupta and Clark, 1998). Based on these differences, Dasgupta and Clark (1998) show examples of measurements of Q from surface seismic data that have helped in the discrimination of lithology (between basement and sedimentary rocks), and in the recognition of areas with concentration of gas.

Chichinina et al. (2006) study attenuation versus offset and azimuth for fractured rocks with an HTI symmetry. They derive an equation for the variation of the attenuation coefficient Q with offset and azimuth (QVOZ), which presents a similar behaviour to that derived by Rüger (1996) for AVOZ. Chichinina et al. (2006) corroborate that attenuation is larger in a direction perpendicular to the fractures and minimum in the isotropy plane oriented parallel to the fractures. Additionally, two interesting findings come from their work; 1) that attenuation

anisotropy is always greater than P-wave velocity anisotropy, 2) that attenuation anisotropy depends strongly on the V_s/V_p ratio of the background rock, whereas the dependence on the fracture parameters is weak. Chichinina et al. (2006) calculate only the relative Q variations with direction, due to the inaccuracies of trying to compute absolute Q. In this thesis I also consider only relative variations in the attributes for fracture characterisation. In chapters 3 and 4 I analyse frequency content versus azimuth as a measure of relative attenuation.

Dasios et al. (2001) compare two methods for estimating attenuation at sonic frequencies (5-30 kHz) from in situ data, the more traditional logarithm spectral ratio (LSR) and the instantaneous frequency (IF) method. They find that the IF method is more stable for sonic data compared to the LSR, specially in data with high background noise levels. In this thesis I use the IF method (discussed in Chapter 3) to calculate attenuation from VSP data.

2.3.5 Scattering

As discussed in the previous sections, when heterogeneities in the earth are much smaller than the wavelength, the elastic constants of the composite media can be replaced by that of an effective medium. If these heterogeneities are caused by aligned fractures then the fracture medium can be replaced by an anisotropic effective elastic tensor. If however the fractures and fracture spacing are closer in size to the wavelength of the propagating wave they will scatter energy complicating the signal (Burns et al., 2007, Willis et al., 2007, Willis et al., 2006). Traditionally this scattered energy has been regarded as noise and has been filtered out in seismic processing.

Burns et al. (2007) show how this scattered energy contains information on large fracture zones, which they refer to as fracture corridors, and can be used to obtain fracture orientations and spacing between the fracture corridors. They show, through numerical and physical studies of vertical parallel fracture zones,

that when seismic data are acquired perpendicular to the fracture corridors in the subsurface, forward- and back-scattered (waves travelling back to the source) energy is generated. However, when the data are acquired parallel to the fracture corridor no backscattered waves are recorded.

If the data are then NMO corrected and stacked in common-azimuth gathers, the scattered energy is minimised in a direction perpendicular to the fractures, and maxmimised parallel to the fractures. They then calculate the autocorrelation of the stacked trace in a time window above (input wavelet) and below (output wavelet) the fractured zone, and deconvolve the resulting autocorrelation of the input wavelet from the output wavelet.

The result of this deconvolution is a trace (transfer function) containing a measure of the scattering due to the fractured layer. A weighted sum of this transfer function (with larger weights away from the zero lag) provides a scattering index. The method is called the scattering index method developed by Willis et al. (2006). Willis et al. (2007) also make use of scattered energy from fracture planes in a modelling study that integrates microseismic events caused by hydraulic fracturing and recordings from time-lapse VSP data.

Chapter 3

Fracture studies on time lapse VSPs from Oman

3.1 Summary

I perform azimuthal frequency studies based on the instantaneous frequency method for five walk-around VSP surveys (two of these being time-lapse or repeat surveys) from a carbonate field in Oman. The attenuation analysis, complemented with travel time and amplitude azimuthal analyses is performed for four down- and up- going events including P and PS wavefields. Dominant directions are found when separating the data into two depth ranges above and below ∼270m. The shallow section shows main orientations of N40E and N70E, whereas the deeper section shows dominant orientations at N40W. Based on theory, these orientations can be interpreted in terms of fracture plane orientations. Additionally, these orientations could be related to the main structural features surrounding the field. When grouping the data for all depth ranges, attributes and wells, no predominant orientation emerges, exposing the complexity of the problem.

To perform frequency content or attenuation studies, high quality wavefield separation and pre-processing of the VSP data is essential. To this end, I rotate the geophone data into a dynamic coordinate frame and test various methods to obtain optimum up- and downgoing wavefields from the VSP data.

3.2 Introduction

The use of amplitude and attenuation studies for fracture characterization has become a topic of increased interest. Lynn et al. (1995) argue that azimuthally dependent P-wave AVO responses can be related to the orientation of open fractures and relative fracture intensity. Maultzsch et al. (2005) interpret P-wave attenuation anisotropy in terms of open fracture orientations. Attenuation studies potentially contain information on fluid saturations and fracture characterization.

In otherwise isotropic media containing vertically aligned fractures, simple models suggest that the variations of travel time and attenuation with azimuth can be written to a good approximation to first order with one term of their Fourier series, i.e. following $cos2\theta$ behaviour. Thus I study the azimuthal anisotropic response of frequency content and angle of rotation of the three component $3C$ geophones to gain information about the fracture network around the borehole.

The main objective of this chapter is to perform azimuthal attenuation studies on a multicomponent time-lapse walk-around vertical seismic profile (VSP). In order to do this I first perform a careful pre-processing of the data.

The data analysed consist of five VSPs around three wells. Three of these surveys were taken around the same well several years apart to detect changes due to steam injection. The VSP data cross three different geological units including a fractured carbonate. However, the reservoir of interest is located below the deepest geophone. Therefore I analyse the up-going wavefield to obtain information about the reservoir.

I start this chapter by reviewing the instantaneous frequency method used to perform attenuation studies on the data. I then briefly review some conventional and more novel techniques used in the processing of the 3-component ($3C$) walkaround VSP. Subsequently, I give a brief geological background of the carbonate field in Oman and introduce the geophysical data. I prepare the data for the frequency analysis by rotating the geophones into the dynamic coordinate frame

separating the wavefields of interest.

Next, I perform azimuthal frequency, travel time and amplitude studies on four seismic events. To this end, I first analyse the data per seismic event versus azimuth and depth. Then, I group the data per attribute and separate them into two depth ranges, above ∼210m (using orientations from events A and B) and below ∼270m (using orientations from events D and E). I find two different main orientations for the shallow and deeper sections, which are N40E and N70E for the shallow section, and N40W for the deeper section. I interpret these to be the orientations of the main fracture planes in each of the latter depth sections. Furthermore, these orientations could be linked to the major structural features surrounding the field.

3.3 Method

Throughout this chapter I work with compressional or P-wave energy. It has been shown in various studies that attenuation and travel time from P-waves are sensitive to the presence of fractures (Liu et al., 2007). I start by introducing the method used for calculating relative attenuation in the frequency domain using the instantaneous frequency method.

While multicomponent seismic data can bring additional information about the area under study (MacBeth and Li, 1999), they also require additional processing steps tailored to extract the relevant information from the three components. It is an industry standard that VSP data, such as those used in this and the next chapter, are acquired with 3-component geophones in the borehole. In the second part of this section I introduce the techniques used in this chapter for the processing of the 3C data. These techniques include rotation of the components into the direction of maximum energy and wavefield separation methods such as polarization analysis. For an exhaustive review on processing methods for VSP data see Macbeth (2002).

3.3.1 Instantaneous frequency

Barnes (1991, 1993) has shown that when a wavelet travels through an attenuating medium, the instantaneous frequency decreases as a function of travel time in that medium. It is thus an applicable method for detecting low frequency shadows related to rocks with a low quality factor Q (Barnes, 1993). In contrast to the spectral frequencies obtained by the Fourier transform, which are precise in frequency but ambiguous in time, the instantaneous frequency of a trace is precise in time but ambiguous in frequency (Barnes, 1993). As we are interested in the frequency content of a given event localised in time and the attenuation related to waves traveling perpendicular to a set of fracture planes, the instantaneous frequency is a suitable method. A thorough review on the properties of instantaneous frequency can be found in Taner et al. (1979), Barnes (1991), Barnes (1993) and Dasios et al. (2001).

I use the instantaneous frequency method based on Dasios et al. (2001) for calculating the weighted instantaneous frequency of the data in order to perform azimuthal studies. The main steps of the algorithm, which makes use of complex trace analysis (Taner et al., 1979), are,

1. For each receiver level, window the seismic traces around the first arrivals; here a Blackman window of 101 milliseconds was used. (Figure 3.1a)

2. Calculate the Hilbert transform and the damped instantaneous frequency (derivative against time of the instantaneous phase) of each trace with the following equation:

$$f(t) = \frac{d\phi(t)}{dt} = \frac{1}{2\pi} \frac{x(t)\frac{dy(t)}{dt} - y(t)\frac{dx(t)}{dt}}{x^2(t) + y^2(t) + \epsilon^2} \tag{3.1}$$

   where $x(t)$ is the seismic trace, $y(t)$ is its Hilbert transform, and $\phi(t)$ is the instantaneous phase of the complex trace $x(t) + iy(t)$. ϵ is a damping factor that minimizes the noisy low amplitude areas without affecting the

instantaneous frequency when the amplitude envelope is large. Figure 3.1b shows the complex trace built by using the seismic trace as the real part and its Hilbert transform as the imaginary part. The instantaneous frequency is then the time derivative of the phase of the complex trace.

3. Weight the instantaneous frequency $f_w(t)$ by the seismic trace amplitude envelope:

$$f_w(t) = \left| \frac{\sum_{tm-T}^{tm+T} f(t)W(t)}{\sum_{tm-T}^{tm+T} W(t)} \right| \tag{3.2}$$

where $W(t)$ is the seismic trace amplitude envelope, with $W(t) = |y(t)|^2$, $2T$ is the weighting window length and tm is the time at which the amplitude envelope reaches its maximum. The instantaneous frequency weighted by the amplitude envelope is shown in Figure 3.1c.

This methodology for calculating azimuthal weighted instantaneous frequency (WIF) in VSP data follows from the work presented in Varela et al. (2006) where the relative attenuation factor Q is calculated on walkaround VSP data with a similar approach.

3.3.2 Azimuthal averaging by quadrants

Often when performing azimuthal studies of a given attribute, the data are fitted to a periodic function to find a consistent azimuthal pattern. However, depending on the quality of the fit, when fitting the data to a cosine2ϕ function, it may be difficult to visualise that the best fit cosine2ϕ function is the one calculated numerically to minimise the errors (see Appendix A). I thus introduce the azimuthal averaging by quadrants of attributes as a method to further facilitate the recognition of the periodic function. It is worth clarifying that the same axis of azimuthal orientations are obtained when the data is fitted directly to a cosine2ϕ or when it is first averaged by quadrants (as explained below), and then

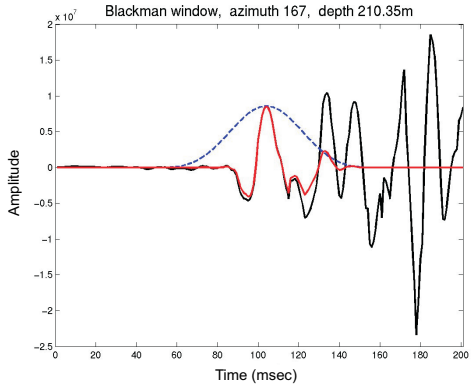

(a) Blackman window (blue) around event, resulting in windowed trace (red)

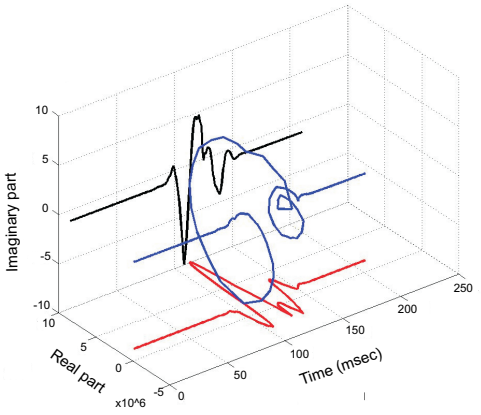

(b) Complex trace

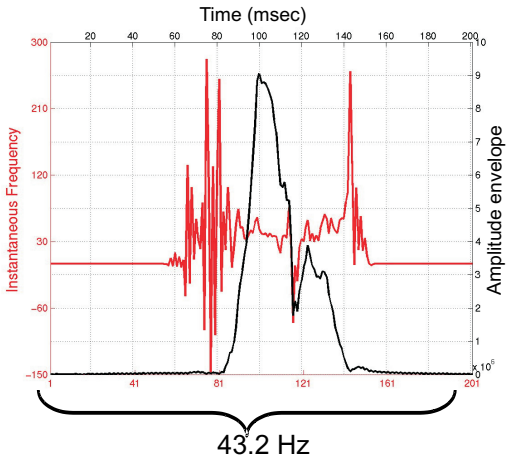

(c) Weighted instantaneous frequency

Figure 3.1: Calculation of weighted instantaneous frequency. a)Blackman window (blue) around event of interest results in a windowed trace (red). The original trace is shown in black. b)Complex trace (blue curve) built by using the windowed trace as the real part (same red curve in part a), and the Hilbert transform of the windowed trace (black curve) as the imaginary part, c)Instantaneous frequency (red curve) weighted by the amplitude envelope (black curve) of the windowed event, results in a weighted instantaneous frequency value of 43.2 Hz for the windowed event shown in a.

fitted to a cosine2ϕ function. The azimuthal averaging by quadrants will help visually recognise and extract the cosine2ϕ component of the data.

I perform an azimuthal analysis by averaging various attributes by quadrants including travel time, amplitude and weighted instantaneous frequency. I explain here the averaging by quadrants through the weighted instantaneous frequency as follows,

- The weighted instantaneous frequency WIF is calculated around a certain event for all available azimuths.
- For a given azimuth, the WIF of those traces with a source-receiver azimuth that falls in a range $\pm 45^o$ of the given azimuth (and those azimuthally opposite to this zone), are averaged. (See Figure 3.2a and b).
- Likewise the WIF of the two remaining and opposite quadrants (zone B of Figure 3.2) are averaged.
- Subsequently, the difference between these two averages is taken (Figure 3.2c) and plotted in polar coordinates (Figure 3.2d).
- The procedure is then repeated for all source-receiver azimuths.

3.3.3 Geophone coordinate rotation

In general, as part of the pre-processing of VSP data, a geophone coordinate rotation is necessary as the orientation of the two horizontal components H_1 and H_2 on the horizontal plane is usually unknown. This is due to the difficulty in controlling their alignment in the borehole. Only the orientation of the vertical component V can be controlled, which is done with a gimbal.

A geophone rotation is thus performed (Appendix B) to orient H_1 and H_2 along the source-receiver direction where the energy is maximised (radial component),

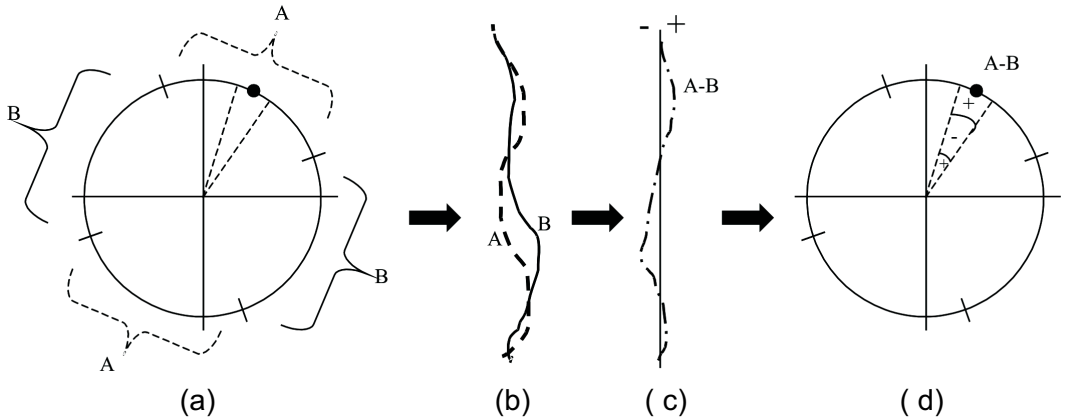

Figure 3.2: Procedure outline for averaging attributes by quadrants. a)represents an attribute plotted in radial coordinates, for a given azimuth and depth, the attributes that fall in a range $\pm\ 45^o$, and those azimuthally opposite this zone, (labeled as area A), are averaged. Similarly for those that fall in area B. b)traces A and B containing the averages of zones A and B for all depths. c)difference between traces A and B. d)difference between traces A and B plotted in polar coordinates, where the radius is proportional to depth.

and perpendicular to the former where the energy is minimised (transverse component). I do this rotation using only a time window containing the first arrivals, which means that the energy in the transverse component in that time window is expected to be zero for P-wave energy. To visualise this, Figure 3.3a shows the partitioning of energy into the three components of a signal arriving at an angle of 45^o with respect to H_1 and 70^o with respect to the vertical axis. The radial component R_h is inline with the source-receiver orientation. The original signal is shown in Figure 3.3b.

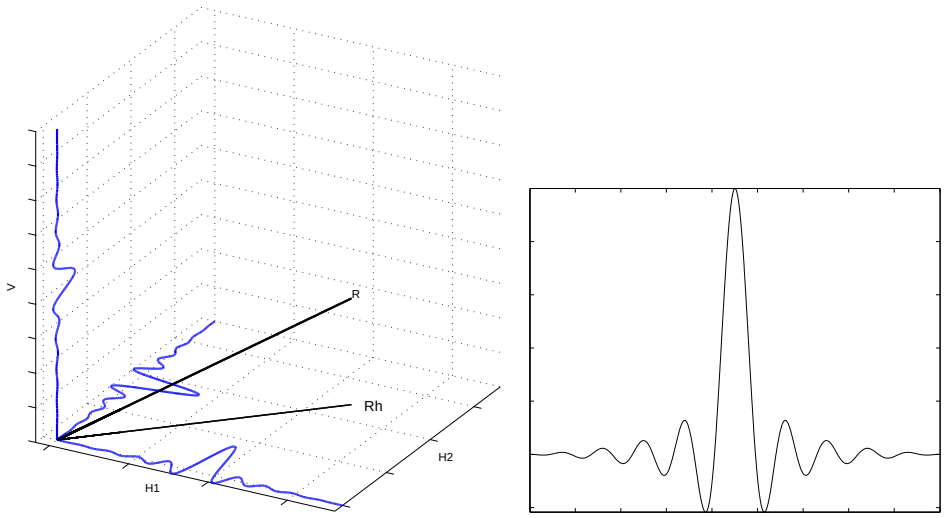

(a) (b)

Figure 3.3: a) Amplitudes recorded on each component for a wave traveling from the direction of the black line labeled R. R_h is the projection of R onto the horizontal plane. b)Original wave recorded along R. The wave is a tapered sinc function.

A second rotation is performed to orient the vertical V and radial (but horizontal) R_h components into the dynamic coordinate system (see Appendix B). This rotation consists of rotating V and R_h (keeping their 90^o separation) around the axis of the horizontal transverse component such that R_h has the original orientation of R in Figure 3.3a. After the rotation, the transverse component is the only component left on the horizontal plane, and will thus be refered to as H.

The former vertical component, which lies on the sagittal plane[1], is normal to R and H and will be referred to as N.

This rotation is performed separately for each source-geophone pair as it varies with depth. Figure 3.4 presents a sketch of the R, N and H orientations for the specific field acquisition geometry of the VSP data presented in the next section.

In this dynamic coordinate system the downgoing P-waves will be recorded on the radial components, while the downgoing S-waves are recorded on the normal and horizontal components. The recordings of the reflected waves will depend upon the specific VSP acquisition geometry (source-receiver offset and depth of geophones) and the depth of the reflectors (Macbeth, 2002). For the acquisition geometry shown in Figure 3.4 the energy of the reflected P-wave will be partitioned between the normal and radial components depending on the angle of incidence of the reflected P-wave and the orientation of the dynamic coordinate frame. Clearly, further processing is necessary for the separation of different wavefields. Some of these procedures are reviewed in the following section.

3.3.4 Wavefield separation methods

The recordings of VSP data consist of wavetrains traveling downward (transmitted waves) and upward (reflected waves), plus the unwanted signals such as multiples and noise. Both the downgoing and upgoing wavefields are useful but they need to be separated before they can be used (Chopra et al., 2004). Since a good separation of the wavefields is essential to perform attenuation studies on a given event, I will compare some of the methodologies used for wavefield separation, review their limitations and requirements and apply them to the VSP data in order to find the optimal one for this study.

In the following explanations, and throughout this thesis (unless stated otherwise) I will work with VSP shotgathers arranged so that time is in the vertical axis

[1]vertical plane between the source and the receiver

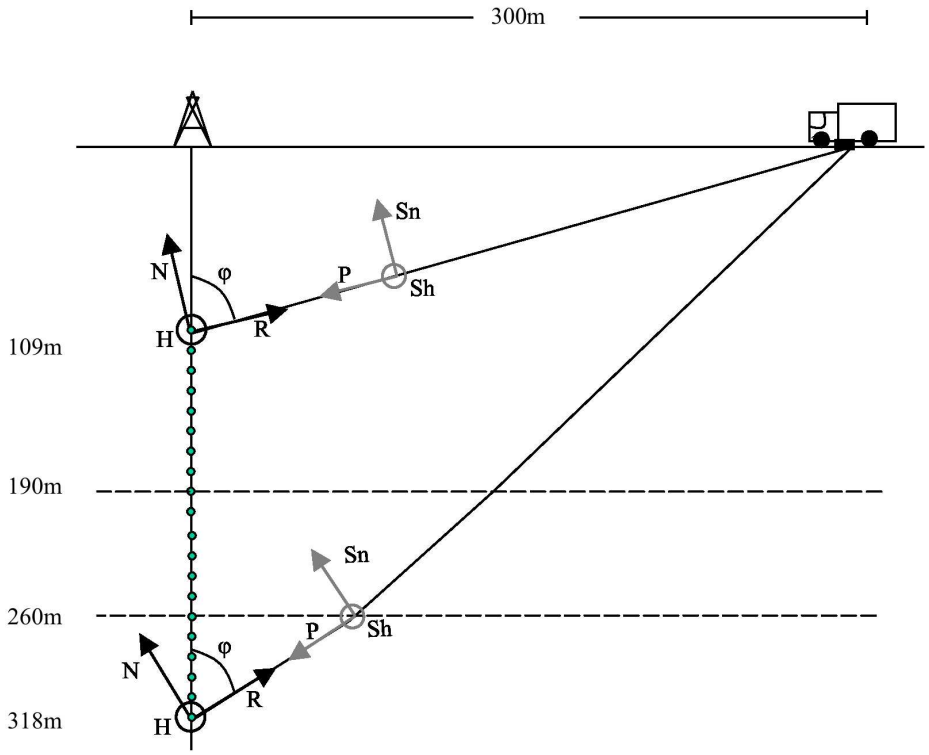

Figure 3.4: Sketch on the sagital plane showing relative positions of geophones, sources, and interfaces. The shallowest and deepest geophones are rotated into the dynamic system which is suited to record direct waves.

increasing downwards, and geophone depth is in the horizontal axis increasing to the right.

Median filter

The median filter is one of the most conventional methods for wavefield separation (Stewart, 1985). It makes use of the linearity of the downgoing $P-$ wavefield and keeps all the events that have the same inclination and direction in the time-depth domain. It functions by taking the middle value of a sequence of numbers arranged in ascending order. The numbers are taken from a moving window of the data to be filtered.

Consider the sequence [-2,4,13,0,8], when arranged in ascending order it results in [-2,0,4,8,13]. The median of this sequence is 4. The number 4 is then located in the middle of the window of the filtered data (where the value 13 was originally placed). More generally, given a sequence of numbers x_i with $1 \leq i \leq 2r+1$, where r is an even number, the median y_r is then,

$$y_r = MED[x_1, \ldots, x_{2r+1}] \tag{3.3}$$

where y_r is smaller or equal than the largest r elements of the sequence x_i and greater or equal than the smallest r elements of x_i and the filter length here is $2r+1$.

In practice, for the wavefield separation of a VSP shotgather whose data are stored in a matrix X_o (where the vertical axis is time and the horizontal axis is receiver depth) there are four main steps: 1)the traces in X_o are aligned in time along the first breaks (such that the first arrivals appear as a horizontal event) and are saved in matrix X. 2)The median filter is calculated (on matrix X) such that the sequence x_i is composed of samples with the same time and different receiver depths, the filtered data are stored in matrix Y. 3) A shift in time (opposite to the shift in step 1) that realigns the first breaks to their original position in time is performed on matrix Y and saved in Y_d. The filtered data Y_d

contains only the downgoing P-waves. 4)If we define Y_u such that $Y_u = Y_d - X_o$, then Y_u contains the upgoing P-waves and all S-waves, as these have a different dip or velocity than the upgoing P-waves.

Note that the number of traces in a shotgather can be a limitation, as there should be enough traces so that the boundary effects of the median filter are lessened. Filter lengths of 5,7 or 9 samples are common.

FK filter

The FK filter applied in the frequency-wavenumber domain is also widely used for wavefield separations (Yilmaz, 1999). Its underlying principle is the decomposition of a wave field into its plane wave components. The FK filter consists of applying a 2D Fourier transform to the seismic data. If the input data are in the time-space (t, x) domain (or receiver depth for VSP) a 1D Fourier transform is applied in the time direction such that the resulting data are in the frequency-space domain (f, x). Subsequently, a 1D Fourier transform is applied to the data (f, x) in the space direction. The resulting data are then in the frequency-wavenumber domain (f, k) (Yilmaz, 1999). This is shown schematically as follows,

$$(t,x) \overset{1-D\ FT\ in\ time}{\longrightarrow} (f,x) \overset{1-D\ FT\ in\ space}{\longrightarrow} (f,k)$$

or explicitly with the following equation (Yilmaz, 1999, page 497),

$$P(x,\omega) = \int P(x,t) exp(-i\omega t) dt \tag{3.4}$$

$$P(k_x,\omega) = \int P(x,\omega) exp(ik_x x) dx \tag{3.5}$$

where $P(x,t)$ is the recorded wavefield, ω is the angular frequency with $\omega = 2\pi f$ and f is the frequency in Hz. Substituting $P(x,\omega)$ in the last equation we obtain,

$$P(k_x,\omega) = \int P(x,t) exp(ik_x x - i\omega t) dx\, dt \tag{3.6}$$

where k_x is the wavenumber, which is the inverse of the wavelength.

Events in the time-offset (t, x) domain that have the same dip, independent of their location, get mapped as a single radial line with a specific dip in the (f, k) domain. Furthermore, positive and negative dips in the time space domain (t, x) get plotted into different sides of the wavelength spectrum in the (f, k) domain. This facilitates the separation of upgoing and downgoing wavefields in VSP data regardless of their velocity.

Spatial aliasing can be a constraint, the steeper the dip of the event, the lower the frequency at which spatial aliasing occurs making the event appear at lower frequencies in the FK domain (Yilmaz, 1987).

Polarization analysis

The application of vector analysis to the recording of a seismic wavefield is known as polarization analysis, and it is used to describe the particle motion of a given wavefield as recorded by the different orthogonal components of the geophones, whether $2C$ or $3C$. Polarization analysis has been commonly used for anisotropic studies on shear-wave splitting (Crampin, 1985), and can also be used for wavefield separation of P and S waves, called polarization filtering.

Polarization analysis helps to simplify the multicomponent data by providing two measurements, ellipticity or linearity, and directionality (Perelberg and Hornbostel, 1994, Hendrick and Hearn, 1999). First the covariance of the three component data, which I will refer here as (x_i, y_i, z_i), is calculated within a time window (usually the length of a full cycle of the dominant wavelength) as follows (Hendrick and Hearn, 1999),

$$M = \sum_{i=1}^{N} \begin{bmatrix} x_i^2 & x_i y_i & x_i z_i \\ y_i x_i & y_i^2 & y_i z_i \\ z_i x_i & z_i y_i & z_i^2 \end{bmatrix} \tag{3.7}$$

where N is the length of the window. The eigenvalues and eigenvectors of the

covariance matrix M are used to calculate the linearity and dip of the three components on that time window as follows (Hendrick and Hearn, 1999),

$$Mu = \lambda u \tag{3.8}$$

we can then find three orthogonal eigenvectors that satisfy equation 3.8 (Hendrick and Hearn, 1999) such that u_1, u_2 and u_3 correspond to the eigenvalues λ_1, λ_2 and λ_3, with $\lambda_1 > \lambda_2 > \lambda_1$.

The linearity if the data within the window is then

$$L = 1 - \left(\frac{\lambda_2}{\lambda_1}\right)^{\gamma} \tag{3.9}$$

where the exponent γ controls the sensitivity of the linearity estimator, and as shown by Hendrick and Hearn (1999) can range between 0.25 to 3. The linearity can vary between 0 and 1 with 0 representing very poor linearity, and 1 perfectly linear particle motion. The orientation of the particle motion is then given by the azimuth ϕ, and dip θ as follows,

$$\phi = \tan^{-1}\left(\frac{m_1}{l_1}\right) \tag{3.10}$$

$$\theta = \tan^{-1}\left(\frac{n_1}{\sqrt{l_1^2 + m_1^2}}\right) \tag{3.11}$$

where l_1, m_1 and n_1 are the elements of the eigenvector corresponding to the largest eigenvalue $u_1 = (l_1, m_1, n_1)$. Additionally, Hendrick and Hearn (1999) define a measurement of the azimuth reliability as $\rho = L\cos\theta$.

The process is then repeated as the window moves a cycle in time onwards and then for all other traces. The P and S waves are expected to be highly linear. A filter can then be designed to separate the P from the S waves based on the linearity and dip.

3.4 Omani field

3.4.1 Geological Background

The field under study is located in the Omani Ghaba Salt Basin, SW of the Maradi Fault zone, which extends for approximately 300Km and strikes NNW. Regional plate movements molded the complex structure, sedimentation and burial histories of the area. The field is thus surrounded to the east by the Huqf–Haushi Uplift with a NNE orientation, to the south by the Central Oman High with an EW orientation, and to the west by the Makarem-Mabrouk high with a N45W orientation as shown in Figure 3.5 (Loosveld et al., 1996).

The acquired VSP data cuts through three geological units, the Fiqa shales, the Natih fractured carbonate formation which extends approximately from 190m to 260m, and the Nahr Umar shale unit, from shallow to deep respectively. The producing hydrocarbon reservoir, Shuaiba, which has a low matrix permeability and a strong fracture network, is located below the deepest receiver of the VSP data, thus only the reflected waves from the top of the reservoir will be recorded. In other fields the Natih fractured carbonate is the main reservoir.

The Middle Cretaceous Natih Formation and Lower Cretaceous Shuaiba Formation consist of chalky carbonates and grainstones, which are porous and fractured. The Santonian-Campanian Fiqa Formation consists of deep marine pelagic shales that form a regional seal to the Natih carbonates. The Nahr Umar Formation of the Middle Cretaceous is a transgressive shale that forms an excellent and widespread seal to the Shuaiba reservoir.

The Natih fractures have been extensively studied (Van der Kolk et al., 2001) at reservoir depths and surface outcrops in the Natih field of the Fahud Salt Basin, located NW of the field under study (see Figure 3.5). At reservoir depths only one set of open fractures with a NE-SW orientation is normally present. However, closer to the surface another set of fractures develops in response to the stress

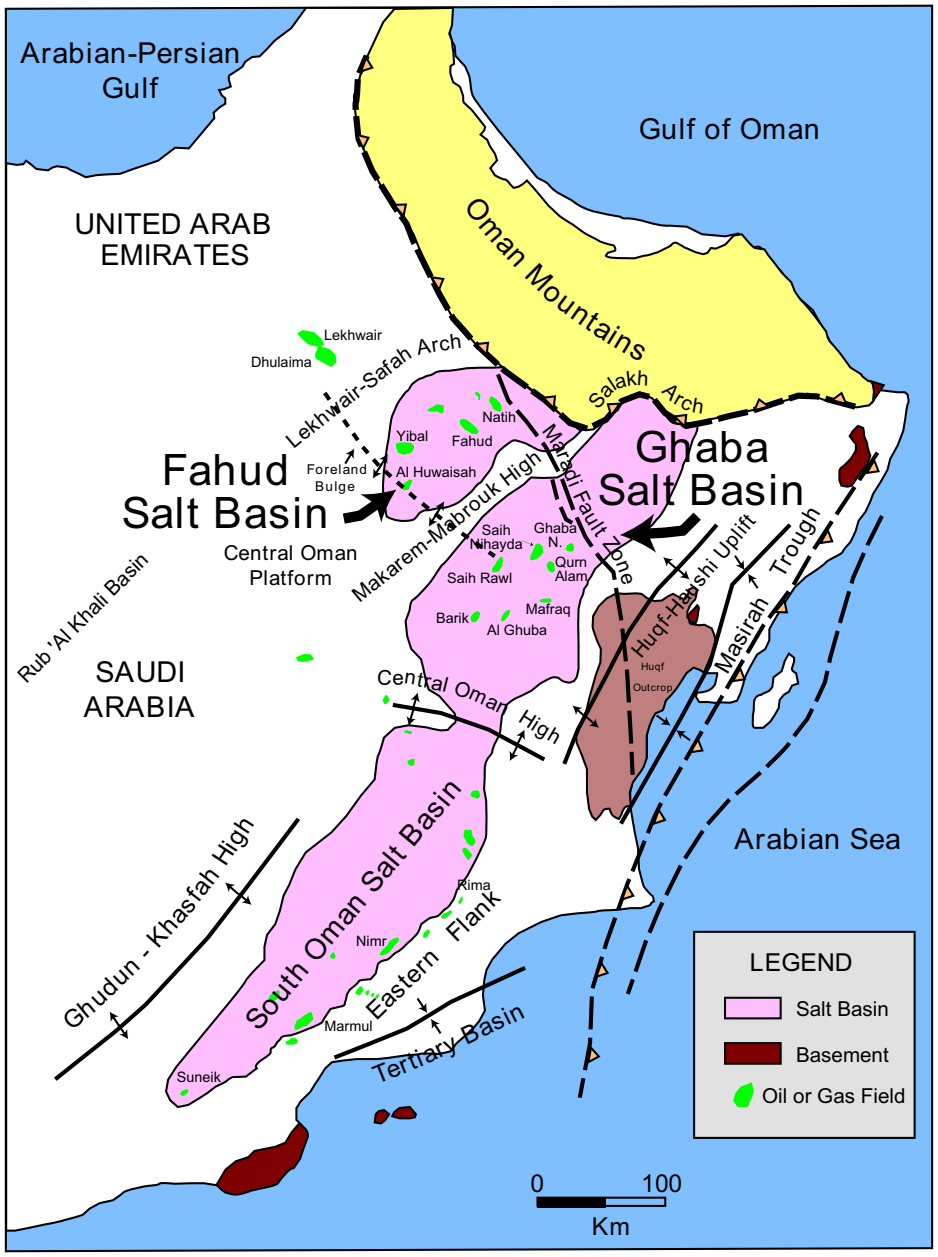

From Pollastro (1999)

Figure 3.5: Geographical location of the Omani Ghaba Salt Basin where the field under study lies.

release. Van der Kolk et al. (2001) argue that these fractures might also extend to the Fiqa shales that are on top of the Natih field.

For a detailed geological history, petroleum system and stratigraphic and structural description of the Ghaba Salt Basin see Pollastro (1999).

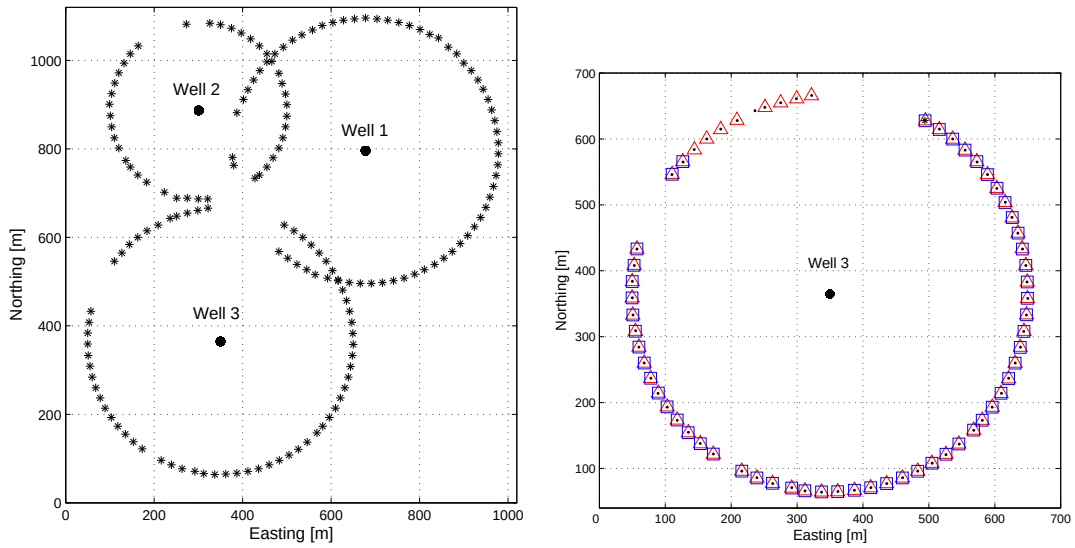

(a) (b)

Figure 3.6: a)Source and receiver location for walk-around VSP data at Wells 1, 2 and 3, acquired in year 2002, b)Source and receiver location for walk-around VSP data at Well 3 for years 2002 (black dots), 2004 (red triangles) and 2005 (blue squares).

3.4.2 Geophysical data

The data consists of five walkaround VSP data sets around three wells. The acquisition layout is shown in Figure 3.6a. One VSP survey was acquired around each well in year 2002, additionally for Well 3 two repeat surveys were acquired in years 2004 and 2005 with permanent geophones. Figure 3.6b shows the source locations for the three surveys around Well 3. For the surveys acquired in 2002 three shots were recorded per shot location to minimise noise. For those acquired in years 2004 and 2005 the number was increased to ten shots per shot location. All surveys have 32 receivers in depth with a regular spacing of 6.75m spanning

from 110m to 318m and an offset of 300m, except for the survey of Well 2 which has a surface offset of 200m.

The history of production and steam injection at the Shuaiba interval in the field under study goes back to 1995. The 2002 VSP data set was acquired in May 2002, the steam injection started at the end of 2003 and continued until February 2005 shortly before the last survey was acquired and production restarted. The 2004 survey was acquired in August of that year. The changes due to steam injection, if any, should thus have a major effect on the 2004 and 2005 data.

3.5 Application and analysis

3.5.1 Angle of rotation

To perform the rotation explained above and in Appendix B, the search for the direction of maximum energy, in a window of 28ms around the first breaks on the horizontal plane, was performed every 0.2^o, which translates into searching for a source location every meter over a circle with a 300m radius or offset. Two angles 180^o apart will invariably yield the same maximum energy on the radial component. To maintain consistency in the polarity of the rotated traces, the angle which resulted in the first break starting with a trough followed by a peak was chosen, as it is the polarity on most of the vertical component data.

Figure 3.7 shows the angle found for each of the VSP surveys per receiver depth. The red line shows the angle of rotation should the P-wave travel as a straight ray from the source to the receiver. The general trend of the angle is to diminish with depth, as it is measured between the incident P-wave and a vertical axis. It is also clear that the angle diminishes significantly with respect to the geometric one at 150m and 250m for all surveys. There is another drop at approximately 220m for all surveys, except for the VSP acquired around Well 3 in 2002.

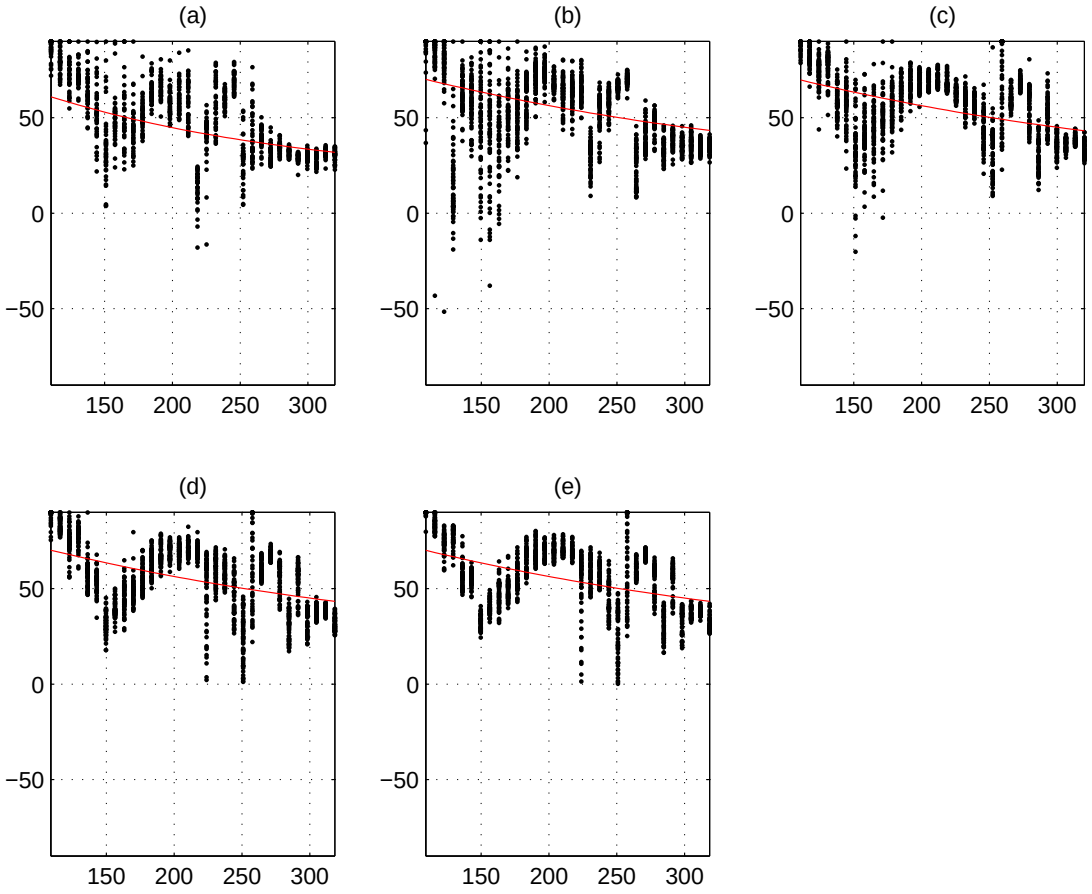

Figure 3.7: Angle of rotation in the sagittal plane around component H (2nd rotation in Appendix B). The horizontal axis is receiver depth, the vertical axis angle of rotation. Black corresponds to angle of maximum energy on the radial component in a window of 28ms around the first breaks, red corresponds to the geometrical angle given straight ray paths and accounting for constant velocities. a) Well 2, year 2002, (b) Well 1, year 2002, (c) Well 3, year 2002, d) Well 3, year 2004, d) Well 3, year 2005.

To understand the behaviour of these sudden drops in the angle of rotation, ray tracing of the first arriving P-wave was computed to calculate the angles of incidence (the angle of rotation should give the angle of incidence of the first P-wave arrival). The geological model for the ray tracing is based on the geological description of the area mentioned above, and the acquisition geometry, from which a sketch is shown in Figure 3.4. Two velocity models are created both with three layers at the depths shown in Figure 3.4. Model 1 has smoothly increasing velocities. In Model 2 the velocity of each of the layers was estimated from the travel times of the first breaks (see Figure 3.8). For the first layer we use the average velocity for the P-wave arriving at each geophone. For the second and third layers the interval velocity is used, calculated from the travel times and receiver spacing of the geophones assuming straight rays. The velocities used for both models appear in the Table 3.1. The velocities found for Model 2 suggest a sharp increase for Layer 2.

Layer	Depth (m)	Thickness (m)	Model 1: Vp (m/s)	Model 2: Vp (m/s)
1	0-190	190	2746	1900
2	190-260	70	3146	4000
3	260-	-	3346	2300

Table 3.1: Parameters for ray tracing in Model 1 and 2.

The sharp increase in velocity at the second layer in Model 2 produces a step towards larger angles of incidence on the geophones, as shown in figures 3.9b and 3.9d. From this analysis it follows that there should be a thin low velocity layer around 150m to produce the sudden drops in incidence angle at this depth.

Figure 3.10 shows the original two horizontal components and vertical component for Well 2 at a source-receiver azimuth of 94^o. For the same gather depicted in Figure 3.10, Figure 3.11 shows the normal, horizontal and radial components calculated with the angles of rotation shown in Figure 3.7. It is clearly seen that the energy of the first arrivals on the H_1, H_2 and V components is transfered to the R component. The same effect applies to the compressional train

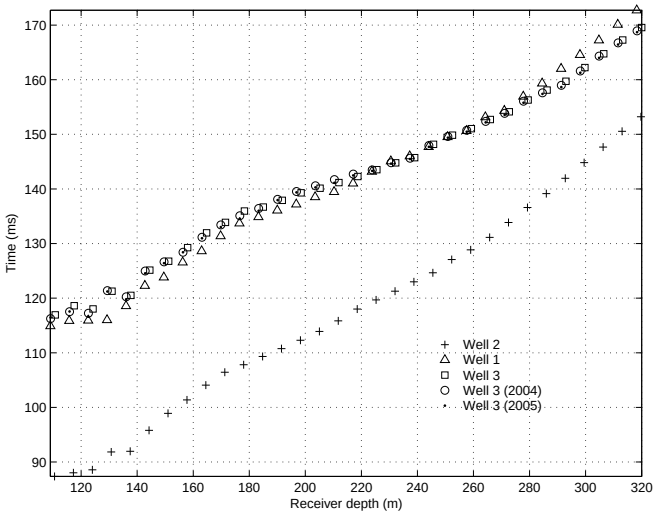

Figure 3.8: Average travel time of first breaks for all azimuths and all wells. Notice the change in dip at 180m and 260m depths.

of downgoing P waves in the 100ms window after the first breaks. As expected the converted PS energy is recorded onto the N and H components, notice the strong conversion of energy from P to S at 250m.

Although appropriate angles of incidence were found for the geophone rotations, as is shown from the energy partitioning in Figure 3.11, most of the upgoing wave trains remain on the R component superimposed on downgoing ones, and we thus continue to the next step in processing.

3.5.2 Wavefield separation

The effectiveness of the covariance or polarization method for wavefield separation, as explained above, will depend on the window length chosen to calculate the covariance matrix between the three components. To find an appropriate window length we calculate the linearity of three traces (components N, H and R at the same geophone depth), shown in Figure 3.12, with window lengths of 16ms, 28ms, 40ms, 50ms and 80ms, corresponding to panels a) to e) of Figure 3.13 respectively. From analysis of Figure 3.13, a window length of 28ms is chosen, as

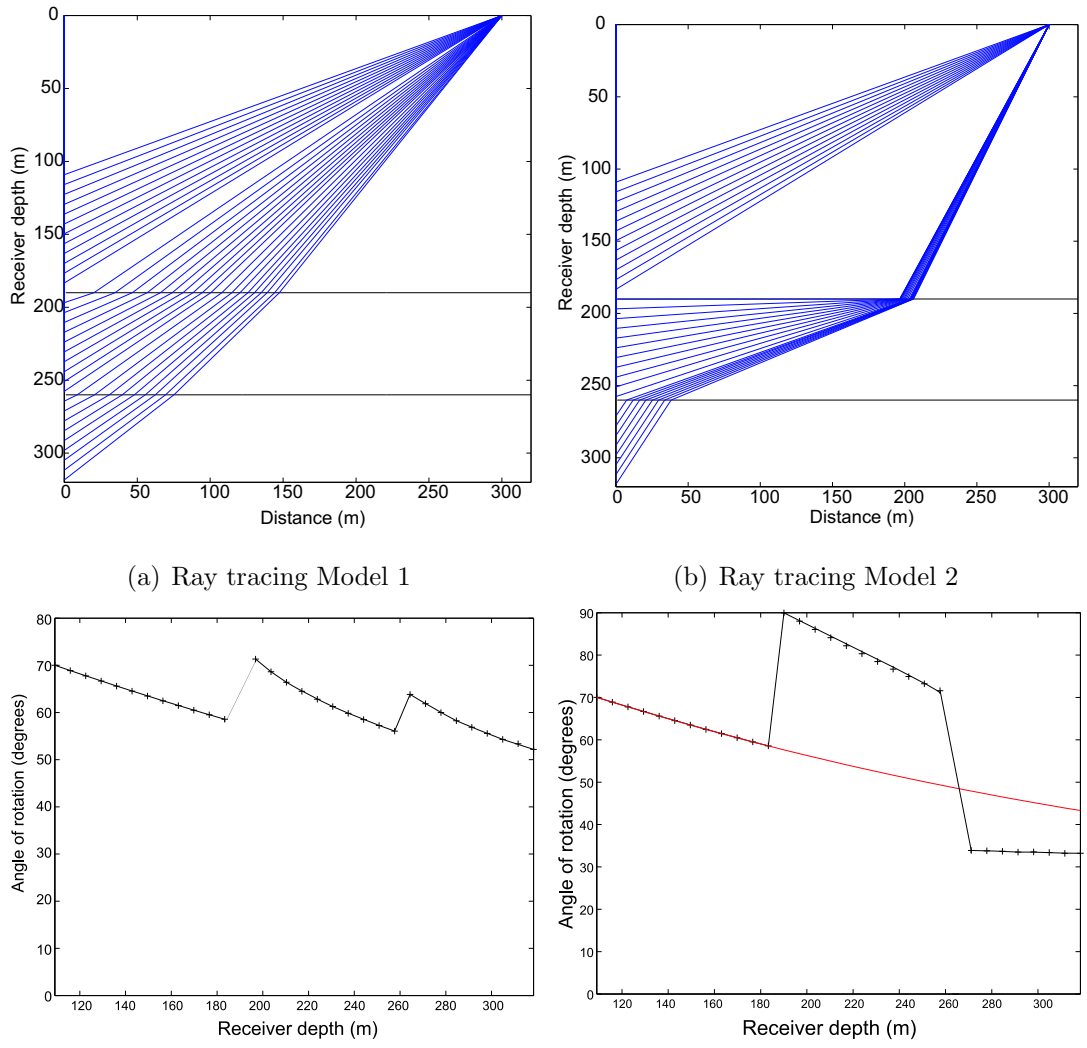

(a) Ray tracing Model 1

(b) Ray tracing Model 2

(c) Incidence angles Model 1

(d) Incidence angles Model 2

Figure 3.9: Ray tracing using properties from Table 3.1. The red line shows angles of incidence for straight rays in a homogeneous medium.

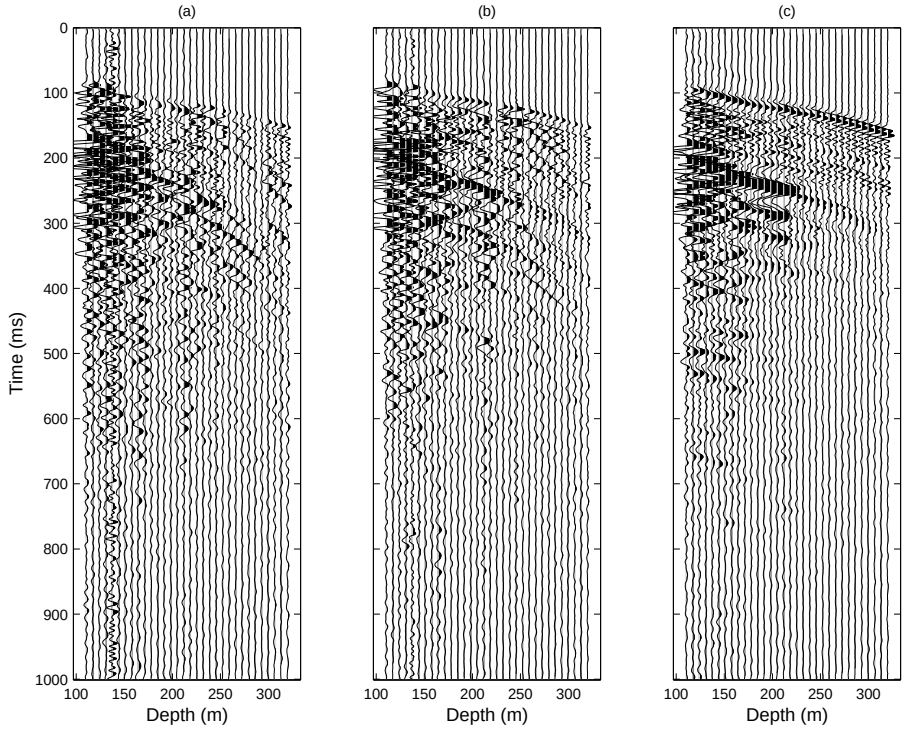

Figure 3.10: Components a) H1, b) H2, and c) vertical for Well 2, azimuth 94^o before geophone rotation.

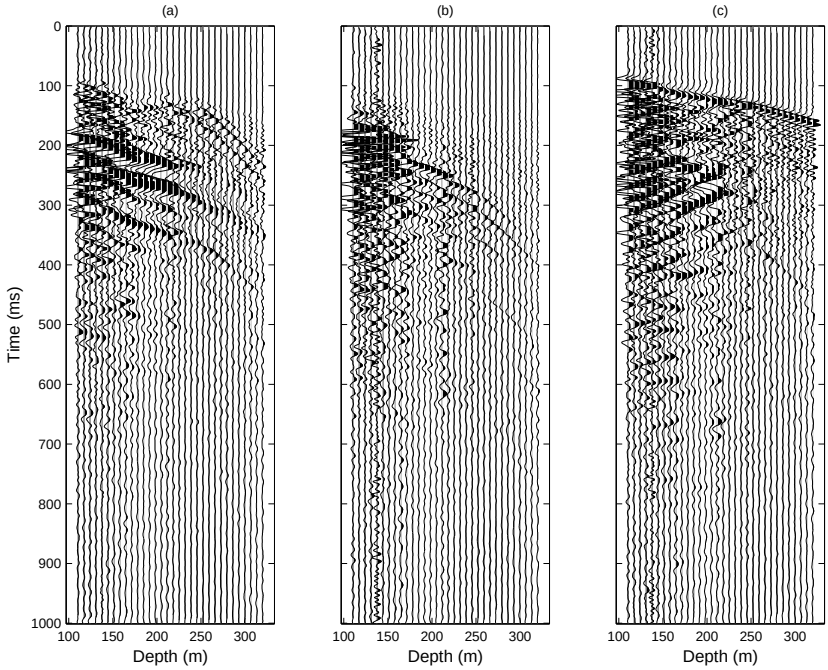

Figure 3.11: Components a) normal, b) horizontal and c) radial for Well 2, azimuth 94^o.

the linearity has optimum smoothness for this window length. Additionally, 28ms is the approximate length of the full cycle of a wavelength around the first breaks (see figures 3.10 and 3.11). Furthermore, this window length maintains consistency with the window used for searching for the angles of rotation discussed in the last section.

Using the ratio of the largest eigenvalue to the second largest in magnitude we calculate the linearity between the three components, panel (a) of Figure 3.14. The dip is calculated from the three eigenvectors (Hendrick and Hearn, 1999) and shown in Figure 3.14b. As expected, the angle between the major axis (aligned with R) and the minor axis of the axis of the ellipsoid is 90^o.

Figures 3.15 and 3.16 show the filtered P and S sections for the N, H and R components. The N and H panels with the S wave energy (Figure 3.16) contain mainly downgoing waves, whereas the R component contains upgoing and downgoing waves. Although in the P-wave R component the energy is allocated correctly around the first breaks, the rest of the energy of the P-wave R is poorly coherent, particularly on the upgoing waves. I thus proceed with a different method.

A median filter of 5 samples is applied to the radial component of the shotgather from Figure 3.11. The resulting filtered downgoing waves are very smooth, and contain only P-wave energy, as is shown in Figure 3.17. However, the residual upgoing panel contains both reflected waves and downgoing PS waves of poor quality.

I apply an FK filter to the same radial components of Figure 3.11, also shown in panel (a) of Figure 3.18. The filter is designed to separate the negative and positive wave trains. Figure 3.18b contains the filtered downgoing waves. The upgoing wavefield shown in panel (c) was obtained by substracting the original radial component from the filtered one. Notice that in panel (c) some downgoing wave events still remain, specifically the converted PS waves at 250m and addi-

tional downgoing energy around the first breaks. Nevertheless, the quality of the upgoing wavefield (Figure 3.18c) is smoother, more coherent and less noisy than the upfield obtained by the median filter (Figure 3.17c). Therefore, since we are particularly interested in the upgoing waves, we choose the FK filter method to perform the wavefield separation.

I apply the FK transformation to the shallowest 1024 samples and the 32 receivers, of the five walk-around VSP's. All of common shot (and azimuth) gathers are padded with zeros before the transformation to avoid noise when transforming back to the time receiver-depth domain.

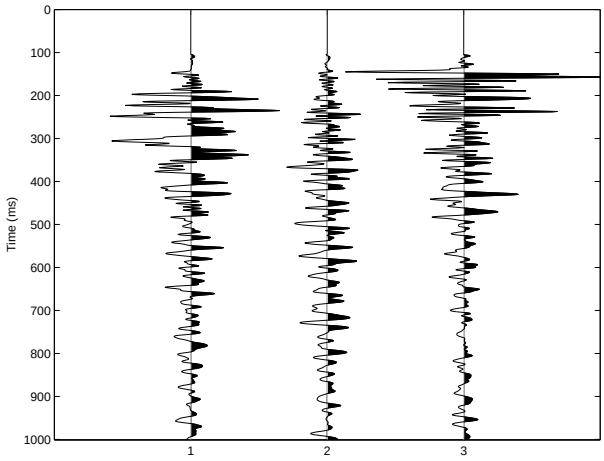

Figure 3.12: Traces used for testing the covariance window length shown on Figure 3.13. Traces 1, 2, and 3 correspond to components N, H and R for receiver number 29, Well 2.

3.5.3 Frequency, travel time and amplitude analysis

I selected five events for analysis of travel time, amplitude and instantaneous frequency. These events, labeled in Figure 3.19, correspond to:

(A) the downgoing first arriving P waves on the radial component,

(B) a reflected (multiple) wave starting at ∼400ms from the first receiver on the upgoing radial component,

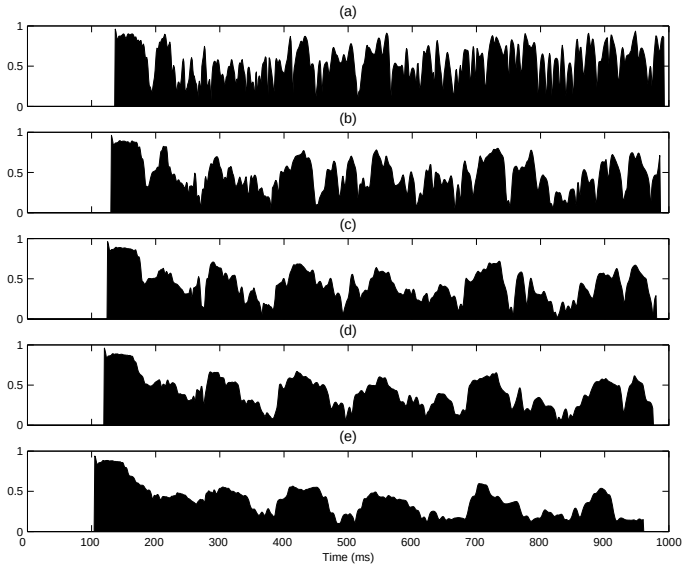

Figure 3.13: Test on window length for calculating the covariance. (a) 16ms, (b) 28ms, (c) 40ms, (d) 50ms, (d) 80ms. Well 2, components N, H and R, receiver number 29.

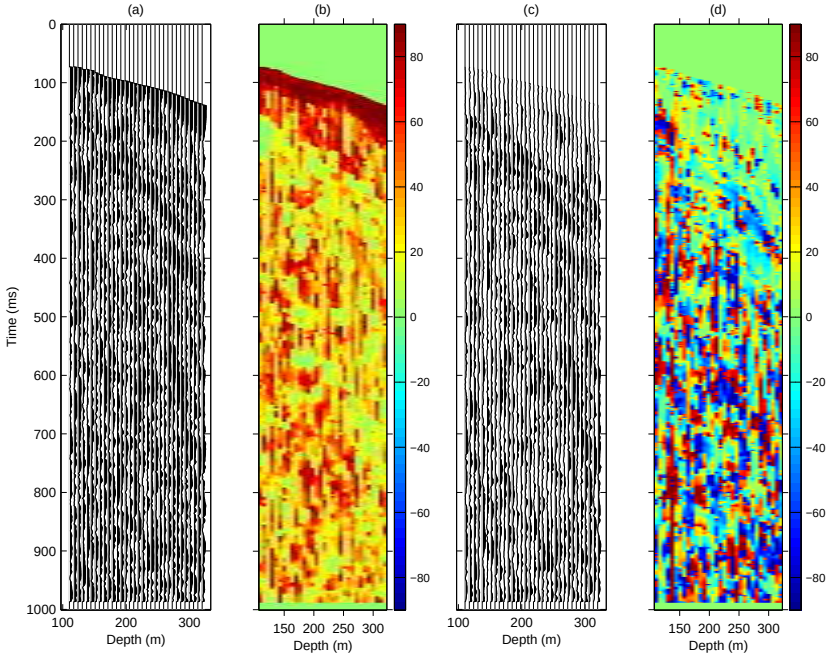

Figure 3.14: Covariance matrix parameters for wavefield separation for components N,H and R shown in Figure 3.11. (a) Linearity, (b) dip of the main axis of the particle motion, (c) measure of confidence of the azimuth, (d) azimuth of the main axis of the particle motion

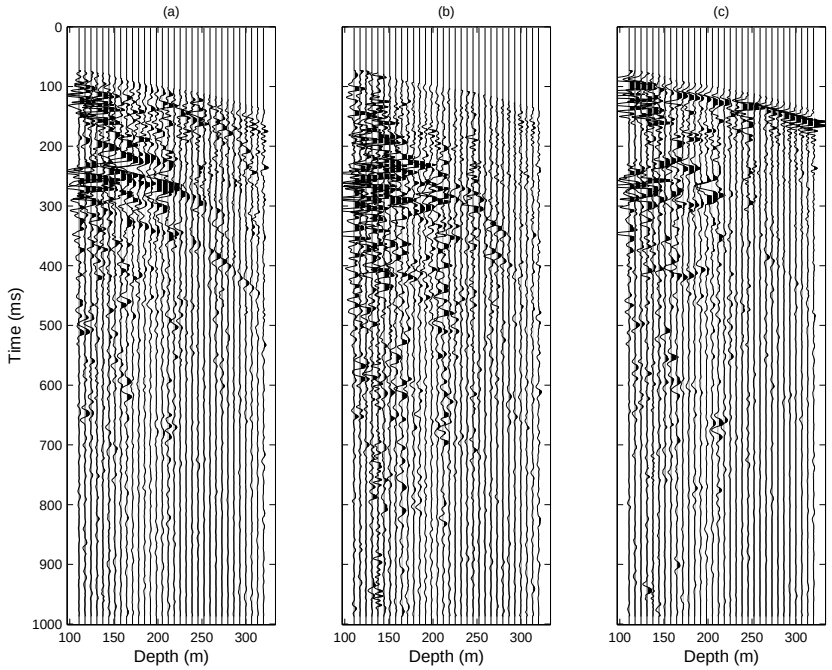

Figure 3.15: P-waves filtered out with the covariance matrix method for the three components shown in Figure 3.11. P energy on the N, H and R components in panels (a), (b) and (c) respectively.

(C) a reflected (multiple) wave starting at ∼450ms on the upgoing R component,

(D) a downgoing PS converted wave from the first arrivals at 250ms on the N component,

(E) a downgoing (multiple) PS converted wave at ∼250m from an event starting at approximately 300ms on the N component.

Notice that events B and C are upgoing events that do not reach the deeper receivers below ∼240m, as seen in Figure 3.19b. They are thus interpreted as multiples of a shallower event, and were chose for interpretation due to their high aplitudes. Notice also that the downgoing PS converted event E does not split from the first arriving P-wave as shown in Figure 3.19a. Event E is thus interpreted as a PS conversion of a multiple event.

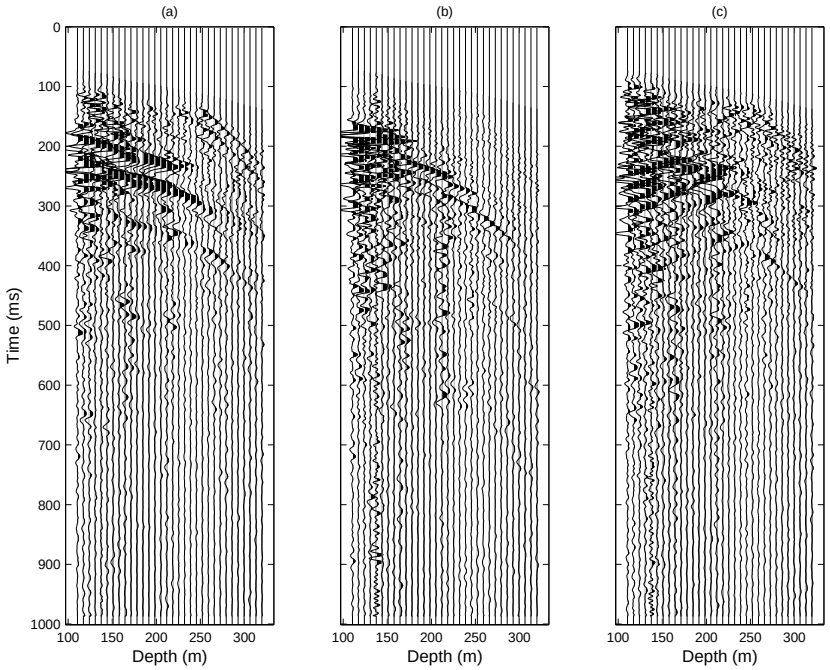

Figure 3.16: S-waves filtered out with the covariance matrix method for the three components shown in Figure 3.11. S energy on the N, H and R components in panels (a), (b) and (c) respectively.

Figure 3.20 shows events A, B, D and E versus azimuth. Panel (a) shows event A on the downgoing R component taken from the deepest receiver (number 32) of Well 3. Panel (b) shows event B on the upgoing R component taken from a shallower receiver (number 11) on Well 3. Panel (c) shows events D and E on the N component taken from the deepest receiver of Well 1. For reference, all panels show the travel time to the first direct P-wave (event A). For the events where the recorded wave has traveled longer (events B and E) a clear anisotropic behaviour in the travel time is observable, as shown in panels (b) and (c).

The frequency content analysis on events A, B, D and E was done on a Butterworth window of 101ms around each event. Figure 3.21 shows events A and B versus azimuth and depth windowed for the frequency analysis (on Well 1), in the downgoing and upgoing R component respectively. Although event C is clearly identifiable from the gather shown in Figure 3.19 it was very difficult to recognise throughout the different surveys and was thus not included in the analysis. This

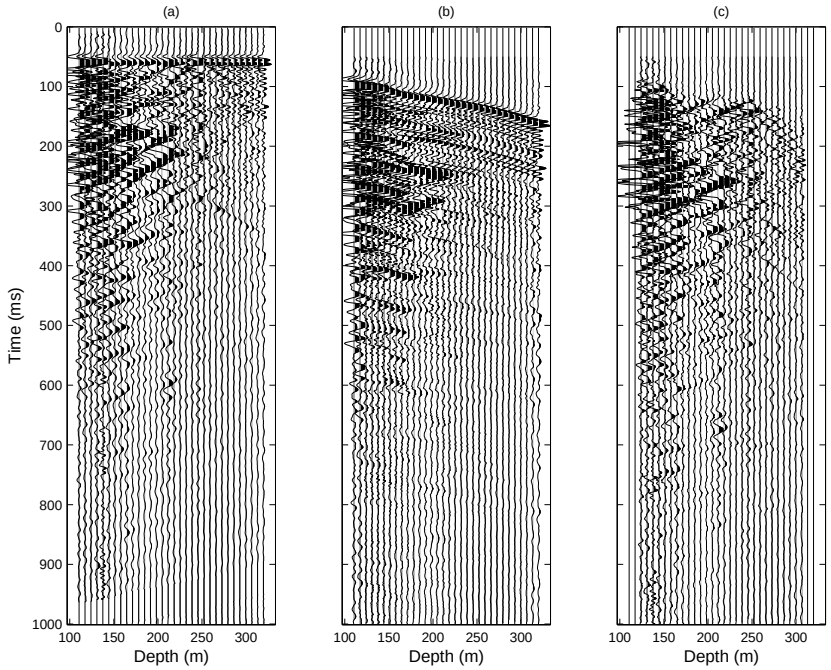

Figure 3.17: Median filter of 5 samples applied on the radial component of the gather shown in Figure 3.11. (a) gather aligned at the first arrivals time with a time shift of 50ms, (b) filtered downgoing waves, (c) upgoing waves.

shows one of the challenges of working with field seismic data.

The weighted instantaneous frequency by quadrants as explained above is shown in radial coordinates on figures 3.27, 3.30, 3.33 and 3.36 for events A, B, D and E respectively. For comparison, the amplitude and travel time averaged by quadrants for events B, D and E are also shown in figures 3.30, 3.33 and 3.36. I will refer to these differences in the attributes averaged by quadrants as the relative attributes. These relative attributes show the directions of minimum and maximum amplitudes of the attributes when fitted to a $cos(2\phi)$ function. Zero degrees (0°) in these figures corresponds to the geographic north, the colorscale corresponds to the frequency difference for that location (calculated with the procedure sketched in Figure 3.2), with dark red corresponding to a positive difference and dark blue to a negative one. The radial direction is receiver depth, or receiver number scaled with radius proportional to depth.

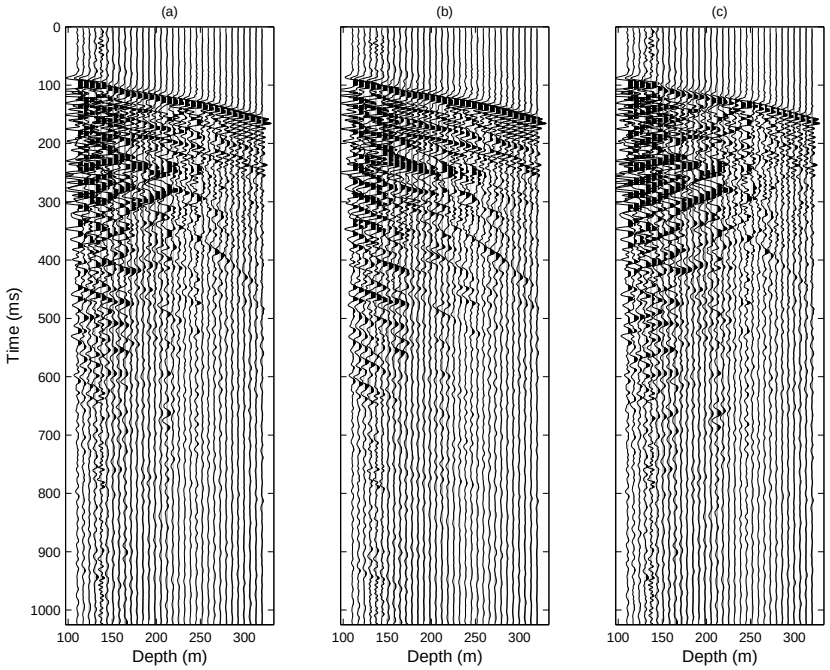

Figure 3.18: FK filter applied to the R component of Figure 3.11. The filter separates the positive wavenumbers from the negative ones. (a) R component, (b) downgoing waves, (c) upgoing waves.

In the following section I discuss in detail the findings from the analysis of events A, B, D and E.

3.5.3.1 Event A: Direct P-wave on R component

The left side of Figure 3.22 shows the travel time, amplitudes and instantaneous frequency versus azimuth (see panels a, c and e respectively) for all 32 receiver depths (for Well 3, year 2002). The relative attributes: travel time, amplitudes and instantaneous frequency differences averaged by quadrants, are shown in the right side panels b, d and f respectively. Although the azimuthal changes in the attributes can be seen from the left side panels, the relative attributes enhance the azimuthal differences making visually clear which is the dominant direction for each attribute. Below I analyse in more detail the behaviour of these attributes for Well 3 in year 2002.

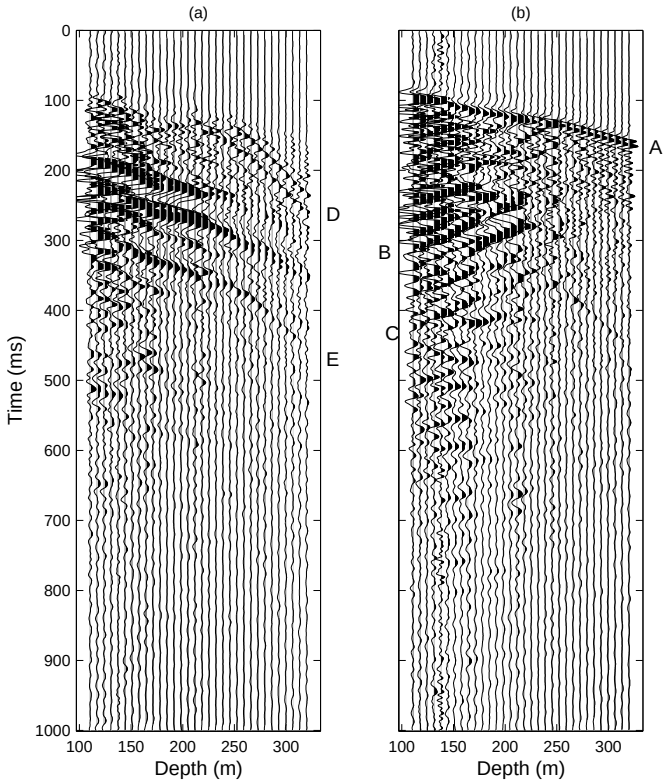

Figure 3.19: Events A, B, C, D and E chosen for attenuation studies. (a) N component, (b) R component. Note that although event A is shown in panel (b) is was analysed from the downgoing P waves shown in panel (b) of Figure 3.18.

Detailed analysis for Well 3, year 2002

The variation with depth of the travel time, amplitude and frequency are shown for all azimuths in Figure 3.22 panels g, h, and i. Changes in velocity are observed in panel g at 180m and 240m. A marked variation of amplitudes with depth is also seen in panel h. The shallow receivers above 140m recorded large negative amplitudes, which decrease in absolute value until 150m. Below 150m the amplitudes become more negative again, reaching a negative peak at 240m. Below 240m the values of the absolute amplitudes vary rapidly from low to high, remaining always negative.

The weighted instantaneous frequency (for this well) tracks the behaviour of

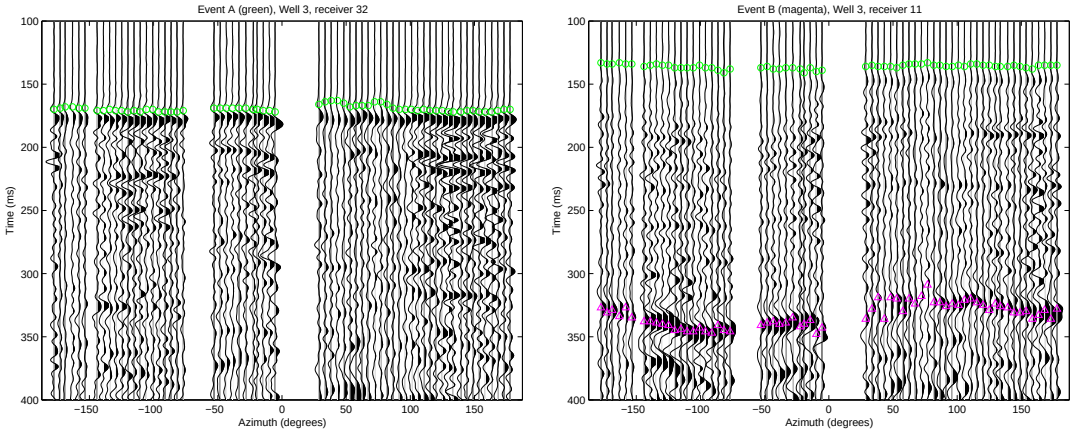

(a) Event A (green) (b) Event B (magenta)

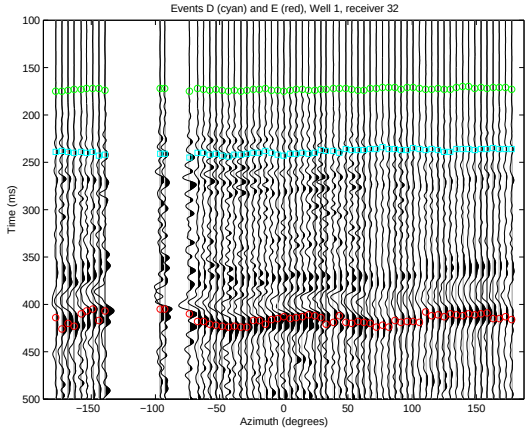

(c) Events D (cyan) and E (red)

Figure 3.20: Events A, B, D and E versus azimuth. Panel (a) shows the downgoing R component taken from the deepest receiver (number 32) of Well 3. Panel (b) shows the upgoing R component taken from a shallower receiver (number 11) on Well 3, and panel (c) shows the N component taken from the deepest receiver of Well 1.

the amplitudes as a mirror image, such that the frequency increases in the ranges where the amplitudes become more negative (higher absolute value), as shown in Figure 3.22 h and i. This effect is clearly observable in the rose diagrams discussed below.

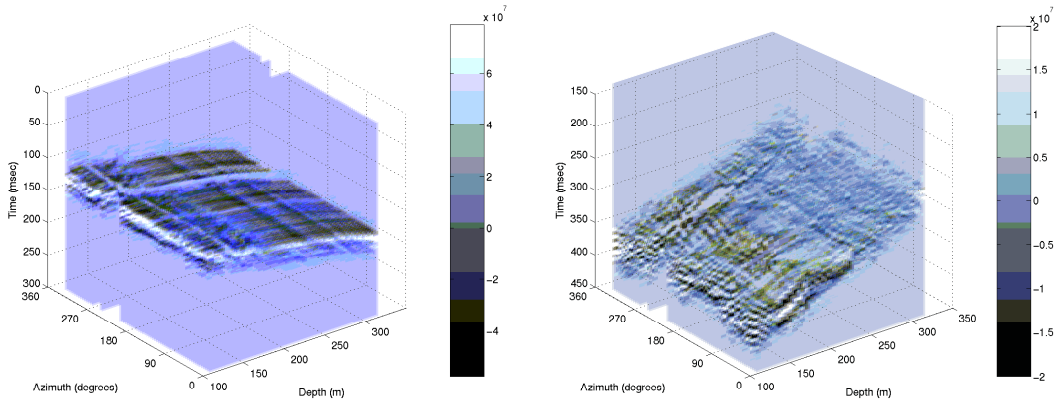

(a) Event A windowed (b) Event B windowed

Figure 3.21: Events A and B windowed for calculation of the instantaneous frequency shown on Well 1. Events A and B were picked on the downgoing and upgoing R component respectively.

Attributes fitted to cosine2ϕ function

I fit each attribute at every receiver level to a function of the form $A1 + A2\cos 2(\phi - \phi_{sym})$. The coefficients A_1 and A_2, and the angle of symmetry ϕ_{sym} inverted from the fit provide insight into the behaviour of the fitted attribute.

Figure 3.23 shows the coefficients A_1 and A_2, and the angle of symmetry ϕ_{sym} found from fitting the travel time of event A per receiver level to the cosine2ϕ function. Panel a shows how the mean of the data per receiver level (A_1) increases with depth as the wave travels longer to the deeper receivers. Additionally, three distinct slopes or velocity ranges in depth are also observed in panel a, with the change in slope occurring at approximately 170m and 250m. These slopes in A_1 suggest a higher velocity between depths 170m to 250m, and a lower velocity with equal values above 170m and below 250m. This change in A_1 at 170m and 250m is also observable in A_2 and ϕ_{sym} (see panels b and c). From the geological background of the area the fractured carbonates from the Natih formation are expected to be in a depth range from 190m to 260m. The changes in velocity can then be attributable to the Natih formation.

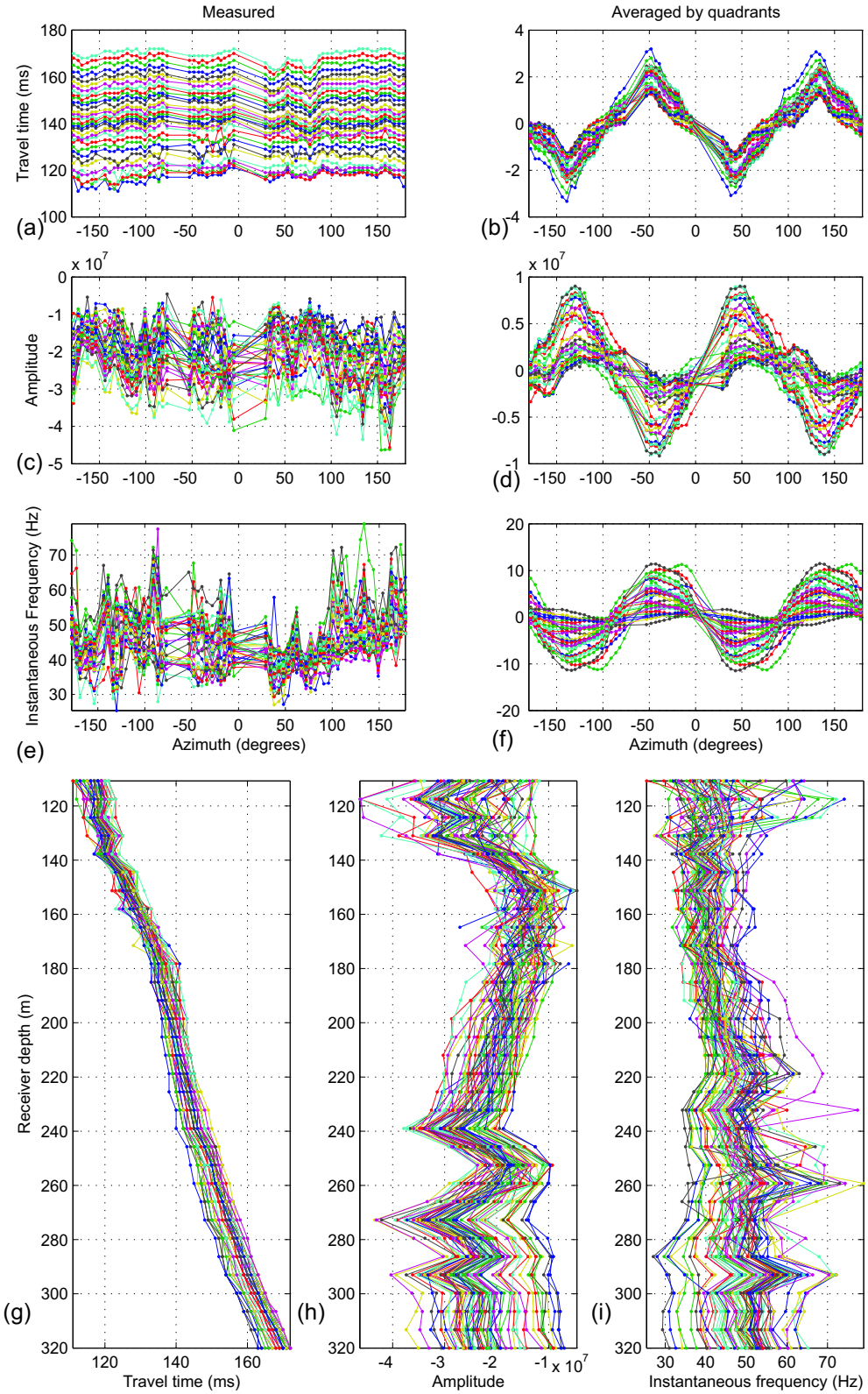

Figure 3.22: Attributes versus azimuth and depth for event A, Well 3. Event A was picked in the downgoing R component.

A decrease in the amplitude of the sinusoidal fit A_2 from the shallowest receivers at 109m down to 200m is observed in Figure 3.23b, suggesting that the azimuthal variations in travel time become minimum at approximately 200m. From 200m to 250m there is a sharp increase in A_2. For the deepest section, deeper than 250m, the value of A_2 stays constant.

The direction of minimum travel time is estimated at $\sim 35°$ for ϕ_{sym} in the shallow section (above 170m), and values close to 40° for the rest of the section as shown in Figure 3.23c. This is also shown in the rose diagram (panel e), which shows a dominant orientation of N40E as the direction of minimum travel time. In more detail, panel f shows the rose diagram for the ranges above (black) and below (green) 250m, both showing the same N40E direction.

The error of the sinusoidal fit, shown as the sum of squared errors divided by the number of samples $\sum \frac{\sqrt{(x_{fit}-x_{measured})^2}}{N}$ is shown in Figure 3.23d. Notice that the error becomes smaller when the amplitude of the fit A_2 is minimum.

Figures 3.24, 3.25 and 3.26 show A_1, A_2, and ϕ_{sym} for the amplitudes, instantaneous frequency and relative instantaneous frequency averaged by quadrants for event A. The changes in the coefficients and angle of symmetry at the two interfaces (at approximately 170m and 250m) are also observable in the amplitudes and frequency content.

Frequency and rose diagrams

The relative frequency for event A is shown in Figure 3.27. Panels a to c show surveys for wells 2, 1 and 3 in 2002, and (d) and (e) show surveys for Well 3 in 2004 and 2005 respectively. A dominant direction of high frequency content in the NW direction is observed in all surveys of Well 3 (panels c, d and e). However, for wells 1 and 2 (panels a and b respectively) the dominant direction is less clear. Thus, I calculate rose diagrams to show the dominant azimuthal directions of the attributes.

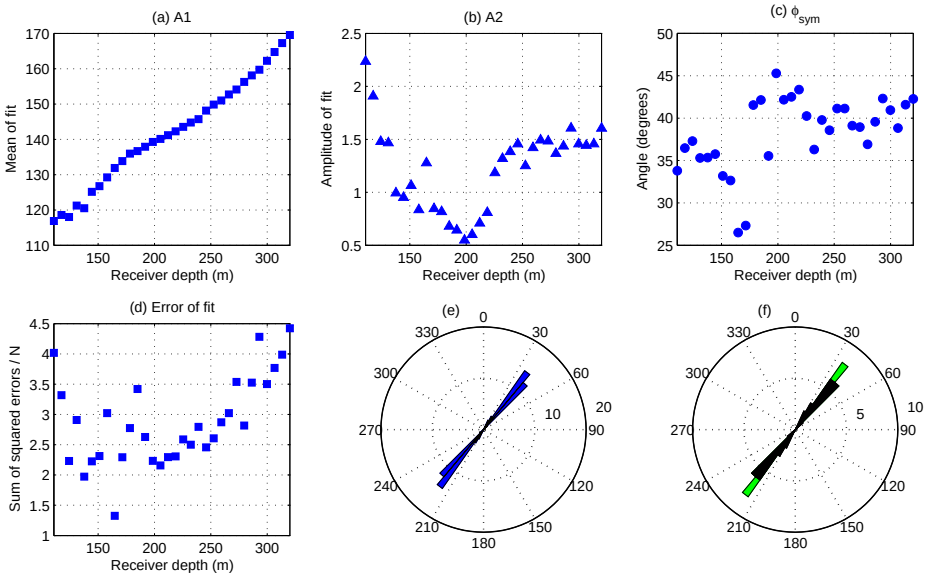

Figure 3.23: Travel time to first breaks of the direct P-wave on R component, Well 3, year 2002, event A. The radial axis on panels e) and f) is the frequency of the radial histogram.

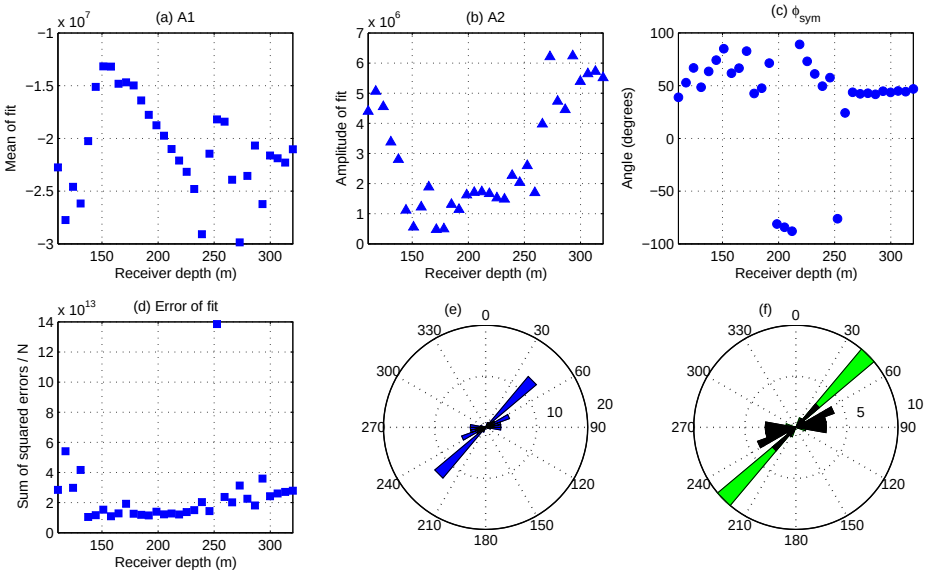

Figure 3.24: Amplitudes of the direct P-wave on R component, Well 3, year 2002, event A.

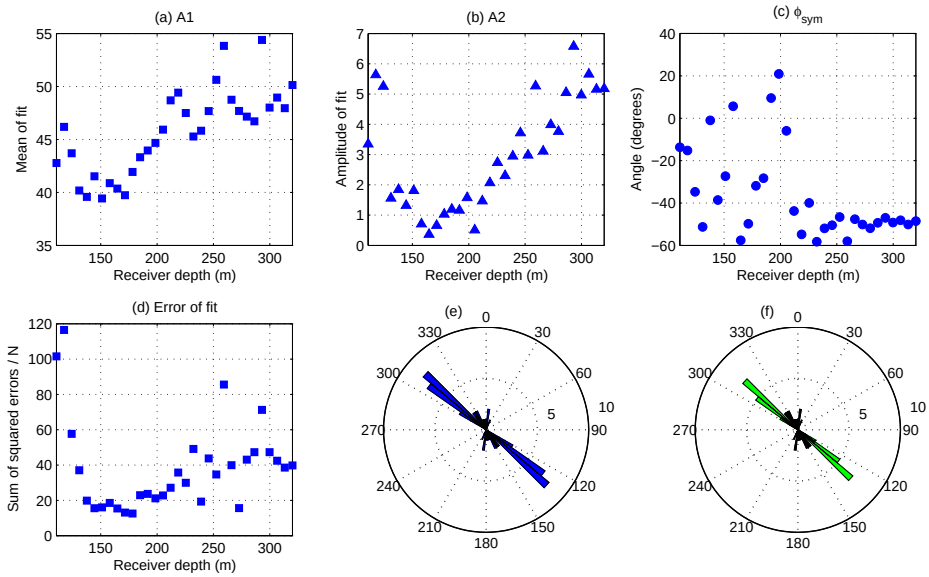

Figure 3.25: Weighted instantaneous frequency of the direct P-wave on R component, Well 3, year 2002, event A.

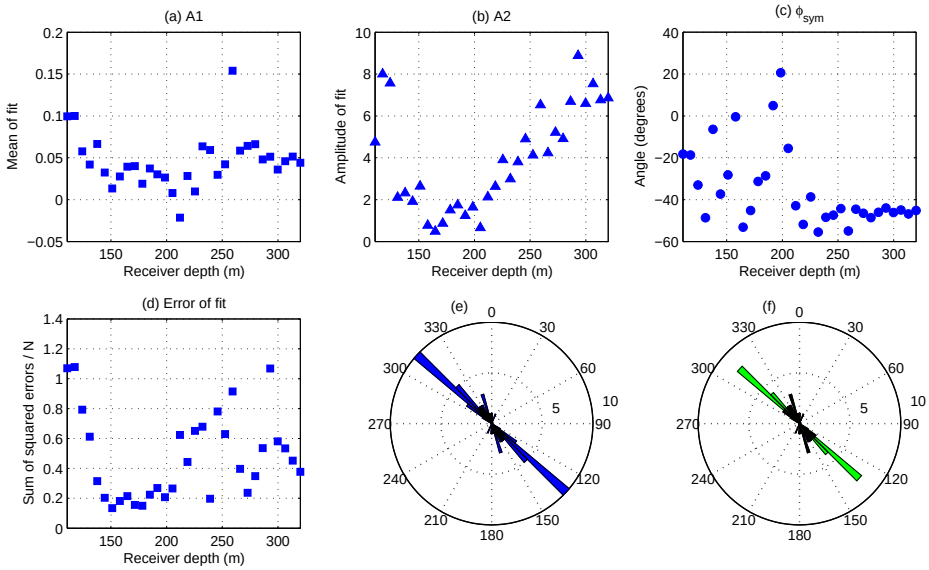

Figure 3.26: Relative instantaneous frequency of the direct P-wave on R component, Well 3, year 2002, event A.

Simple models based on rock physics theories (Chapter 2) show that in the presence of a single set of vertically aligned fractures the directions of minimum travel time, maximum amplitude and maximum frequency content are equal. However, the comparison of the rose diagrams from these attributes (shown in figures 3.23, 3.24, 3.25 and 3.26 for Well 3, year 2002) show that the directions of minimum travel time and maximum amplitude coincide, but differ (by $\sim 90^{\circ}$) from the direction of maximum weighted instantaneous frequency and the instantaneous frequency averaged by quadrants. Furthermore, for the same well in years 2004 and 2005 the same effect occurs, with the main directions being equal to those of year 2002 (see Figure 3.28) .

In terms of changes in orientations with time, I find that there are more differences in orientations between the different wells than within the same Well 3 in the different years, which is shown in the rose diagrams of Figure 3.28.

From this analysis I find that the orientations obtained by the instantaneous frequency is the same whether it is shown as the weighted instantaneous frequency or the frequency difference averaged by quadrants (see Figure 3.28). Thus, in the summary Table 3.2 below and the analyses of the other events I will only refer to the direction obtained from the relative attributes.

Well, year	Min travel-time	Max amplitude	Max IF
Well 1, 2002	N80W	N72W	s:NS, d:N45W
Well 2, 2002	s:NS, d:N15E	s:N45E, d:N70E	s:N45W, d:N15E
Well 3, 2002	N45E	N45E	N45W
Well 3, 2004	N45E	N45E	N45W
Well 3, 2005	N45E	N45E	N45W

Table 3.2: Orientations of rose diagrams showing directions of minimum travel time, maximum amplitude and maximum relative frequency for event A. Shallow receiver orientations are denoted by s (above 250m), and deeper receivers by d (below 250m).

The deeper and shallow receivers (below and above 250m respectively) have the

same dominant orientations except for Well 2 for all the attributes and Well 1 for relative frequency.

When comparing all surveys for year 2002, Table 3.2 and Figure 3.28 show that there are four dominant directions, which are approximately N-S, N45E, N45W and N80W.

Based on the observations above, my interpretation from the rose diagrams of event A (Figure 3.28 and Table 3.2) is that the direct P-wave is responding to more than one set of vertically aligned fractures. Perhaps some of the attributes shown are more sensitive to open or closed fractures than others. However, with the information provided this remains a speculative matter.

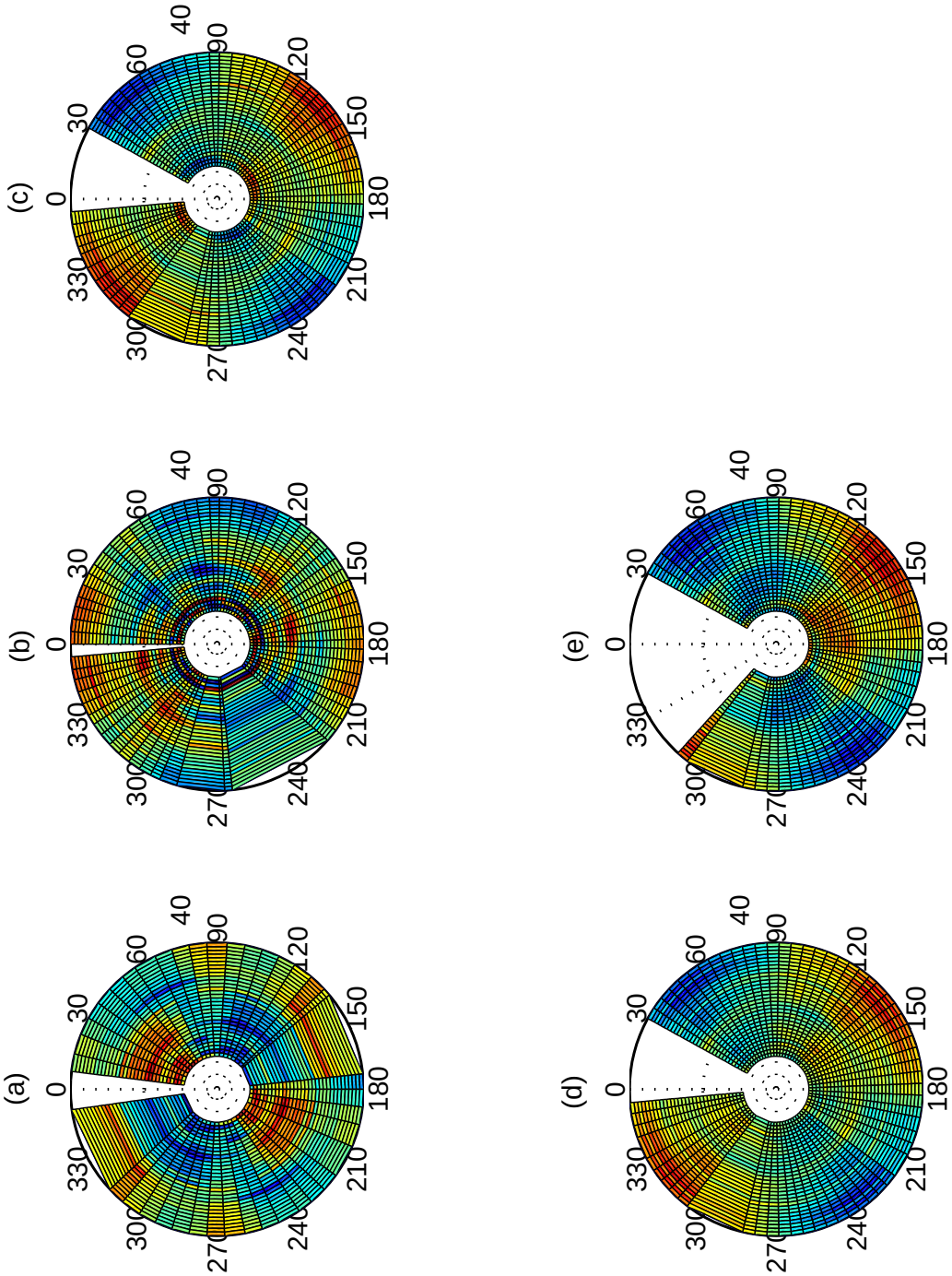

Figure 3.27: Frequency difference, for event A of Figure 3.19. The radial axis is receiver depth, the azimuthal axis is source-receiver azimuth, and the color scale corresponds to the average frequency difference. (a) to (c) shows surveys for wells 2, 1 and 3 in 2002, and (d) and (e) show surveys for well 3 in 2004 and 2005 respectively.

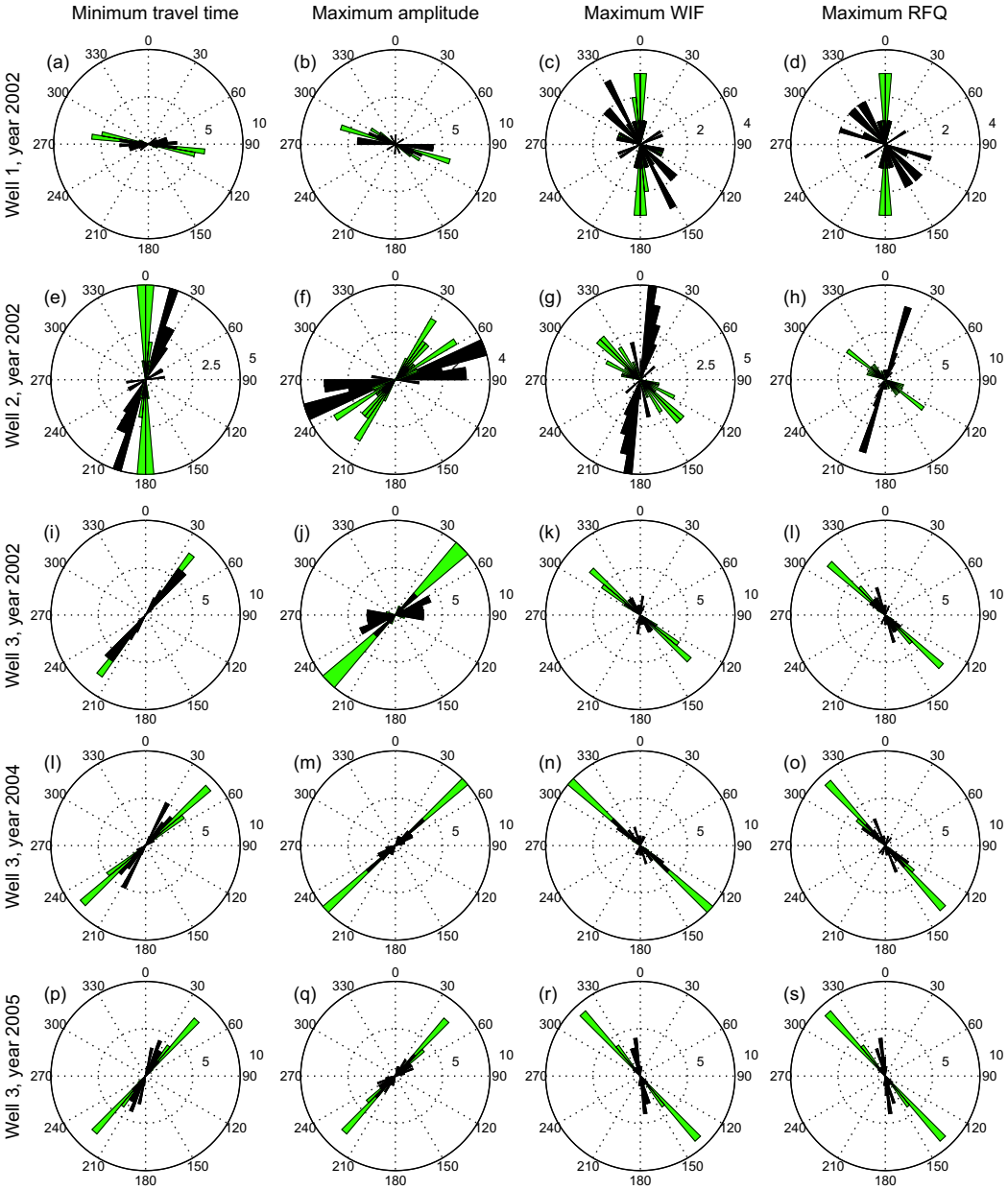

Figure 3.28: Compilation of rose diagrams for event A, all wells and attributes. The rose diagrams show the direction of minimum travel time, maximum amplitude, maximum weighted instantaneous frequency (WIF) and maximum relative instantaneous frequency averaged by quadrants (RFQ). Rose diagrams for wells 1 and 2 are only for year 2002. Well 3 has diagrams for years 2002, 2004 and 2005.

3.5.3.2 Event B: upgoing wave in R component

Event B is an upgoing wave in the R component that spans receivers 4 to 16, corresponding to depths of 129m to 210m.

There is a strongly marked azimuthal variation in the travel time with the frequency of one sinusoid (Figure 3.29a) suggesting that B is a dipping event. The shorter travel times at 90° and larger travel times at −90° suggest a layer with an approximate NS strike and dipping to the west.

In contrast to the alignment in depth of the azimuthal symmetry plane for event A, the angle of symmetry for event B has more variation with depth (see panels b, d and f of Figure 3.29). A zone of high amplitudes between depths of 150m to 180m is observed in Figure 3.29h.

Figure 3.30 shows the variation with depth and azimuth of the relative travel time, amplitude and frequency content. The difference in depth ranges of the different panels in Figure 3.30 reflect the fact that event B was trackable or recognised in Well 2 (which has the smallest offset of 200m) at only four receiver levels, and in ∼11 receiver levels in the other surveys which have an offset of 300m (i.e. Well 1).

The rose diagrams from Figure 3.31 show two dominant orientations with directions N60E (×5) and NS (×4). The remaining orientations have either less recurrence (N20W, ×1), present significant scattering in the rose diagram (EW, ×1), and/or present two main orientations in the same diagram (N10E & N75E, ×2 and N75E & N60W, ×1). A summary of the observed orientations for all attributes on event B are shown in Table 3.3.

The complexity of these diagrams suggests again more than one set of fractures.

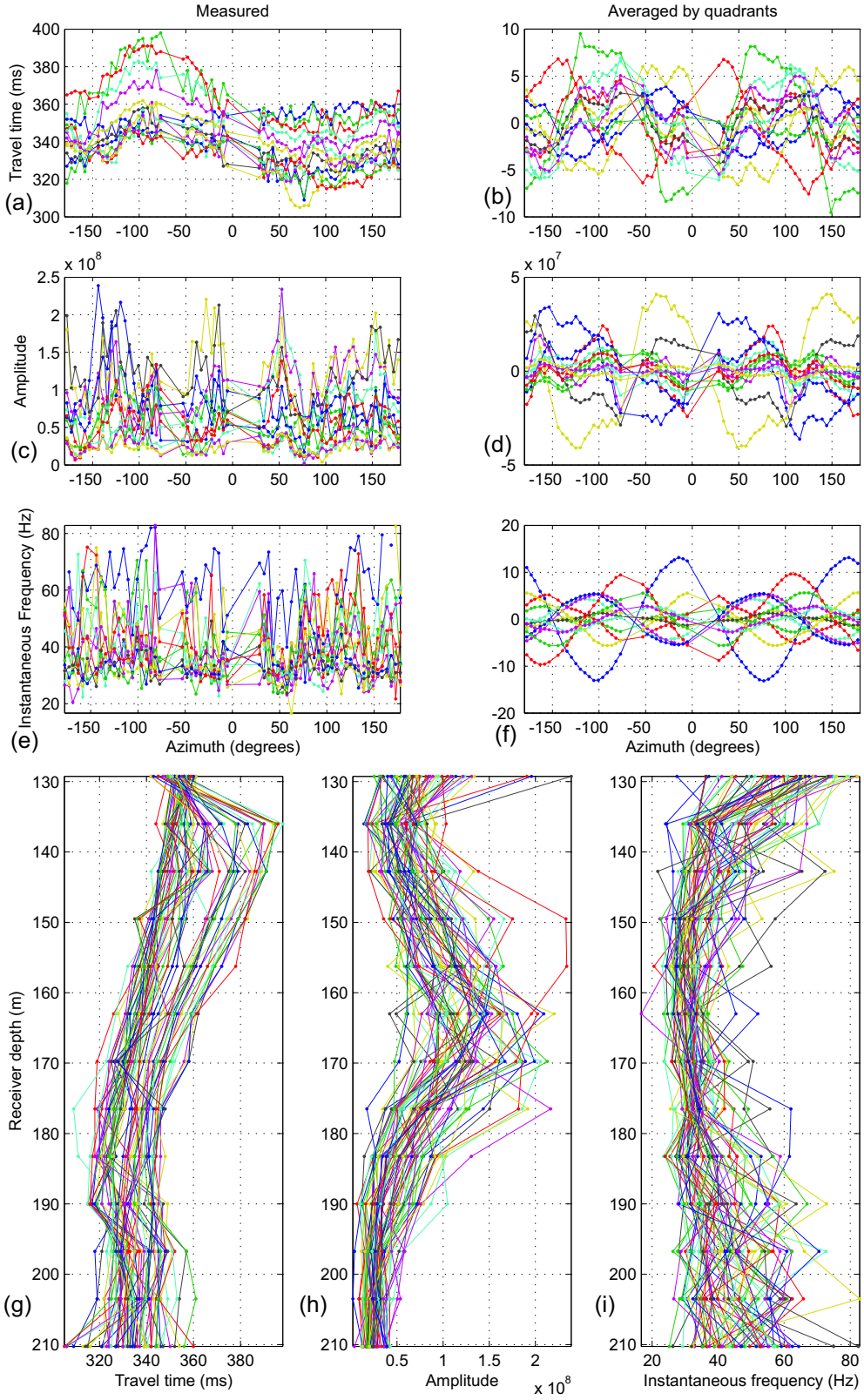

Figure 3.29: Attributes versus azimuth and depth for event B, Well 3. Event B was picked in the upgoing R component.

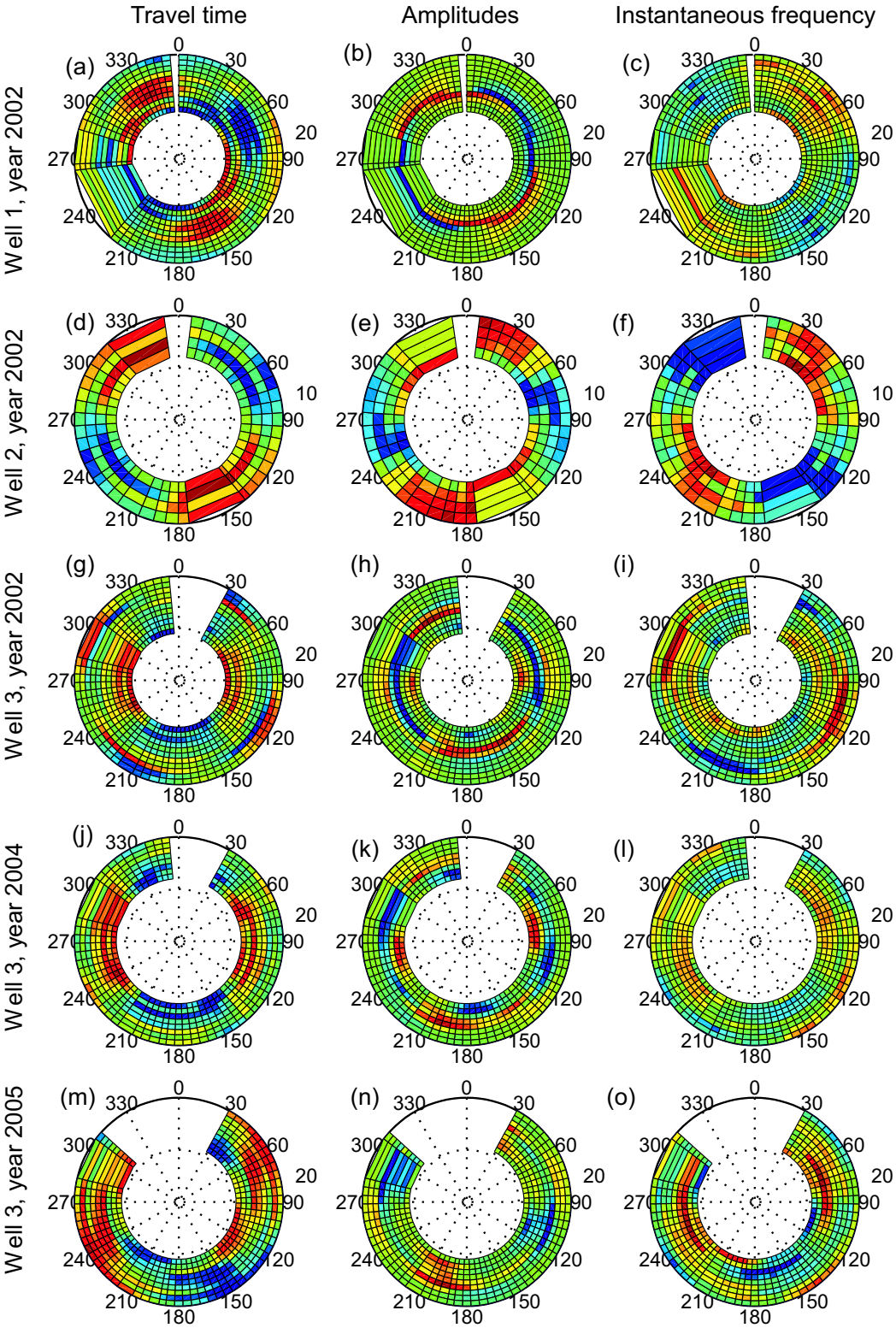

Figure 3.30: Relative travel time, amplitude and frequency differences, for event B. Red shows high positive values and blue negative ones. The radial axis is proportional to depth or receiver level. Event B is shown in Figure 3.19.

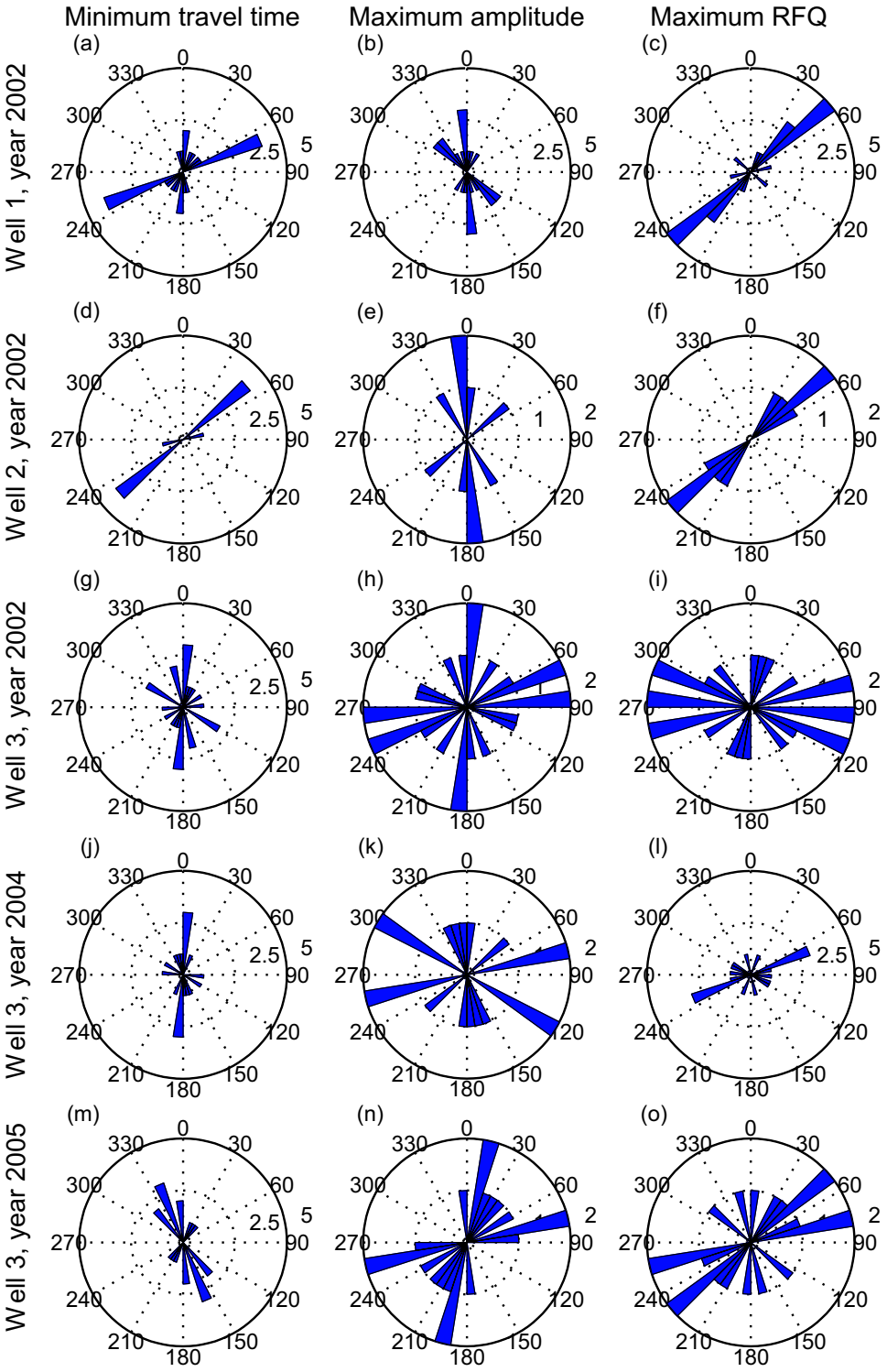

Figure 3.31: Compilation of rose diagrams for event B, all wells and attributes. The rose diagrams show the direction of minimum travel time, maximum amplitude, maximum weighted instantaneous frequency (WIF) and maximum relative instantaneous frequency averaged by quadrants (RFQ). Rose diagrams for wells 1 and 2 are only for year 2002. Well 3 has diagrams for years 2002, 2004 and 2005.

Well, year	Min travel-time	Max amplitude	Max IF
Well 1, 2002	a	b	a
Well 2, 2002	a	b	a
Well 3, 2002	b	d*	e*
Well 3, 2004	b	f*	a
Well 3, 2005	c	d*	a*

Table 3.3: Orientations of rose diagrams showing directions of minimum travel time, maximum amplitude and maximum relative frequency for event B. a=N70E,b=NS,c=N20W,d=N10E & N75E,f=N75E & N60W,e=EW,*:denotes one or two main orientations with scattering in the rose diagram.

3.5.3.3 Event D: downgoing converted PS wave

Event D is a downgoing converted PS-wave that splits from the direct arriving P-wave at an interface at ∼180ms in Well 3 (year 2002), and ends at ∼250ms. The striking feature of event D is that the azimuthal variations in both amplitude and frequency content are clear even before the data are averaged by quadrants, as shown in Figure 3.32, panels c, e, d and f. Due to its nature, event D spans only 8 (or a fourth) of the receiver levels.

Figure 3.33 shows the variations with depth and azimuth of the attributes analysed. The symmetry planes calculated from the azimuthal variations of the attributes show three dominant directions, N75E (×6), N40W (×6), and N30E (×3), as illustrated in Figure 3.34 and listed in Table 3.4.

Well, year	Min travel-time	Max amplitude	Max IF
Well 1, 2002	a	b	a
Well 2, 2002	b	b	a
Well 3, 2002	a	c	c
Well 3, 2004	a	c	c
Well 3, 2005	a	c	c

Table 3.4: Orientations of rose diagrams showing directions of minimum travel time, maximum amplitude and maximum relative frequency for event D. a=N75W, b=N20E, c=N40W.

For Well 3 in all the three years surveyed, the orientations provided by the amplitude and frequency of event D coincide in a N40W direction. On the other hand, for wells 1 and 2 the amplitudes point in a N30E direction whereas the frequency has a N75W orientation, approximately 90° apart for the same event. This hints to the presence of an orthogonal fracture network whose dominating set of fractures varies spatially.

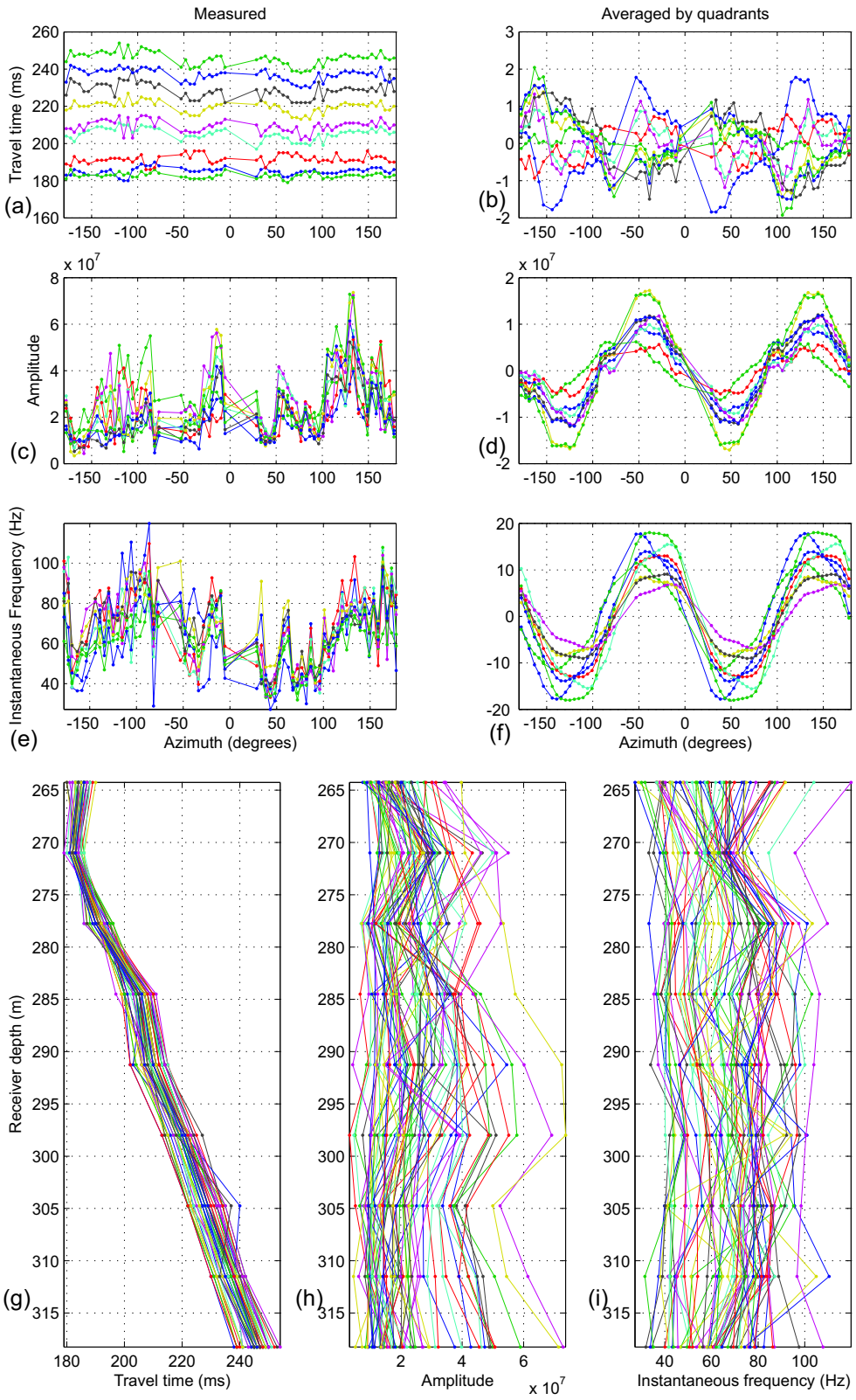

Figure 3.32: Attributes versus azimuth and depth for event D, Well 3. Event D was picked in the N component.

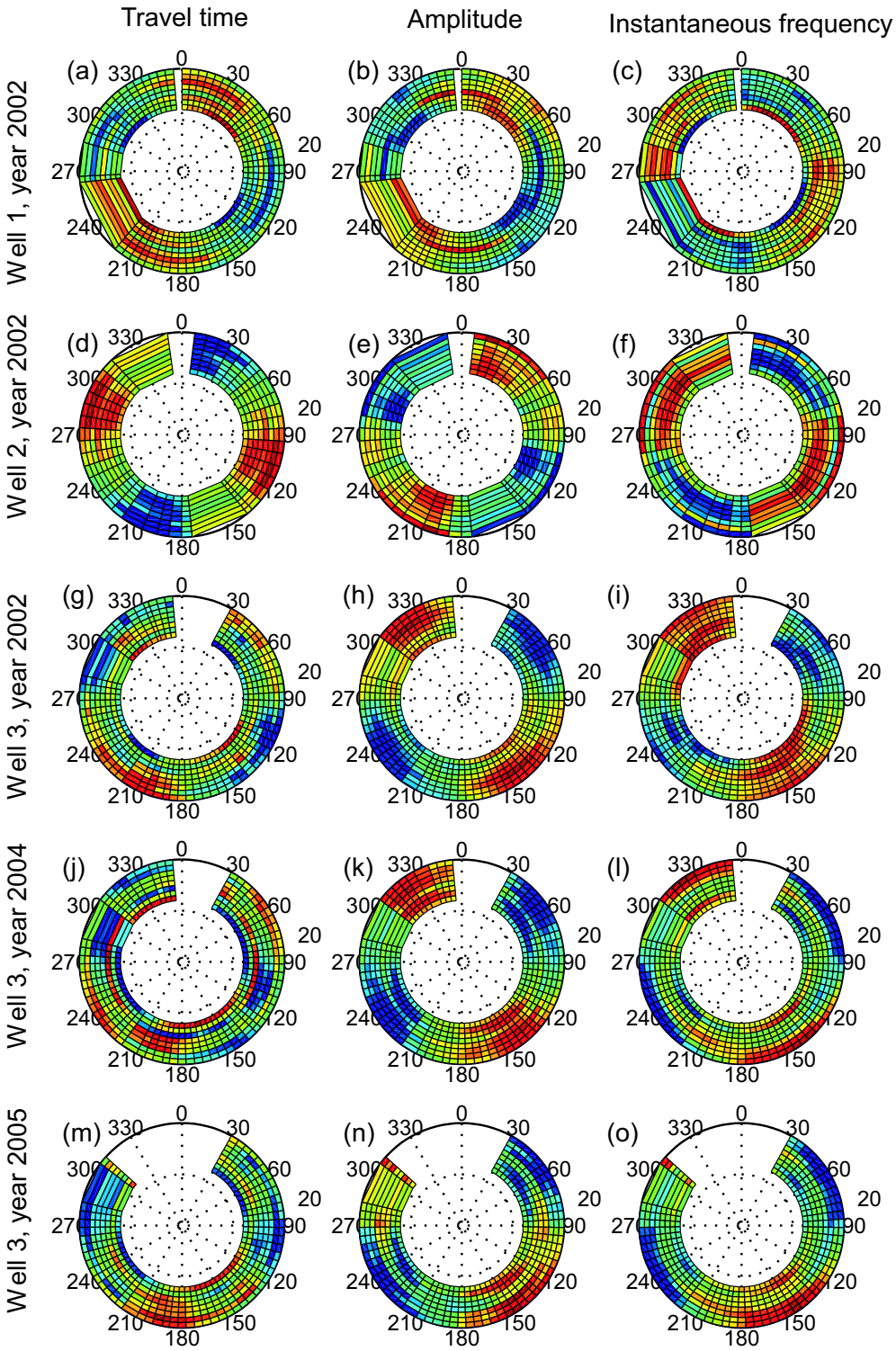

Figure 3.33: Relative differences in travel time, amplitude and instantaneous frequency for event D.

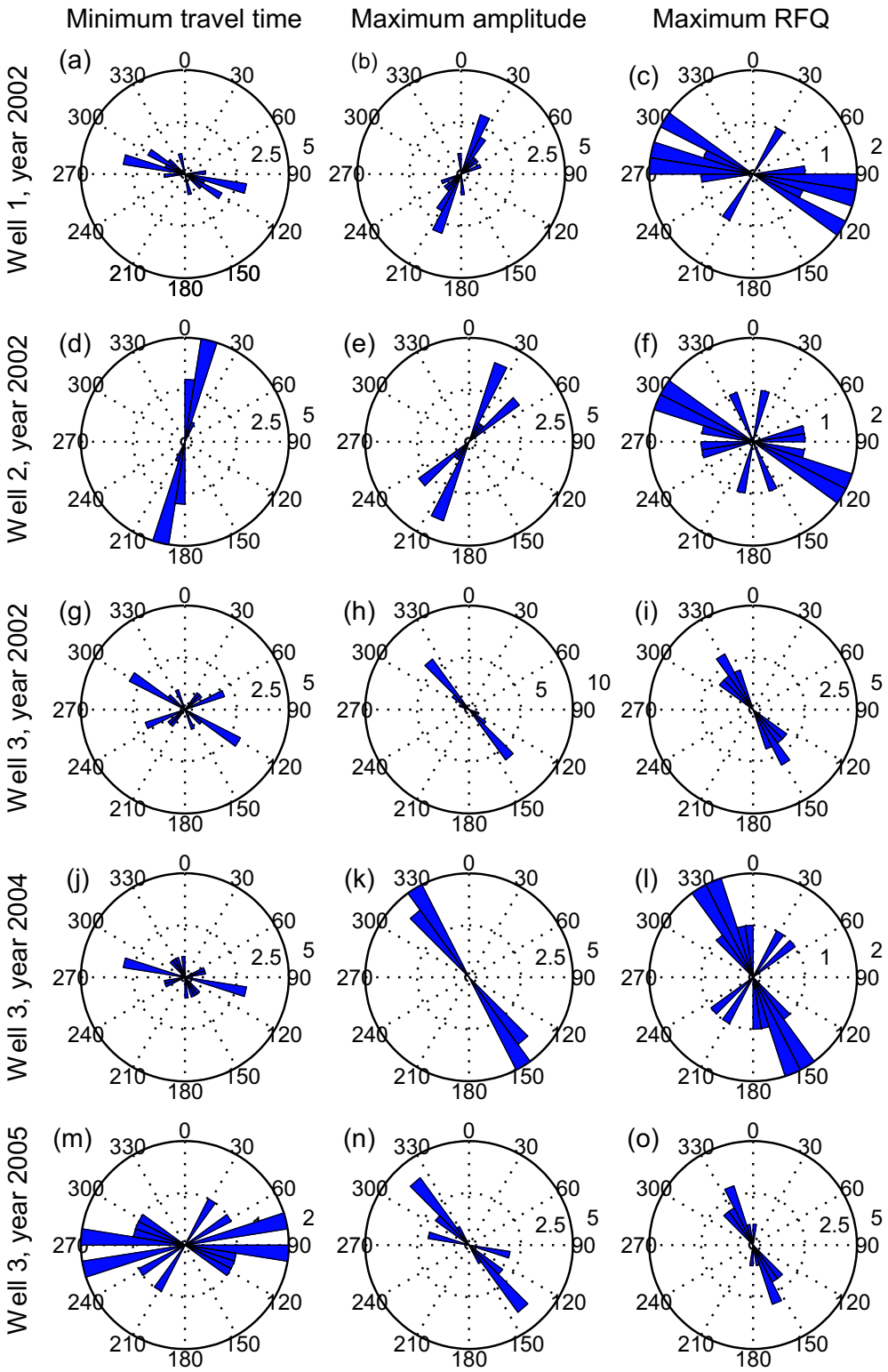

Figure 3.34: Rose diagrams showing directions for minimum travel time, maximum amplitude and maximum weighted instantaneous frequency for event D.

3.5.3.4 Event E: downgoing converted PS wave

Event E is a downgoing converted PS-wave in the N component, that was recorded in only the deepest 5 receiver levels. For Well 3 (year 2002) event E spans times from 360ms to 420ms.

Figure 3.35 shows significant azimuthal variation in the travel time and amplitudes with a consistent pattern in depth. The uniformity of the angle of symmetry with depth is displayed in Figure 3.36. In more detail, the rose diagrams of Figure 3.37 show five different patterns, four of them showing orientations N60E (×3), N45W (×3), EW (× 2) and N20E (×1). The fifth pattern shows no dominant direction, which could be influenced by the fact that the wave spans very few (maximum 5) receiver levels.

Well, year	Min travel-time	Max amplitude	Max IF
Well 1, 2002	d	a	e
Well 2, 2002	d	d	d
Well 3, 2002	b	c	d
Well 3, 2004	b	c	b
Well 3, 2005	e	c	d

Table 3.5: Orientations of rose diagrams showing directions of minimum travel time, maximum amplitude and maximum relative frequency for event E. a=N75W, b=N20E, c=N40W, d=no dominant orientation, e=EW.

3.5.4 Summary and discussion

I have analysed the travel time, amplitude and instantaneous frequency as it varies with azimuth and depth for the five different VSP surveys through four different seismic events. In this section I compile the information extracted from the analysis of the four different events in a search for dominant orientations. I group the data per attribute and separate them into two depth ranges, above ∼210m

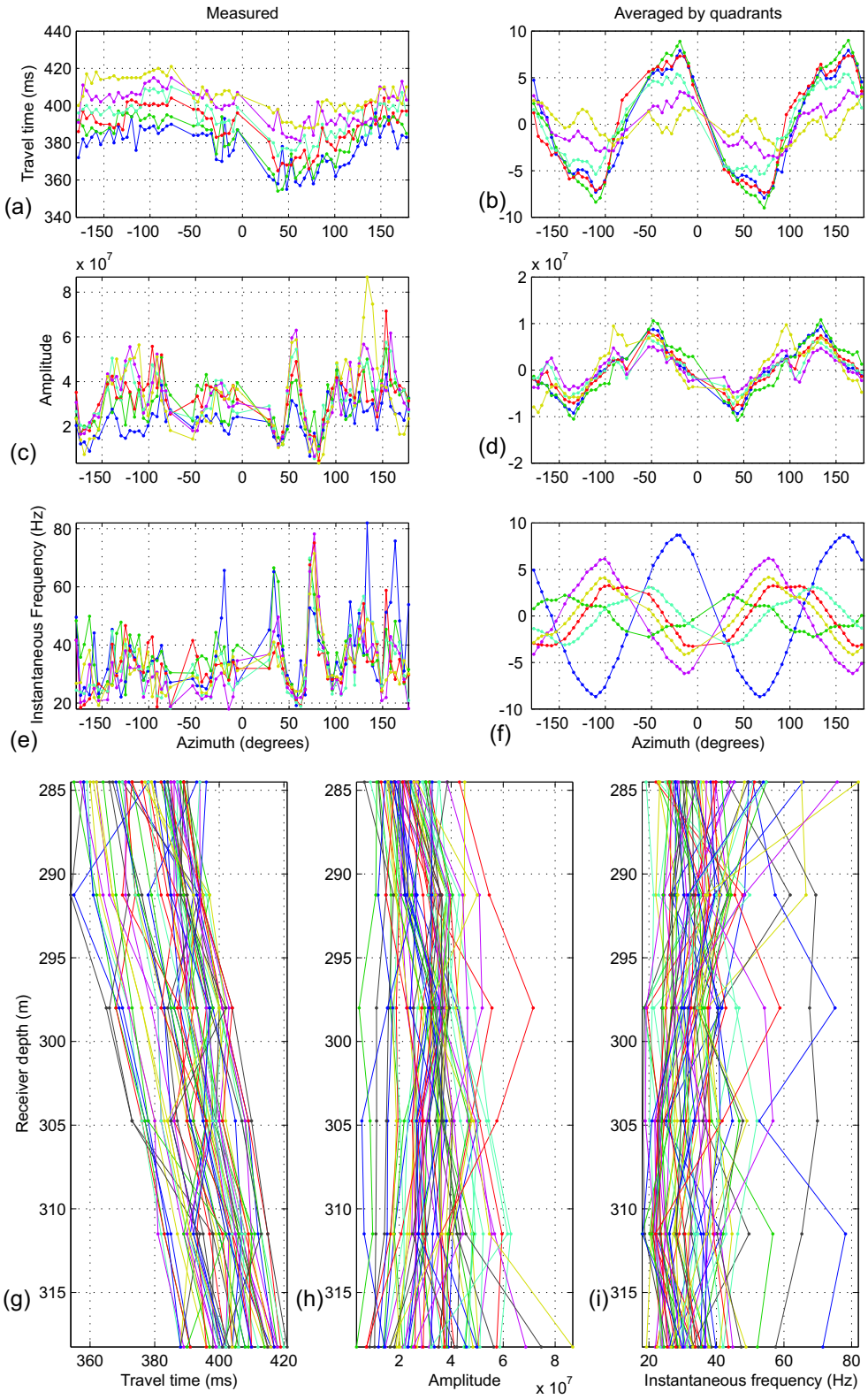

Figure 3.35: Attributes versus azimuth and depth for event E, Well 3. Event E was picked in the N component.

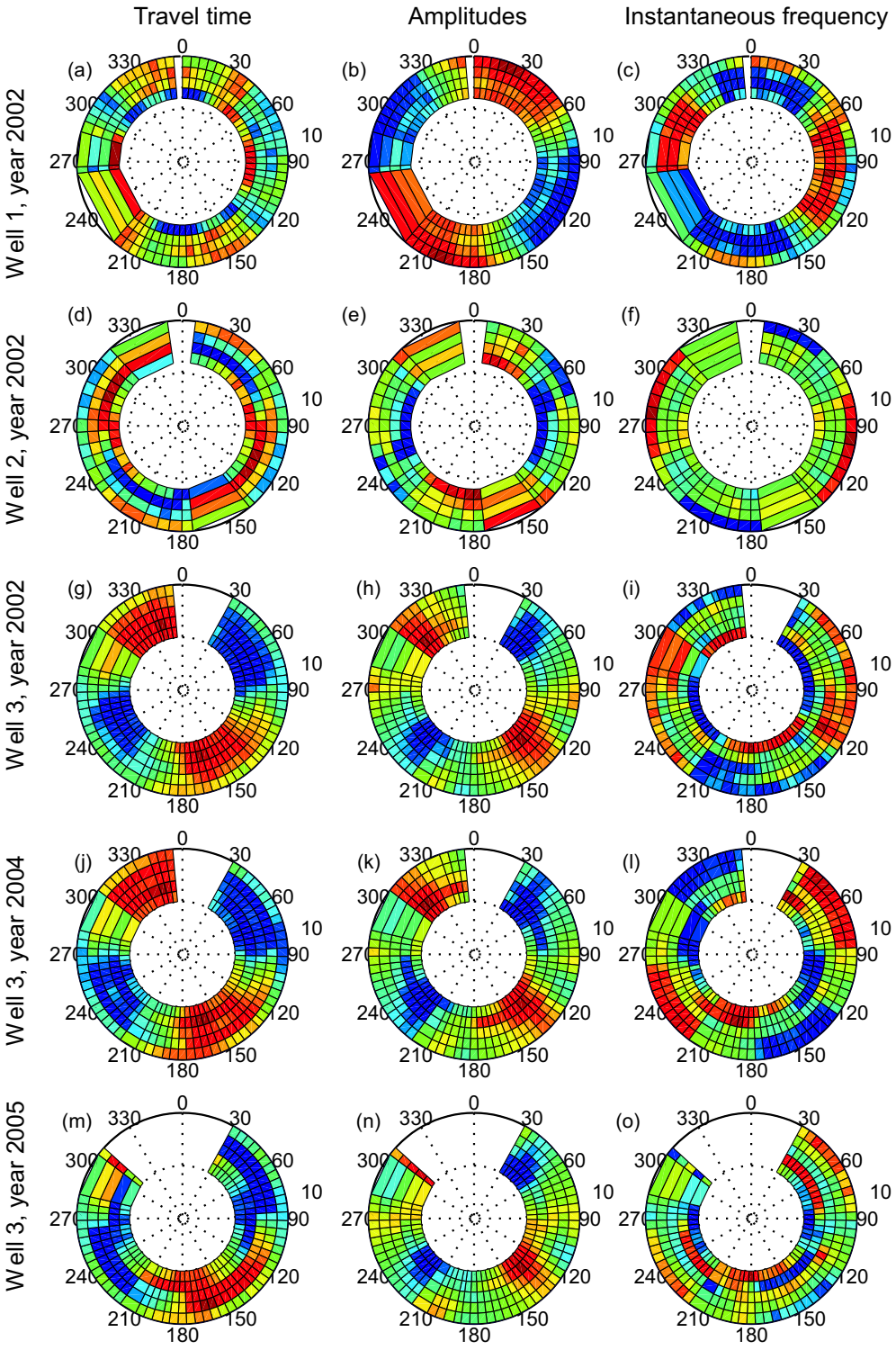

Figure 3.36: Relative differences in travel time, amplitude and instantaneous frequency for event E.

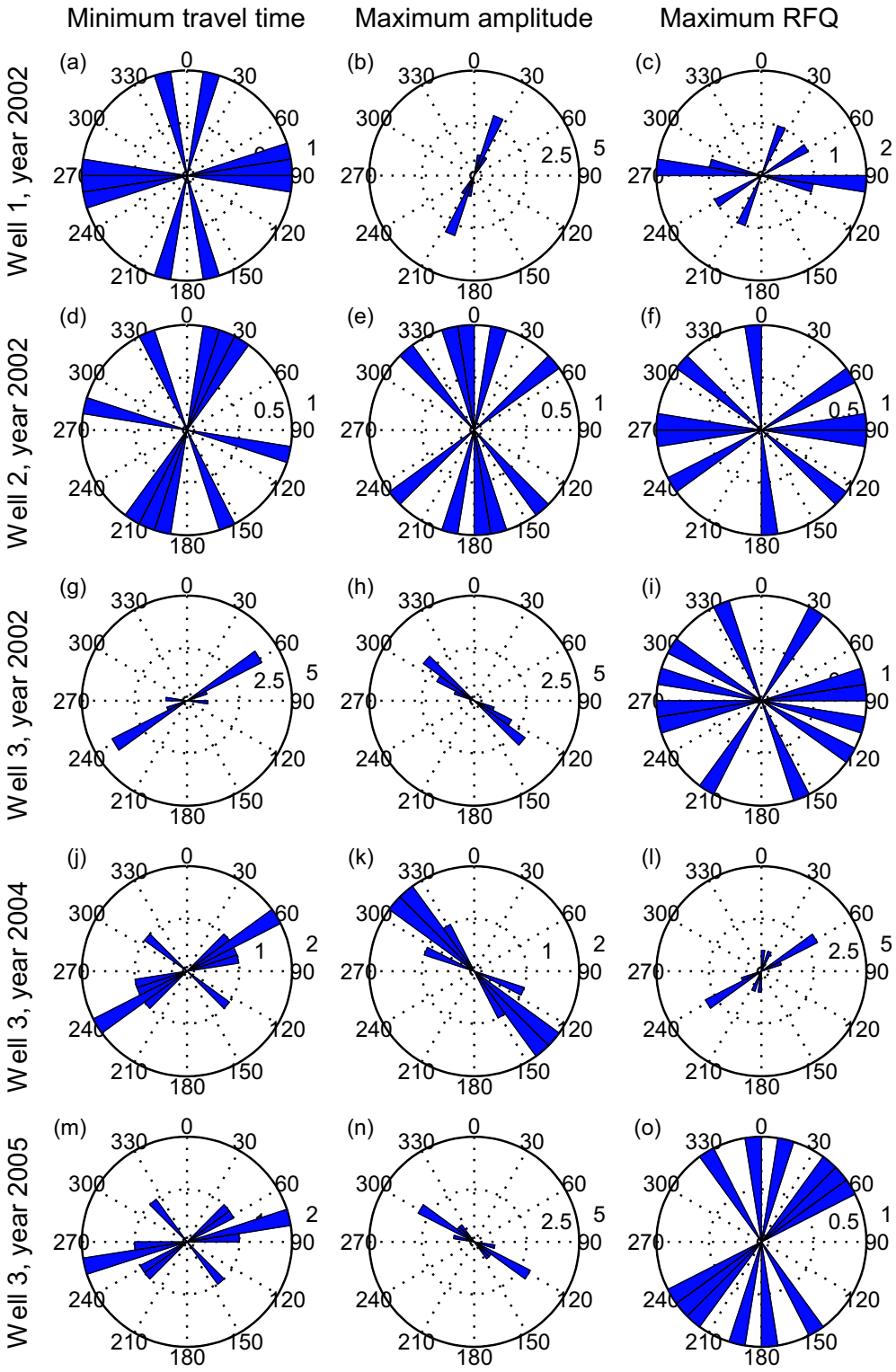

Figure 3.37: Rose diagrams showing directions for minimum travel time, maximum amplitude and maximum weighted instantaneous frequency for event E.

(using orientations from events A and B) and below ∼270m (using orientations from events D and E).

In the deeper section, the amplitude and frequency have a dominant orientation in a N40W direction (Figure 3.38 i and j). However, the travel time shows two main orientations, a primary one pointing N80W, and a secondary one in a N30E direction (panel h). The general NW orientation could be interpreted as the primary fracture orientation for this section.

In contrast to the deeper section, the shallow section shows dominant orientations pointing NE. In more detail, the amplitudes show a dominant orientation of N40E and the frequency shows two orientations: a main one at N70E, and a secondary one at N40W (see Figure 3.38 f and g). The travel time shows two directions with equal weight in a NS and N40E direction (Figure 3.38e). For this section, the NE orientation is persistent, and could be interpreted as the main orientation of the fracture planes for the shallow receiver levels.

In terms of sensitivity of the attributes, the travel time and amplitudes for all receiver levels respond more to the deeper section than to the shallow one, pointing N80W and N40W respectively (Figure 3.38 b and c). However, the instantaneous frequency shows two orientations with equal weights pointing N40W and N70E, suggesting that this attribute is equally sensitive to both fracture networks (panel d).

I compare the resulting main orientations with that provided by Heidbach et al. (2008) in a map of the maximum horizontal stress for Oman (see Figure 3.39). Although the coverage of the data by Heidbach et al. (2008) for Oman is poor, one of the measurements lies in the proximity of the field under study. The orientation of the maximum horizontal stress shown by this measurement is N40E, and results from an earthquake located at latitude 20.91° and longitude 57.72° as shown in Figure 3.39. Furthermore, from the geological and structural description of the area, the field is surrounded by the Maradi Fault Zone located

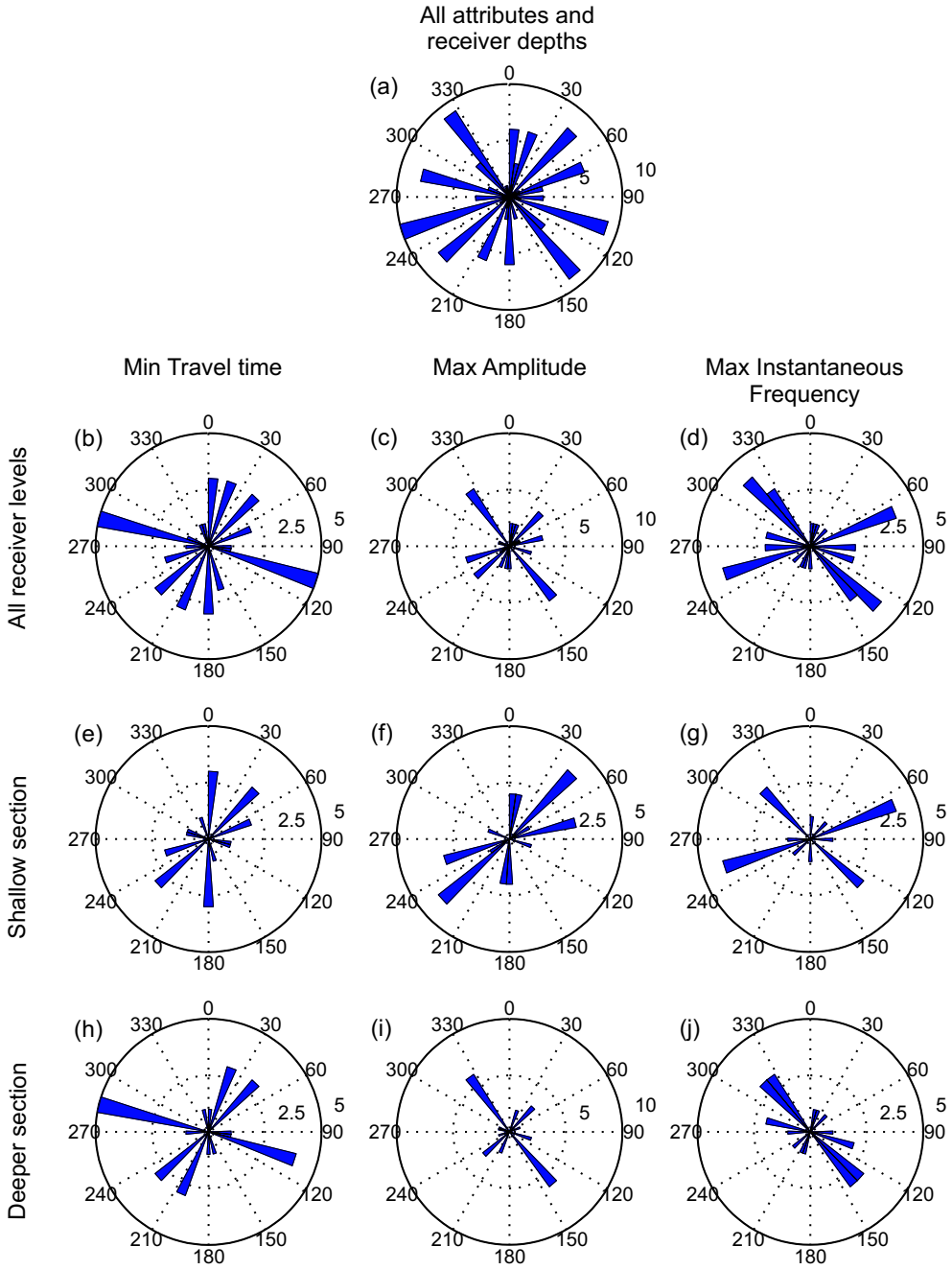

Figure 3.38: Compilation of main orientations for all wells a) all attributes and receiver depths, b)minimum travel time, for receiver depths, c) amplitude, receiver depths, d) maximum instantaneous frequency, all receiver depths, e)travel time for shallow receivers, f)amplitude for shallow receivers, g)frequency for shallow receivers, h)travel time for deeper receivers, i)amplitude for deeper receivers, j)frequency for deeper receivers.

northeast of the field, with a major axis in the N30W direction. To the west it is surrounded by an anticline from the Fahud Salt basin with the axis of the fold in a N60W orientation, and to the southeast by an anticline from the Huqf-Haushi Uplift with its axis at N50E (see Figure 3.5). This is a complex setting, as the field lies in between these regions with structural features oriented in different directions. In brief, a possible interpretation is that the Maradi Fault Zone has had more influence on the deeper section of the field compared to the shallower section whose orientations are more inline with those of the anticlines to the south east (Huqf-Haushi Uplift) and the geneal axis of the Ghaba Basin.

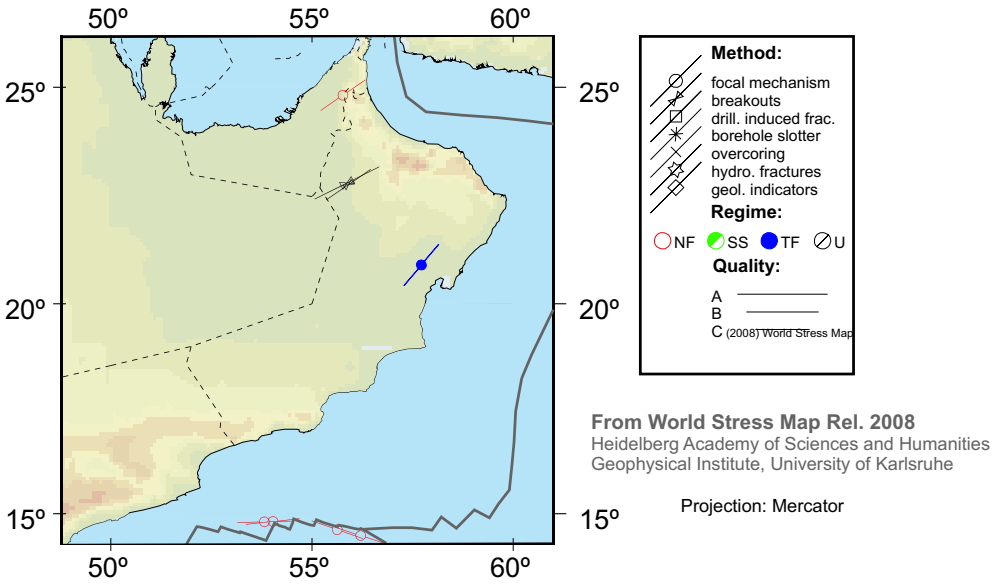

Figure 3.39: Regional stress map from Oman taken from the World Stress Map, Heidbach et al. (2008). TF marks thrust faulting near subduction zones, SS marks strike-slip faulting near oceanic and continental transforms, and NF normal faulting near oceanic spreading ridges.

When grouping all the data collected (all attributes, wells and receiver levels), no predominant orientation is persistent, further exposing the complexity of the problem, as shown in Figure 3.38a.

3.6 Conclusions

I processed five 3-component VSP surveys, two of them being repeated surveys, to perform attenuation studies. The three component geophones are rotated into a dynamic coordinate frame finding the angles of incidence of the direct arriving $P-$wave. The synthetic modelling of the angles of incidence from ray tracing suggests a low velocity layer at ∼150m to match the response of the angles of rotation.

Given the importance of a good separation of the upgoing and downgoing wavefields, I tested several methods on the data. I found that the FK filter produced the better results in the upgoing wave field for the gather tested. Thus, I used the FK filter for these data.

I analysed the travel time, amplitude and instantaneous frequency as it varies with azimuth and depth for the five different VSP surveys through four seismic events. These events are (A) the downgoing first arriving P waves on the radial component, (B) a reflected wave starting at ∼400ms from the first receiver on the upgoing radial component, (D) a downgoing PS converted wave from the first arrivals at 250ms on the N component, and (E) a downgoing PS converted wave at ∼250m from an event starting at approximately 300ms on the N component. Event B is recorded only by the shallow receivers (above 210m), and events D and E are recorded only by the deeper receivers (below ∼270m). I analyse the data grouped all together, separated by attribute and further separated them into two depth ranges to separate the Fiqa shales and the Natih carbonates (above 250m) from the Nahr Umar shale (below 250m).

When grouping all the data collected, no predominant orientation is observed, exposing the complexity of the problem. However, main orientations can be distinguished for the two depth ranges mentioned. The shallow section presents a more dominant N40E orientation, with two secondary orientations pointing N40W and NS. The deeper section shows a main orientation in a N40W and two

secondary ones at N70W and N40E. I thus interpret the main orientations in each section as that of the predominant fracture network for that depth range. These predominant orientations could be related to those of the nearby Maradi Fault Zone to the north east (for the deeper section), and the Huqf-Haushi Uplift to the south east (for the shallower section), as they present similar orientations of their major axis.

This study shows that in structurally complex areas (such as this one), azimuthal anisotropic studies benefit from the integration of various independent attributes, such as amplitude, travel time and frequency content or attenuation. Furthermore, it shows that even when no regional orientations are found, separate depth ranges may present dominant orientations.

Finally, I do not find any observable time-lapse effect in terms of changes in main orientations of the attributes for Well 3, which has surveys in three different years (2002, 2004 and 2005). As the reservoir in the study area is located below the deepest receiver, the reflected waves are analysed to gain information about the reservoir. However the lack of coherency of the event for the deeper receivers hinders the study on the response of the reservoir as was the case for event C (not included in the analysis).

Chapter 4

Fracture studies on time lapse VSPs from Weyburn

4.1 Summary

I present an analysis of a time-lapse 3D 3-component, multilevel vertical seismic profile (VSP) data set from the Weyburn field, Canada, which has undergone CO_2 injection for enhanced oil recovery. The aim of this study is to analyse and compare changes in various attributes such as frequency content, travel time, amplitudes and angle of rotation variations in relation to the present fracture network. I show through this study the potential of these attributes on P-waves for fracture characterization.

4.2 Introduction

Numerous studies have been made of azimuthal variation of seismic attributes and its relation to fractures (Lefeuvre, 2005, Sayers and Rickett, 1997, MacBeth and Li, 1999, Maultzsch, 2005). In this chapter I present a case study on azimuthal anisotropy observations of various independent seismic attributes.

The continuous injection of CO_2 into a subsurface unit will displace former fluids, hence the appropriate use of this technique may improve oil recovery and

increase production. As reservoir fluids change, so do the elastic moduli of the rock and its acoustic properties or impedances, which seismic data are sensitive to. Hence, anomalies in time-lapse data may be indicative of reservoir changes due to CO_2 injection. Time lapse seismic data have the potential for a dynamic characterization of the reservoir and tracking of fluid fronts. The data set used in this Chapter has undergone steam injection between the two time-lapse VSP surveys. Thus changes between the surveys could be due to a change in fluid saturation. Nevertheless, other factors such as changes in near-surface conditions and poor shot repeatability will cause changes in the time lapse surveys that can lead to misinterpretations.

I start this chapter by introducing the field under study. I review some of the relevant information from its exploration history and previous studies, give a geological background and present the geophysical data available for this study. Next I review the methodology used for fracture analysis. Following that, I analyse the data using the various attributes versus direction.

Finally, I show that there is a dominant trend in the rose diagrams of the different attributes in a NE-SW direction, that coincides with the orientation described by independent studies as that of the primary fracture network. There are three other less dominant orientations recognised, one of which has the orientation of the secondary fracture network which has been described to be in a NW-SE direction. I find that the time-lapse changes in the orientations extracted from the attributes are of second order compared to those found within the same survey and attribute for different offsets. More specifically, I found changes in orientation in 6 out of 8 common-offset surveys between offsets 1100m to 1500m, and only 3 out of 8 changes in orientations between the base and the monitor surveys.

4.3 Weyburn field

4.3.1 Geological setting

The Weyburn field is located in the northeast flank of the Williston Basin, in southeast Saskatchewan, Canada. This mature field has a surface area of approximately 180 km^2 and produces oil of approximately 29 API from the Midale carbonates of the Mississippian Charles Formation. Figure 4.1 (modified from Burrowes and Gilboy (2000)) shows a stratigraphic column of the geological formations of the area, highlighting the Midale carbonates. The top of the reservoir is located at a mean depth of 1450m (Burrowes and Gilboy, 2000), and consists of two main units, the upper Marly dolostone and the lower Vuggy limestones. The Marly dolostone, has a thickness between 7m and 10m, a porosity of 26% and a permeability that can reach up to 100md. The Vuggy unit has a thickness between 17m and 20m, porosity of 11% and a higher permeability of up to 500md, and is composed of limestones (Herawati and Davis, 2003 and Li, 2002).

The reservoir rock presents abrupt vertical facies transitions which are interpreted to represent the erosional remnants of a marginal ramp (Li, 2003). The reservoir is situated between the overlying Midale Evaporite anhydrates and the underlying low permeability dolomites and anhydrites of the Frobisher beds. The Weyburn Midale reservoir presents a main network of subvertical fractures open and cemented in a SW-NE orientation, while in some areas a secondary SE-NW orientation has been found (Burrowes and Gilboy, 2000, Li, 2003). These fractures have been studied in numerous well cores and borehole image logs. Fracture densities have been found to be highest in the upper Vuggy and lowest in the Marly, where they have an estimated spacing of 0.3 to 10m respectively (Burrowes and Gilboy, 2000).

The Midale beds lie underneath the Ratcliffe beds, which consists of the Midale and Oungre evaporites, also of the Mississipian Charles Formation. Overlying the

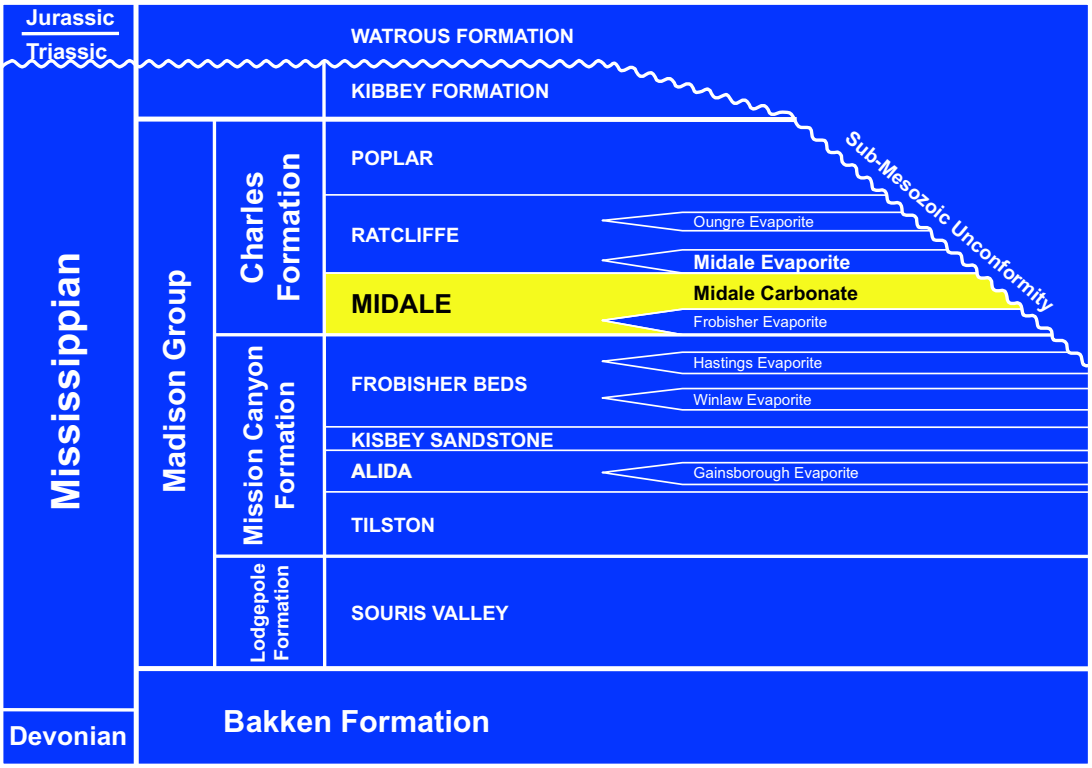

Figure 4.1: Stratigraphy of the Weyburn field. Figure modified from Burrowes and Gilboy (2000).

Charles Formation lies the Kibbey Formation of Mississipian age which is separated from the Watrous Formation by a sub-mesozoic unconformity (see Figure 4.1).

4.3.2 Field history and CO_2 injection

The production history of the field goes back to its discovery in 1954, followed by waterfloods in the mid 60's, infill drilling in the 80's and horizontal drilling in the 90's. In 2000 when Encana acquired the base survey, approximately 24% of the 2.4 billion barrels of oil in place had been recovered with approximately 1000 wells, of which 137 were horizontal. The operator PanCanadian converted 19 of the horizontal wells into CO_2 injectors for enhancing oil recovery, producing an additional 10-15% of the original oil in place (Galikeev and Davis, 2003, Terrell et al., 2002). 3D surface seismic data around the VSP borehole were acquired at the time of the base survey. By September 2001, 23 billion cubic feet (bcf) of CO_2 had been injected via horizontal wells. Large amounts of CO_2 have been injected into the Marly unit. Due to the differences in permeability and pressure, the CO_2 is expected to also sweep the Vuggy unit. The displaced oil is in turn produced by vertical and horizontal wells.

Previous studies by Encana on the time-lapse surface seismic data have found that 4D attributes, such as amplitude and travel time differences between the baseline and monitor surveys, are sensitive to the changes in pore fluids during the CO_2 injection (Li, 2002).

It is expected that the study of 4D converted P-S waves will lead to a better understanding of pressure versus saturation effects, and that a 3C 4D VSP analysis may provide new insights in the study of fractures.

4.3.3 Geophysical Data

The geophysical data analysed consist of a time-lapse 3D VSP data set with 247 surface sources and 80 receiver levels in depth, each with a 3-component geophone. Source-receiver locations vary from a zero offset VSP to 1500m offset. Figure 4.2a shows source locations for the base and monitor surveys, which will be referred to as S1 and S2 respectively. The geophone depths start at 189m and go down to 1389m with a spacing of 15m. Figure 4.3b shows a projection in 3D of source and receivers for S1; notice that for the largest offsets the ratio of offset to geophone depth can be larger than 1.

The deepest geophones are shallower than the top of the reservoir, thus to gain an insight into the reservoir properties the reflected waves from the top of the reservoir should be studied. However, in this analysis only the down-going direct P-waves are analysed which have the potential of providing information on the fracture network of the overburden.

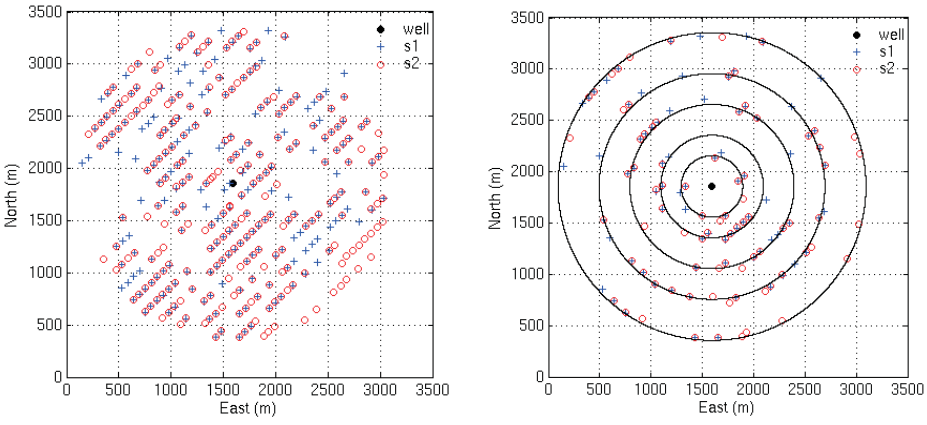

(a) (b)

Figure 4.2: (a) Acquisition mapview of the 3D time-lapse VSP at Weyburn for the base (S1) and monitor (S2) surveys. (b) Source locations for common-offset gathers at 300m, 500m, 800m 1100m and 1500m.

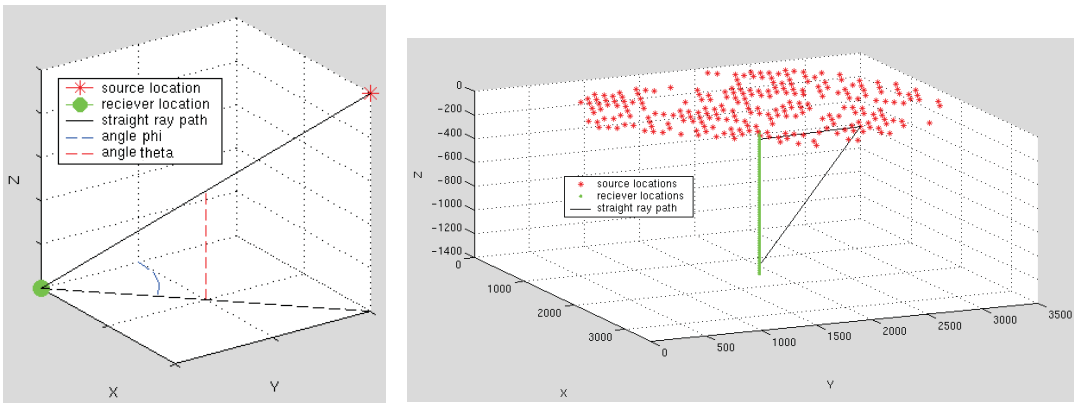

(a) (b)

Figure 4.3: a) Angles of rotation θ and ϕ; ϕ on the xy planes varies with azimuth and θ varies with depth. b) 3D view of all source and receiver locations for survey S1. Notice that the angle θ (shown in a) varies significantly depending on the depth of the receiver. Both axis are scaled equally.

4.4 Method

4.4.1 Common-offset sorting

For each survey the data have been sorted into common-offset gathers every 100m ± 50m, resulting in 15 walk-around (WAR) VSP's for both surveys and one zero offset VSP for survey S1. For this analysis five WAR VSP's with offsets 300m, 500m, 800m, 1100m and 1500m were selected for analysis, see Figure 4.2b.

4.4.2 First breaks

The travel time and amplitude information of the first break picks will be used in an analysis of the first arriving P-wave, as well as for the geophone rotation explained below. The picking was done with an algorithm that finds the maximum (or minimum) amplitude within a time window specified interactively. To ensure correct picking of first arrivals, picking was done on the sum of the squares of the three components, x, y and z.

4.4.3 Geophone Rotation

Given that offsets can be comparable to the geophone depths, or larger -as shown in Figure 4.3b- a 3-component rotation into the maximum energy of the first break picks was computed. The two angles taken into consideration for this rotation are ϕ which varies with azimuth, and θ which in this Chapter is the angle measured between the horizontal plane and the incident P-wave, as shown in Figure 4.3a. After rotation the three geophone components turn into R, N and H (see Appendix A or Chapter 3). The R component is expected to contain the downgoing direct P-wave.

4.4.4 Wavefield separation

The up- and down-going wave fields were separated with a median filter of 5 samples. The convenient use of a median filter for wavefield separations in VSP data has long been known (Stewart, 1985). Preliminary tests on optimum filter lengths were computed for 3, 5 and 7 samples. An explanation on median filters is provided in Chapter 3.

4.4.5 Peak frequency

I performed windowed Fourier transforms (around the first arriving P-waves for the common-offset gathers selected) in order to study possible azimuthal variations of frequency peaks with azimuth. Specifically, to determine whether in the orientation of the fracture plane the frequency content or frequency peak of the traces differs from that of waves traveling perpendicular to the fracture plane. For a given offset and receiver level the maximum frequency peaks versus azimuth were fitted to a trigonometric function as explained below.

4.5 Analysis of attributes versus direction (AVD)

For all receiver levels, various independent seismic attributes, such as a)angle of maximum energy for rotation θ, b)travel time, c)amplitudes and d)frequency peaks are analysed against azimuth in a quest for consistent patterns that might provide insight into the surrounding fracture network. Additionally, I analyse possible indications of pore fluid changes due to CO_2 injection between surveys S1 and S2.

In Chapter 2 I showed how vertically aligned fractures have an HTI symmetry. In general, attributes acquired at different azimuths on such a symmetry will thus present a sinusoidal behaviour completing one period every 180°. Therefore, for a given receiver depth the attributes versus azimuth are fitted to a trigonometric function of the form,

$$Attribute(\phi) = A_1 + A_2 \cos 2(\phi - \phi_{sym}) \tag{4.1}$$

where A_1 is the mean of the attribute versus azimuth, A_2 is the maximum deviation of the attribute from the mean, and ϕ_{sym} is the axis of symmetry.

4.5.1 Angle of maximum energy

I search for the angles θ and ϕ that will maximise the energy of the first arriving P-wave in the R component. In Figure 4.4 I show the angles found for a common-shot gather with an offset of 1100m and a source-receiver azimuth of -133^o. Assuming straight ray paths, in an isotropic medium, with no velocity variations with depth, the angle of rotation to orient the geophone into the component of maximum energy is given geometrically, by Figure 4.3a, and calculated for the common offset gather example in Figure 4.4. However, as velocities increase with depth the ray will bend, decreasing θ for a given source offset and receiver depth location. This effect can clearly be seen in Figure 4.4a where the maximum energy

θ is in general smaller than the geometric θ. Additionally, if the medium is not isotropic, the anisotropy will further complicate this response.

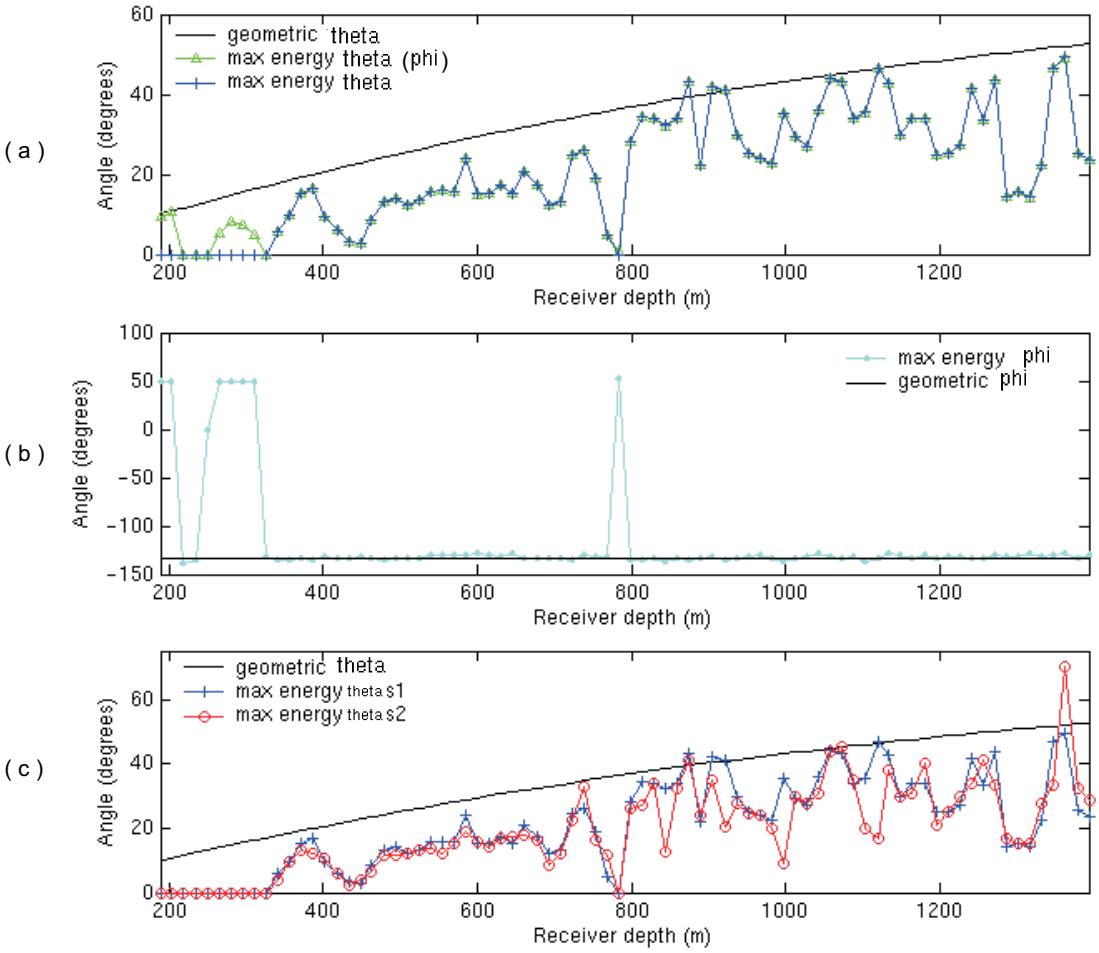

Figure 4.4: Angles used for rotation into direction of maximum energy of the first breaks of a common-shot gather compared with the geometric angles given by straight rays. Offset is 1100m and azimuth is -133^o. a) Survey S1 θ increases with depth and is, as expected, overall smaller than the geometric angle. b)Angle ϕ c) Angle θ compared for surveys S1 and S2.

As expected, the angle ϕ (which refers to azimuth) only takes two values, that of the correct azimuth and its opposite 180 degrees apart as shown in Figure 4.4b. The shallowest 8 receiver levels present high noise levels and thus are not included in this main analysis

θ for survey S2 has a tendency to be smaller than that for survey S1, which is

shown in Figure 4.4c. I interpret this behaviour to be caused by an increase in velocities for survey S2 compared to S1. Furthermore, this effect can be seen in Figure 4.5, where the angle of rotation θ is shown as a function of depth for all common-shot gathers at all the azimuths available. Figure 4.5 also indicates a change towards larger azimuthal variations in θ for S1 than for S2.

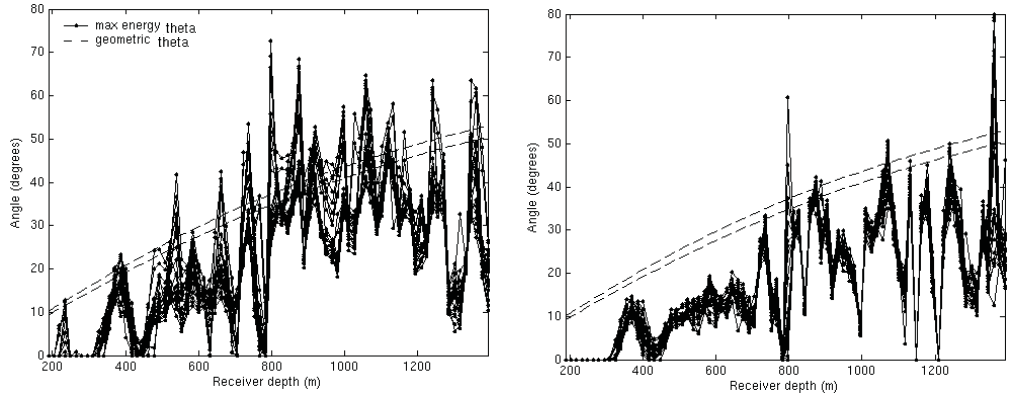

(a) (b)

Figure 4.5: Angle (θ) of maximum energy vs. receiver depth for all azimuths. a) Survey S1. b) Survey S2.

The azimuthal variations of θ confirm the hypothesis of equation 4.1 as shown in Figure 4.6 for selected receiver depths, and Figure 4.6b where the mean of θ for all receiver depths versus azimuth is shown. Here the azimuth of minimum θ lies approximately at 70^o (N70E).

Figure 4.7 shows the rose diagrams indicating the direction from which the incident P-waves arrive closer to the horizontal. This orientation is expected to coincide with the higher velocities encountered in a direction parallel to the fracture plane. Two main orientations are dominant in Figure 4.7. A NW-SE orientation for offset 1500 in surveys S1 and S2, and a NE-SW orientation for offset 1100m in survey S2. Offset 1100 in survey S1 shows both of these orientations, see Figure 4.7 a) to d).

Figures 4.8 and 4.9 show the 3-component VSP data before and after rotation for offset 1100m, azimuth -133^o and surveys S1 and S2 respectively. At a depth

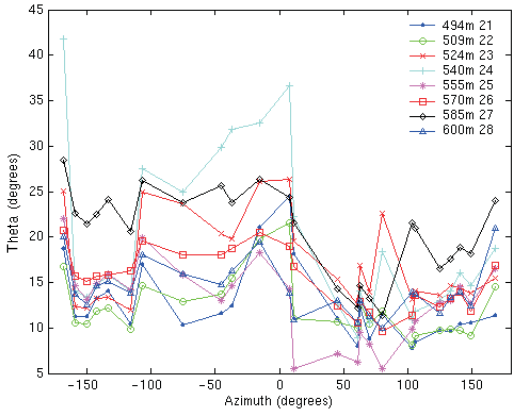

(a) Selected geophones

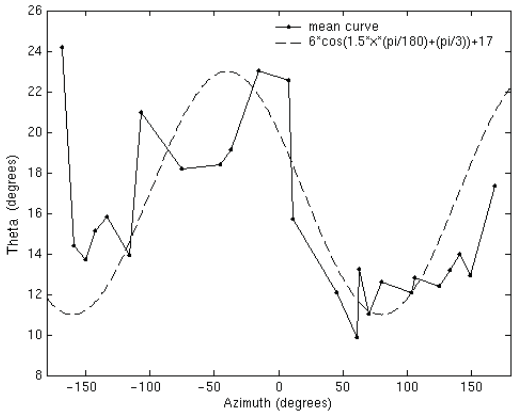

(b) Mean of (a)

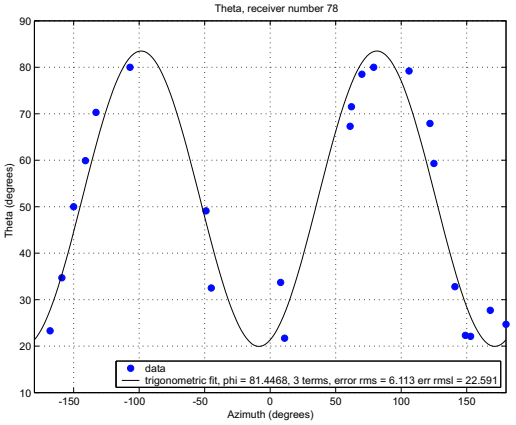

(c) Offset 1100, S2, receiver 78

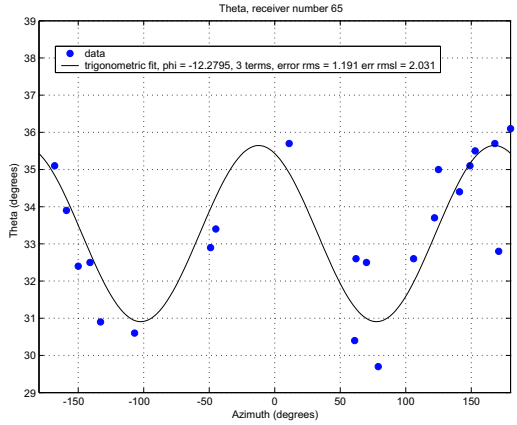

(d) Offset 1100, S2, receiver 65

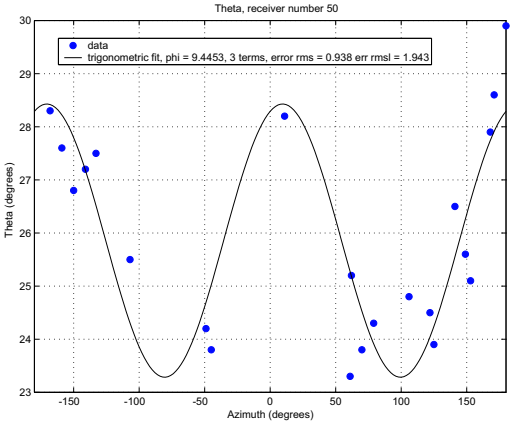

(e) Offset 1100, S2, receiver 50

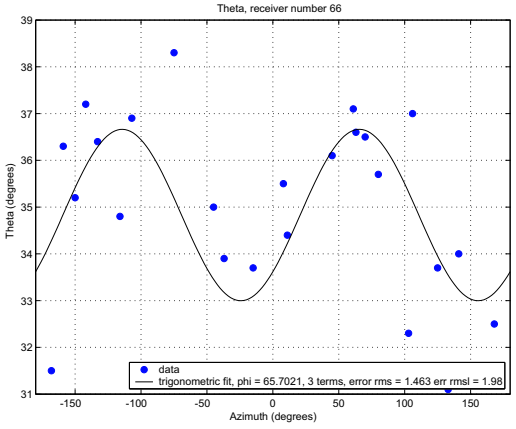

(f) Offset 1100, S2, receiver 66

Figure 4.6: Angle of maximum energy versus azimuth, selected examples. a) θ versus azimuth for survey S1, offset 1100m and selected receiver depths. The legend shows the receiver depth in meters and the receiver number. b) Mean of a) with a fitted trigonometric function. c) to f) examples of sinusoidal fits.

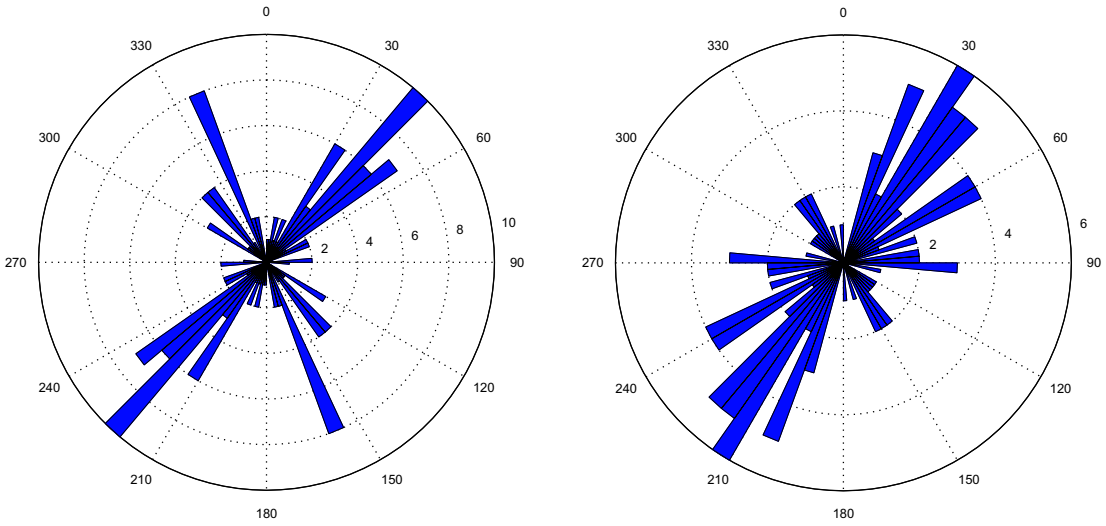

(a) Offset 1100m, Survey 1

(b) Offset 1100m, Survey 2

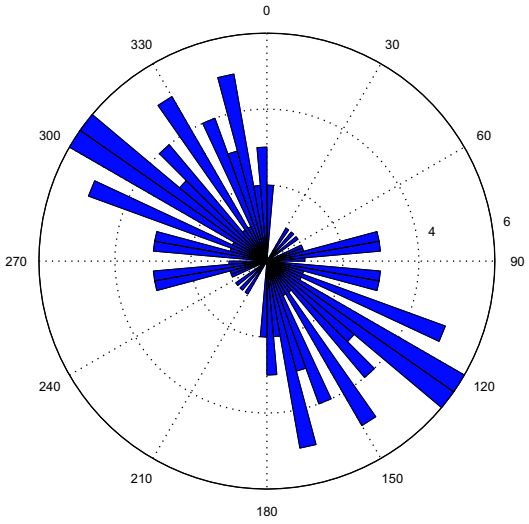

(c) Offset 1500m, Survey 1

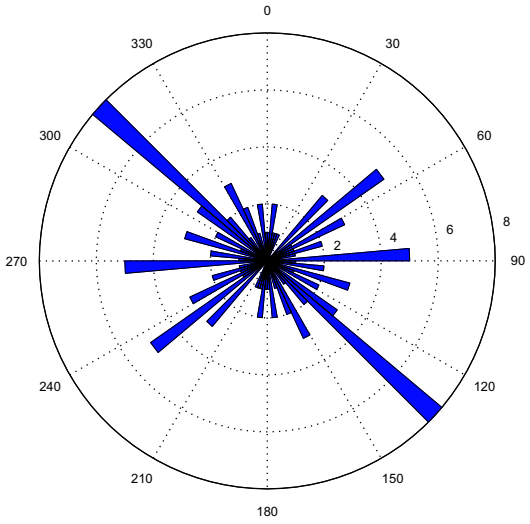

(d) Offset 1500m, Survey 2

Figure 4.7: Rose diagrams indicating the direction of the minimum angle of rotation for surveys S1 and S2, and offsets 1100m and 1500m.

of 800m there is a strong drop in amplitudes in the first arriving P-waves (R component) due to fractioning of energy into P and P-S waves at an interface. The steep dips correspond to P-S waves and the gentle dips to the P waves. In this study only the direct P-waves are analysed.

I further separated the up- and downgoing P-waves using a median filter of 5 samples. Figure 4.10 shows a comparison of amplitudes before and after the median filter for the R component of Figure 4.8. However, as in this study I am only analysing the direct arriving P-wave, I use the amplitudes without the median filtering to avoid any possible artifacts or suppression of the azimuthal changes.

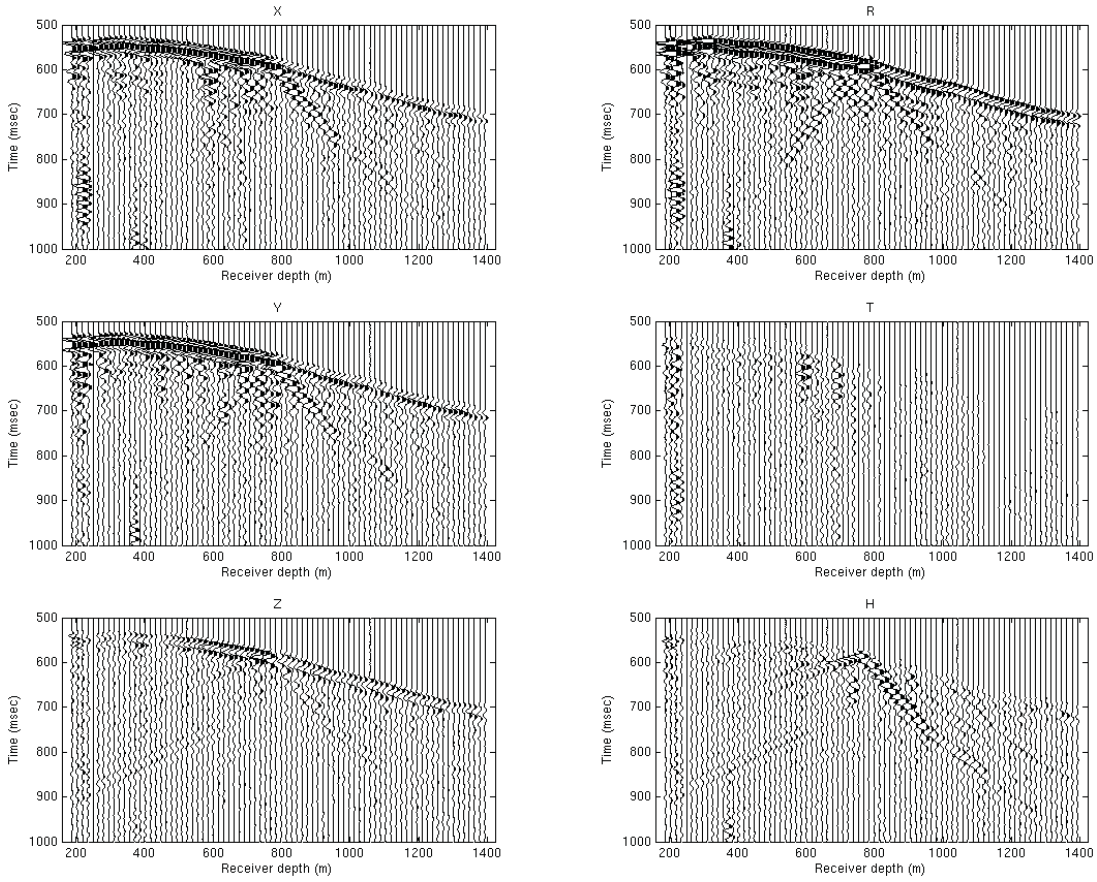

Figure 4.8: VSP data before and after rotation into direction of maximum energy. Base survey S1, offset is 1100m, azimuth is -133^o.

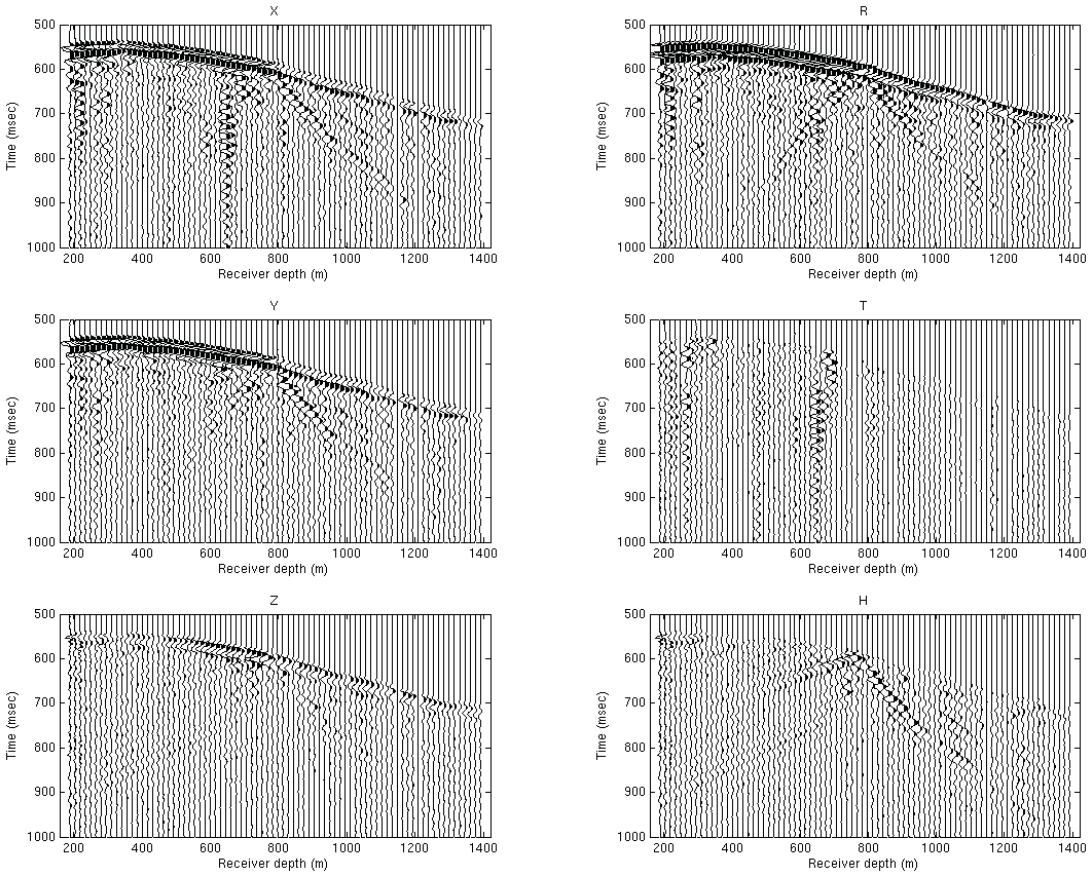

Figure 4.9: Same as Figure 4.8 but for survey S2.

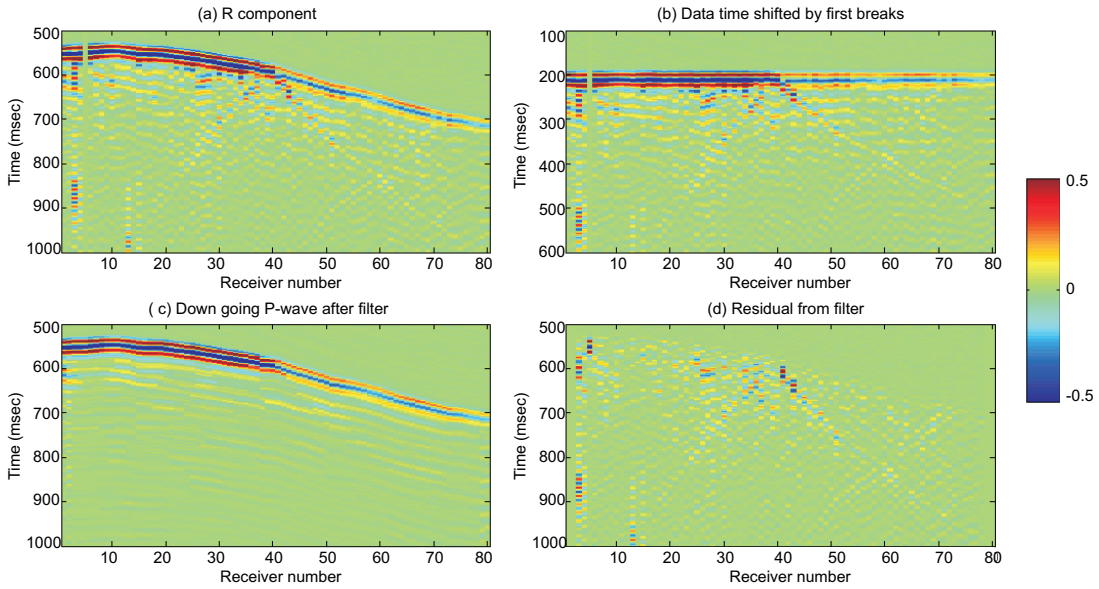

Figure 4.10: Separation of up- and down-going waves with a median filter of 5 samples. (a) R component (from Figure 4.8), (b) R flattened on the first breaks, (c) down-going wave field after median filter, (d) up-going wavefield obtained by substracting panel (a) minus panel (d). The colorscale refers to amplitudes.

4.5.2 Travel time and velocities

An azimuthal analysis of the first arriving P-wave travel times was performed. Figures 4.11a and 4.11b present travel times versus azimuth for all receiver depths for offset 1100m and surveys S1 and S2 respectively. In both cases, the azimuthal variations follow the same pattern from one receiver level to the next. I fit the travel time versus azimuth to the periodic function described in equation 4.1 for each receiver, in order to find the angle of minimum travel time, which is expected to correlate with the fracture plane. Figure 4.12 shows the parameters A1, A2 and axis of symmetry from the sinusoidal fit (equation 4.1) at an offset of 1500m. In general for travel times, A1 increases with depth, A2 decreases with depth and there are two distinct trends for the symmetry plane ϕ_{sym} for depths below and above 800m (see Figure 4.12). Figure 4.11c shows the mean of the travel time for all receiver depths for surveys S1 and S2. The average minimum travel time is found at azimuths 42^o (N42E) and 48^o (N48E) for surveys S1 and S2, with S1 and S2 presenting a maximum amplitude variation from the mean of 5ms and 8ms respectively.

Figure 4.13 shows rose diagrams with the direction of minimum travel time for offsets 1100m and 1500m and surveys S1 and S2. Three of the rose diagrams, point in a NE-SW orientation, which has been described by Li (2003) as the main fracture plane direction. This response is expected, as travel times should be shorter in the direction of the fracture plane and longer coming from a direction perpendicular to the fracture plane. For the smaller offsets of 300m, 500m and 800m similar rose diagrams were calculated, however their results have not been incorporated as the number of azimuths (or sources) for these offsets was considered insufficient for a robust analysis.

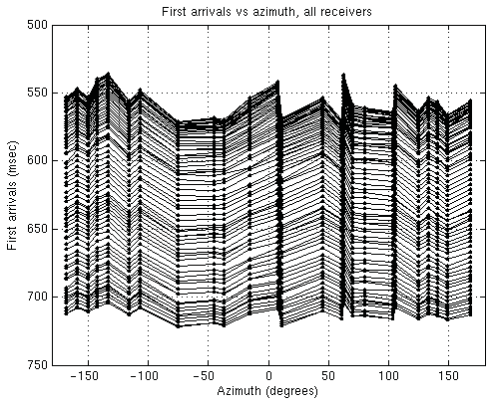

(a) Travel times for S1

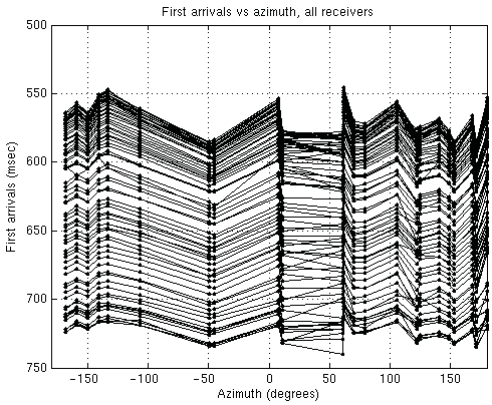

(b) Travel times for S2

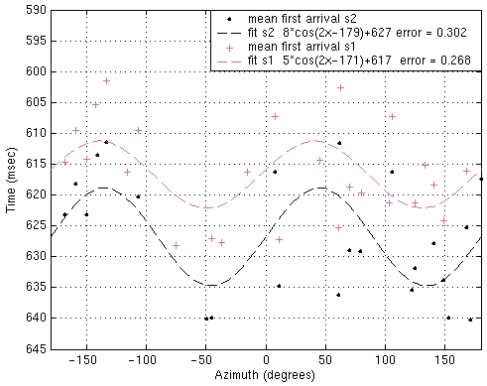

(c) Mean travel time for S1 and S2

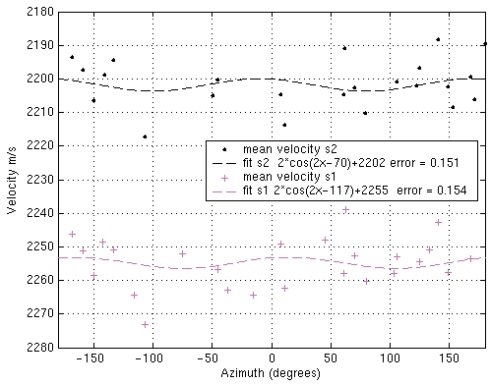

(d) Mean velocities for S1 and S2

Figure 4.11: Comparison of travel time and velocities of first arrivals for surveys S1 and S2 versus azimuth for all receiver depths at an offset of 1100m. a) Travel time for all receiver depths for S1, b) travel time for all receiver depths for S2, c) mean of travel time for all receiver depths for surveys S1 and S2, d) mean of velocities for all receiver depths for surveys S1 and S2. Notice that velocities are higher and travel times lower for S2. The error shown is relative root mean square.

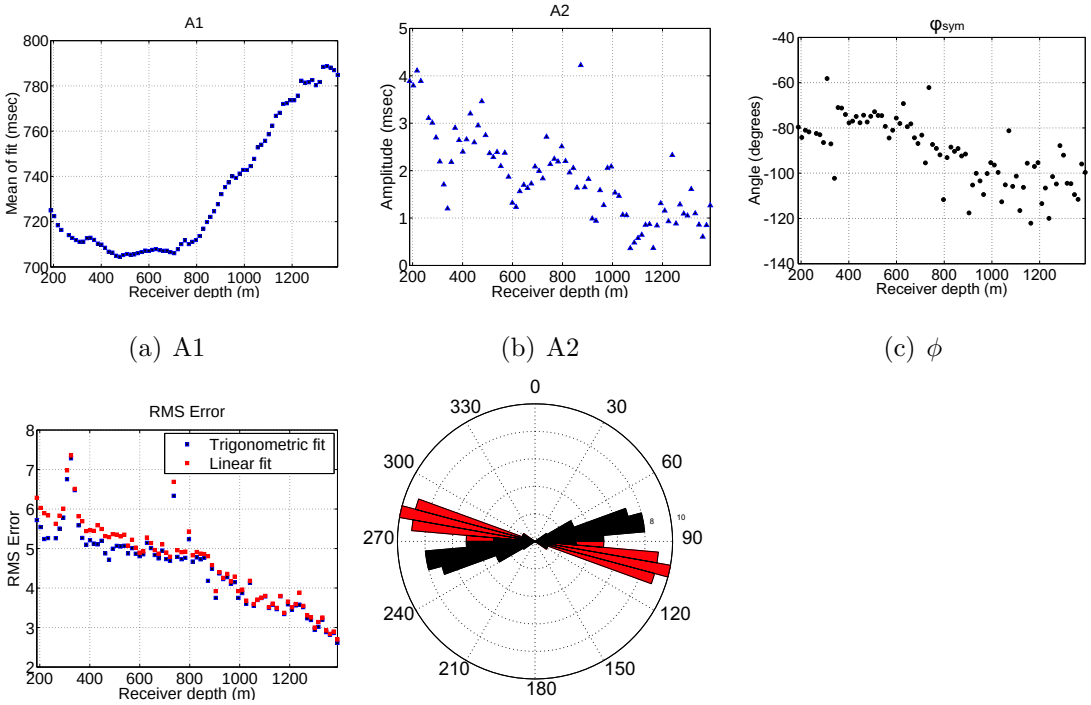

(a) A1 (b) A2 (c) ϕ

(d) Error of fit (e) Minimum travel time

Figure 4.12: Parameters of sinusoidal fit to travel time of first arriving P-waves. Offset 1500m, survey S1. Red corresponds to depths above 800m and black below 800m.

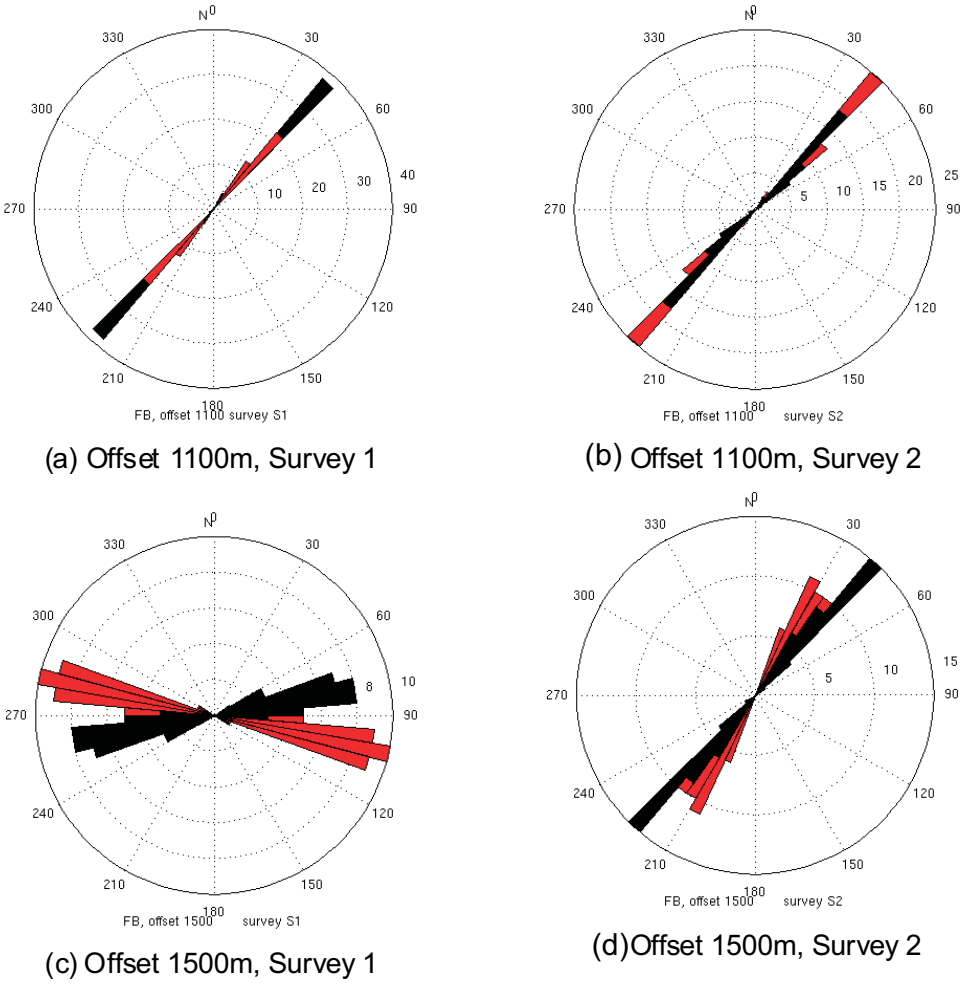

(a) Offset 1100m, Survey 1

(b) Offset 1100m, Survey 2

(c) Offset 1500m, Survey 1

(d)Offset 1500m, Survey 2

Figure 4.13: Comparison of rose diagrams for azimuth of minimum travel time of first breaks. Offsets from top to bottom 1100 and 1500m. Red corresponds to depths above 800m and black below 800m.

4.5.3 Amplitudes

A similar process was followed for amplitudes of the first arriving P-waves on the R component. Figure 4.14 shows the parameters A1, A2 and ϕ_{sym} versus depth for offset 1500 in survey S1. In general there is a drop in amplitudes, and thus in A1 for depths larger than 800m. Similarly A2 and ϕ_{sym} display different trends above and below the same interface.

Figure 4.15 shows the resulting rose diagrams with the direction of maximum amplitude in the sinusoidal fits. For offset 1100m the azimuth of maximum amplitude runs in a N45E direction for S1 and in a north-south direction for S2. For offset 1500m the azimuth of maximum amplitude presents a N70E direction for S1, and an E-W direction for S2.

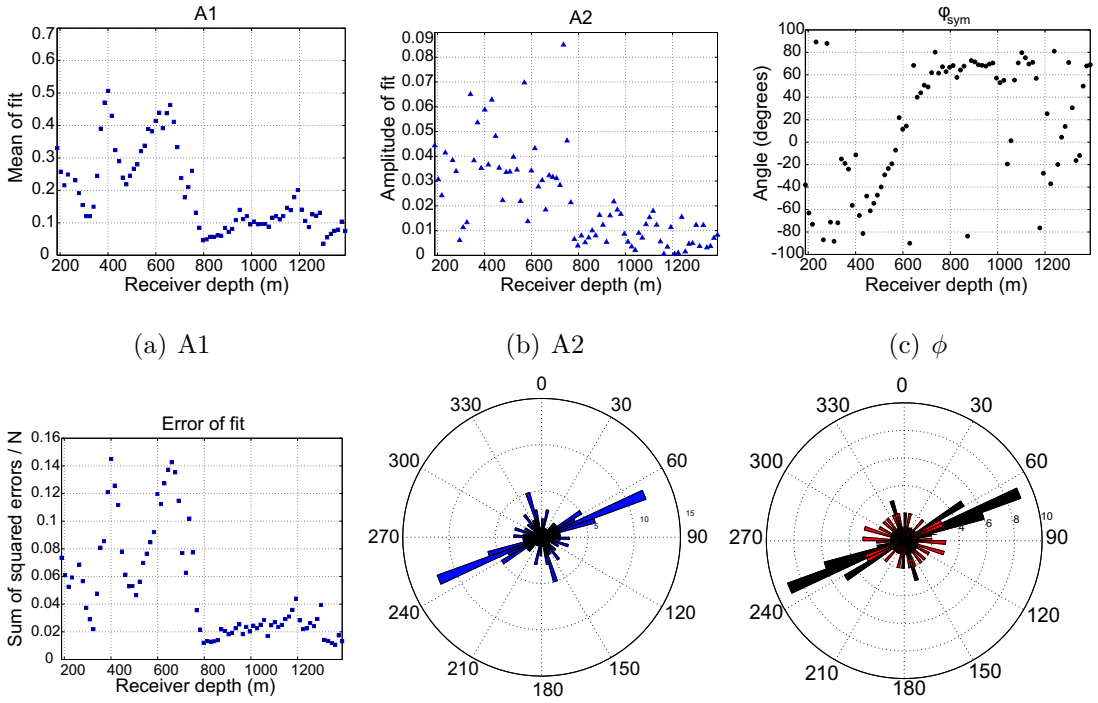

(a) A1 (b) A2 (c) ϕ

(d) Error of fit (e) Maximum amplitude (f) Maximum amplitude

Figure 4.14: Parameters of sinusoidal fit of common-offset gathers to amplitudes. Offset 1500m, survey S1. In panel (f) red corresponds to depths above 800m and black below 800m.

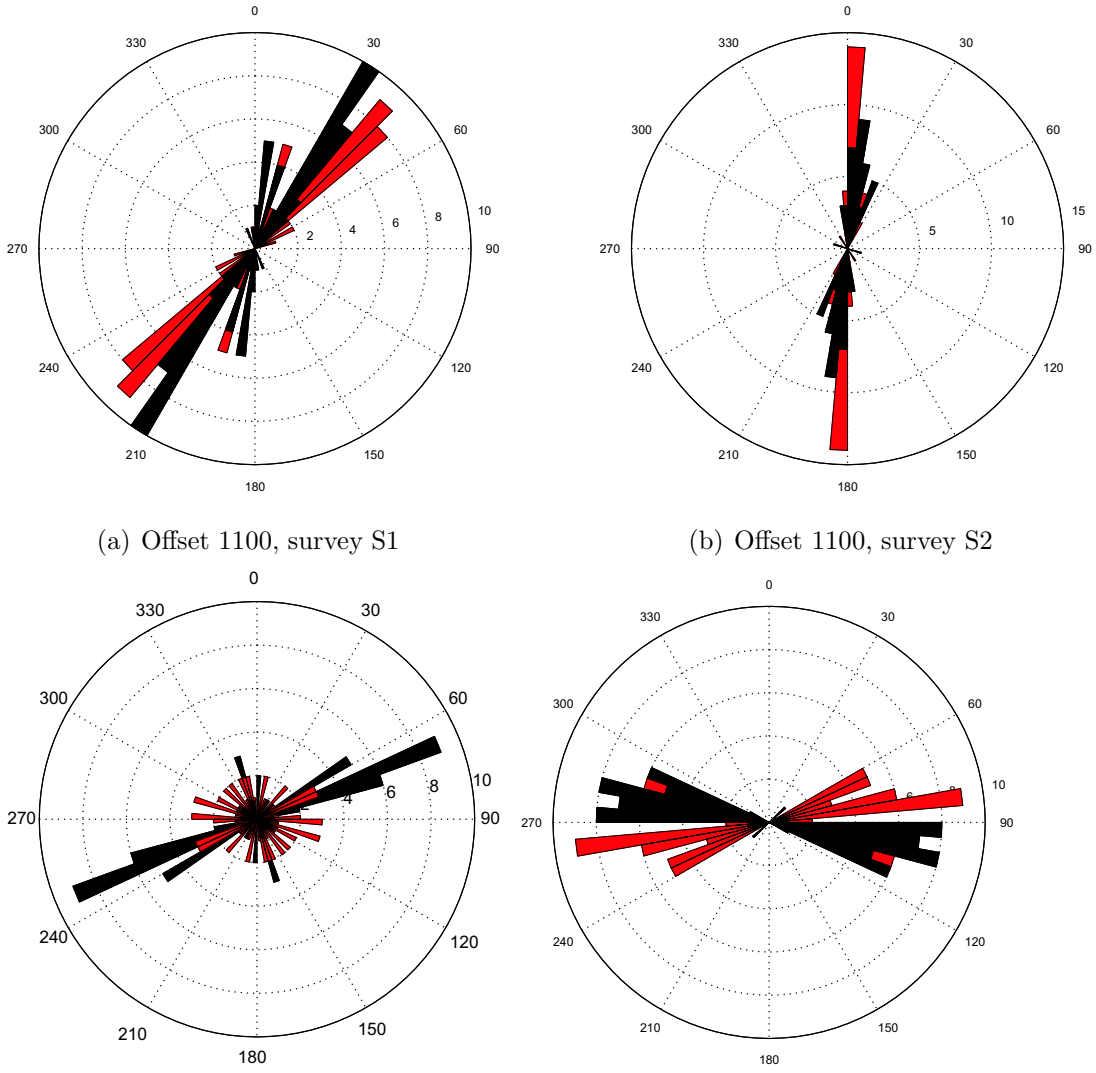

(a) Offset 1100, survey S1

(b) Offset 1100, survey S2

(c) Offset 1500, survey S1

(d) Offset 1500, survey S2

Figure 4.15: Rose diagrams of amplitudes for surveys S1 and S2 and offsets 1100m and 1500m. Red corresponds to depths above 800m and black below 800m.

4.5.4 Frequency peaks

I calculate the Fourier transforms for the common-offset gathers windowed around the first breaks. Figure 4.16a shows an example of a common offset gather with the picked first P-wave arrivals. Furthermore, Figure 4.16b shows the alignment of these traces at the first arrivals. Figure 4.16c shows the Fourier transform of each of these traces windowed around the first breaks and their corresponding maximum frequency or frequency peak (red dots), where a clear azimuthal behaviour is observed.

I illustrate the process of creating the rose diagram for the frequency peaks in Figure 4.17. Figure 4.17a shows the frequency spectra for a given trace; Figure 4.17b shows the data fitted to a trigonometric function versus offset for a given receiver depth. Figure 4.17c shows the histogram for the angle of maximum frequency resulting from all receiver depths, and Figure 4.17d shows the same histogram in polar coordinates. Furthermore, Figure 4.17e shows the variation of the mean of the peak frequency (A_1 in equation 4.1) with depth, where it is clear that there is a loss in the frequency content with depth, or a shift of the peak frequencies towards lower values.

Figure 4.17f shows the RMS error of the fit to equation 4.1 compared to the error when fitting the data versus azimuth to a constant value. It is clear that for all receiver depths the error is smaller when fitting the data to a trigonometric function, which accounts for the anisotropy in the medium. Furthermore, Figure 4.17g shows the difference in the RMS error obtained by subtracting the trigonometric-fit error minus the linear-fit error. Again, it is seen in Figure 4.17g that this difference is positive.

I calculate rose diagrams for the azimuth of maximum peak frequency. It is expected that these correlate with the direction of the fracture plane, should the media through which the P-waves travelled have vertically aligned fractures. These rose diagrams are shown in Figure 4.19 for surveys S1 and S2 and offsets

1100m and 1500m.

Analysis

There is a dominant trend in the rose diagrams of the different attributes. Table 4.1 summarises the main direction encountered from all attributes, where we find that 9 out of 16 rose diagrams have a NE-SW orientation. Furthermore, there are 3 with a EW orientation, 2 with a NS orientation and 2 with a NW-SE direction. The main orientation found coincides with the predominant orientation of the fracture network described by Li (2002) for this field. Furthermore, Li (2002) describes a secondary orientation in a NE-SW direction. It is thus clear that the different P-wave attributes analysed are sensitive to the fracture network present in the field.

Survey	Offset(m)	Travel-time	Amplitude	Frequency peak	Angle of rot.
S1	1100	a	a	a	a and c
	1500	b	b	a	c
S2	1100	a	d	d	a
	1500	a	b	a	c

Table 4.1: Dominant orientations of rose diagrams for the multiple attributes analysed. In the table, a,b,c and d refer to the main orientations as follows, a:NE-SW, b:EW, c:NW-SE, and d:NS.

We find that the changes in the main orientations of the diagrams between surveys S1 and S2 are less frequent than the changes in orientations within the same survey and attribute at different offsets. Table 4.2 summarises the time lapse changes found, showing that only 3 of the 8 cases present a change in orientation. The changes between offsets 1100m and 1500m (with the same survey and attribute) are recorded in Table 4.3, and show that in 6 out of 8 cases a different orientation is observed when the offset is increased.

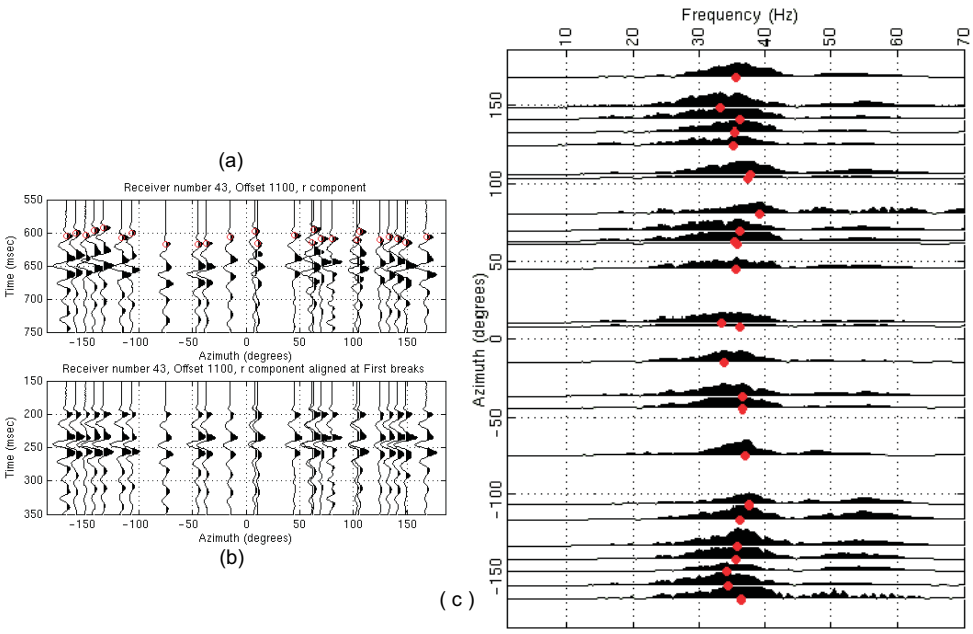

Figure 4.16: a) Original common offset gather with marked first breaks, b) Same common offset gather as in (a) but flattened at the first breaks, (c) Fourier Transform and frequency peaks (red dots) of the traces in (b) windowed by the first breaks.

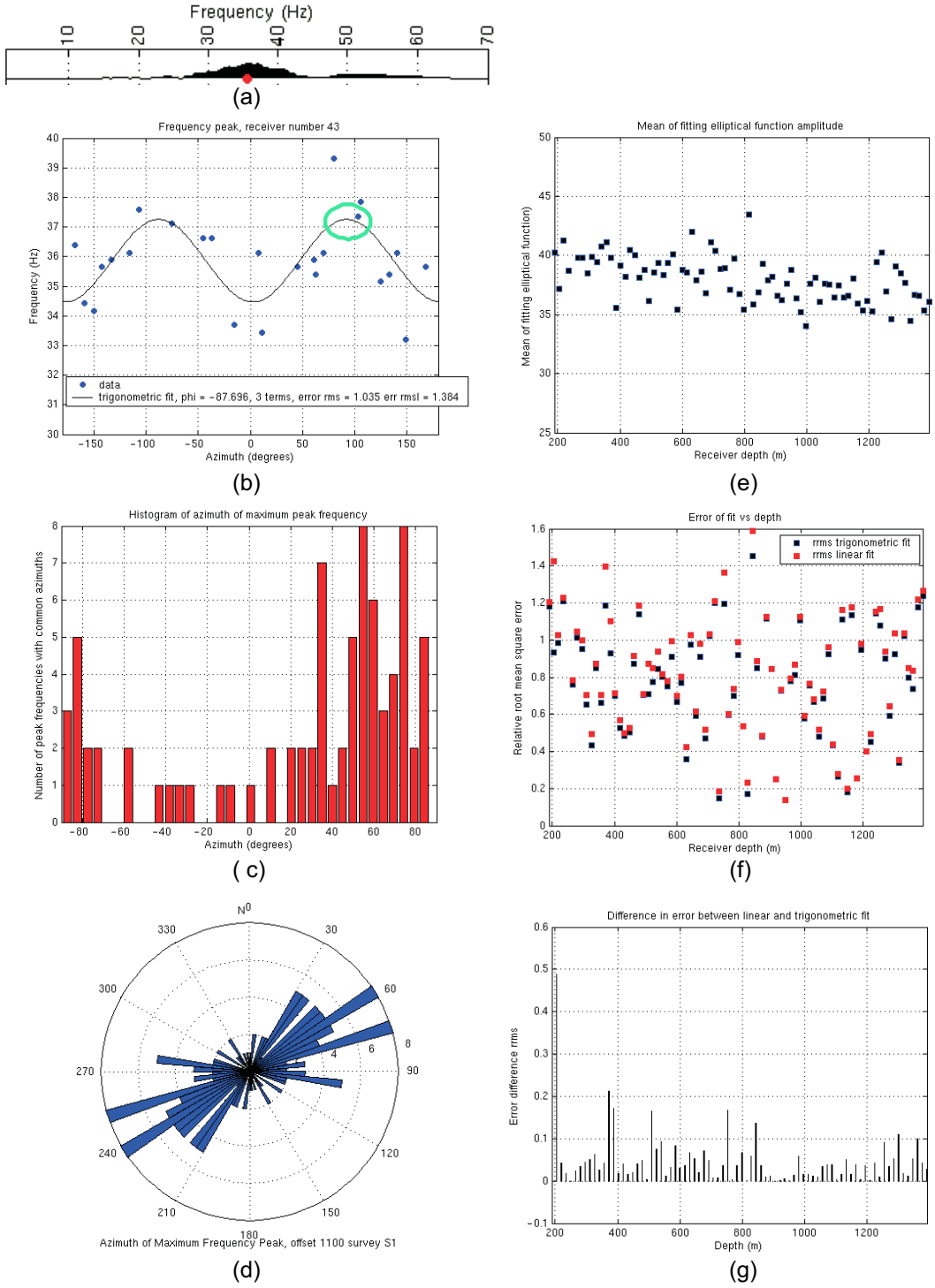

Figure 4.17: Process of creating rose diagram for frequency peaks and errors associated with sinusoidal fit.

Offset	Travel-time	Amplitude	Frequency peak	Angle of rot.
Change at 1100m	0	1	1	0
S1→S2	a	a→d	a→d	a
Change at 1500m	1	0	0	0
S1→S2	b→a	b	a	c

Table 4.2: Record of time-lapse changes in orientations of rose diagrams for different attributes. 1:a change in orientation is observed, 0:no orientation change observed. a, b, c and d are the orientations referred to in Table 4.1.

Survey	Travel-time	Amplitude	Frequency peak	Angle of rot.
Change in S1	1	1	0	1
1100m→1500m	a→b	a→b	a	a→c
Change in S2	0	1	1	1
1100m→1500m	a	d→b	d→a	a→c

Table 4.3: Changes in rose diagram orientations between offsets 1100m and 1500m within the same survey. 1:a change in orientation is observed, 0:no orientation change observed. a, b, c and d are the orientations referred to in Table 4.1.

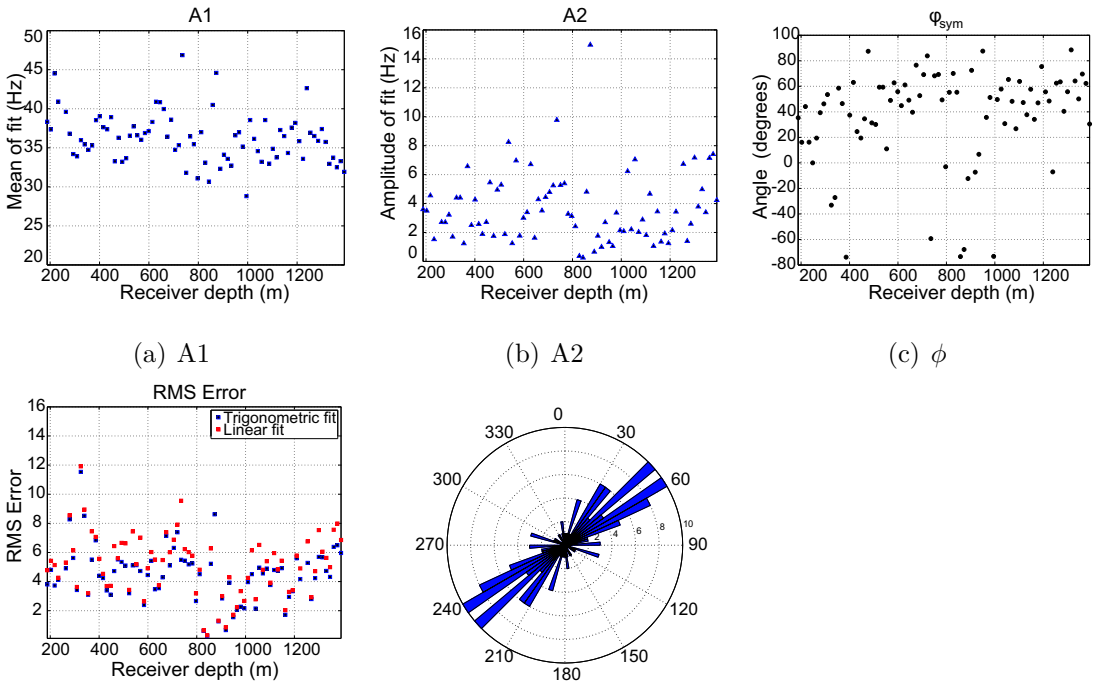

(a) A1 (b) A2 (c) ϕ

(d) Error of fit (e) Maximum frequency peak

Figure 4.18: Parameters of sinusoidal fit to frequency peaks of first breaks. Offset 1500m, survey S1.

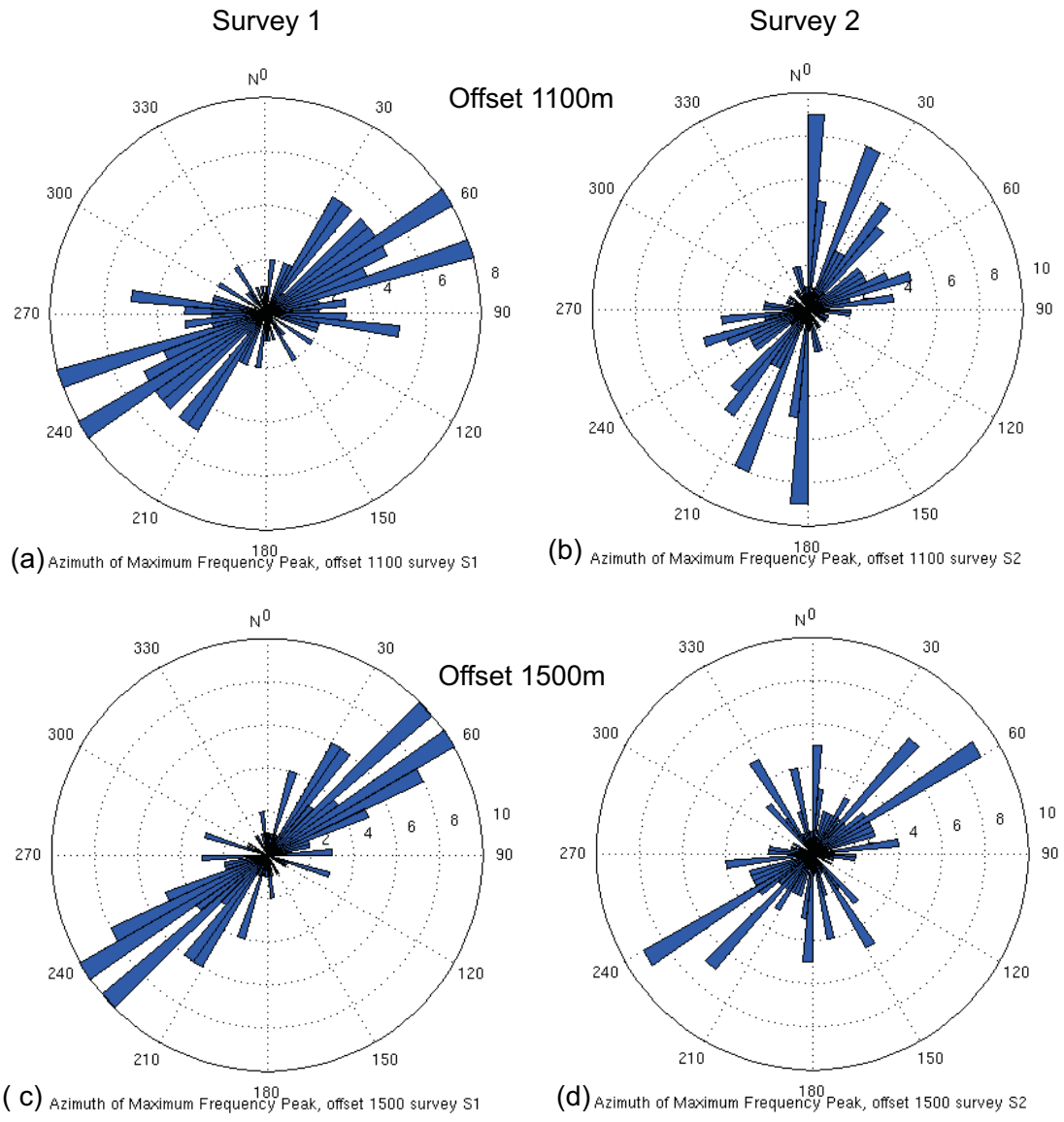

Figure 4.19: Rose diagrams of maximum peak frequency of first breaks.

4.6 Conclusions

A multi-attribute azimuthal analysis of the direct P-waves is performed. The various independent attributes include travel time, frequency peaks, angle of incidence and amplitudes.

Various common-offset sub-surveys are considered for the azimuthal analysis, however, only those with large offsets have sufficient azimuthal coverage for a robust analysis.

Rose diagrams are created for each attribute for different offsets and the base and monitor surveys. In general there is a dominant trend in the rose diagrams of the different attributes, in a NE-SW direction, that coincides with that described by independent studies as the orientation of the primary fracture network (Burrowes and Gilboy, 2000, Li, 2002). There are three other less dominant orientations recognised, one of which has the orientation of the secondary fracture network which has been described to be in a NW-SE direction (Burrowes and Gilboy, 2000, Li, 2002). However, it must be noted that most previous studies on this field have been undertaken on the Weyburn Midale reservoir (Burrowes and Gilboy, 2000, Li, 2002, Li, 2003, Herawati and Davis, 2003, Kendall et al., 2003), which lies underneath the deepest geophone. It is thus interesting that the overburden rocks studied in this chapter present the same main anisotropic orientations as those from the fractured Midale beds. This suggests that the regional stresses that caused the fracturing in the Marly and Vuggy units of the Midale beds have also affected the overlying Ratcliffe and Poplar beds of the Charles Formation. The sharp difference in behavior of the data at 800m could be interpreted as a change caused by a transition from the Kibbey to the Charles Formation or across the unconformity that separates the Watrous from the Kibbey formations.

In terms of the orientations extracted from the attributes, the time-lapse changes in these data are of second order compared to those found within the same survey and attribute for different offsets. More specifically, we found changes in 6 out

of 8 common-offset surveys between offsets 1100m to 1500m, and only 3 out of 8 changes in orientations between the base and the monitor surveys.

Chapter 5

Method: SVD-AVOZ, theory and modelling

5.1 Summary

I develop a technique for inversion of fracture properties from azimuthal AVO (AVOZ). Unlike traditional analytical equations and approximations for describing variations in reflection coefficients with azimuth and incidence angles, the presented method describes the AVOZ variations in terms of an optimal set of basis functions calculated by applying singular value decomposition to the AVOZ response of modelled data. This construction becomes useful as we can find a relationship with the fracture density of the modelled data. This relationship can in turn be used for fracture density inversion from AVOZ data, provided that the rock properties of the rocks involved are considered in the range of the modelled ones. For the purpose of presenting the method I consider a two layer model containing an isotropic layer over an HTI anisotropic halfspace, where the anisotropy of the lower layer is due to the presence of vertical aligned fractures. I illustrate the method and its application to surface seismic data with a synthetic example of multi-azimuth common-offset gathers with different fracture densities. I find that we can invert for the fracture density of synthetic data through the AVOZ relationship and the method presented.

5.2 Introduction

Amplitude versus offset analysis (AVO) has become standard practice in geophysical exploration due to the usefulness of the parameterization of the approximations to the Zoeppritz equations. Even though the Zoeppritz equations can be evaluated numerically it is often more insightful to use approximations (Mavko et al., 1999) as these relate the physical properties of the medium to the reflection coefficient in a simpler way, and inversion for the physical properties becomes possible (Rüger, 2001).

One of the most common approximations is given by Shuey (1985), who rewrites the approximation given by Aki and Richards (1980) as follows,

$$Rpp(\theta) \approx A + B\sin^2\theta + C\sin^2\theta\tan^2\theta \tag{5.1}$$

where,

$$\begin{aligned} A &= \tfrac{1}{2}\left(\tfrac{\Delta Vp}{\bar{Vp}} + \tfrac{\Delta\rho}{\bar{\rho}}\right) = \tfrac{1}{2}\tfrac{\Delta Z}{\bar{Z}} \\ B &= -2(1-\tfrac{\bar{\sigma}}{1-\bar{\sigma}})A - \tfrac{1}{2}\tfrac{1-\bar{\sigma}}{1\bar{\sigma}}\tfrac{\Delta Vp}{\bar{Vp}} + \tfrac{\Delta\sigma}{(1-\bar{\sigma})^2} \\ C &= \tfrac{1}{2}\tfrac{\Delta Vp}{\bar{Vp}} \end{aligned}$$

where ΔVp is the difference in compressional wave velocities of the media across the interface, such that $\Delta Vp = Vp_2 - Vp_1$. The Δ symbol denotes differences for other properties as well, and averages are denoted by a bar, so that $\bar{Vp} = \frac{Vp_2+Vp_1}{2}$. ρ is density, σ is Poisson's ratio and Z is impedance, with $Z = \rho Vp$.

Castagna and Backus (1993) discuss the usefulness of this approximation by linking the terms A, B, and C to the near, mid and far ranges of the angle of incidence respectively. Thomsen (1990) presents a similar equation where the expression for B is $B = (\frac{\Delta Vp}{Vp} - (\frac{2\bar{Vs}}{Vp})^2\frac{\Delta G}{G})$. There are other approximations to the Zoeppritz equations (Smith and Gidlow, 1987, Hilterman, 1989). In general the assumptions underlying these approximations are that (Mavko et al., 1999, Rüger, 2001):

- The rock is linear, elastic and isotropic
- The waves are plane waves
- The elastic properties of the medium at both sides of the reflecting boundary are similar, with small relative changes in Vp, Vs and density.
- The incidence angle is sufficiently smaller than the critical angle (less than about 30°, Mavko et al., 1999).

In turn, these approximations work poorly for large angles of incidence, and it is at those angles of incidence that the anisotropic effect - caused by the presence of fractures- can become significant, as illustrated in Figures 5.1 and 5.2. In the isotropic case (for a fixed azimuth), Riede et al. (2005) present a method for AVO analysis based on calculating a set of basis functions for AVO by modelling the exact AVO response when the rock is saturated with different fluids. This approach allows the reflection coefficients in the near-mid and large angle domains to be accurately represented during AVO analysis. They then use these basis functions to invert for the fluid content from the measured AVO response.

It is widely accepted that seismic anisotropy is an important tool for understanding fracture systems. Studies on the effects of fractures on seismic signals range through theoretical implications (Rüger, 1996, Chapman, 2003), physical and numerical modeling experiments (Wang et al., 2007) and field seismic data examples and interpretations (Maultzsch et al., 2003, Liu et al., 2007). The azimuthal variation of AVO gradient is a common attribute which is linked to the fracture network.

For the purpose of quantitatively characterizing fractures we extend Riede et al.'s method for azimuthal variations and investigate its use for fracture density discrimination. In our method we describe the AVOZ response of field data in terms of the principal components of modelled azimuthal reflection coefficients. We do this by numerically modeling the AVOZ response due to the presence of

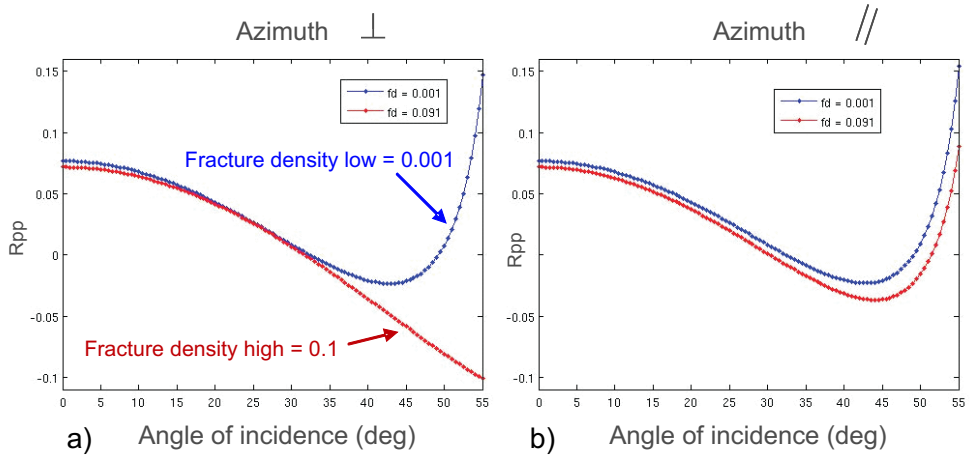

Figure 5.1: Effect of fracture density on AVO for an interface between an isotropic layer over an anisotropic halfspace, a) in a direction perpendicular to the fractures of the bottom layer, and b) in a direction parallel to the fractures. The blue and red lines correspond to low (0.001) and high (0.091) fracture densities of the bottom layer accordingly.

fractures in a given reservoir based on well log and rock physics data available from the area, as well as a rock physics model.

In our method we invert for the fracture density of a fractured reservoir rock based on relationships found between seismic modeling of a fractured rock and its field data counterpart. With this we hope to be able to move towards a more quantitative description of a fracture network from analysis of seismic data.

5.3 Background: Singular value decomposition (SVD)

Definition: Eigenvalue decomposition

If A is a real symmetric matrix of dimensions $n \times n$, then there is an orthogonal matrix Q and a diagonal matrix Λ such that $A = Q\Lambda Q^T$, where the columns of Q are the eigenvectors of A, and the diagonal elements of Λ are the eigen-

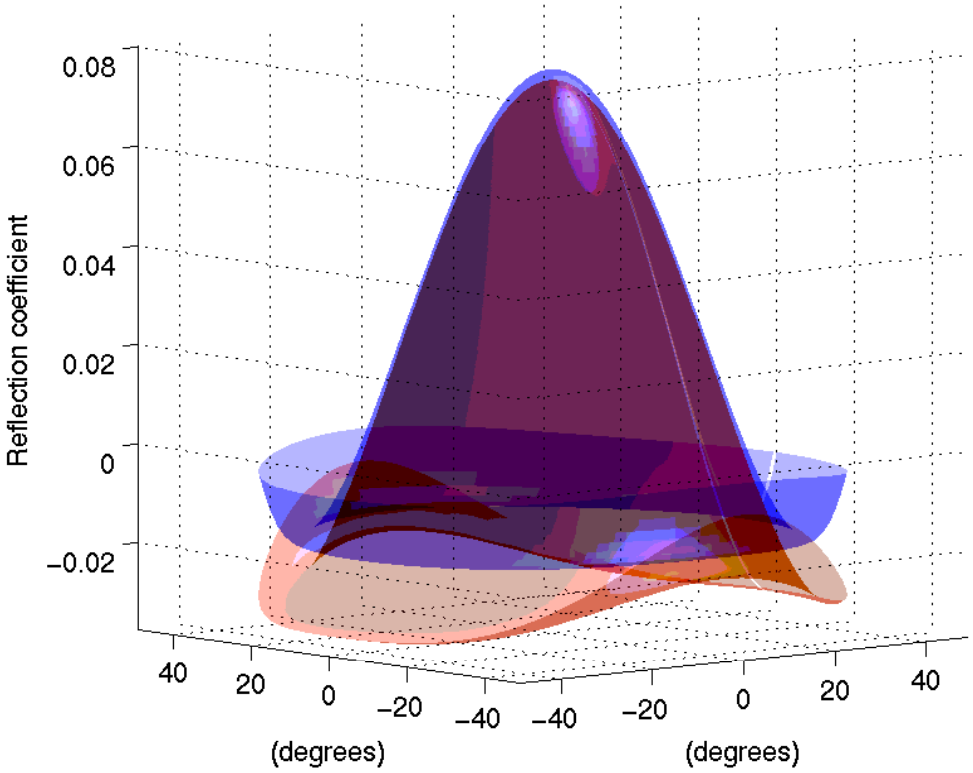

Figure 5.2: Effect of fracture density on reflection coefficients versus azimuth and angle of incidence (increasing in the radial direction) corresponding to the rock properties of Model 1 (see Synthetic Example). Blue and red surfaces correspond to null or very low (0.005), and high (0.135) fracture densities respectively.

values of A. Here Q forms an orthonormal basis for $\Re^n$. This decomposition is known as the spectral decomposition, diagonalization (Hadi, 1996), or eigenvalue decomposition (EVD) of A (Kalman, 1996).

Definition: Singular value decomposition

The SVD is then a generalization of the EVD for an arbitrary matrix A of $m \times n$ dimensions[1] (Strang, 2006). The SVD is defined (Strang, 2006, page 331) as "Any

[1] $A_{m \times n}$ has m rows and n columns

m by n matrix A can be factored into

$$A = USV^T = (orthogonal)(diagonal)(orthogonal) \tag{5.2}$$

The columns of U (m by m) are eigenvectors of AA^T, and the columns of V (n by n) are eigenvectors of A^TA. The r singular values on the diagonal of S (m by n) are square roots of the nonzero eigenvalues of both AA^T and A^TA."[2]

The columns of U and V are also known as the left and right singular vectors of A (Kalman, 1996). S is an m by n matrix where only the entries s_{ii}, with $1 \leq i \leq m$ are non-zero, and the diagonal elements s_{ii} can be arranged in non-increasing order. Furthermore, if we normalise the columns of U and V then $U^TU = I_m$, and $V^TV = I_n$, U and V are orthogonal matrices with orthonormal columns.

In more detail, if we create matrices $\tilde{A} = AA^T$ and $\hat{A} = A^TA$ for $m < n$. We can find the eigenvectors u and v and eigenvalues λ of $\tilde{A}$ and $\hat{A}$ by solving for,

$$\tilde{A}u = \lambda u \tag{5.3}$$

and

$$\hat{A}v = \lambda v \tag{5.4}$$

after normalizing u and v, the matrices U, V and S can be formed such that,

$$U = [u_1 u_2 \dots u_m], \tag{5.5}$$

$$V = [v_1 v_2 \dots v_n], \tag{5.6}$$

and

$$S_{m\times n} = \begin{bmatrix} \sqrt{\lambda_1} & 0\dots & 0 & 0\dots & 0 \\ 0 & \ddots & 0 & \vdots & \\ \vdots & & & 0\dots & 0 \\ 0 & 0\dots & \sqrt{\lambda_m} & 0\dots & 0 \end{bmatrix} \tag{5.7}$$

[2]Note that there are alternative formulations (Belsley et al., 2005), for example $A_{m\times n} = U_{m\times n}S_{n\times n}V_{n\times n}$

where the eigenvector and eigenvalue pairs have the same subscripts. If on the other hand $m > n$, the matrix $S_{m\times n}$ would be padded with zeros as above in the last $m - n$ rows.

For positive definite matrices[3] S is equal to Λ, and USV^T is identical to $Q\Lambda Q^T$. For complex matrices S remains the same, and U and V become unitary, which is the complex version of orthogonal. In turn, when taking the conjugate transpose (or Hermitian transpose[4] H) we have $U^HU = I$ and $V^HV = I$, which results in $A = USV^H$ (Strang, 2006).

Furthermore, it can be shown that,

$$A = \sum_{k=1}^{N} \sqrt{\lambda_k} u_k v_k^T \tag{5.8}$$

where the matrix resulting from the product of $u_k v_k^T$ is a rank one $m \times n$ matrix known as the kth eigenimage of matrix A. Because u_k and v_k are eigenvectors of symmetric matrices AA^T and A^TA respectively, they are orthogonal (Potter, 1978, page 184). In turn, these eigenimages form an orthogonal basis for A (Vrabie et al., 2004).

Vrabie et al. (2004) point out that in noise free data if the m recorded signals are linearly independent, the matrix A is full rank and its perfect reconstruction will require all eigenimages. If however, the vectors in A are linearly dependent, the rank of A is one, and its perfect reconstruction is possible with just the first few eigenimages.

Some of the characteristics of the SVD factorization that have made it popular among scientists are: a) it identifies the dimensions with most variation of a data set, b) it recognizes and orders these directions from most to least variation, c) it

[3]A real symmetric matrix A is positive definite if all the eigenvalues of A satisfy $\lambda_i > 0$ (Strang, 2006, page 318).

[4]The Hermitian transpose of a matrix is obtained by calculating the transpose of the matrix followed by the complex conjugate.

provides a way for an optimum approximation of data using fewer dimensions. In the next section I briefly present some of the applications in geophysics that these characteristics have led to. Shlens (2005) gives a very comprehensive tutorial on singular value decomposition and its relationship to principal component analysis (PCA).

5.3.1 SVD applications in geophysics

SVD in image processing

One of SVD's main uses has been in the field of image processing. As image processing provides a graphical way of understanding the method, I start with an example from this field.

Take, as a first example matrix A, which is a black and white photo of one of Scotland's abbeys as shown in Figure 5.3a, with 1296 rows and 2304 columns. I calculate the eigenimage decomposition, obtained by $u_k v_k^T$, as shown in Figure 5.3 b) to j), where k is the kth eigenimage.

We can now reconstruct image A with different precisions depending on the number of singular values we choose to use in the reconstruction. Although the first few singular values carry most of the information -and thus allow for a rough reconstruction of the image with fewer data- any additional singular values used will carry information concerning the details of the image that make it sharp. I calculate the reconstruction of the abbey photo with different numbers of eigenvalues, or summation of eigenimages used, as shown in Figure 5.4. Some of these eigenimages are shown in Figure 5.3.

The singular values that led to this decomposition are shown in Figure 5.5a). For didactical purposes I also show the corresponding matrices U and V in Figure 5.5 c) to f). Compared to a seismic section (or to the reflection coefficients versus offset variations discussed later in this chapter) this photo has a much higher

(a) Original

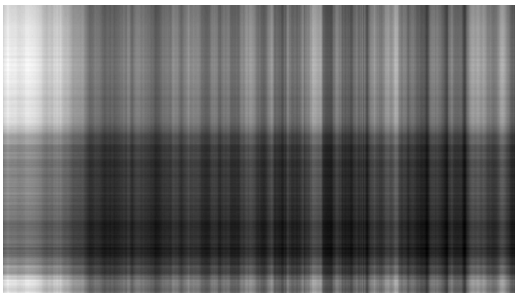

(b) Eigenimage 1

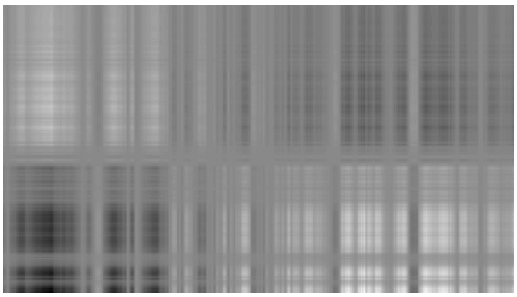

(c) Eigenimage 2

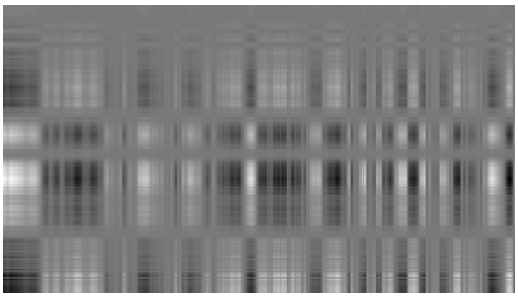

(d) Eigenimage 3

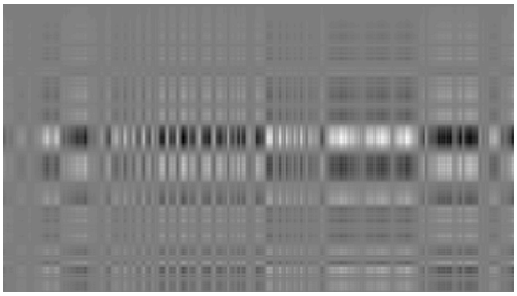

(e) Eigenimage 4

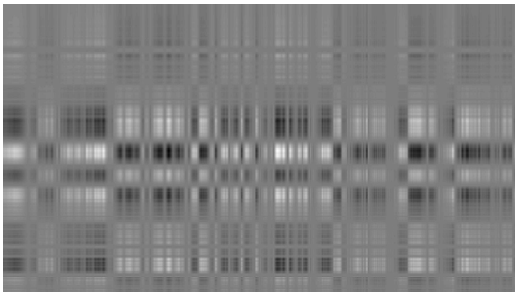

(f) Eigenimage 5

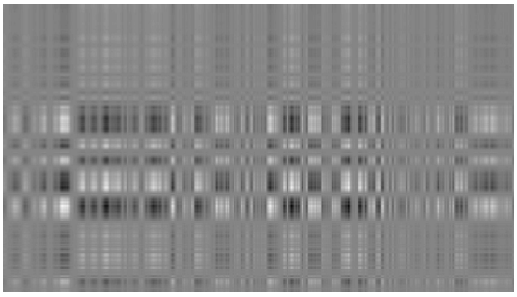

(g) Eigenimage 8

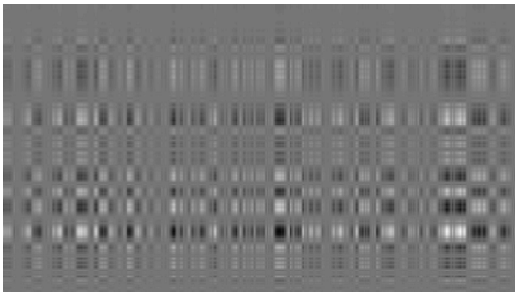

(h) Eigenimage 10

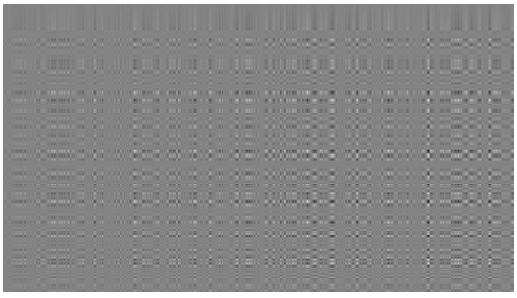

(i) Eigenimage 50

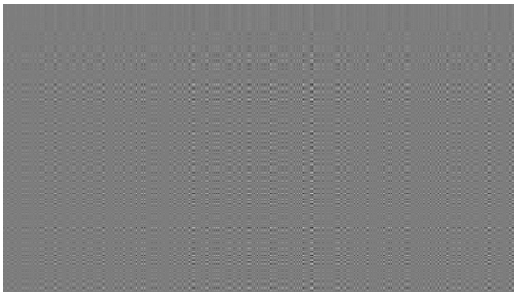

(j) Eigenimage 100

Figure 5.3: Eigenimage decomposition of a photo using SVD.

(a) Original

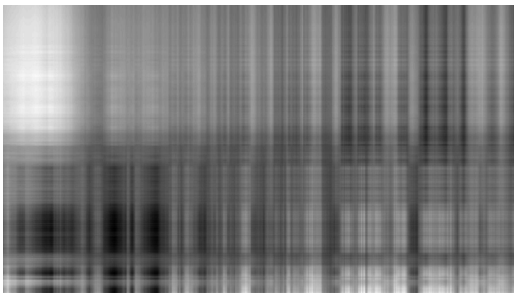

(b) i (index for eigenimages used)≤ 2

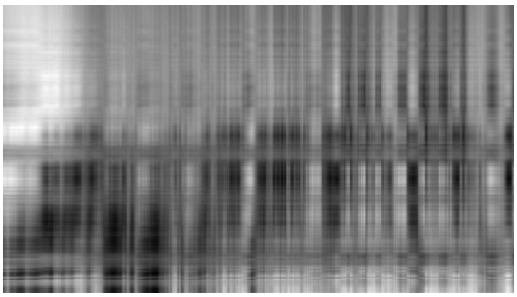

(c) $i \leq 3$

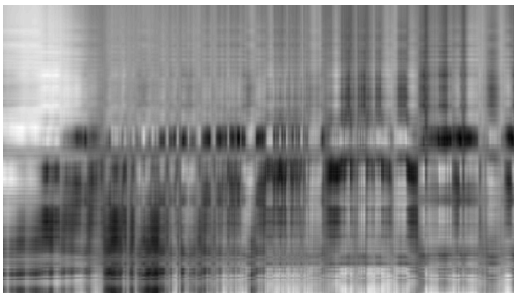

(d) $i \leq 4$

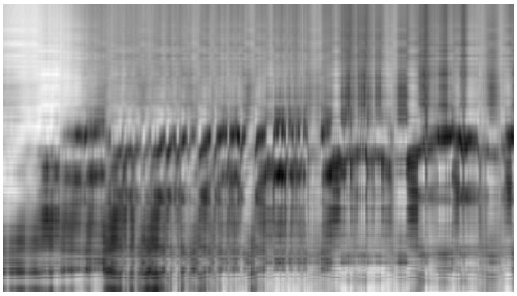

(e) $i \leq 5$

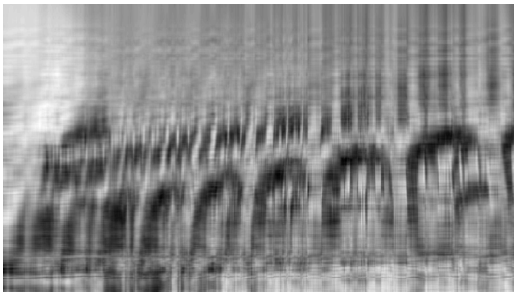

(f) $i \leq 8$

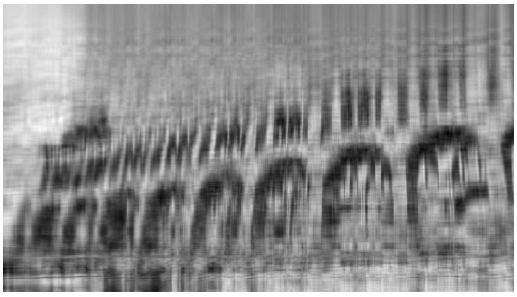

(g) $i \leq 10$

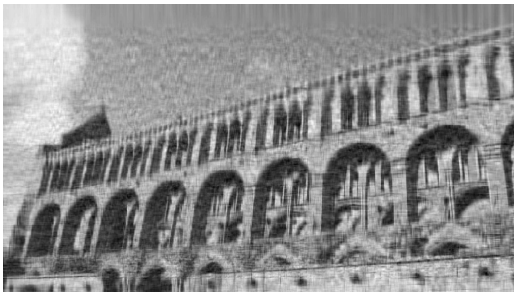

(h) $i \leq 30$

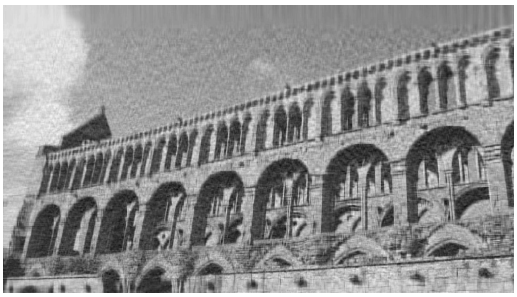

(i) $i \leq 50$

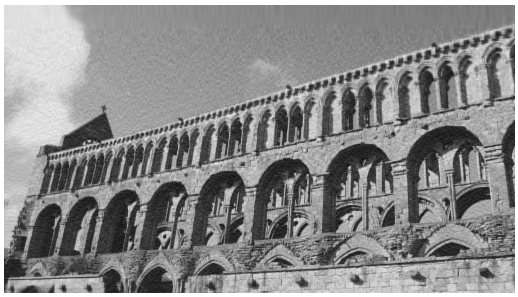

(j) $i \leq 100$

Figure 5.4: Photo reconstruction using eigenimages from SVD.

degree of sharpness, variation and high frequency content, thus the number of eigenvalues needed for its reconstruction is much larger.

Figure 5.6 shows the cumulative sum of the singular values in percentage. Although panel (a) implies that a full reconstruction of the image requires all the singular values, panel (b) shows that 59% of the information from the singular values is given by the first (largest) 100 singular values out of 1296.

SVD for filtering noise in VSP's

Teakle et al. (1995) use a method based on SVD to cancel coherent tube waves in high frequency seismic data, getting better results in comparison to using an FK filter. They split the seismic section into linearly independent eigenimages, where each eigenimage has a characteristic content of the seismic record, and its contribution to the energy of the seismic section is given by the magnitude of the eigenvalue. To remove the tube waves they must first be precisely aligned, and their amplitudes balanced before performing the eigenanalysis. They then subtract those eigenimages corresponding to random and coherent noise from the total composition of eigenimages.

Others have used a combination of SVD, independent component analysis (ICA) and $f-k$ filters to remove coherent noise from seismic data, as did Mari (2006). Independent of the choice of filter used, in order to isolate a specific wave type, he first a) flattens the wave in the seismic section, b) filters by the choice of method, and c) performs an inverse flattening operation. He enhanced the reflected waves and suppressed the surface, air and refracted waves in a complicated low-depth reservoir underlying a thick weathered zone. He successfully validated his results by calibrating them with well seismic data. Mari (2006) bases the SVD-ICA method on that proposed by Vrabie et al. (2004), as he claims it can provide better results than the classical SVD filter.

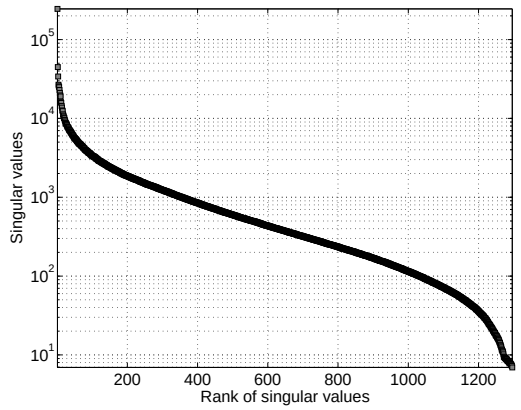

(a) Singular values

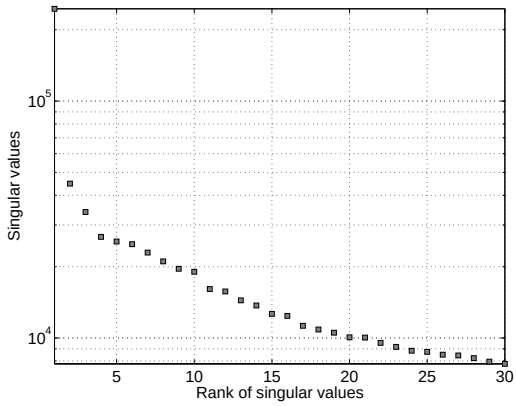

(b) Singular values, first 30

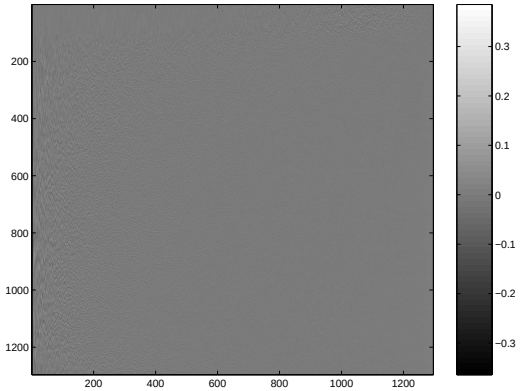

(c) U

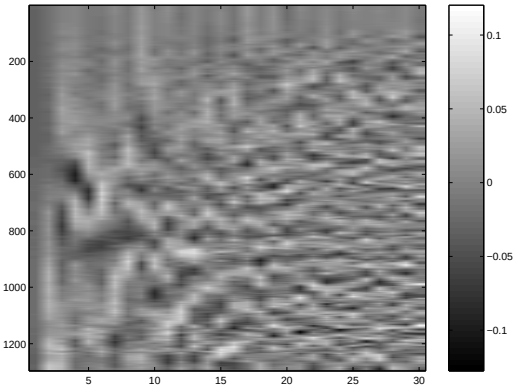

(d) U first 30 eigenvectors

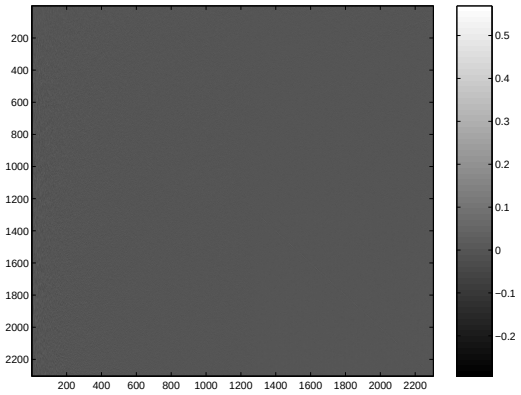

(e) V

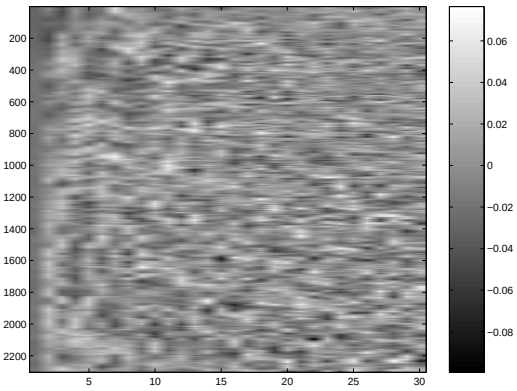

(f) V first 30 eigenvectors

Figure 5.5: SVD matrices and singular values for photo decomposition. a), c) and e) correspond to singular values, matrices U and V' respectively. b), d) and f) are the first 50 entries of a), and first 30 entries for c) and e) accordingly.

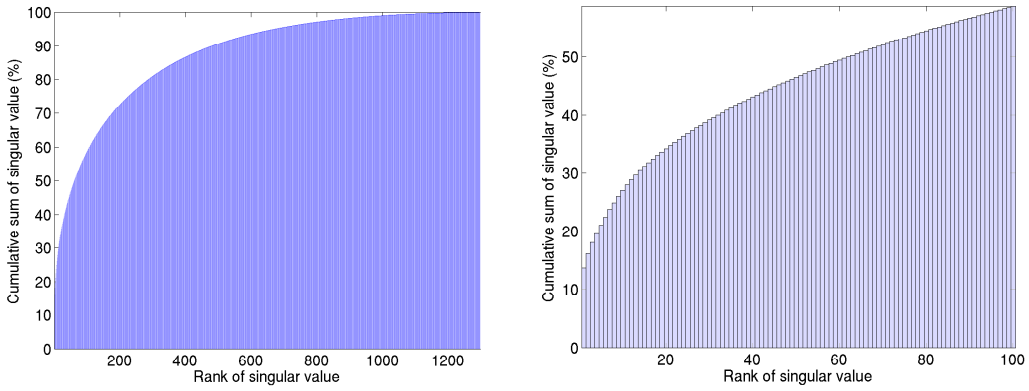

(a) Cumulative sum of singular values (b) First 100 values of (a)

Figure 5.6: Cumulative sum of singular values.

SVD for wavefield separations

Further to the applications to noise suppression, SVD has been used for separation of up-going and down-going wavefields in VSP data (Freire and Ulrych, 1988) and for the separation of PP from PS waves (van der Baan, 2006). These wavefield separations function in similar fashion as explained above for the examples of coherent noise suppression. Additionally, the independent eigen-images obtained may provide information not recognised without the factorization.

SVD for polarization filters

de Franco and Musacchio (2001) use SVD to create a polarization filter for 3-component (3C) seismic data. They work under the assumption that the particle motion is essentially 2-D, thus using only the first two eigen-images to construct the filter, and disregarding the minimum eigenvalue as polarized noise. Compared to the covariance-based algorithm commonly used for polarization analysis, de Franco and Musacchio's method is the more efficient for enhancement of the signal-to-noise and faster in computer time (90% less time consuming).

SVD for 4D seismic

SVD has also been used in stacked 4D seismic data processing to separate geological, time-lapse and noise factors. Reid et al. (2003) give a clear example of this. They construct the matrix A of equation 5.2 with two neighboring traces from the base survey and the two corresponding traces of the monitor survey. This leads to A being $m \times n$, where m is the number of samples in each trace and n equal to the number of traces. They then reconstruct the eigenimages corresponding to each eigenvalue and find that:

- The eigenimage produced with the two largest eigenvalues corresponds to the geological features of the seismic image.
- The eigenimage produced by substracting the eigenimage of the second largest eigenvalue from the original data contains mostly the time-lapse changes.
- The eigenimages from the remaining two smallest eigenvalues are dominated by random and incoherent noise.

Furthermore, they pick the oil-water contact from the SVD decomposition and compare that to the one picked through traditional methods. [5] They find that the mapped contact from the SVD eigen decomposition is more reliable, clearly showing the contact where the traditional methods fail to do so.

Attribute extraction in AVO via principal component analysis

In a work that forms the starting point for the next section, Saleh and de Bruin (2000) present a comprehensive account of principal component analysis as a tool for robust AVO crossplotting and attribute analysis.

[5] Traditional methods use the Hilbert transform to convert the trough and peak in the seismic trace corresponding to the original and new oil-water contact into a peak-peak. This is to facilitate the selection of the contact in the seismic trace.

Their goal is to find optimal AVO attributes to crossplot, so that the scattering in the crossplot is maximum and the attributes crossplotted are robust against noise-induced slope changes in the background trend. They start by viewing conventional AVO attributes as a least squares solution to an approximation problem. To explain this they propose the following situation:

1. Let θ_i, i=1,...,N be the angle of incidence of a plane wave at one subsurface point for a P-P wave

2. Let r_i be the reflection coefficient corresponding to θ_i, and define $x_i = \sin^2\theta_i$. Furthermore let ϕ_i be a set of N dimensional independent vectors. Then, if we collect for a given subsurface point all vectors r_i into an N dimensional vector r, r can be written as:

$$r = \sum_{i=1}^{N} \alpha_i \phi_i, \tag{5.9}$$

   where α_i's are parameters that will depend on the choice of ϕ_i's.

3. The estimate of r, denoted $\tilde{r}$, with just two basis functions ϕ_i, will then be given by,

$$\tilde{r} = \alpha_1\phi_1 + \alpha_2\phi_2 \;=\; \Phi\alpha \approx r, \tag{5.10}$$

   with

$$\Phi = [\phi_1 \; \phi_2], \tag{5.11}$$

   and

$$\alpha = \begin{bmatrix} \alpha_1 \\ \alpha_2 \end{bmatrix} \tag{5.12}$$

4. For a given set of ϕ_1 and ϕ_2, the least squares solution to equation 5.10 is given by,

$$\alpha = \left(\Phi^T\Phi\right)^{-1}\Phi^T r \tag{5.13}$$

5. With the above explanation, Saleh and de Bruin (2000) point out that the ϕ's and α's corresponding to some common AVO attributes would then be given by the relationships shown in Table 5.1.

AVO attributes	basis functions
Intercept and gradient	$\phi_1 = [1\ 1 \cdots 1]^T$ $\phi_2 = [x_1\ x_2 \cdots x_N]^T$ $\alpha_1 = Intercept$, $\alpha_2 = Gradient$
Near-far amplitudes	$\phi_1 = [1\ \cdots 1\ 0 \cdots 0]^T$ $\phi_2 = [0\ \cdots 0\ 1 \cdots 1]^T$ $\alpha_1 = Near\ amplitudes$, $\alpha_2 = Far\ amplitudes$
Stack-gradient	$\phi_1 = [1\ 1 \cdots 1]^T$ $\phi_2 = [(x_1 - \bar{x})\ (x_2 - \bar{x}) \cdots (x_N - \bar{x})]^T$ $\alpha_1 = Stack,\ \alpha_2 = gradient$ where, $\bar{x} = \frac{1}{N}\sum_{i=1}^{N} x_i$

Table 5.1: Traditional AVO basis functions used for crossplotting, from Saleh and de Bruin (2000).

Saleh and de Bruin (2000) find the following shortcomings of the functions presented in Table 5.1.

- From the intercept and gradient functions, ϕ_1 and ϕ_2 are not orthogonal causing an undesirable correlation between α_1 and α_2.
- For the plotting of the near and far amplitudes, ϕ_1 and ϕ_2 are orthogonal and so α_1 and α_2 are uncorrelated, but the form of ϕ_1 and ϕ_2 is not optimal resulting in a poor performance in terms of approximation and minimization of errors.
- The stack-gradient method is regarded as having the optimal functions amongst the three, as the ϕ_1 and ϕ_2 are an orthogonal expansion of first order polynomials. However Saleh and de Bruin (2000) propose that ϕ_1 and ϕ_2 be normalised to guarantee immunity from white noise-induced slope distortions.

Saleh and de Bruin (2000) also propose a set of new attributes for AVO cross-

plotting, these are derived as follows:

- Let $r^1, r^2, \ldots, r^m$ be the offset dependent reflection vectors for a target horizon of m different subsurface reflecting points (r^i is N-dimensional).
- The mean vector $\bar{r}$ and the covariance matrix C are then

$$\bar{r} = \frac{1}{m} \sum_{i=1}^{m} r^i, \tag{5.14}$$

$$C = \frac{1}{m} \sum_{i=1}^{m} \left(r^i - \bar{r}\right) \left(r^i - \bar{r}\right)^T \tag{5.15}$$

- They then propose ϕ_1 and ϕ_2 to be the eigenvectors corresponding to the two largest eigenvalues of C. α_1 and α_2 are then calculated for each r^i using equation 5.13.

5.3.2 AVO with SVD for fluid discrimination

This work generalises those of Causse and Hokstad (2005), Causse et al. (2007a), Causse et al. (2007b) and Riede et al. (2005). Causse and Hokstad (2005) developed a method to improve the accuracy of the estimated AVO intercept and gradient by constructing a set of optimal basis functions through singular value decomposition. They developed the method in a different context, for corrections to non-hyperbolic travel-time and applied it to AVO for a more precise calculation of intercept and gradient. Riede et al. (2005) and Causse et al. (2007a) used the same principles as Causse and Hokstad (2005) and applied them for classifying pore fluids and lithological facies from AVO. Their methodology starts from the AVO approximations in the general form, given by the equation

$$R(\theta) = C_1 F_1(\theta) + C_2 F_2(\theta) + C_3 F_3(\theta) + \ldots \tag{5.16}$$

in which the reflection coefficient R as a function of angle of incidence θ is written as a linear combination of functions F_i and coefficients or weights C_i . In

commonly used approximations, such as those from Shuey (1985) or Aki and Richards (1980) the F_i's are trigonometric functions, with $F_1 = 1$, $F_2 = \sin^2(\theta)$ and $F_3 = \tan^2(\theta) + \sin^2(\theta)$ for the former.

Riede et al.'s (2005) approach departed from that, and consisted of finding a set of basis functions with the property that they are orthonormal, accurately describe the AVO response at all incidence angles, and can be related to the fluid content of the rock for any given AVO response. For this, prior information from well log or core data is used to create a number of reference or expected AVO responses, which are modelled with the exact Zoeppritz equations. These reference curves are arranged into a matrix, R, with every row corresponding to a different angle of incidence, and every column to the AVO response of a different realization of the distribution of rock properties. Subsequently this matrix is factorized using singular value decomposition (SVD), as shown in equation 5.17,

$$R = FDV^T, \tag{5.17}$$

where F and V are orthonormal matrices containing the normalized eigenvectors of RR^T and R^TR, respectively, in their columns. D is a diagonal matrix with the singular values of RR^T or R^TR arranged in decreasing order. Equation 5.17 can be further compacted into equation 5.18:

$$R = FW \tag{5.18}$$

This factorization becomes useful as the columns of F contain the different basis functions F_i, while the rows of W have the coefficients C_i. In comparison with the analytical Aki and Richards (1980) approximation, or the best fit to the reflection coefficient using the two and three term AVO response, Riede's method is closer to the exact AVO response (Riede et al., 2005).

5.4 Method: AVOZ with SVD for fracture properties inversion

The most commonly used azimuthal AVO approximation to the exact reflection coefficients is given by Rüger (1996) for an HTI medium as follows,

$$\begin{aligned} R_p^{HTI}(i,\phi) &= A + \left(B^{iso} + B^{ani}\cos^2(\phi - \phi_{sym})\right)\sin^2 i \\ &\quad + \frac{1}{2}\left[\frac{\Delta Vp}{\bar{V}p} + \Delta\varepsilon^{(V)}\cos^4\phi + \Delta\delta^{(V)}\sin^2\phi\cos^2\phi\right]\sin^2 i\tan^2 i \end{aligned} \tag{5.19}$$

where,

$$\begin{aligned} A &= \tfrac{1}{2}\tfrac{\Delta Z}{Z} \\ B^{iso} &= \tfrac{1}{2}\left[\tfrac{\Delta Vp}{\bar{V}p} - (\tfrac{2\bar{V}s}{\bar{V}p})^2\tfrac{\Delta G}{G}\right] \\ B^{ani} &= \tfrac{1}{2}\left[\Delta\delta^{(V)} + 2(\tfrac{2\bar{V}s}{\bar{V}p})^2\Delta\gamma\right] \end{aligned}$$

where ϕ_{sym} is the symmetry plane of the HTI medium.

However, the fit of Rüger's approximation to the exact response loses accuracy at far offsets when the three anisotropic parameters δ, γ and ϵ of the HTI medium are nonzero (Rüger, 2001). We aim to extend the Riede et al. (2005) approach, which is accurate at far offsets, to account for azimuthal variations and for fracture density classification. We write the reflection coefficients as a function of azimuth φ, angle of incidence θ and fracture density fd with equation 5.20:

$$R(\theta,\varphi,fd) = C_1(\theta,fd)F_1(\varphi) + C_2(\theta,fd)F_2(\varphi) + C_3(\theta,fd)F_3(\varphi) + \ldots \tag{5.20}$$

We use the same decomposition as in equations 5.17 and 5.18 with the difference that now the rows of matrix R vary with azimuth φ as do the functions F_i.

Take a simple model of a reflecting boundary between an isotropic medium overlying an HTI medium, where the anisotropy in the HTI medium is due to a

set of parallel vertical fractures with unknown fracture density fd. For simplicity, assume that the P-wave, S-wave and density of media are known. I model the exact reflection coefficient for different fracture densities in the HTI medium and allow for a small variation in the P-wave, S-wave and density of both media. The set of modelled reflection coefficients is stored in a matrix R with every row containing a different azimuthal angle for a given angle of incidence, set of elastic constants of both media and fracture density. The singular value decomposition is applied (equation 5.17) and the three resulting matrices of the factorization are grouped into two matrices F and W (equation 5.18), such that F contains the basis functions F_i varying with azimuth φ and W contains the weighting functions C_i which depend on the incidence angle θ and the fracture density, fd as in equation 5.20.

If we now measure the reflection coefficient $R^m(\theta, \phi, fd)$ (m for measured) of the model and use equation 5.20 to express it in terms of the basis functions F_i, we can then solve for the coefficients of the model C_i^m. Finally, we invert for the fracture density from the measured data by mapping its coefficients C_i^m into the coefficients of the modelled curves $C_i(\theta, fd)$ whose dependence on fracture density is known. Thus the method proposed here is based on the classification of fracture density from the weighting functions C_i in equation 5.20.

The workflow of this technique is divided into two branches, as shown in Figure 5.7: that of the modelled reference curves, which is the top part of Figure 5.7, and that of the integration of the field AVO response and inversion for fracture density, summarised in the lower part of Figure 5.7. The main steps of the algorithm are:

a) Rock properties Set the means and standard deviations of the rock properties for the layers above and below the interface of interest. Base this information on well log, or other petrophysical data available.

b) Model elastic constants Model the elastic constants of the fractured layer for different values of fracture density using a rock physics theory.

c) Reference curves Create a family of reference AVOZ curves and store them in matrix R. Matrix R is arranged such that every row has a different azimuthal angle and every column a different angle of incidence.

d) SVD on R Calculate the singular value decomposition of matrix R, obtain the basis functions and weighting coefficients.

e) Coefficients vs fracture density Find a suitable relationship between the coefficients resulting from the SVD and the fracture density used in calculating the reference curves of matrix R.

f) AVOZ with optimal basis functions Write the measured AVOZ response R^m in terms of the basis functions F_i that resulted from the SVD of the modelled curves. We do this by finding a least squares solution to equation $R^m = FC^m$, with $C^m = (F^T F)^{-1} F^T R^m$. The inverted coefficients from the measured data are then C_i^m.

g) Invert for fracture density Map the inverted coefficients C_i^m of the measured data into the modelled coefficients C_i. Invert for fracture density from the relationship between the modelled weights C_i and the fracture density used when creating the reference curves of matrix R.

I explain each one of these steps in more detail with a modelling example in the following sections.

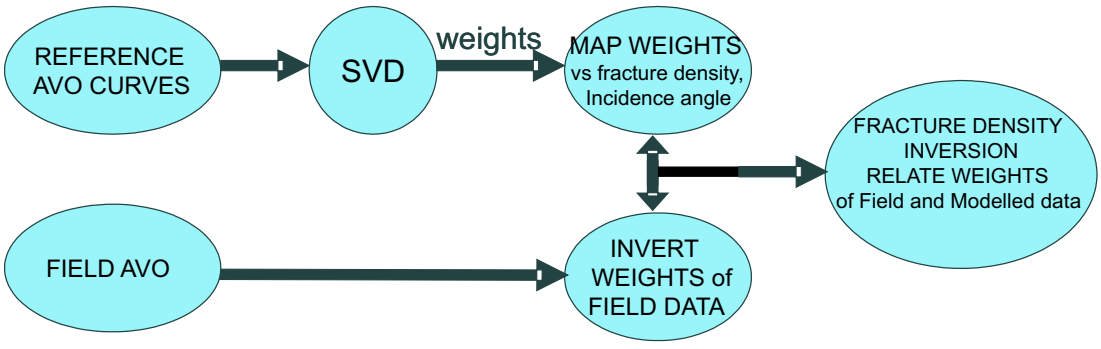

Figure 5.7: Simplified workflow of inversion for fracture properties from azimuthal AVO using singular value decomposition.

5.4.1 Building rock property models

Figure 5.8 sketches the generation of the family of reference AVOZ curves referred to in the top left of Figure 5.7. The starting point of the rock property model is based on information available from the studied area such as well log, core data, FMI logs and outcrops, as shown in the starting point (bottom left corner of Figure 5.8). From these data the mean and standard deviation of the P- and S-wave velocities and densities are calculated, and a Gaussian distribution with n random realizations for each of these rock properties is created, as shown in the second step (top section) of Figure 5.8. A realization from each of these distributions is drawn. Similarly, we choose a range of fracture densities to be modelled. Subsequently, we use Chapman's (2003) rock physics model to calculate the elastic constants of the fractured layer for each of the drawn realizations.

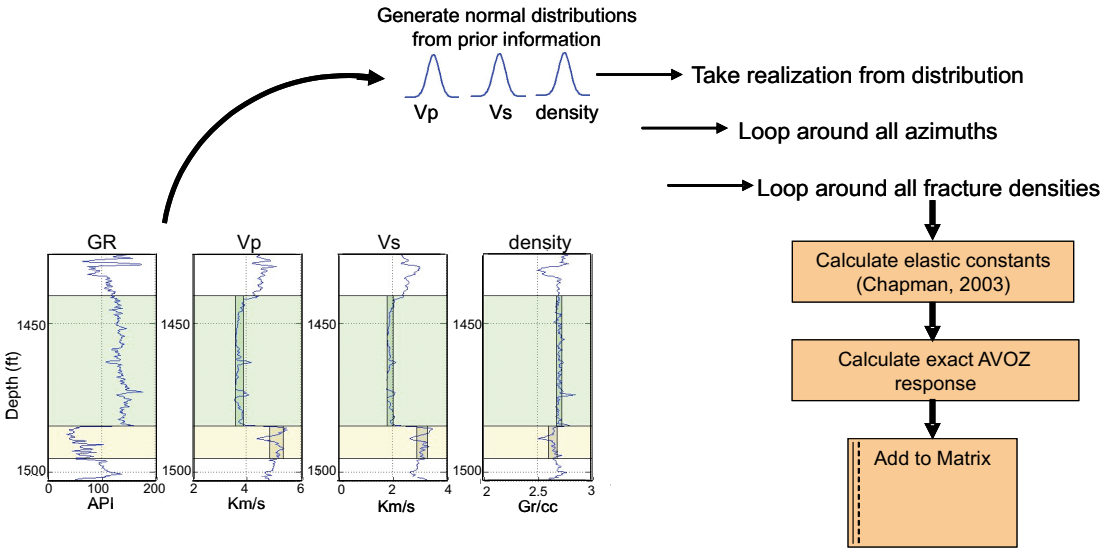

Figure 5.8: Diagram for building rock models.

Rock Model 1

In order to illustrate the method, I create a simple two layer model with a 400m isotropic layer overlying an anisotropic halfspace. The top layer has a P-wave velocity of 3.88km/s, S-wave velocity of 1.98km/s and density of 2.71g/cc. The background properties of the anisotropic half space are: P-wave velocity of

4.59km/s, S-wave velocity of 2.76km/s and density of 2.665g/cc, listed in Table 5.2.

The anisotropy in the bottom layer is due to the presence of vertically aligned fractures that result in an HTI symmetry. The parameters used for calculating the elastic constants of the anisotropic layer with Chapman's theory are shown in Table 5.3. Note that in Chapman's (2003) theory two sets of fractures or cracks can be specified. The smaller set of cracks (microcracks) are randomly oriented and have the same size as the pores. As shown in Table 5.3, in this example the microcrack density is set to zero. The larger set of fractures are parallel, causing the medium to be transversely isotropic. It is the fracture density of the larger fractures that I will vary in the modelling of the reflection coefficients and eventually invert for. As shown in Table 5.3 the radius of the larger fractures can also be specified.

I create distributions of rock properties only for the P- and S-wave velocities and density of both layers. The assigned distributions are shown in Table 5.4. When drawing the realizations from the specified distributions, I only use those that lead to a real reflection coefficient for all angles of incidence, azimuths and fracture densities considered. I show in Figure 5.9 the histograms of the rock properties used in this example. Here the number of realizations, N, (per common offset, azimuth and fracture density) is 10. The modelled fracture density for the anisotropic layer starts from 0 and goes up to 0.14 in steps of 0.005.

Parameter	Value
Thickness (m)	400
Vp (km/s)	3.877
Vs (km/s)	1.979
Density (g/cc)	2.71

Table 5.2: Properties of the isotropic top layer of Model 1.

I then compute the exact AVO response using Fryer and Frazer's (1987) algorithm for the N realizations drawn for each value of fracture density, azimuthal

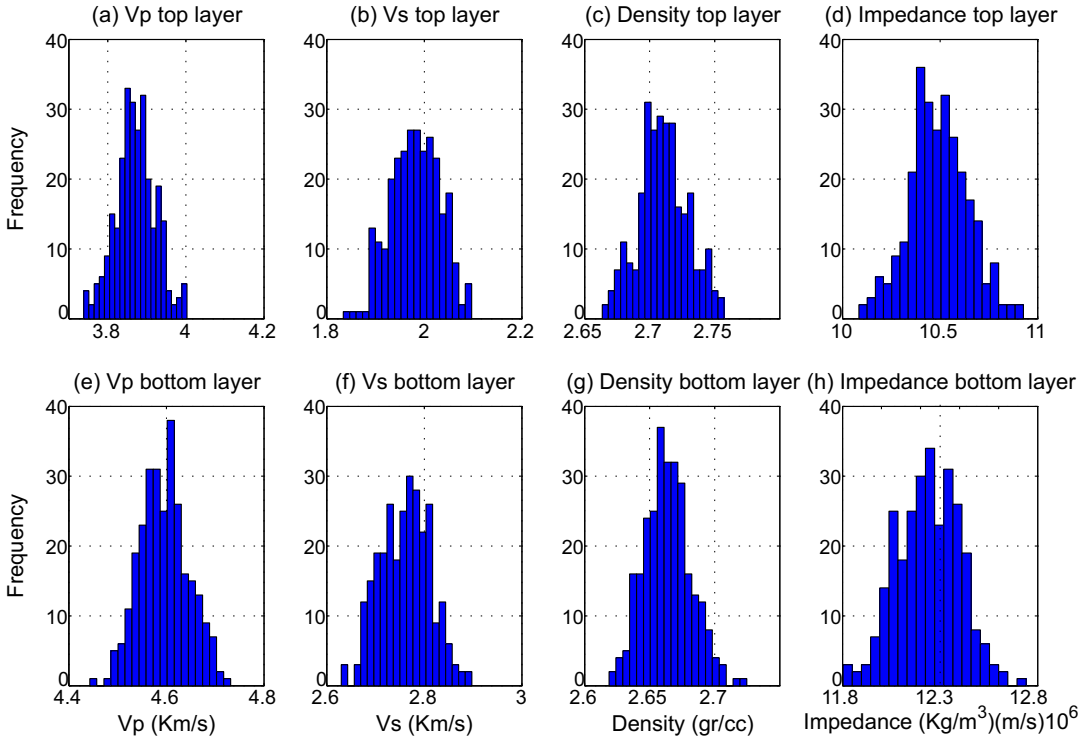

Figure 5.9: Histogram of rock properties used. The number of samples in each histogram is 280, which corresponds to 28 fracture density values times 10 realizations each.

Parameter	Value
Central frequency (Hz)	30
Fracture length (m)	1
Fracture aspect ratio	0.0001
Porosity from pores	0.075
Microcrack density	0
Relaxation time (s)	8 x 10^{-6}
Fluid modulus (Pa)	2.5x 10^{7}
Vp (km/s)	4.597
Vs (km/s)	2.761
Density (g/cc)	2.665
Thickness (m)	halfspace

Table 5.3: Properties of the fractured bottom layer with HTI symmetry of Model 1.

	Vp (km/s)	Vs (km/s)	Density (g/cc)
Layer 1	3.877±0.05	1.9795±0.05	2.71±0.02
Layer 2	4.597±0.05	2.761±0.05	2.665±0.02

Table 5.4: Mean and standard deviations of Gaussian distributions for rock properties of the top and bottom layers of Model 1.

and incidence angles, and store it in matrix, R, shown in the bottom right box of Figure 5.8. The matrix R is ordered with azimuthal angles increasing with every row, and in turn every column contains the AVOZ response of a different realization, including different angles of incidence. Figure 5.10 shows the family of reflection coefficients stored in R for two different azimuths (panels a and b) and four different incidence angles (panels c to f). To visualise how the variations in rock properties change the modelled reflection coefficients, I calculate the reflection coefficients for different fracture densities using only the mean values of the rock properties shown in Table 5.4 and zero standard deviation. The resulting reflection coefficients are shown in Figure 5.11.

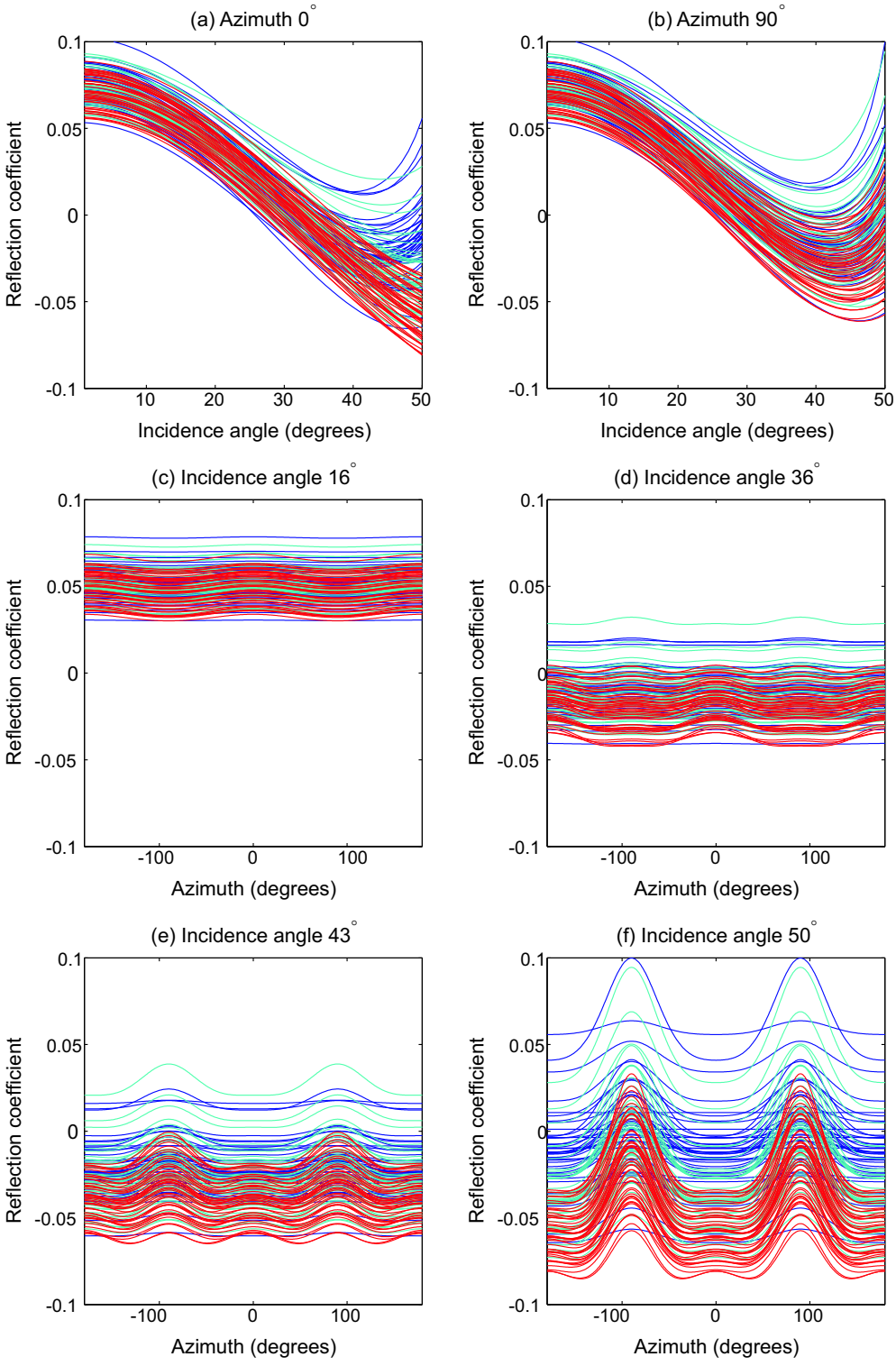

Figure 5.10: Family of reflection coefficients stored in matrix R. Blue, cyan and red correspond to the low, middle and high fracture density values. Panels a and b are in a direction perpendicular and parallel to the fracture plane. Curves were created using the parameters from tables 5.2, 5.3 and 5.4. Note: for visualisation purposes only half of the curves in R are displayed.

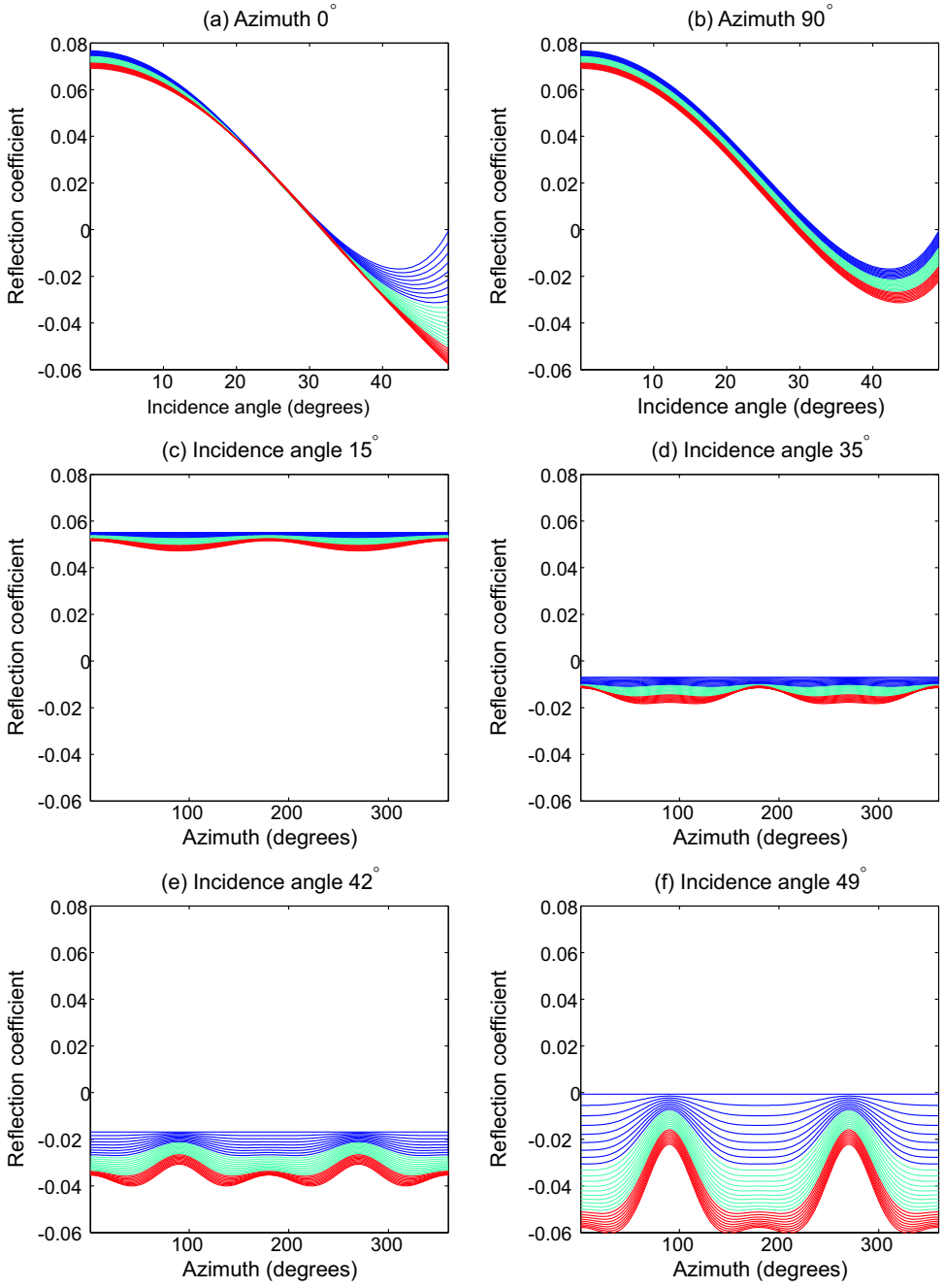

Figure 5.11: Same as Figure 5.10 but using zero as the standard deviation for the parameters in Table 5.4.

The matrix R is later decomposed using SVD, as in Equation 5.17, to obtain the basis functions F_i and their corresponding weights C_i of Equation 5.20.

5.4.2 AVOZ with optimal basis functions

The functions F_i calculated for Model 1 are shown in Figure 5.12. Notice the resemblance in Figure 5.12 between F_2 and F_3 with cosineϕ and cosine2ϕ functions respectively, which reminds us of the Fourier decomposition. Similarly F_1 is nearly a constant. It is thus expected that F_1 will have behaviour independent of fracture density, providing the mean reflection coefficient (for all azimuths) at a certain incidence angle. We expect that for increasing angles of incidence the effect of -or weight related to- F_2 increases. Similarly, for large angles of incidence the weights associated with F_3 will be at their largest.

It must be noted that these basis functions and relationships are specific for the distributions of rock properties chosen for Model 1. Whereas the process for obtaining the basis functions is independent of the rock properties used, the relationships used for the inversion, and the significance of each basis function will vary depending on the starting rock properties and distributions given to each one of them.

Once the basis functions are obtained we can approximate the azimuthal response of the reflection coefficient for a given angle of incidence in terms of F_1, F_2 and F_3 (as shown in Figure 5.13).

Figure 5.13 shows the estimate of a given AVOZ response, whose rock properties fall in the range of modelled distributions of properties, in terms of two (blue dashed line) and three (red line) basis functions. The exact AVOZ response is shown in black dots. A high fracture density (0.095) and a large angle of incidence ($40\,^\circ$) are chosen as they provide an example of marked azimuthal variations with a significant contribution of F_3. This example shows that the use of three basis functions is sufficient to capture the AVOZ behavior even for large incidence

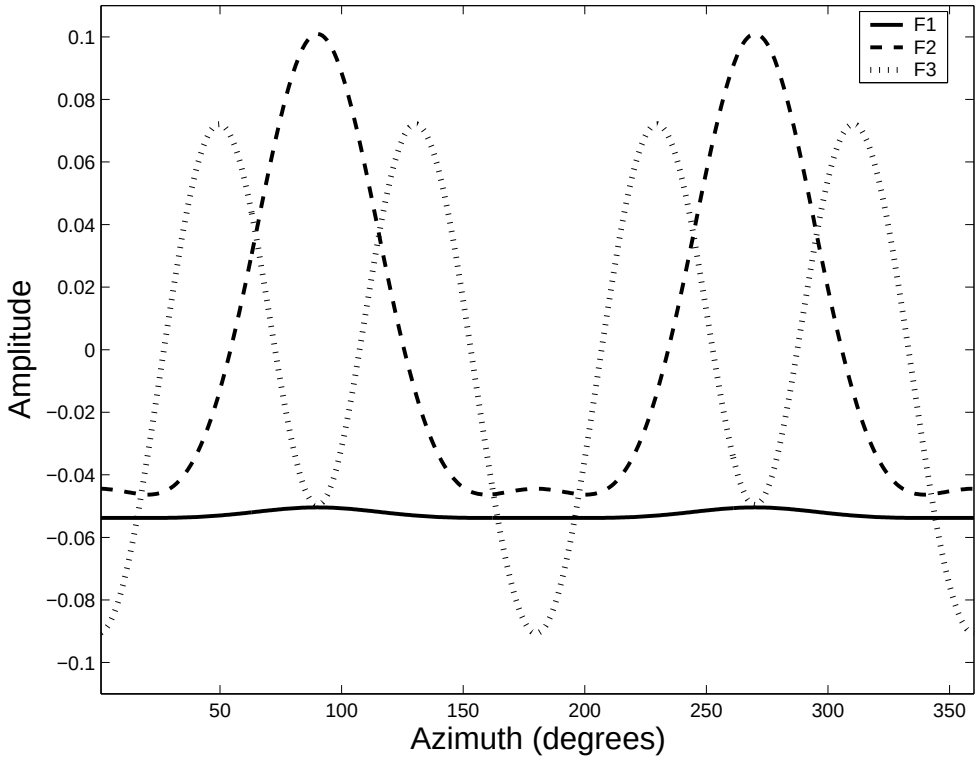

Figure 5.12: Basis functions F_1, F_2 and F_3 (from equation 5.20) for reflection coefficients as a function of azimuth corresponding to Model 1.

angles and a highly fractured rock.

5.4.3 Coefficients versus fracture density

The key to the inversion process, explained in detail in the next section, consists of finding a relationship between the weights or coefficients C_1, C_2 and C_3 in Equation 5.20, which correspond to the highest eigenvalues, and the range of modelled fracture densities. We thus create a map of the C_i's versus fracture density and angle of incidence as shown in Figure 5.14. Figure 5.14a shows C_1 increasing from negative to positive as the angles of incidence increase. Only for large angles of incidence (greater than 35 °) does C_1 vary with fracture density. The variation of C_2 with fracture density is subtle as well, though in the near angle (less than 15 °) it tends to dencrease with increasing fracture density, and in the far angle domain (greater than 37 °) it varies non-linearly with increasing

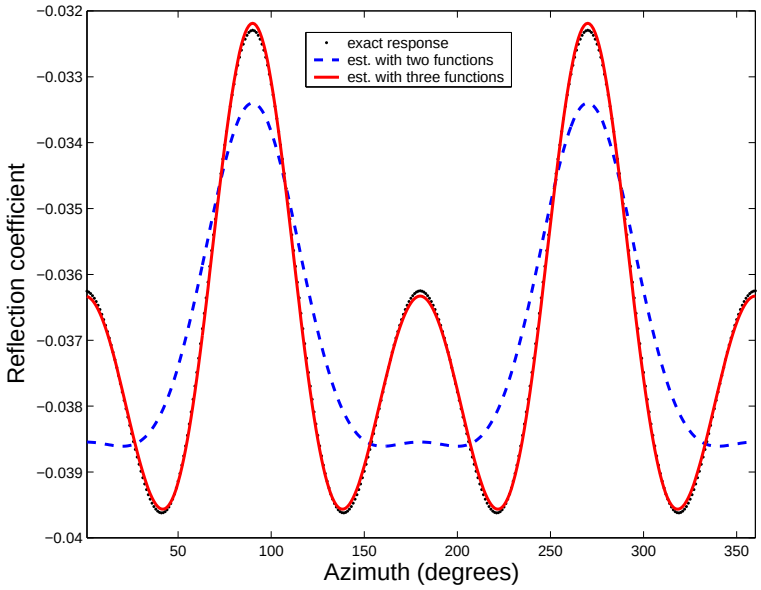

Figure 5.13: Estimation of reflection coefficient with the singular value decomposition method described in the text. The approximation (red line) with the three functions from Figure 5.12 is very close to the exact response (black dots), the approximation with only two Functions is also shown (dashed line). The reflection coefficient corresponds to Model 1 with a high fracture density of 0.095, and angle of incidence 40°.

fracture density as shown in Figure 5.14b. However, for almost all angles of incidence (except those greater than 45° and less than 10°) Figure 5.14c shows that C_3 decreases almost linearly with increasing fracture density. It is mostly from this effect, but also from the inclusion of C_1 and C_2 that the inversion process discussed below is possible.

Once again it must be noted that these relationships hold for the rock properties from Model 1. New relationships between the C_i's and the fracture density will arise when different rock properties are used. Thus at this stage an analysis is essential to determine which coefficient(s) should be used for the following inversion.

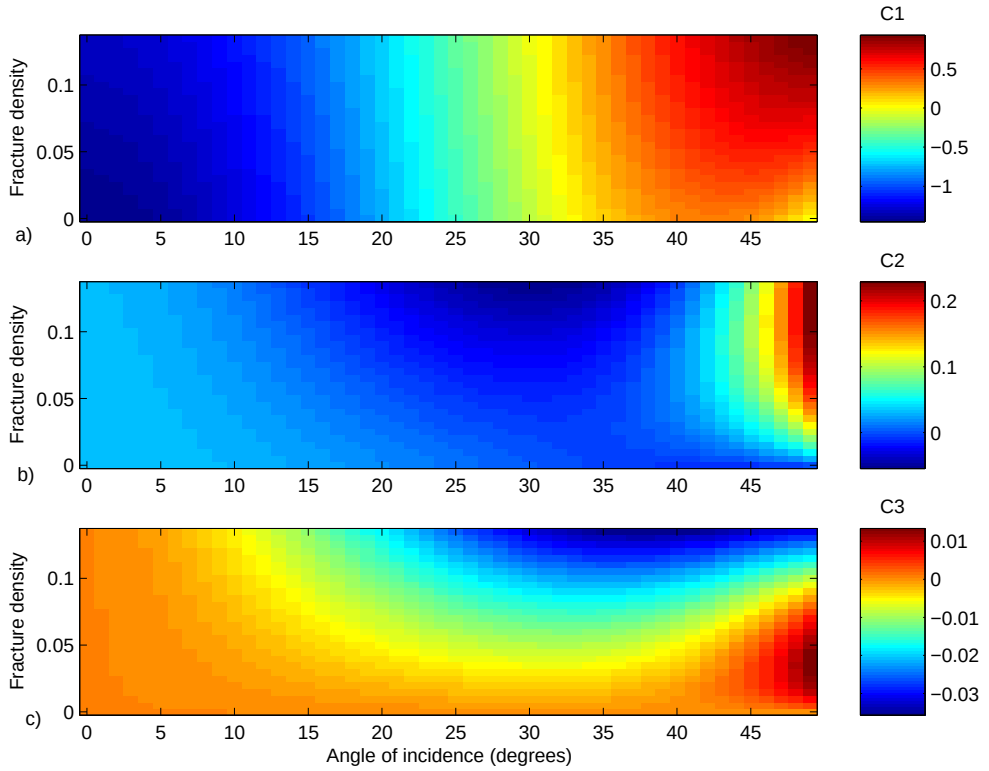

Figure 5.14: Maps of C_1, C_2 and C_3 versus angle of incidence and fracture density for Model 1.

5.4.4 Fracture properties inversion

Since, as mentioned above, we model reflection coefficients for a given interface but we measure amplitudes from the seismic data, we first scale the amplitudes to make them comparable to the reflection coefficients. For this scaling a calibration is required. For example, if the zero offset reflection coefficient is known, then the amplitudes at any offset and incidence angle can be scaled by dividing them by the seismic amplitude at zero offset and multiplying them by the reflection coefficient at zero offset. I will refer to the scaled amplitudes as the measured reflection coefficients R^m.

We take the measured AVOZ reflection coefficients $R^m(\theta, \varphi)$ and write them in terms of the three first optimal basis functions F_1, F_2 and F_3 and solve for the corresponding C_i^m coefficients as in equation 5.22 such that,

$$\begin{aligned} FC^m &= R^m \\ C^m &= (F^T F)^{-1} F^T R^m \end{aligned} \tag{5.21}$$

where F is a matrix with the first three basis functions. After obtaining C^m the measured reflection coefficient is written as,

$$R^m(\theta, \varphi) = C_1^m(\theta) F_1(\varphi) + C_2^m(\theta) F_2(\varphi) + C_3^m(\theta) F_3(\varphi) + \ldots \tag{5.22}$$

The C_i^m coefficients are then overlapped onto the maps of modelled C_i's vs. fracture density and angle of incidence (see Figure 5.14), from which the fracture density of the field data can be inverted.

Figure 5.15 shows the difference between the measured C_i^m's and the reference C_i maps of Figure 5.14 for the reflection coefficients shown in Figure 5.13. The contour lines in Figure 5.15 are drawn at every 10 % difference with the dashed line showing the lowest 10 %. The inverted fracture density is drawn from the area corresponding to the intersection of the lowest 10 % difference of the panels in Figures 5.15a, 5.15b and 5.15c. From Figure 5.15b and 5.15c it becomes clear that C_2 is constraining the angle of incidence range while C_3 constrains the fracture density range. It must be noted that although the variation of C_3 with fracture density clearly allows for the inversion process, the range of values (and magnitude) of C_3 in this example is very small, from -0.03 to 0.01 (Figure 5.14c), and will be -by construction- always smaller than the values of C_1 and C_2.

Similarly, we can map the standard deviation of the C_i's versus fracture density and angle of incidence and regard it as a relative indicator of the uncertainty of the C_i maps.

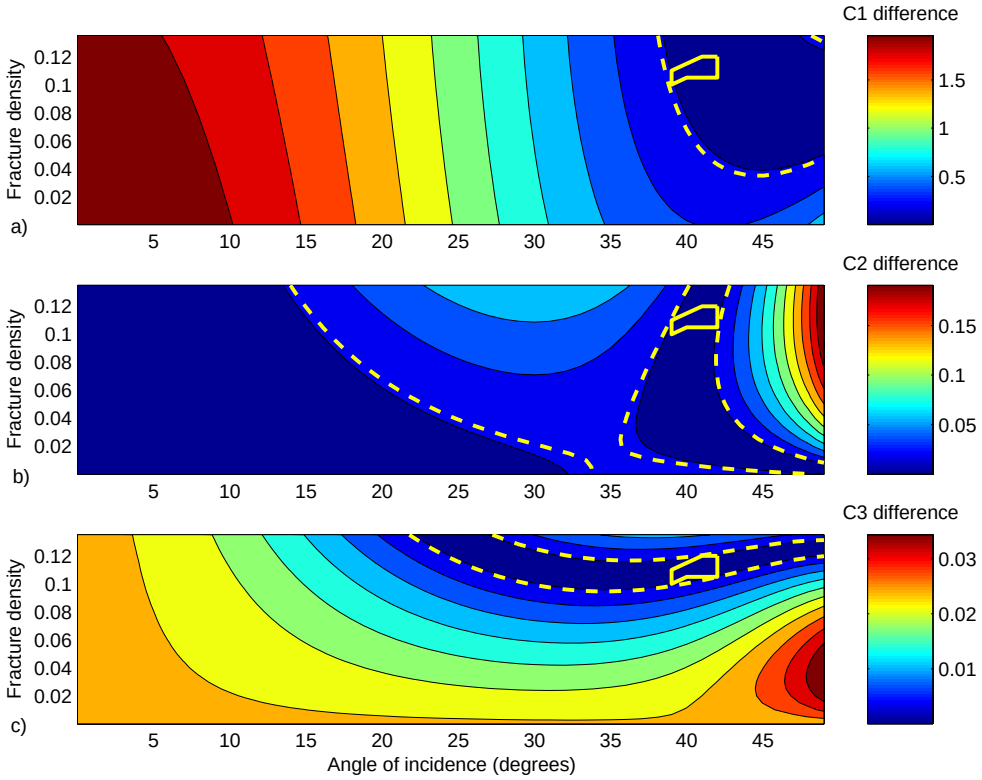

Figure 5.15: Inversion for fracture density for reflection coefficients shown in Figure 5.13. Panels a), b) and c) show the difference between the inverted C_i^m's and the reference C_i's, contour lines are drawn every 10% difference with the dashed line showing the lowest 10%. The inversion for fracture density is drawn from the area corresponding to the intersection of the lowest 10% difference in all three panels.

5.5 Synthetic seismic example

I use the rock properties from Model 1 listed in tables 5.2 and 5.3 and create two sets of synthetic gathers where the anisotropy in the lower layer is due to vertical fractures in an EW direction with low (0.04) and high (0.08) fracture densities.

I generate synthetic surface-seismic data using ANISEIS, and a circular acquisition geometry such that the CMP gathers sorted into common-offsets have 60 source-receiver azimuths spanned evenly every 6°. The offsets range from 100m to 600m, in steps of 100m, corresponding to angles of incidence from 7° to 37° accordingly.

Figure 5.16 shows the synthetic seismic data, the measured reflection coefficients fitted with the optimal basis functions, and the inverted fracture density from the difference maps between C_i^m and C_i.

In more detail, the left column of Figure 5.16 shows the common-offset and midpoint gathers with varying azimuthal angle for offsets of 300m (5.16a), 400m (5.16b) and 500m (5.16c), with the first breaks shown in red. The azimuthal variations already become evident from these gathers, but they are more clearly seen to increase with offset in the second column to the right, where the amplitudes picked from the synthetic gathers are shown (blue dots) after calibration to the reflection coefficients. The approximation of these calibrated reflection coefficients using the optimal basis functions are shown in the same column with a solid red line.

The three rightmost columns in Figure 5.16 show the C_i minus C_i^m difference maps and inverted fracture densities. The inverted values are taken from the lowest 5% difference.

The modelled fracture density for all panels in Figure 5.16 is a low value of 0.04. Inverted fracture density means and standard deviations for panels a), b) and c) are 0.035 ± 0.0086, 0.023 ± 0.006 and 0.035 ± 0.0043 respectively.

The same synthetic experiment was done with a high modelled fracture density of 0.08. These results are shown in Figure 5.17 and sumarised for both fracture densities in Table 5.5.

5.5.1 Discussion of results

From the results shown in Table 5.5 we find that the inverted fracture density matches the modelled one (within the error) for this example (except for the 400m offset and modelled fracture density of 0.04, where the inverted value is lower). Additionally, as the offsets increase the error related to the inversion process

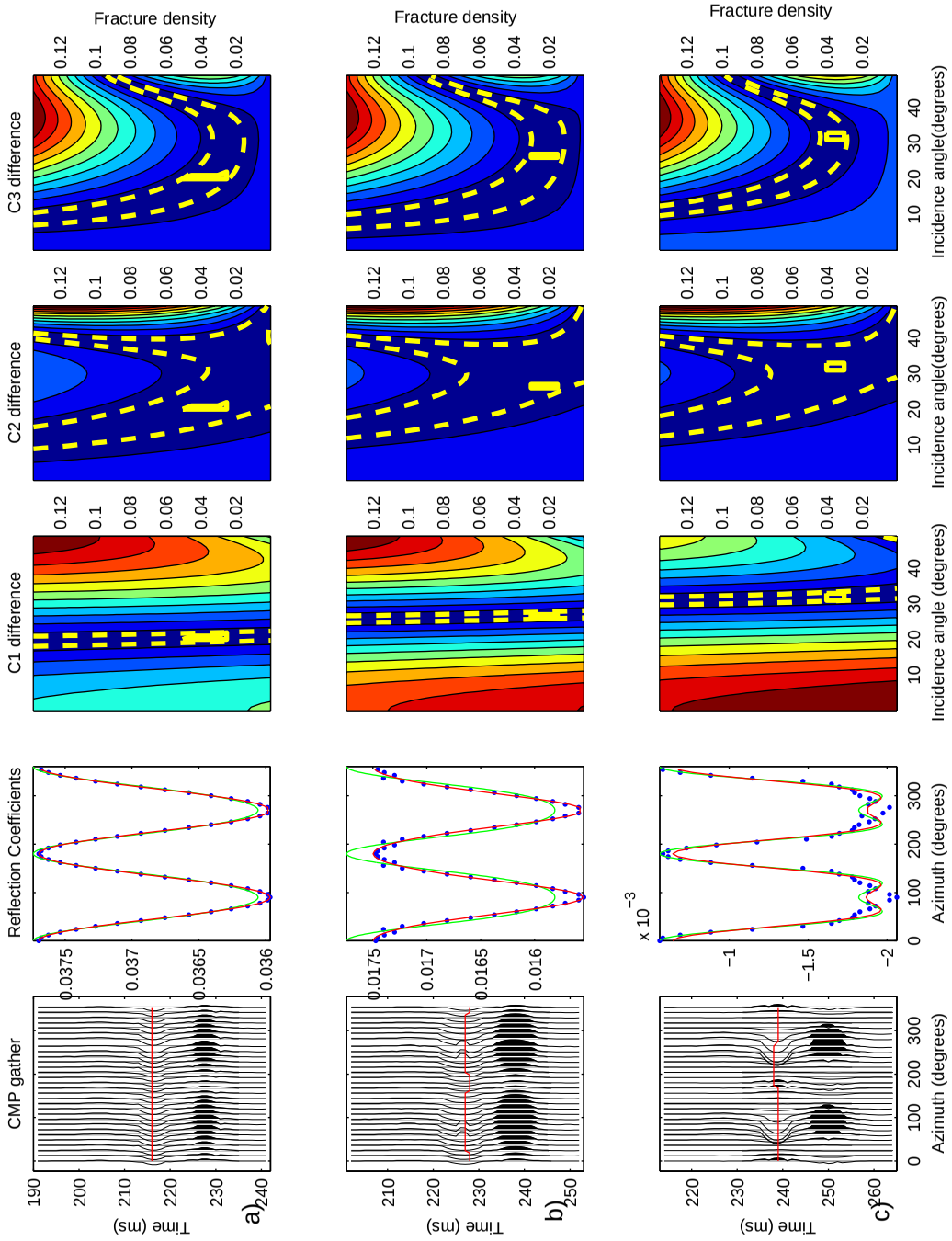

Figure 5.16: Inversion for fracture density from synthetic common-mid-point and common-offset gathers for a modelled fracture density of 0.04. Panels in rows a), b) and c) correspond to synthetic gathers with an offset of 300m (20 °), 400m (26 °) and 500m (32 °).

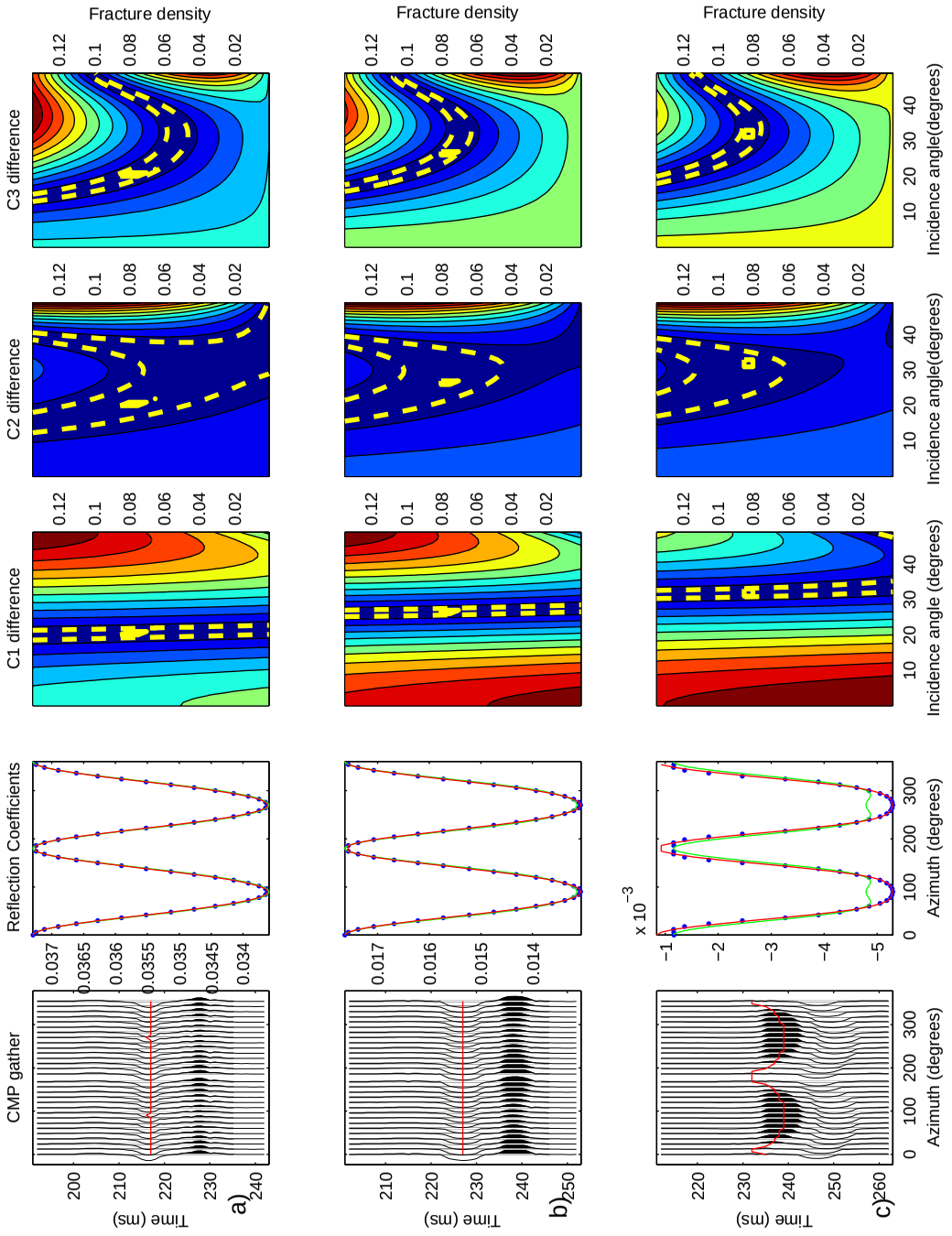

Figure 5.17: Similar to Figure 5.16 but for a modelled fracture density of 0.08. Inverted fracture density means and standard deviations for panels a), b) and c) are 0.076 ± 0.0067, 0.076 ± 0.0042 and 0.082 ± 0.0027 respectively.

becomes smaller. This is explained by the increased effect of fractures at large offsets. From Figures 5.16 and 5.17 we also find that we can invert for fracture density using just C_1 for constraining the incidence angle and C_3 for obtaining the corresponding fracture density.

Offset	Inverted Fracture Density: Mean	Inverted Fracture Density: Error	Modeled Fracture Density Mean
300 m	0.035	0.0086	0.04
400 m	0.023	0.006	0.04
500 m	0.035	0.0043	0.04
300 m	0.076	0.0067	0.08
400 m	0.076	0.0042	0.08
500 m	0.082	0.0027	0.08

Table 5.5: Inverted fracture density mean and standard deviations.

Notice from Table 5.5 that for a given offset the errors in the inversion decrease as the modelled fracture density increases, which translates into a more accurate inversion of fracture properties when the reservoir in question is highly fractured.

I performed the same study as that depicted in Figures 5.16 and 5.17 for smaller offsets/angles of incidence and found that due to the diminished effect of fracture density in the bottom layer at these angles the inversion results are only robust for angles of incidence of 20 ° or higher.

It must be noted that in this synthetic example the calibration from amplitudes picked from the synthetic gathers and their corresponding reflection coefficients is straightforward as we know the properties of the medium. However, for field data this calibration adds a degree of difficulty to the problem.

5.6 Conclusions

I show that the AVO analysis method using singular value decomposition developed by Riede et al. (2005) can be adapted for azimuthal AVO studies by a technique which involves rotating the matrix of reflection coefficients and writing the basis functions in terms of azimuth. The method of azimuthal AVO with SVD presents high accuracy in writing the field AVOZ response (in terms of the new basis functions) at large angles of incidence where the effect of fractures can become significant.

The main steps of the method for fracture density inversion from a two layer model of an isotropic medium over an HTI medium containing vertical fractures are:

a) Rock properties Use petrophyisical or well log information to set the means and standard deviations of P-wave, S-wave and density of the media on both sides of the reflecting boundary.

b) Model elastic constants Model the elastic constants of the fractured layer for different values of fracture density using a rock physics theory. Use the rock properties set in a) and a range of fracture densities.

c) Reference curves Create a family of reference AVOZ curves with varying fracture density and incidence angle using the range of elastic properties set in a). Store these AVOZ curves in matrix R such that every row has a different azimuthal angle and every column a different angle of incidence and rock properties.

d) SVD on R Calculate the singular value decomposition of matrix R, obtain the basis functions and weighting coefficients.

e) Coefficients vs fracture density Find a suitable relationship between the coefficients resulting from the SVD and the fracture density used in calculating the reference AVOZ curves.

f) AVOZ with optimal basis functions Integrate the measured reflection coefficients by fiting them to the basis functions obtained from the SVD of the reference curves. Solve in turn for the coefficients solving for the C_i^m of the measured data.

g) Invert for fracture density Map the inverted coefficients C_i^m of the measured data into the modelled coefficients C_i. Invert for fracture density from the relationship between the modelled weights C_i and the fracture density used when creating the reference curves of matrix R.

I tested the method for a two layer model of an isotropic layer over an anisotropic HTI halfspace for values of high and low fracture densities and find that for the model used there is a robust relationship between fracture density and the weights obtained from the singular value decomposition of the reference curves. Specifically, I find that for the model used the inversion is constrained by the third coefficient of the basis functions, since it captures the more subtle far offset variations where the effect of fractures is at its maximum.

Possible complications in the application of the method to field seismic data will be in the calibration process from the amplitudes picked on the gathers to the reflection coefficients. The method is presented here for a simple case of one layer over a halfspace. However for a more realistic approach, an extension to include the effect of more layers should be added.

As the inversion relies on the input modelled azimuthal AVO curves, a careful choice of the model parameters (rock properties) is essential for the inversion process. The inverted fracture density values will only be valid if the rock properties of the field data fall within the range of the modelled ones.

Future extensions of the method presented in this chapter could include inversion for different fracture properties. For example, we could model fracture compliance instead of fracture density, which is also a representative parameter of the fractured rock. Furthermore, I develop the method for P-wave data, but

studies on the application of the method to S- and PS- waves could lead to a combined inversion for properties of the fractures and their saturating fluids.

The inversion method is currently set to invert for fracture density from common offset data only. Nevertheless, in a laterally homogeneous medium, an inversion that would use data from different offsets simultaneously may lead to more stable results. Thus, it is worthwhile undertaking tests that exploit this possibility. Furthermore, due to the small value of the coefficients used for the inversion, investigations into a method for stabilising the inversion, perhaps with the use of a damping factor, are highly recommended.

As mentioned in Chapter 2, the variation of the velocity with the frequency of the measurement has been studied by various authors (Biot, 1956, Mavko and Jizba, 1991, Dvorkin et al., 1995, Endres and Knight, 1997, Chapman, 2003). Yet, it was previously thought that the steep change in velocities or dispersion curve occurred between the seismic and laboratory measurements. Thus, only in recent years has the effect of velocity dispersion been used for the characterisation of rocks (Castagna et al., 2003, Wilson et al., 2009). One of the main outcomes of Chapman's (2003) theory is that the steep change in velocity with frequency or dispersion can occur in the seismic frequency band, depending on the size of the fractures. Fracture size is a parameter more directly related to the permeability of the rock than fracture density, and is thus an important parameter in hydrocarbon exploration. The method I present in this chapter could be modified to model the reflection coefficient at different frequencies due to different fracture sizes. Consequently, it could be used to invert for fracture size from seismic data, and thus provide a measure of the permeability of the reservoir.

Chapter 6

Fracture density inversion from a physical geological model

6.1 Summary

In this chapter I adapt the method introduced in chapter 5 to invert for fracture density from a laboratory-scale earth model dataset. This approach has the advantage of knowing the physical properties and the structure of the subsurface under study, while using data acquired with techniques for field 3D surface seismic. I invert for fracture density using two different levels of uncertainty in the reflection coefficients modelled. The inversion works well for both cases for incidence angles greater than 33° and smaller than 45° (when the data reach the critical angle). A more accurate result is obtained when a smaller standard deviation is used in the distribution of velocities and densities of the modelled reflection coefficients. This shows that the method is applicable to data only when there is a tight constraint in the rock properties of the background rock media.

6.2 Introduction

Over the last two decades many studies have been published on both fracture characterization from seismic data (surface seismic and VSP), and theories that

describe the effect of fractures in wave propagation. Although in comparison very few studies have been published on fracture studies from physical earth models, in recent years the number of such studies found in the literature is increasing (Gibson et al., 2000, Fatkhan and McDonald, 2001, Blacquire and van Veldhuizen, 2003, Wandler et al., 2007, Wang et al., 2007, Alhussain et al., 2007, Evans et al., 2007). The data set used in this chapter was acquired by the CNPC Geophysical Key Lab from China University of Petroleum in Beijing.

Seismic data from a physical geological model can provide a useful link between theory and field experiments (Wandler et al., 2007). Seismic sources generally produce spherical waves, yet plane waves are a common and good approximation used in numerical modelling of seismic waves. However, at large angles of incidence, close to the critical angle this approximation can break down. And it is at large incidence angles where the azimuthal anisotropic effect, such as that caused by the presence of fractures, is observable. As Alhussain et al. (2007) remark, spherical waves must then be analysed, which can be done by either numerical full-wave form modelling or physical modelling.

On the other hand, even though in physical models it may be possible to record waves traveling at large incidence angles (and perhaps past the critical angle), such recordings may be influenced by scattering effects from the geological model. Additionally, multiples and other coherent unwanted waves (i.e. ghosts) may be recorded as well (Blacquire and van Veldhuizen, 2003).

In this chapter I apply the principles explained in chapter 5 to the laboratory-scale earth model. In section 6.3 I introduce the physical model, its layout and properties. Then in section 6.4 I inspect the seismic data acquired from the model and the amplitudes of the reflections at the top of the fractured layer and search for a suitable scaling from amplitudes to reflection coefficients.

In section 6.5 I generate two groups of realizations of the reflection coefficients at the top of the fractured layer that will form the basis for the inversion. In

section 6.6 I then find the basis functions and coefficients that best describe the measured amplitudes (scaled). Finally, in section 6.7 I invert for fracture density from both groups of modelled realizations, and in section 6.8 I draw conclusions for the inversion application.

6.3 The laboratory-scale earth model

The seismic data used in this chapter were acquired from a laboratory-scale earth model. This physical earth model consists of several horizontal approximately isotropic layers made of an Epoxylite material with a fractured layer in between them. The model was acquired at a scale of 1:10000[1], with the frequencies also scaled up by 10000:1. From here onwards I will refer only to the scaled up dimensions of the model.

6.3.1 Physical properties

Figure 6.1 shows the layout and geometry of the model (in the XZ plane) with the numbers on the right referring to the interfaces. The whole model is submerged in a water tank, under a 10 meter thick water layer in which the source is fired. From top to bottom there are four layers, three of which are isotropic, composed of an Epoxylite material. The second and fourth isotropic layers have the same physical properties. The P- and S-wave velocities, density and thickness of each layer are listed in Table 6.1. In this chapter I will analyse the reflection from interface 2 between the isotropic layer 2 and the underlying fractured anisotropic layer 3.

The material of the anisotropic layer is a set of epoxy bonded fibre sheets that simulate vertical fractures with high azimuthal P-wave and S-wave anisotropy of 20%, and a fracture density of 0.2, as reported by Wang et al. (2007). It is worth

[1]1mm of the physical model is 10m

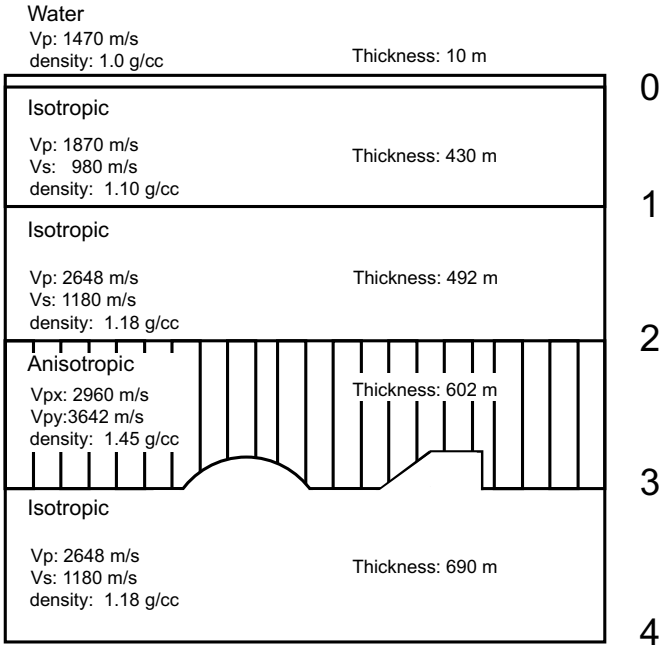

Figure 6.1: Diagram of physical model (Figure modified from Wang et al., 2007). The data set was acquired with two structural features at the bottom of the fractured layer. The numbering on the right hand side corresponds to the interface.

Layer	Vp (m/s)	Vs (m/s)	ρ (g/cm^3)	Thickness (m)
0) Water	1470	-	1	10
1) Isotropic	1870	980	1.10	430
2) Isotropic	2648	1180	1.18	492
3) Anisotropic	Vpx=2960 Vpy=3642	Vs1=2010 Vs2=1490	1.45	602
4) Isotropic	2648	1180	1.18	690

Table 6.1: Rock properties of the physical modelling data set for Figure 6.1.

clarifying that although I will refer to the anisotropic layer as the fractured layer, no actual fractures are present in the model. The fracture density of the model is thus a proxy for the anisotropy of the effective medium. Other physical model experiments, such as that by Rathore et al. (1994), have created synthetic sandstones with controlled fracture sizes and orientations where the fracture density parameter is well defined.

The elastic constants of the anisotropic layer, from the data in Figure 6.1, were measured by Wang et al. (2007) using the experimental method from Cheadle et al. (1991). Cheadle et al. (1991) use the Kelvin-Christoffel equations (which yield phase velocities provided a set of stiffness values of the material) to derive the elastic constants (or stiffness values) of a material with orthorhombic symmetry, given a set of measured group velocities in different directions and the density of the material. Through this method, Wang et al. (2007) find that the anisotropic layer with vertical bonded fibre sheets, exhibits a weak orthorhombic symmetry with elastic constants given by,

$$C_{ij}^{ORT} = \begin{pmatrix} 12.7040 & 7.8650 & 8.1990 & 0 & 0 & 0 \\ 7.8650 & 19.2330 & 9.3200 & 0 & 0 & 0 \\ 8.1990 & 9.3200 & 22.1620 & 0 & 0 & 0 \\ 0 & 0 & 0 & 5.8580 & 0 & 0 \\ 0 & 0 & 0 & 0 & 3.2990 & 0 \\ 0 & 0 & 0 & 0 & 0 & 3.2190 \end{pmatrix} \tag{6.1}$$

It is believed that in the construction process of the model the effect of gravity caused the symmetry of the fractured layer to be weakly orthorhombic, instead of HTI. Wang et al. (2007) do not report measuring the symmetry of the isotropic layers. It is believed that the gravity effect caused the isotropic layers to present a weakly VTI symmetry. However in this chapter, I will use the isotropic properties for the isotropic layers reported by Wang et al. (2007).

The corresponding anisotropic parameters ϵ and γ of the fractured layer are given in Table 6.2. In the following sections I show how the weak orthorhombic elastic constants from equation 6.1 can be approximated by an HTI medium.

Furthermore, there are two geometrical features at the bottom of the fractured layer: a dome and a geometrical feature with sharp edges. Wang et al. (2007) discuss their effect on the acquired seismic data. As I will focus on the reflection at the top of the fractured layer, they will not be discussed in this chapter.

ϵ	γ
0.372	0.410

Table 6.2: Anisotropic parameters ϵ and γ and density of the fractured layer from Figure 6.1. ϵ and γ are given by $\epsilon = (c_{33} - c_{11})/(2c_{11})$ and $\gamma = (c_{44} - c_{66})/(2c_{66})$

6.3.2 Acquisition, extraction and sorting

As mentioned above, the 3D seismic data were acquired in a water tank by the CNPC Geophysical Key Lab, at the China University of Petroleum in Beijing. The receiver and shot lines are set parallel (Y-direction) and perpendicular (X-direction) to the fracture strike respectively. As described by Wang et al. (2007), four shots are located in the center of the spread and fired, subsequently the spread is moved to a different location. The shot line and receiver line intervals are 240m, and the shot and receiver intervals are 40m, as shown in Figure 6.2a.

I will only work with a portion of the entire 3D seismic data set; a supergather with common midpoints (CMP's) at the center of the model. I use only this supergather to maximise the offset and azimuthal[2] spread of the data used, as any CMP gathers with common mid points at the edges of the survey will have a poorer or less even azimuthal and offset coverage. Figure 6.2a shows all the CMP's used (marked by black dots). Furthermore, Figure 6.2a shows the source and receivers used for the illumination of one of the CMP's of the supergather. Figure 6.2b shows the offset azimuthal spread for the supergather and for the CMP highlighted in Figure 6.2a.

When I stack the supergather it is equivalent to moving the source and receiver locations such that they illuminate only one point in the subsurface. I model the raypaths for this fictional CMP in the subsurface by calculating the ray trajectory assuming straight rays and maintaining the original offset and azimuth. This is

[2]The azimuths for Figure 6.2b and throughout this chapter are measured as $\arctan(\frac{gy-sy}{gx-sx})$, where (gx,gy), and (sx,sy) are the coordinates of the geophones and source locations respectively.

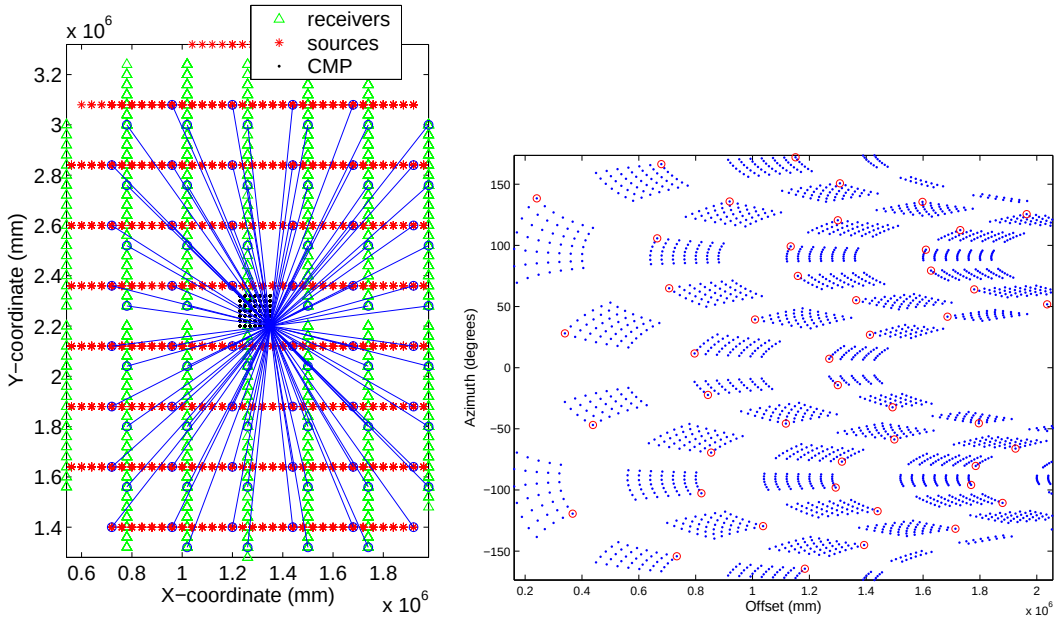

(a) Supergather used

(b) Azimuth vs. offset

Figure 6.2: Acquisition geometry of source and receiver locations. a)The black dots show the CMP's of the supergather used, the blue lines connect the source and receivers for one CMP of the supergather. b) Azimuth versus offset for the supergather used. The red circles correspond to the CMP bin selected in a).

shown in Figure 6.3a, which simulates a more thorough distribution of source and receiver locations.

I sort the data into common offset gathers grouping them every 50m. The range of offsets for the supergather vary from 161m to 2008m, so after grouping them there are 37 common offset gathers from 160m every 50m to 1960m. From here onward I will refer to the grouped common-offset gathers only. The source and receivers that are live for three different offset gathers (160m, 1360m and 1760m) are shown in Figure 6.4.

A handicap of the acquisition setup for the AVOZ analysis is that for the extremes of short and large offsets (greater than 1360m) there is a significant gap in source-receiver locations at azimuths 0^o and 180^o (X-direction perpendicular to the fracture plane). This is clearly shown in figures 6.3b and 6.4a and 6.4c.

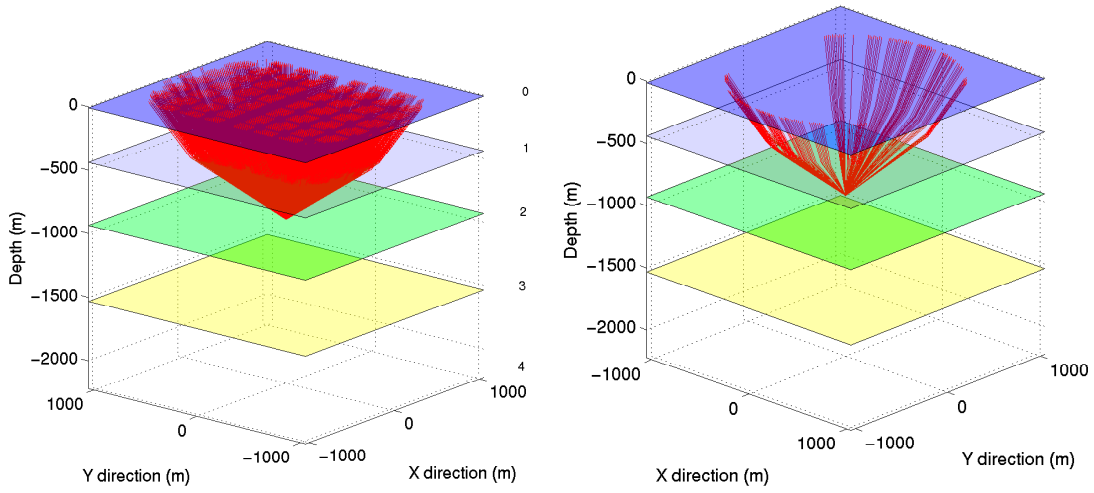

(a) All source-receiver pairs (b) Common offset 1760m

Figure 6.3: Ray traces for reflections at the top of the fractured layer. The super-gather is shown as imaging a single depth point. a) For all source-receiver pairs (2185 traces in total), b) Rays at a common offset of 1760 with 104 traces. The numbers to the right of a) correspond to the interfaces shown in Figure 6.1.

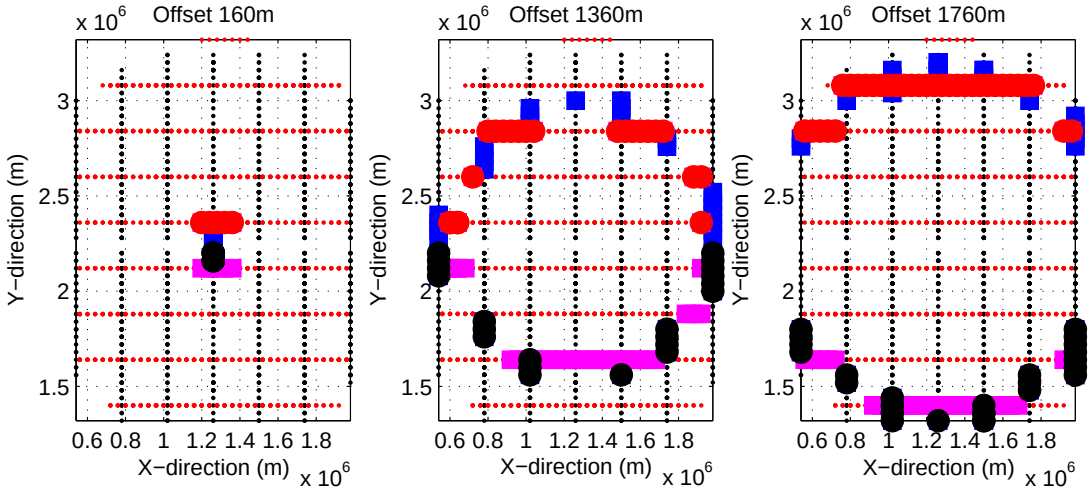

Figure 6.4: Source and receivers locations sorted by common offset every 50m. The highlighted red sources are recorded by the black geophones and correspond to negative azimuths. The positive azimuths are fired from the magenta sources and recorded by the blue geophones.

For a more detailed description of the acquisition process and parameters of this data set see Wang et al. (2007).

6.3.3 Seismic data inspection: reflection top of fractured layer

Amplitudes

In this chapter I will focus on the application of the method to the reflection at the top of the fractured layer (labeled as interface 2 in Figure 6.1) using the P-wave vertical component. Selected common offset gathers around this interface are shown in Figure 6.5. Figure 6.5 also shows the event picked and the amplitudes versus azimuth for each gather. This Figure exhibits three aspects of particular interest:

- At short offsets (<= 610m) there is a significant difference in amplitudes between positive and negative azimuths.
- As offsets increase the azimuthal variations in both the positive and negative azimuthal ranges become stronger.
- There is a gap in the acquisition of data around azimuth 0^o.

As I am interested in the azimuthal variations caused by the anisotropy in the fractured layer, I also show the common-azimuth gathers for all available offsets surrounding the orientations perpendicular (azimuth=0^o) and parallel (azimuth=90^o) to the fracture plane as these are expected to present the maximum variations. These gathers are shown in figures 6.6 and 6.7 respectively.

In general the event is shown in the seismic traces as a negative trough with the magnitude of the amplitude decreasing as the offsets get larger. The uneven coverage in different directions makes the comparison between figures 6.6 and

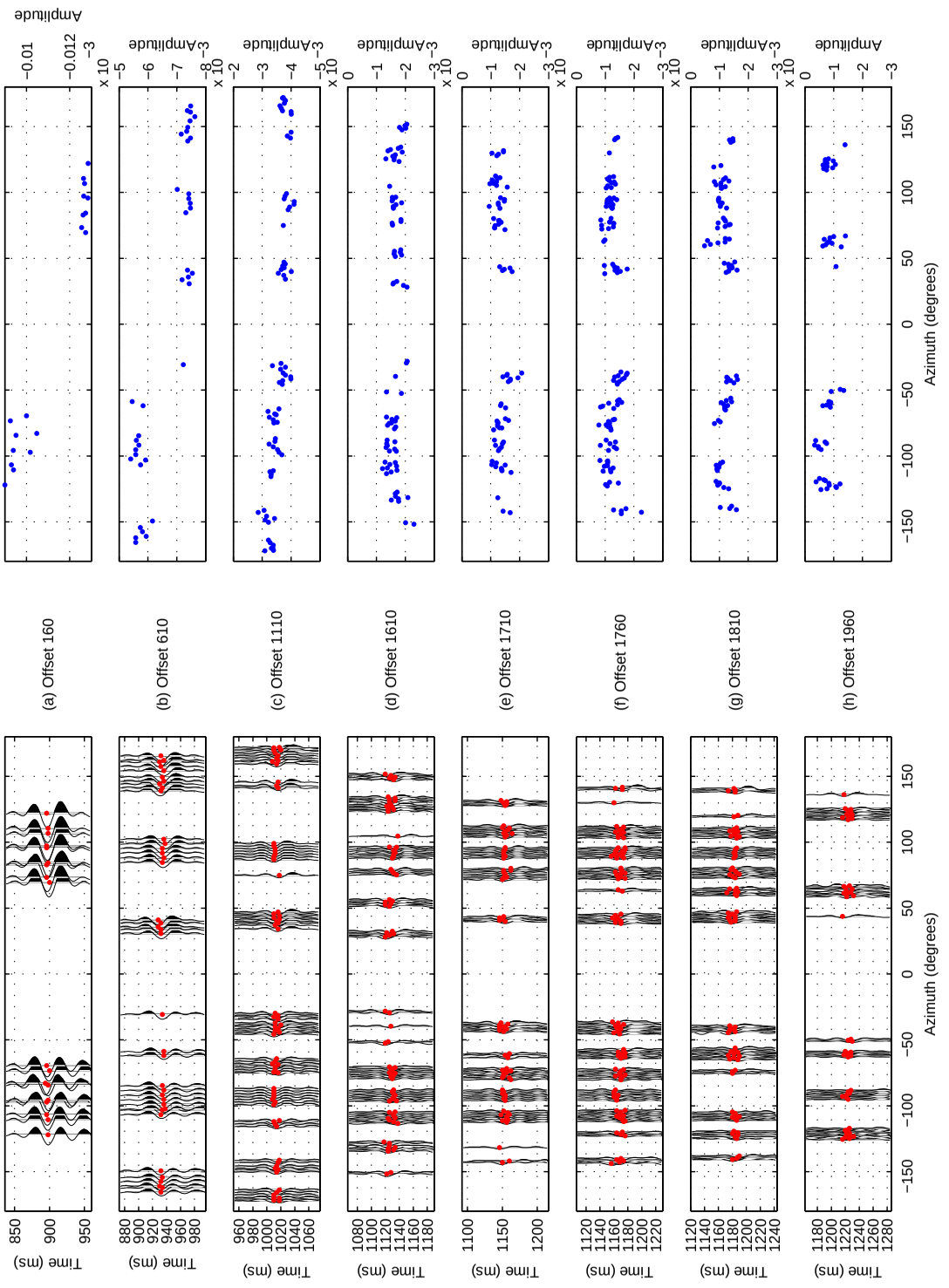

Figure 6.5: Gathers around reflection at top of the fracture layer (left) and respective amplitudes versus azimuth for selected offsets (right). The amplitude axis on the right has a spread of 0.004 for (a); for subplots (b) to (h) the spread is 0.003. The picked event is indicated by the red dots.

6.7 difficult. The amplitudes picked from these gathers are shown in Figure 6.8c where they can be compared at the same scale. The anomalous spread in amplitudes at short offsets is again noticeable. Furthermore, I compare the picked amplitudes for all azimuths in Figure 6.8b, where it is clear that there is an anomalous behaviour in the amplitudes at short offsets for all azimuths.

Travel time

The travel time to the top of the fractured layer is robust compared to the amplitudes, and does not show any change with azimuth. This can be seen from figures 6.8a where the travel time versus offset is displayed for all azimuths. This can be seen in more detail in Figure 6.9c and d where a map is created with the common-mid point in the center of the map and the values of the travel time are displayed (in colorscale) at the offset and azimuth between the source and receivers. Compared to Figure 6.9a and b which shows the same display for amplitudes, the travel time attribute is more consistent.

6.3.4 Scaling amplitudes to reflection coefficients

Acquisition footprint

To try to understand the anomalous behaviour at short offsets I examine the amplitudes according to the corresponding source and receiver coordinates, as in Figure 6.10, where it is clearly seen that different sources have led to the two distinct trends. This is also obvious from Figure 6.4 where for positive azimuths the sources are located in the lower half of the grid and for negative azimuths in the upper half.

We expect from the theory that at short offsets (in any direction) there should not be any significant changes in the amplitude. Additionally, we know that the two different trends are the result of different sources. Based on this I argue that

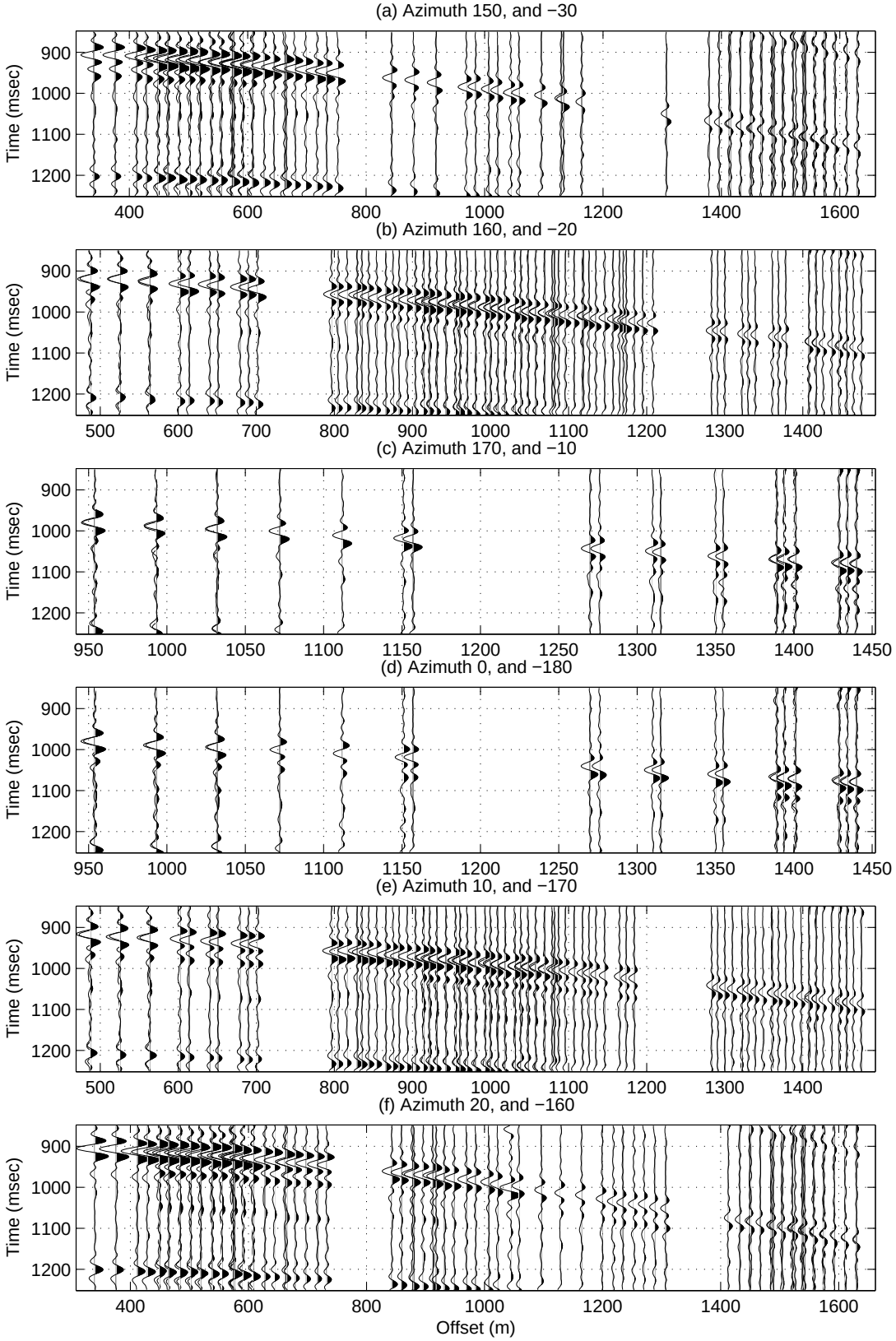

Figure 6.6: Gathers around reflection at the top of the fracture layer for fixed azimuths close to 0^o.

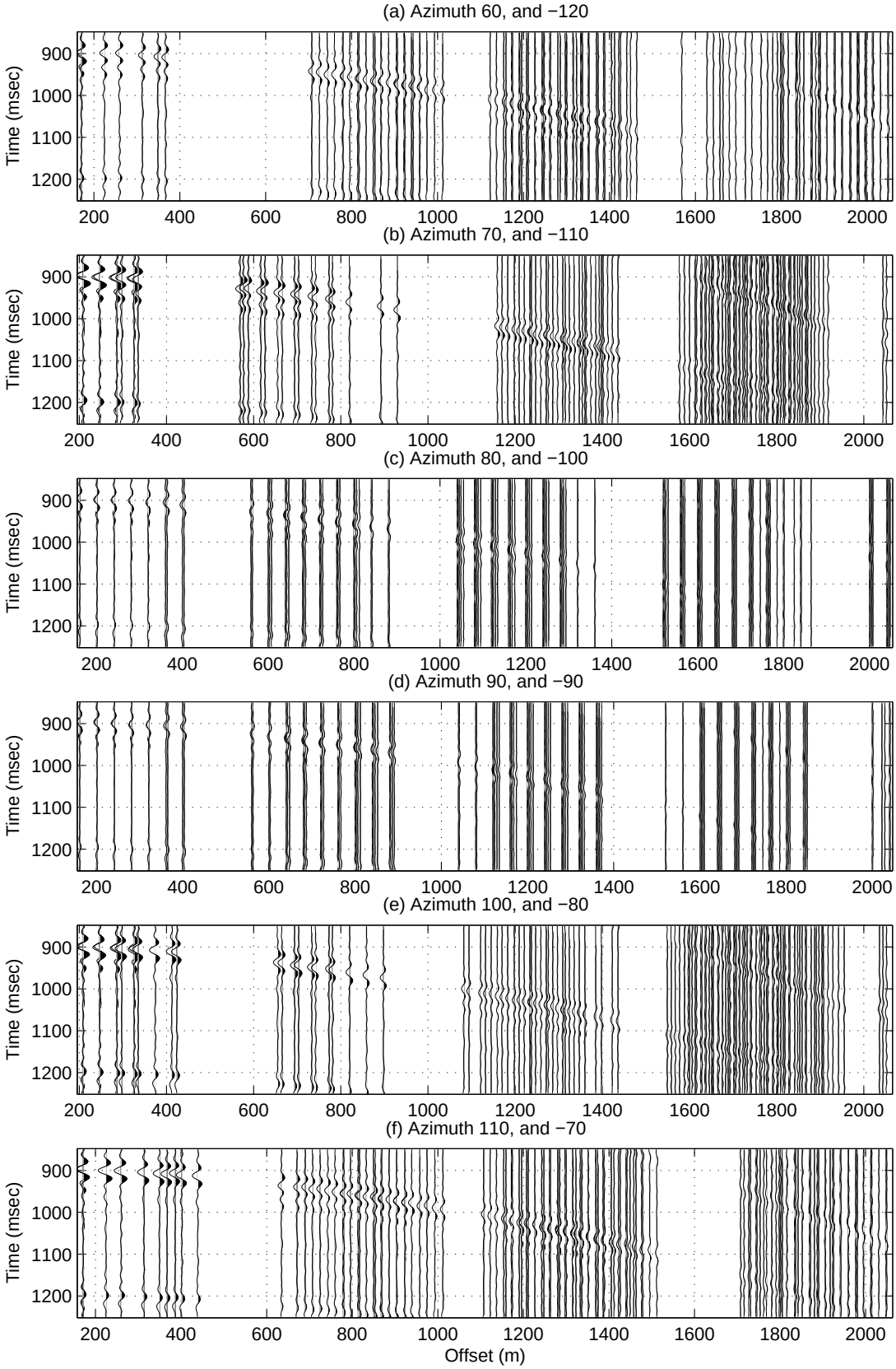

Figure 6.7: Gathers around reflection at the top of the fracture layer for fixed azimuths close to 90^o.

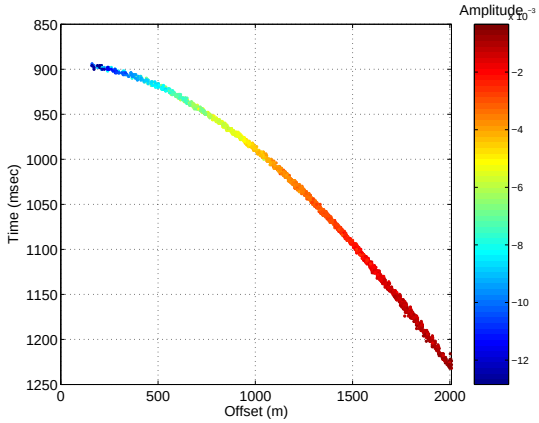

(a) Travel time versus offset and amplitude

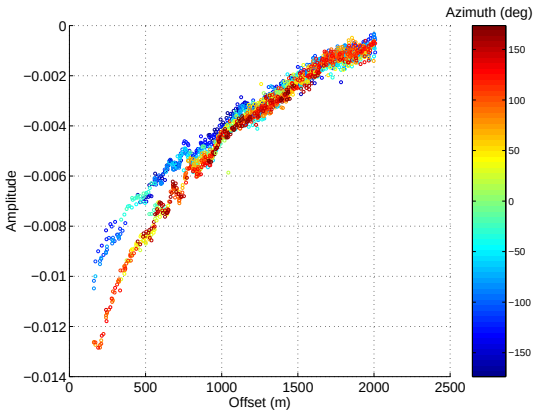

(b) Amplitude versus offset and azimuth

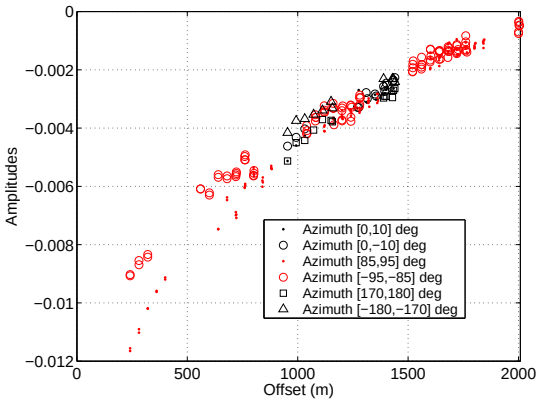

(c) Same as (b) for selected azimuths

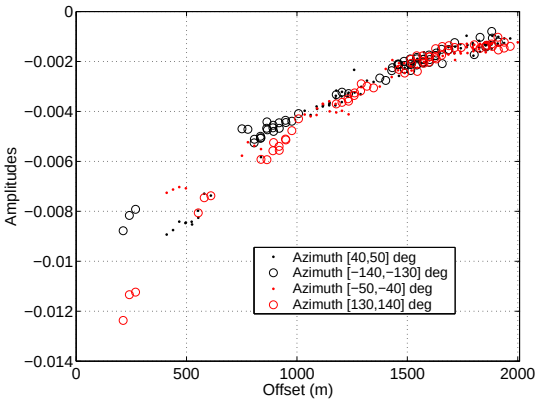

(d) Same as (b) for selected azimuths

Figure 6.8: a)Travel time versus offset and amplitude, b) Amplitudes versus offset and azimuth for the top of the fractured layer, c) data for selected azimuths close to 0^o and 90^o, d) data for selected azimuths close to 45^o and 135^o

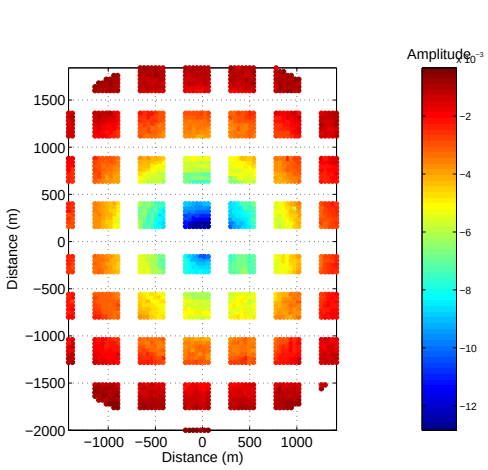

(a) Amplitude vs. offset and azimuth scattered.

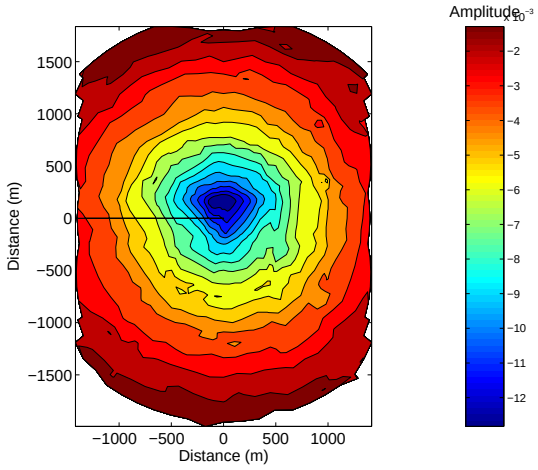

(b) Amplitude vs. offset and azimuth interpolated.

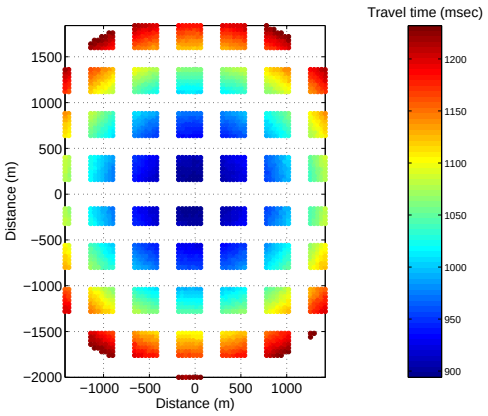

(c) Travel time vs. offset and azimuth scattered.

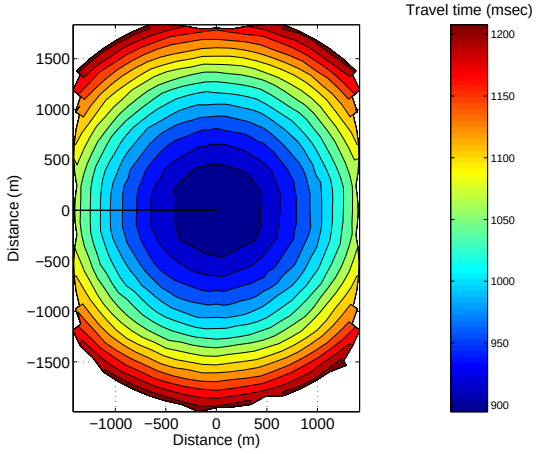

(d) Travel time vs. offset and azimuth interpolated.

Figure 6.9: Amplitude and travel time versus offset and azimuth for the top of the fractured layer. a) and b) show amplitudes scattered and interpolated respectively. Similarly, c) and d) show travel time for scattered and interpolated data.

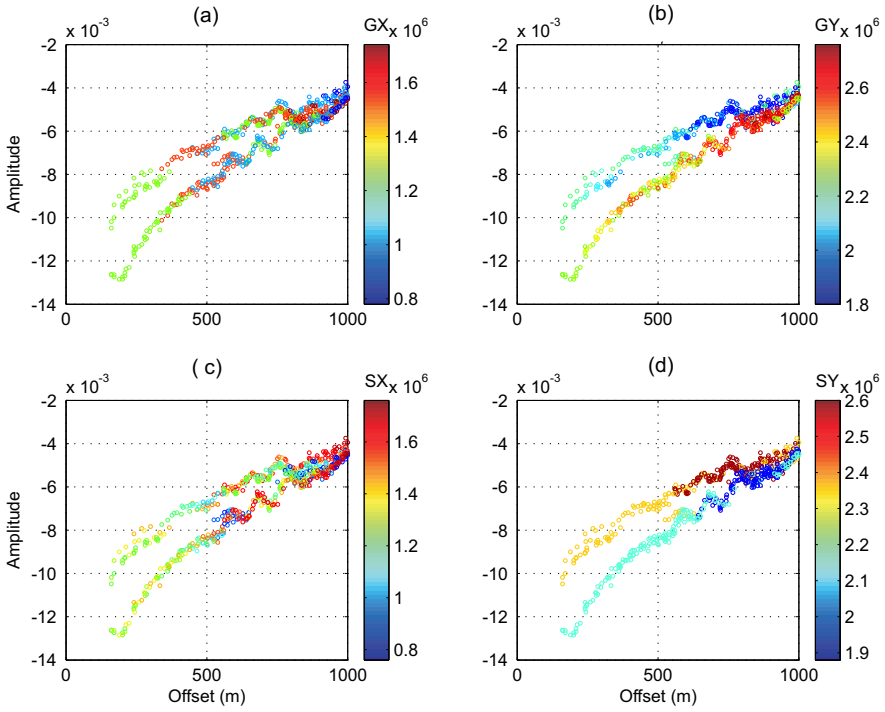

Figure 6.10: Amplitudes versus offset color coded by source and receiver locations. a) Geophone x-coordinate, b) Geophone y-coordinate, c) Source x-coordinate, d) source y-coordinate

the two trends are an artefact of the acquisition, and not a true response of the model.

Scaling by shot-point

The method to be applied in this chapter deals with reflection coefficients (as explained in chapter 3), however in the seismic data, as well as the data used in this chapter, we measure the amplitudes of the seismic wave, not the reflection coefficient. I thus convert the amplitudes to reflection coefficients by multiplying them by a scaling factor. From the above discussion on the acquisition footprint from different sources, I choose a scaling factor that will vary with the source being fired.

Assuming lateral homogeneity I find the multiplicative scaling factor per shot point by calculating the modelled reflection coefficient per shot point and using it as reference, such that,

$$\begin{aligned} AS &= R \\ S &= (A^T A)^{-1} A^T R \end{aligned} \tag{6.2}$$

where A is the amplitude measured, R the modelled reflection coefficients[3] from the earth model and S the scaling factor. The resulting scaling factor S per shot point is displayed in Figure 6.11 where we see the variations by shot number, offset, azimuth and measured amplitude. Furthermore, Figure 6.12 shows the scaling factor by source and geophone locations.

The final amplitudes scaled to reflection coefficients are shown in Figure 6.13 where the black circles are the modelled reflection coefficients and the red dots are the amplitudes scaled. In this graph the data for all azimuths are shown. For reasons of simplicity I will refer from here onwards to the scaled amplitudes

[3]the reflection coefficients are calculated using the elastic constants for the fractured layer and velocities and densities for layers 1 and 2 given in section 6.3

as the *measured* reflection coefficients. And it is from these measured reflection coefficients that I will proceed to invert for fracture density.

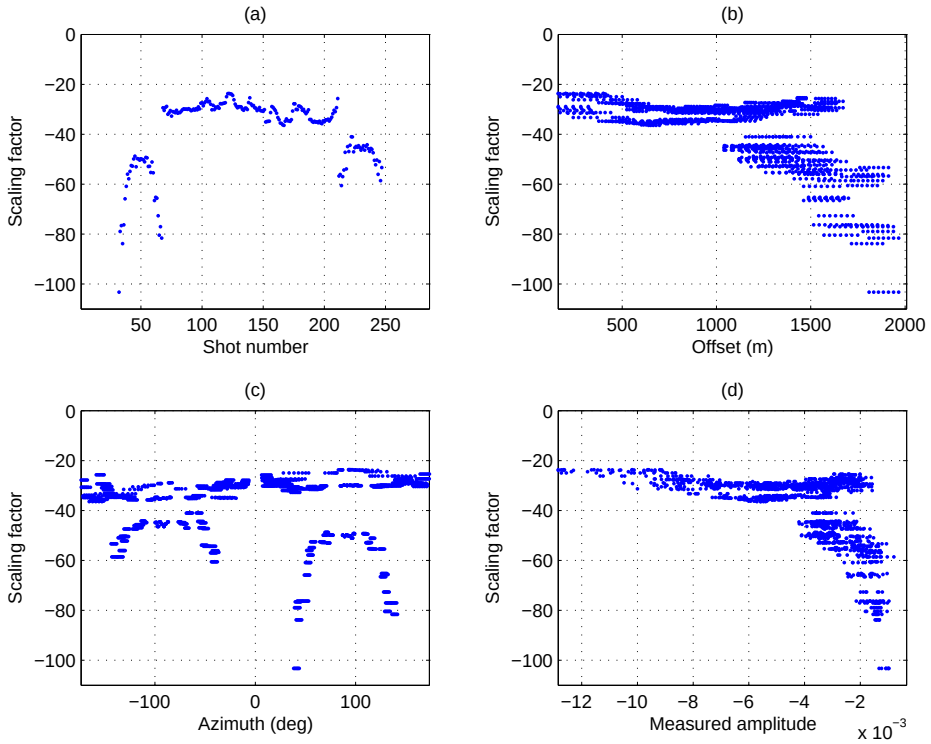

Figure 6.11: Scaling factor by shot point versus offset, azimuth and measured amplitudes.

6.4 Building rock models

6.4.1 HTI approximation

In this chapter I use Chapman's (2003) poroelastic theory to calculate the elastic constants of the fractured layer with different fracture densities. This theory will calculate the elastic constants of an HTI or VTI medium for a given fracture density given a series of other parameters. However, the fracture medium of our laboratory scale earth model presents an orthorhombic symmetry instead of an HTI one. Given that the anisotropy in the medium is due to vertical fractures, and that it is only weakly orthorhombic, I propose to use an HTI approxima-

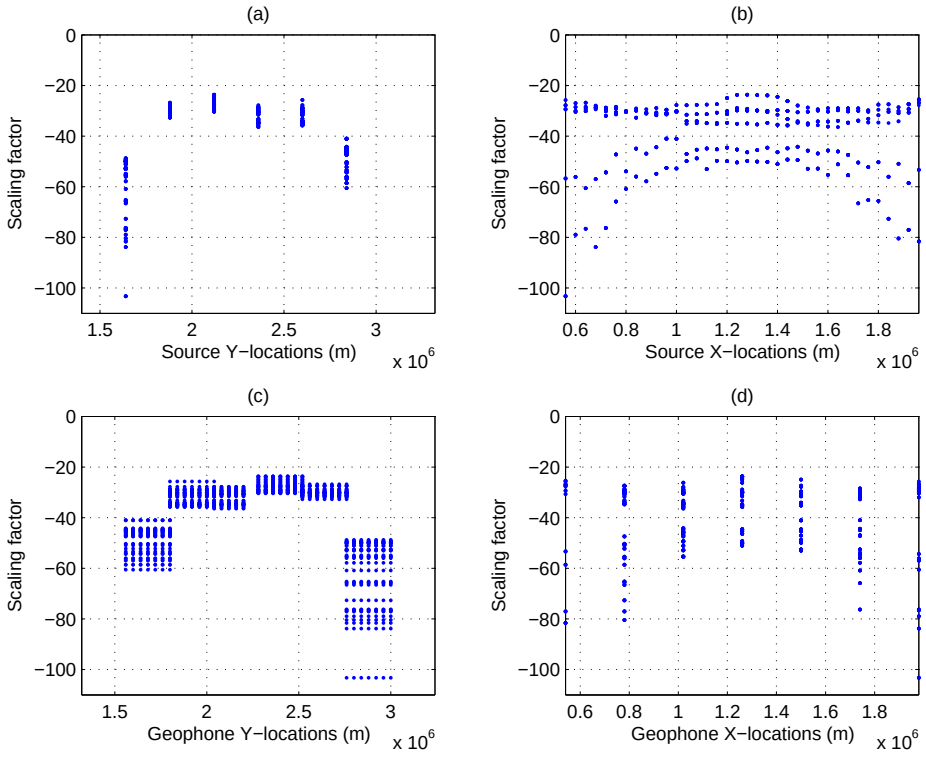

Figure 6.12: Scaling factor by shot point versus source and receiver locations.

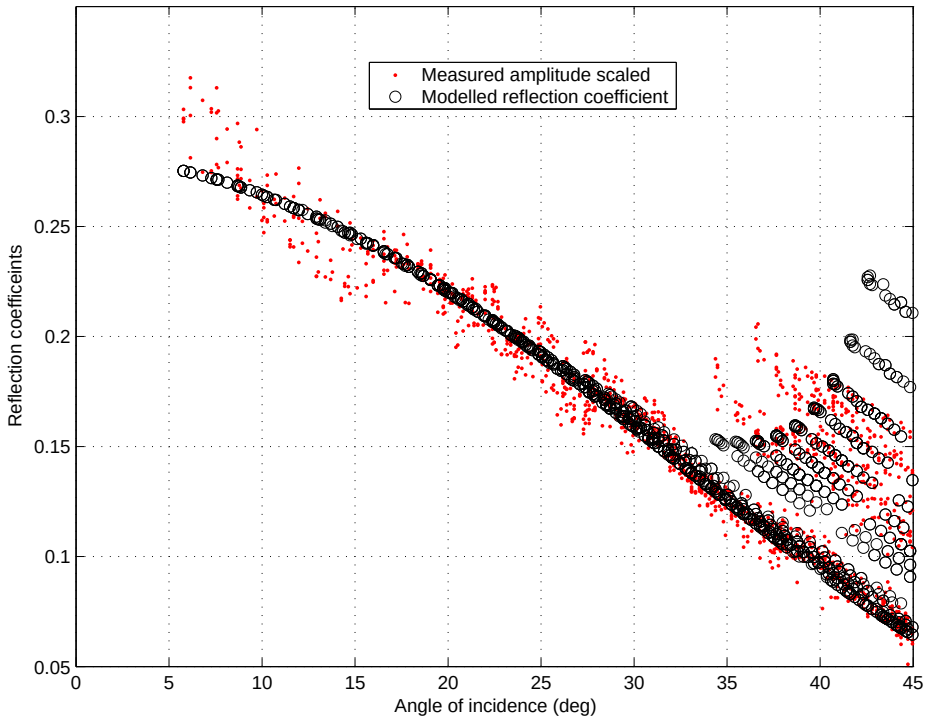

Figure 6.13: Scaled amplitudes to reflection coefficients by shot point for reflections at the top of the fractured layer. All the azimuths are displayed.

tion instead of the orthorhombic elastic constants, so they can be modeled with different fracture densities. I thus try to find the best approximation to the orthorhombic elastic constants using an HTI symmetry.

For this purpose, I set a start point and search range for the physical properties required by the Chapman theory (in the range of those given) that would best approximate the orthorhombic fracture layer using an HTI symmetry and the fracture density of the physical model (which is 0.2). Table 6.3 lists the property, mean search value, search variation, the best estimate found, and the related value given by Wang et al. (2007).

Property name	Mean search value	Search variation	Best estimate	Given by geological model
Vp (m/s)	3600	$\pm$ 800	4139.4	Vpx=2960 Vpy=3642
Vs (m/s)	2010	$\pm$ 720	2058.0	$Vs1$=2010 $Vs2$=1490
ρ (g/cc)	1.45	$\pm$ 0.05	1.447	1.45
Porosity	0.075	$\pm$ 0.04	0.0687	-
af	1.00	$\pm$ 0.2	1.1777	-
cd	0.0	+ 0.02	0.0091	-
ar	0.0001	$\pm$ 0.00005	0.000086	-

Table 6.3: Rock properties and the search parameters used for generating an HTI approximation of the orthorhombic elastic constants of the fractured layer. Note that the Vp, Vs and density searched for are those of the unfractured material. af is the fracture length in meters, cd is the microcrack density, and ar is the crack and fracture aspect ratio. The other fixed parameters from the Chapman model are the time constant parameter $\tau = 8 \times 10^{-6}$s and the fluid modulus $K_f = 25$MPa.

The values in the best-estimate column of Table 6.3 were reached after 10^6 iterations for random values within the search parameters (columns 2 and

3 of Table 6.3) that would minimize the root mean square error between the original orthorhombic and the estimated HTI elastic constants, $error = \frac{1}{12}\sum_{i,j}\sqrt{(C_{ij}^{ortho} - C_{ij}^{HTI})^2}$. The root mean square error[4] reached is 10.3515.

With the properties listed in the fourth column of Table 6.3 I calculate the elastic constants with HTI symmetry, using Chapman's (2003) theory, that would best fit the orthorhombic elastic constants of the fractured layer given by equation 6.1. These modelled HTI elastic constants are,

$$C_{ij}^{HTI} = \begin{pmatrix} 12.71 & 6.45 & 6.45 & 0 & 0 & 0 \\ 6.45 & 21.73 & 9.47 & 0 & 0 & 0 \\ 6.45 & 9.47 & 21.73 & 0 & 0 & 0 \\ 0 & 0 & 0 & 6.13 & 0 & 0 \\ 0 & 0 & 0 & 0 & 3.52 & 0 \\ 0 & 0 & 0 & 0 & 0 & 3.52 \end{pmatrix} \tag{6.3}$$

I evaluate how well the HTI approximation (equation 6.3) matches the orthorhombic elastic constants (equation 6.1) by comparing the slowness surfaces for the P, S1 and S2 waves. The slowness surfaces are computed by solving for the eigenvalues and eigenvectors of the Christoffel equation (Tsvankin, 2001),

$$\begin{aligned} [G_{ik} - \rho V^2 \delta_{ik}]U_k &= 0 \\ det[G_{ik} - \rho V^2 \delta_{ik}] \end{aligned} \tag{6.4}$$

where G_{ik} is the Christoffel matrix that depends on the stiffness tensor and the direction of propagation $G_{ik} = c_{ijkl} n j n_l$. U_k is the polarization vector, δ_{ik} is the Kroenecker delta and ρ and V are density and velocity. The solution to the Christoffel equation in terms of G_{ik} for any anisotropic medium is given by Tsvankin (2001, page 56). For any given direction n in anisotropic medium the equation yields three values for the velocity V corresponding to the P-wave, S1 and S2 waves.

[4]The division by 12 in the RMS error refers to the number of non-zero elements in the C_{ij} tensor for HTI and orthorhombic symmetries.

Figure 6.14 a, d and g shows the slowness surfaces for the P-wave in the XY, XZ and YZ planes respectively. I find that the slowness surfaces are sufficiently similar in the three planes for the P-wave, which is the wave type that I will deal with throughout this chapter. Of the three different wave types, the P-wave in the HTI medium is the one closest to its equivalent in the orthorhombic medium, when compared to the S1 or S2 waves (see Figure 6.14 b, c, e, f, h and g).

Additionally, I evaluate the HTI approximation by comparing the reflection coefficients in directions perpendicular and parallel to the fracture plane, as shown in Figure 6.15, and find that they are comparable enough in shape and magnitude for the HTI approximation to be used with the chosen parameters.

6.4.2 Model groups A and B

Rock properties distribution

I will create two model groups for evaluations of the reflection coefficient. For each group I will only vary three parameters in each layer: P-wave velocity, S-wave velocity and density. I assign a normal distribution to each of these rock properties with the means and standard deviations listed in Table 6.4. The two groups of models will be called groups A and B.

		$Vp \pm std\ (m/s)$	$Vs \pm std\ (m/s)$	Density $\pm std\ (gr/cc)$
Group A	Top layer	2737.3 ± 50	1002.8 ± 50	1.15 ± 0.05
	Fractured layer	4139.4 ± 50	2058 ± 50	1.447 ± 0.05
Group B	Top layer	2737.3 ± 10	1002.8 ± 10	1.15 ± 0.01
	Fractured layer	4139.4 ± 10	2058 ± 10	1.447 ± 0.01

Table 6.4: Mean and standard deviations for distribution of rock properties used to create model groups A and B.

Both groups present the same mean for all the rock properties and only the standard deviation will vary, with A having larger standard deviations and B

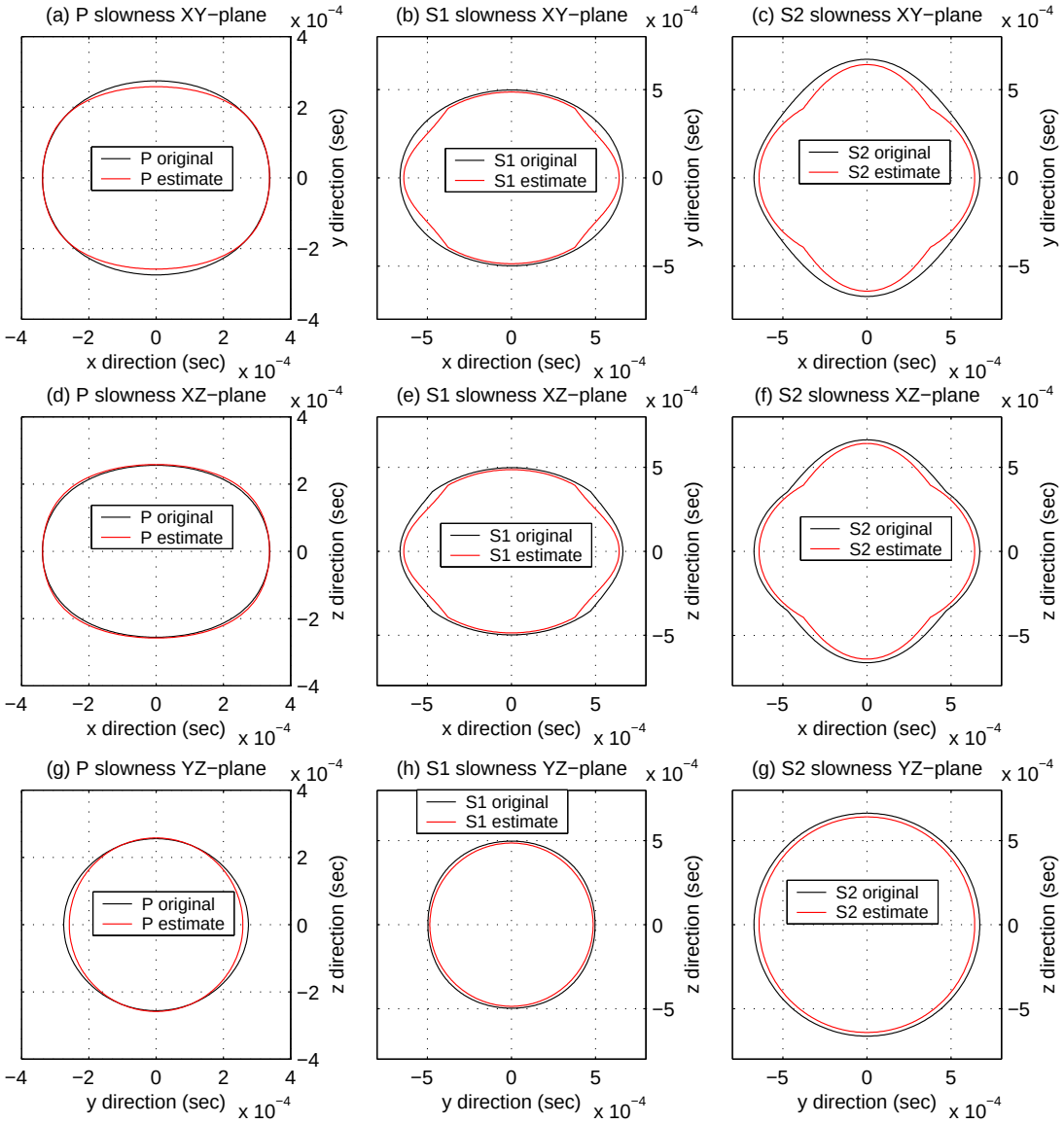

Figure 6.14: Comparison of slowness surfaces between the orthorhombic C_{ij} given for the physical model and the estimated HTI C_{ij} for waves P, S1 and S2. Note that all the axes for the P-wave slowness (left column) have only half the range of those for the S1 and S2-slownesses (center and right columns).

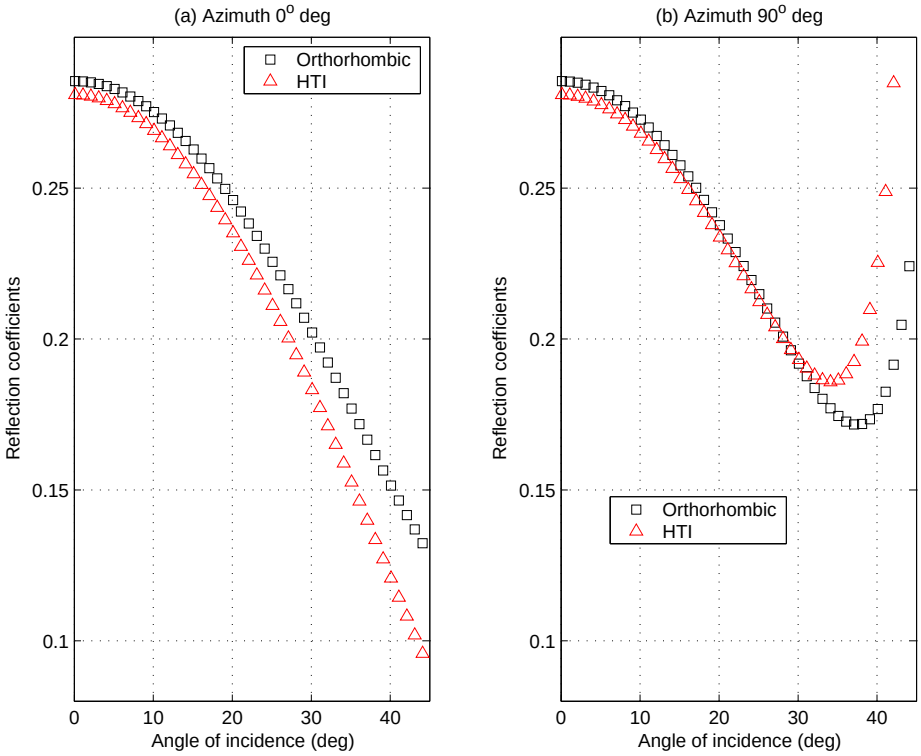

Figure 6.15: Modeled reflection coefficients with given orthorhombic and approximated HTI elastic constants. (a) Azimuth 0^o, perpendicular to the fracture plane, (b) Azimuth 90^o, parallel to the fracture plane.

smaller ones. The exact values are listed in Table 6.4. The histograms from the P-wave velocity, S-wave velocity, density and resulting impedance are shown in Figure 6.16 for group A and Figure 6.17 for group B.

Modelled reflection coefficients

The two groups of reflection coefficients from the distributions of rock properties of groups A and B are calculated as follows.

- Let the modelled fracture densities have a uniform distribution ranging from 0 to 0.3 in steps of 0.01, for a total of 30 entries.
- Let the angles of incidence have a uniform distribution ranging from 1^o to 55^o in steps of 1^o, and the azimuths range from -180^o at 1^o intervals to 180^o.
- For each fracture density draw a realization from the P-wave, S-wave and density distributions of the top and the bottom layers and calculate the resulting reflection coefficient. Repeat this step 20 times (drawing a different realization each time) for the same value of fracture density, azimuth and angle of incidence.
- Accommodate the resulting reflection coefficients in a matrix R such that every row has a different azimuthal angle and every column a different model/angle of incidence. Matrix R has then 361 rows (equal to the number of azimuths) and 33000 columns (number of angles of incidence (55) $\times$ number of fracture densities (30) $\times$ number of realizations (20)).

The resulting reflection coefficients are shown versus azimuth for different angles of incidence in figures 6.18 for Group A and 6.19 for Group B. As expected, there is a larger spread in the range of modelled reflection coefficients for Group A than for Group B, particularly at large offsets (compare 6.18f with 6.19f).

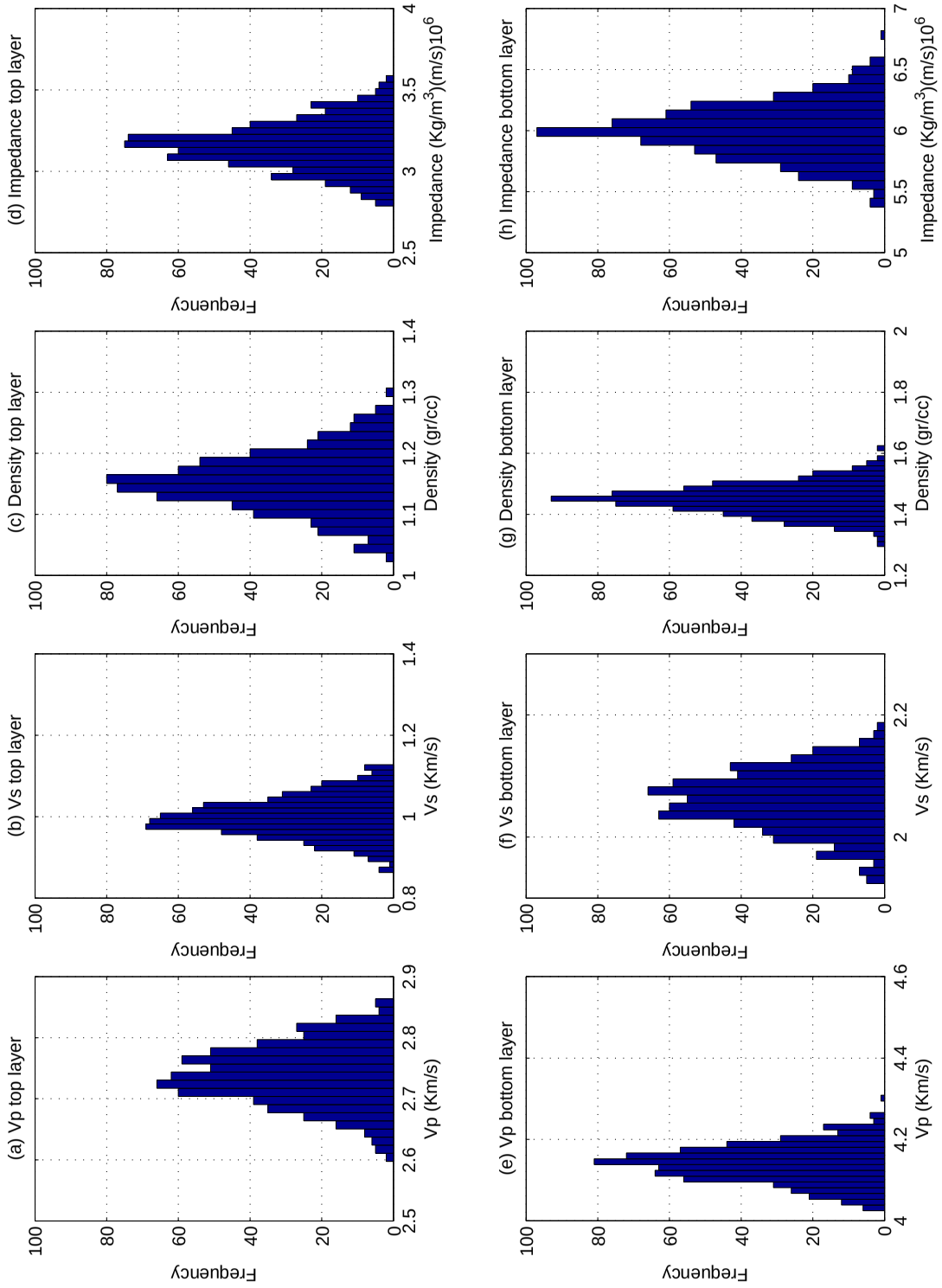

Figure 6.16: Histogram showing distribution of rock properties used in model group A for study of interface 2 (see Figure 6.1), between the top of the fractured layer and the isotropic layer above it.

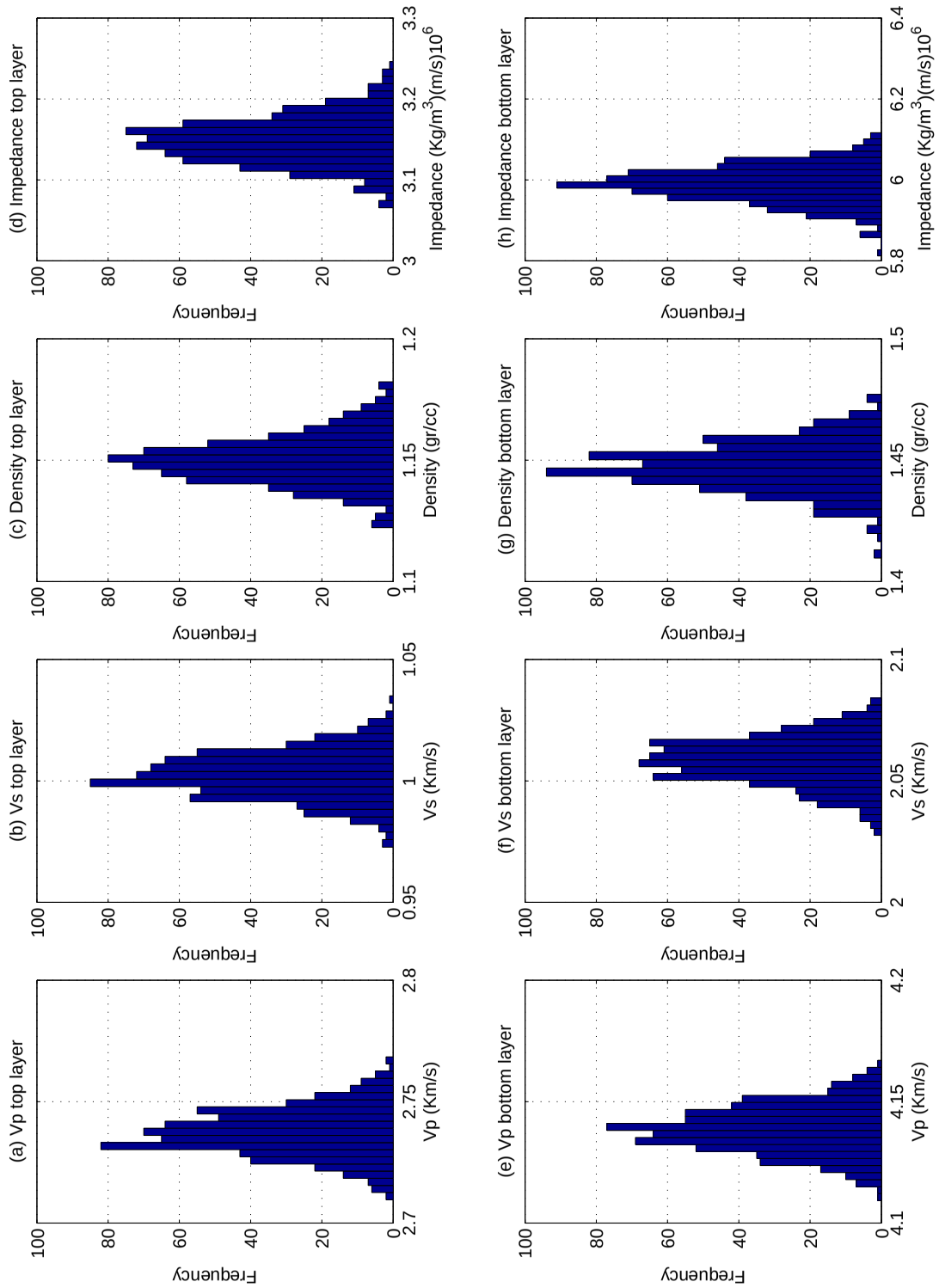

Figure 6.17: Histogram showing distribution of rock properties used in model group B for study of interface 2 (see Figure 6.1), between the top of the fractured layer and the isotropic layer above it.

6.4.3 Critical angle

Landrø and Tsvankin (2007) use the critical angle between an isotropic and TI or orthorhombic medium as a means to invert for anisotropic parameters of the anisotropic medium. Here I calculate the critical angle numerically to evaluate its sensitivity to the approximations of the elastic constants and fracture density. I calculate the critical angle versus azimuthal angle for the following cases:

1. Using the original rock properties and elastic constants given by Wang et al. (2007) for the top and bottom layers (layers 2 and 3 from Figure 1.1).

2. Using the HTI approximation for the fractured layer, and the original rock properties for layer 2.

3. Using the HTI approximation for the fractured layer and the estimated rock properties for layer 2.

The critical angle for all the above cases are shown in Figure 6.20a, where it reaches its maximum at azimuth 0^o (perpendicular to the fracture plane) and minimum at azimuth 90^o (parallel to the fracture plane).

Using the rock properties and elastic constants of case 3 mentioned above, I calculate the critical angle for different fracture densities in the fractured layer. Figure 6.20b shows how as the fracture density increases, the critical angle increases significantly in the direction perpendicular to the fracture plane.

6.5 Optimal basis functions and AVOZ

6.5.1 Approach I: basis functions vary with azimuth

I calculate the singular value decomposition of matrix R for both groups A and B. The resulting basis functions and coefficients from both groups will be referred to

as models A and B. Given the large size of the resulting matrix (361 ×33000), for computational limitations I calculate only the first 50 singular-values and their corresponding singular-vectors, such that the sizes of the resulting matrices are,

$$R_{361\times 33000} \approx F_{361\times 50} D_{50\times 50} (V_{33000\times 50})^T \tag{6.5}$$

This is not detrimental in any way for the method, as in the reconstruction I will only use the first three singular-values and singular-vectors.

The resulting optimal basis functions for models A and B are shown in figures 6.21 and 6.22. As the index of the basis function increases so does its frequency, as is obvious from figures 6.21 a, b, c, d and 6.22 a, b, c and d. Notice that apart from the sign difference of F_2 and F_4 between models A and B, the general shape of the functions is very similar (see Figure 6.23a). In fact, after changing the sign to make them comparable (see Figure 6.23b where the basis functions between models A and B appear indistinguishable) it is fair to say that the functions are basically the same. The difference between the basis functions of Models A and B are shown in Figure 6.23c, where the difference increases as the index of the function increases.

The first 50 singular values obtained from both groups are shown in figures 6.24 a and b. The systematic decrease in the singular value as the index increases is seen in both 6.24 a and 6.24b.

AVOZ with optimal basis functions

I use the first few basis functions to fit the measured reflection coefficients per common offset for all azimuths. I find the coefficients that multiply the basis functions to best approximate the measured reflection coefficients with the following procedure. When using the first three basis functions for a fixed angle of

incidence i, we then have,

$$R_i(\phi) \approx c_{1i}F_1(\phi) + c_{2i}F_2(\phi) + c_{3i}F_3(\phi) \tag{6.6}$$

where ϕ is the azimuthal angle and F_1, F_2 and F_3 are the basis functions. Expanding on the angle of incidence we have,

$$\begin{aligned}
r_i(1) &\approx c_{1i}F_1(1) + c_{2i}F_2(1) + c_{3i}F_3(1) \\
r_i(2) &\approx c_{1i}F_1(2) + c_{2i}F_2(2) + c_{3i}F_3(2) \\
r_i(3) &\approx c_{1i}F_1(3) + c_{2i}F_2(3) + c_{3i}F_3(3) \\
\vdots &\approx \vdots \\
r_i(n) &\approx c_{1i}F_1(n) + c_{2i}F_2(n) + c_{3i}F_3(n)
\end{aligned} \tag{6.7}$$

which is the same as,

$$\begin{bmatrix} r_i(1) \\ r_i(2) \\ r_i(3) \\ \vdots \\ r_i(n) \end{bmatrix} \approx \begin{bmatrix} F_1(1) & F_2(1) & F_3(1) \\ F_1(2) & F_2(2) & F_3(2) \\ F_1(3) & F_2(3) & F_3(3) \\ \vdots & & \vdots \\ F_1(n) & F_2(n) & F_3(n) \end{bmatrix} \begin{bmatrix} c_{1i} \\ c_{2i} \\ c_{3i} \end{bmatrix} \tag{6.8}$$

or in matrix form,

$$R \approx FC$$

We can then calculate the best fitting coefficients c_1, c_2 and c_3, for angle of incidence i, with,

$$C \approx (F^T F)^{-1} F^T R \tag{6.9}$$

Using C from equation 6.9 we can then calculate the approximation of the reflection coefficient using three basis functions.

Similarly we can calculate the fit using different numbers of functions. Figures 6.25 and 6.26 (left) show the estimated coefficients using two, three and nine basis functions at the locations (azimuths) where there are measurements. The

right side of figures 6.25 and 6.26 show the estimated reflection coefficients for all azimuths using two (dashed line) and three (solid line) basis functions. Additionally it shows the expected reflection coefficients using the elastic constants and physical properties given by Wang et al. (2007), and the measured amplitudes scaled.

In general, for offsets between 1000m ($\theta = 33^o$) and 1500m ($\theta = 45^o$) the fit using the optimal basis functions is very good. The selected offsets from figures 6.25 and 6.26 fall in that range. For offsets smaller than 1000m ($\theta < 33^o$) there are no consistent azimuthal changes in the measured reflection coefficients (nor in the modelled one as seen in Figure 6.15) and the fit becomes meaningless.

At offsets greater than 1500m ($\theta > 45^o$) the modelled reflection coefficient reaches the critical angle in a direction parallel to the fracture plane. Since in the measured amplitudes we don't see the strongly marked amplitude changes that are predicted after the critical angle, the data from this offset range should be taken carefully, and should perhaps not be given as much weight.

The similarity of the first three basis functions between models A and B (figures 6.21 and 6.22) explains the similarity of their respective fits shown in figures 6.25 and 6.26.

The inverted c_1, c_2 and c_3 coefficients per common offset gather are shown in figures 6.27 and 6.28 respectively. The marked change occurring after 1500m for all three coefficients for both models is due to the change in the reflection coefficient from an entirely real to a complex number with a non-zero imaginary part. The change in sign of c_1 and c_3 between models A and B (figures 6.27a and 6.28a, and 6.27c and 6.28c) is explained by the differences between the basis functions of models A and B (figures 6.21 and 6.22).

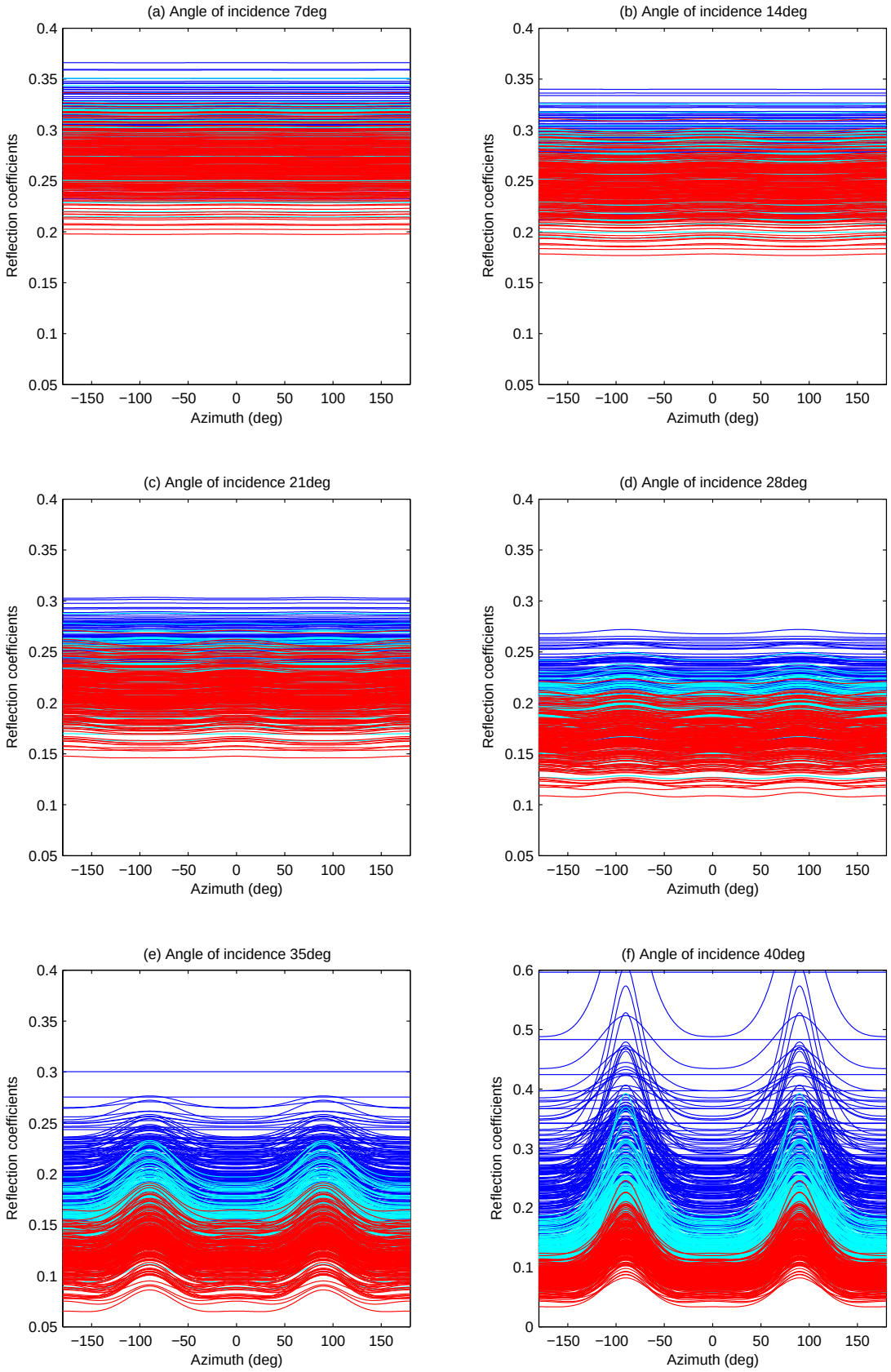

Figure 6.18: Modelled reflection coefficients per angle of incidence for Group A. Blue, cyan and red curves correspond to low (fd<0.096), medium (0.096 <fdr< 0.19) and high (fd> 0.19) fracture density respectively.

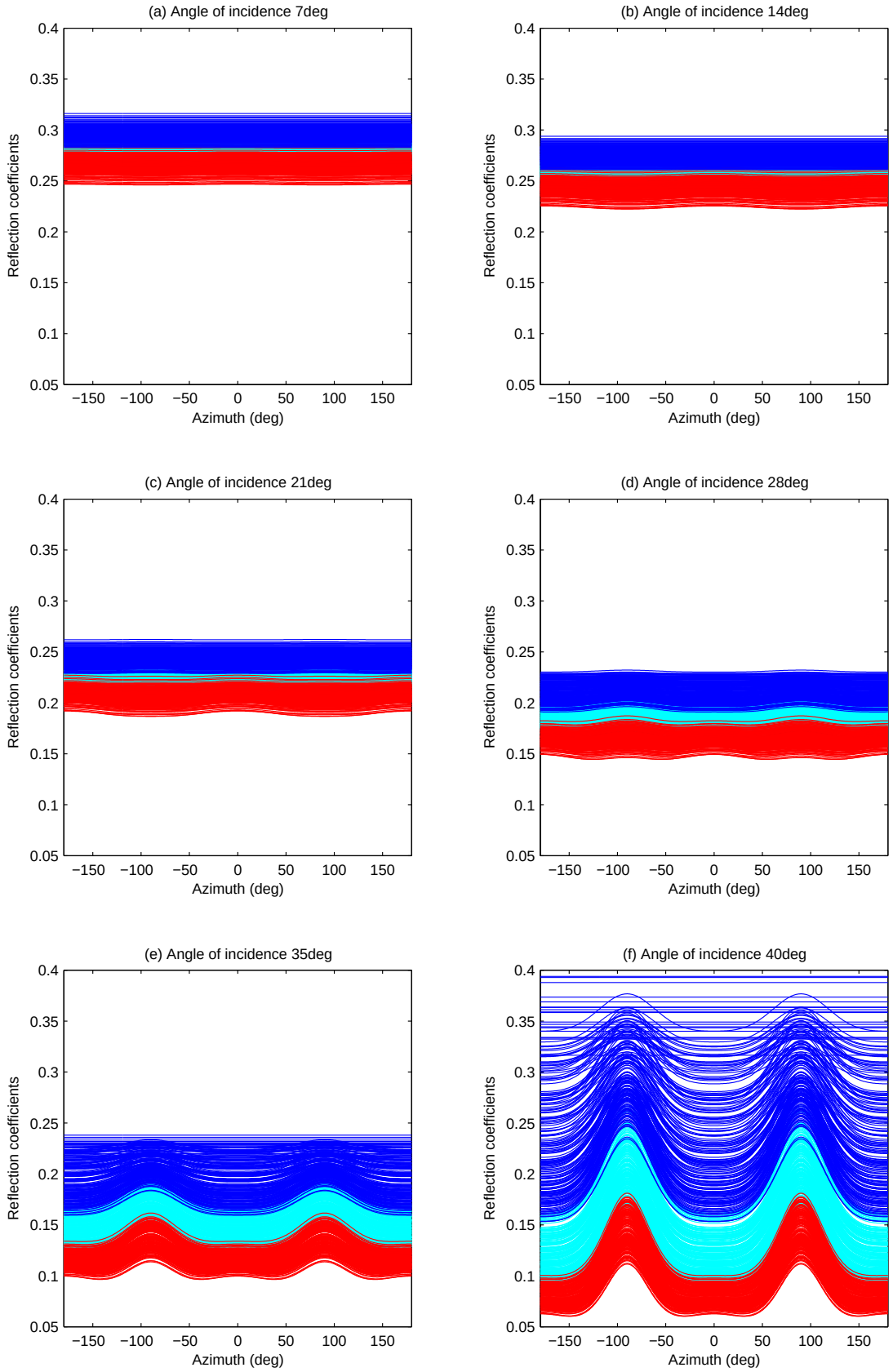

Figure 6.19: Modelled reflection coefficients per angle of incidence for Group B. Blue, cyan and red curves correspond to low (fd<0.096), medium (0.096 <fdr< 0.19) and high (fd> 0.19) fracture density respectively.

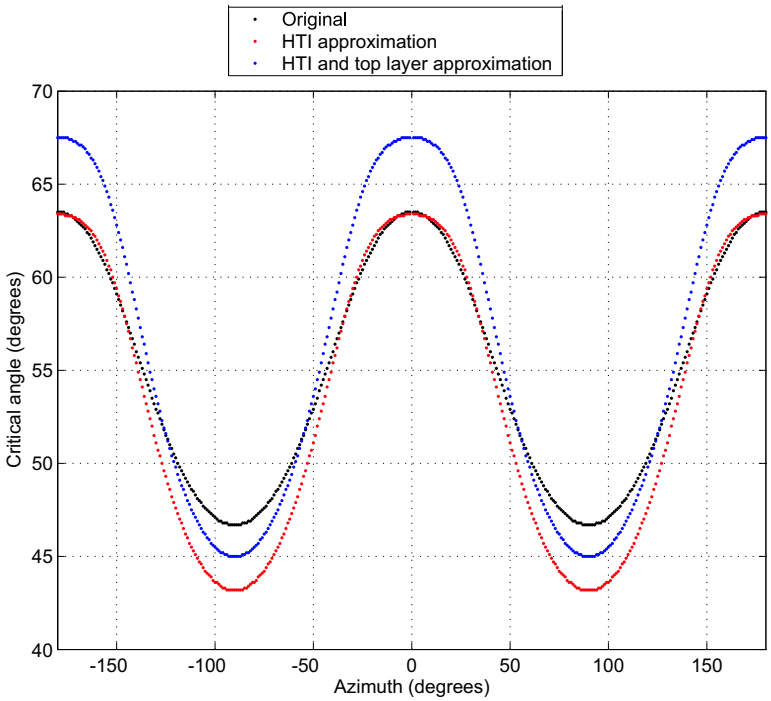

(a) Fixed fracture density (0.2) various approximations

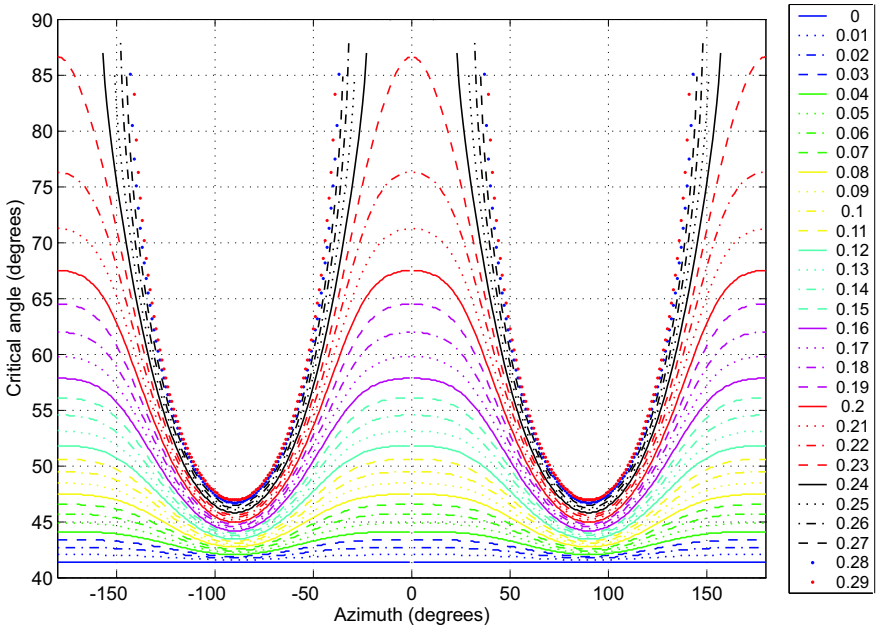

(b) HTI with varying fracture density

Figure 6.20: Critical angle for a)a fixed fracture density of 0.2 and various approximations b)HTI with varying fracture density.

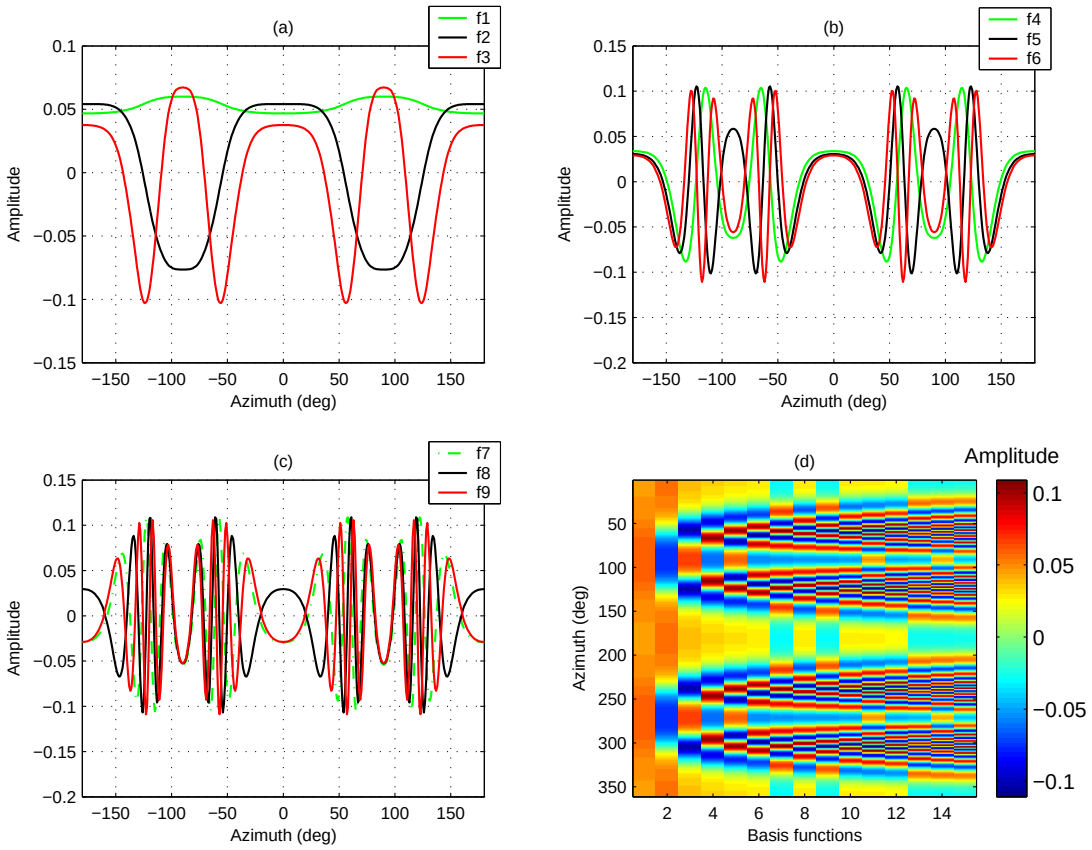

Figure 6.21: Optimal basis functions for interface at the top of the fractured layer, for Model A.

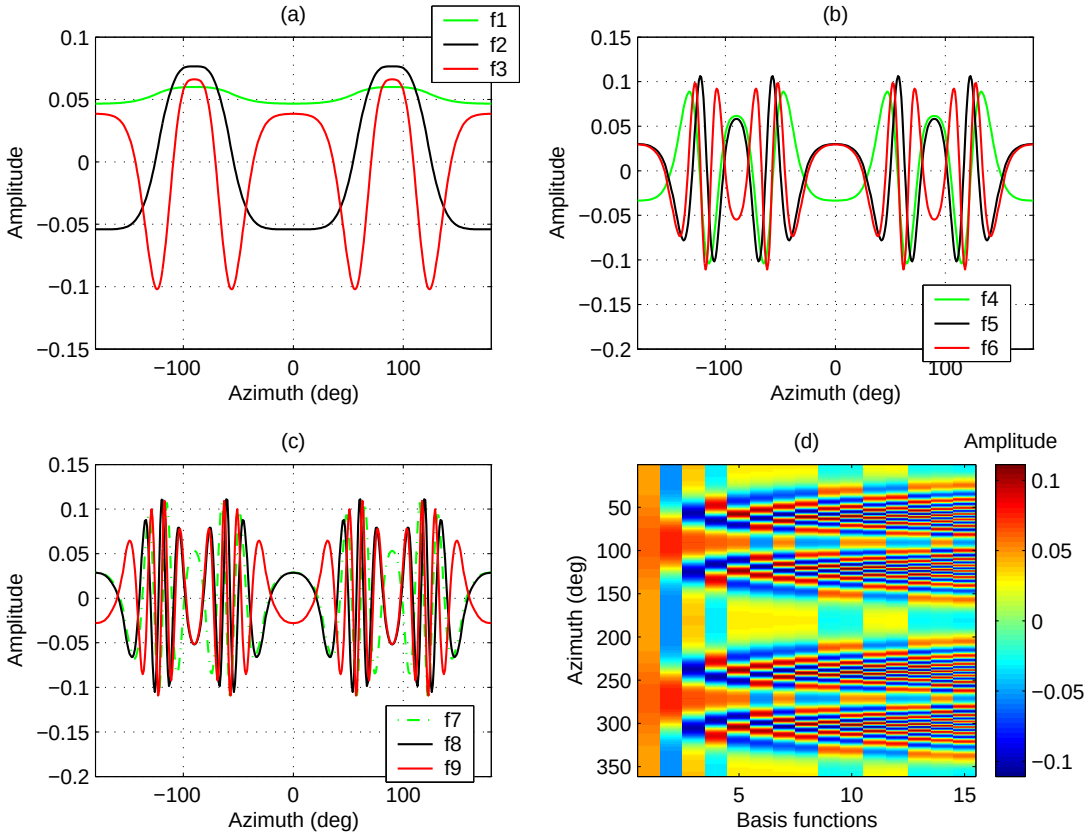

Figure 6.22: Similar to Figure 6.21 but for Model B.

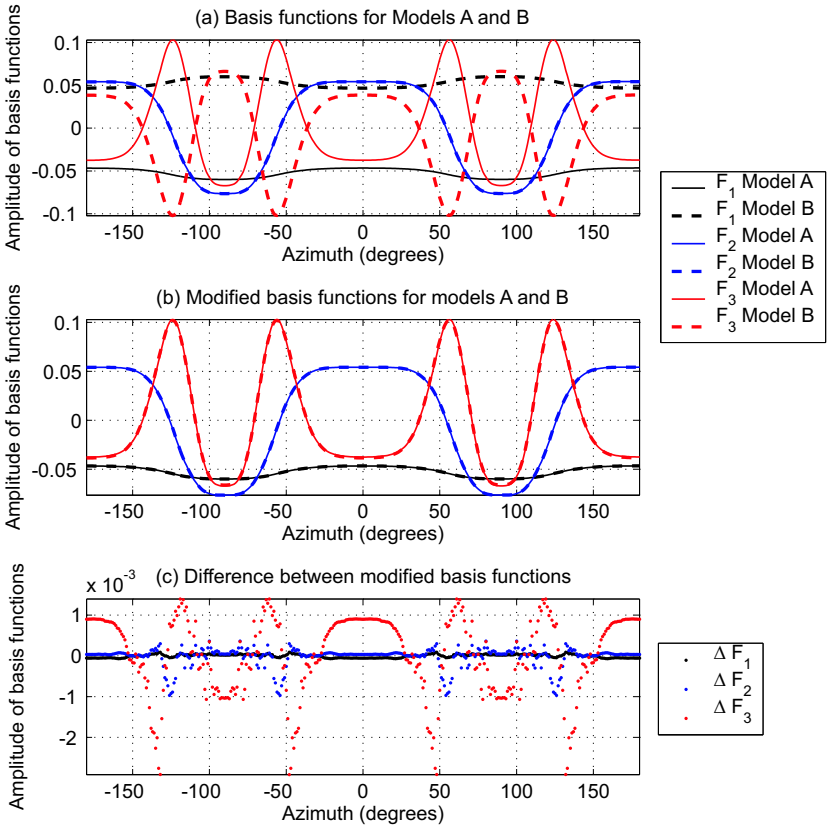

Figure 6.23: Comparison of basis functions for models A and B.

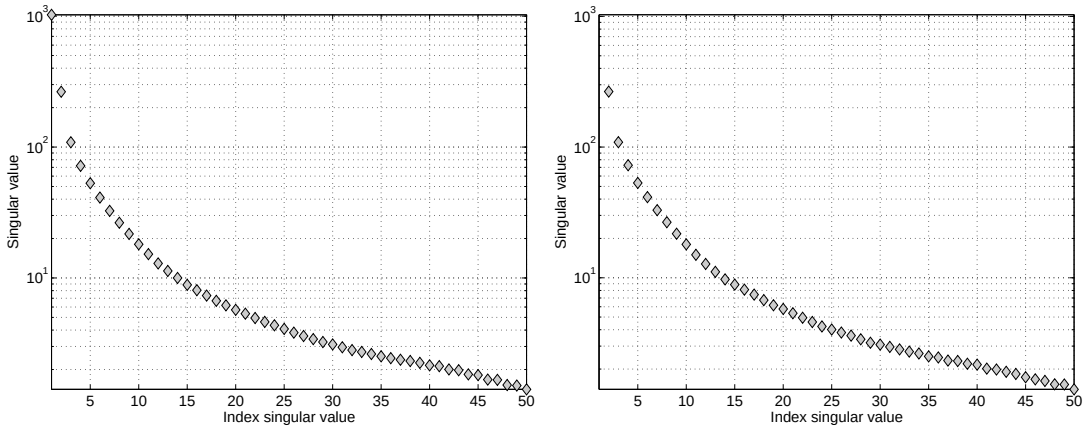

(a) Model A (b) Model B

Figure 6.24: 50 largest singular values from decomposition of realizations from models (a) A and (b) B.

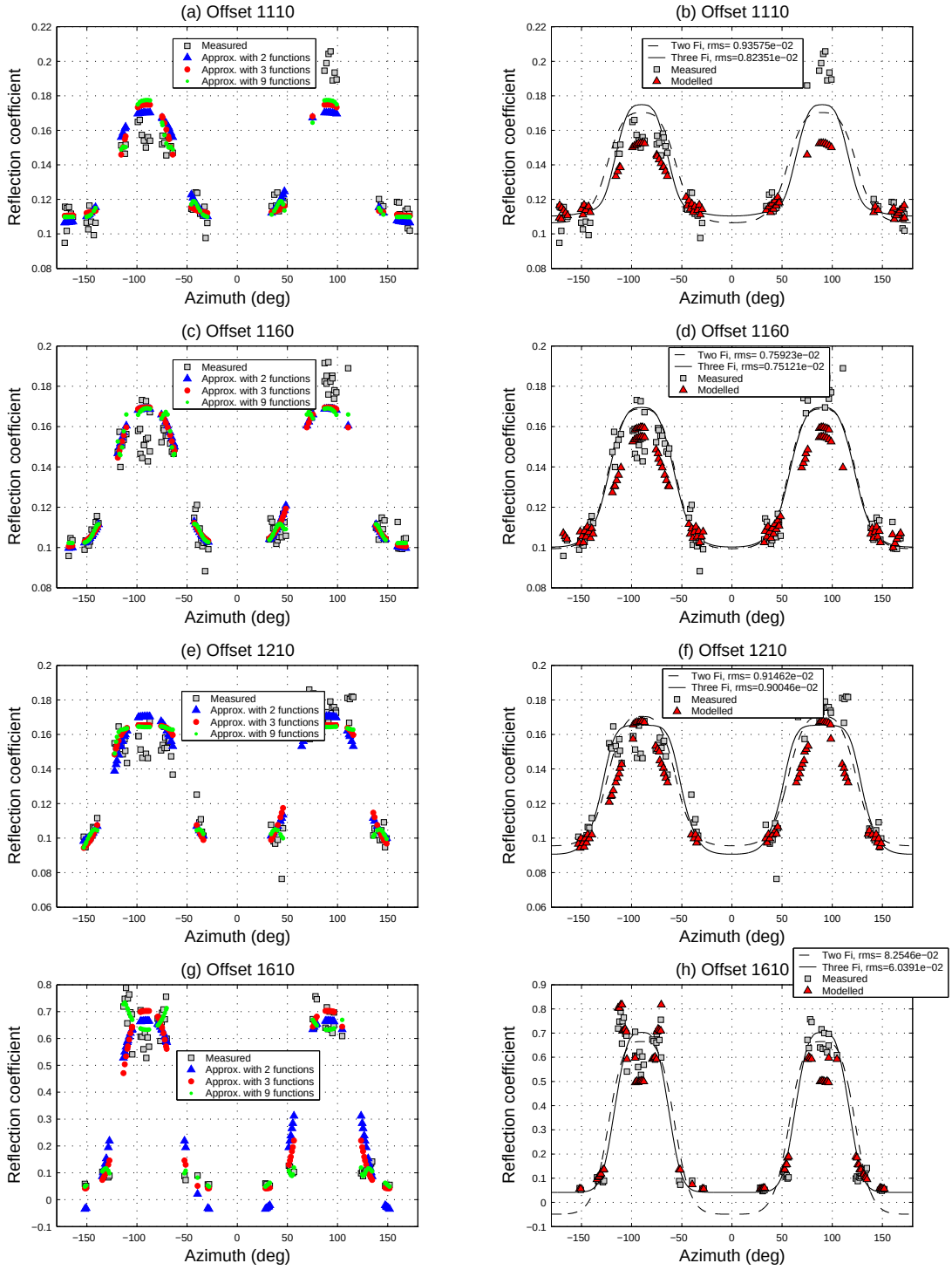

Figure 6.25: Fit to scaled reflection coefficients with 2, 3, and 9 basis functions for selected offsets of the top of the fractured layer (left) for Model A using approach I. Approximation with 2 and 3 basis functions compared to the modelled reflection coefficient and the measured amplitudes scaled (right).

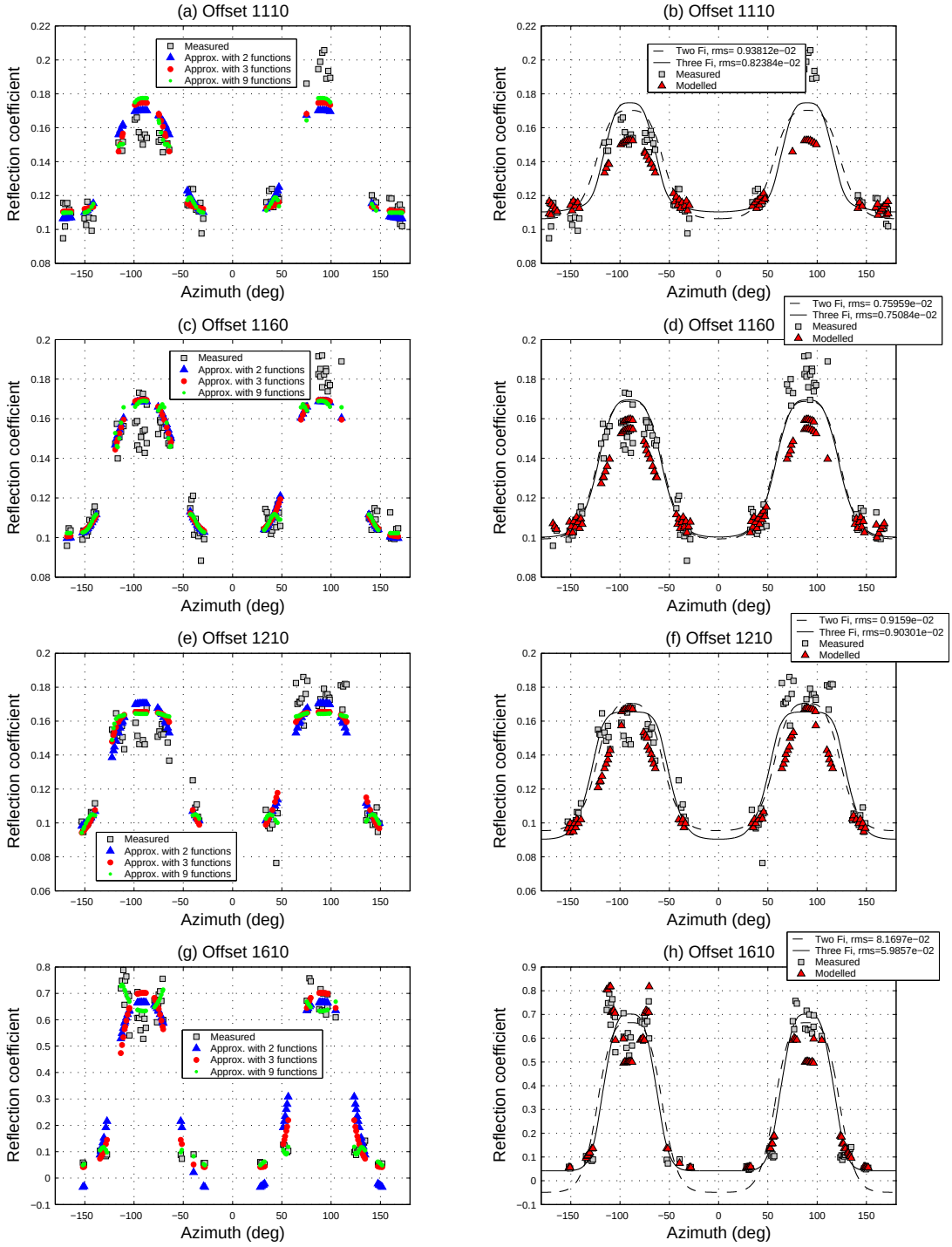

Figure 6.26: Fit to scaled reflection coefficients with 2, 3, and 9 basis functions for selected offsets of the top of the fractured layer (left) Model B using approach I. Approximation with 2 and 3 basis functions compared to the modelled reflection coefficient and the measured amplitudes scaled (right).

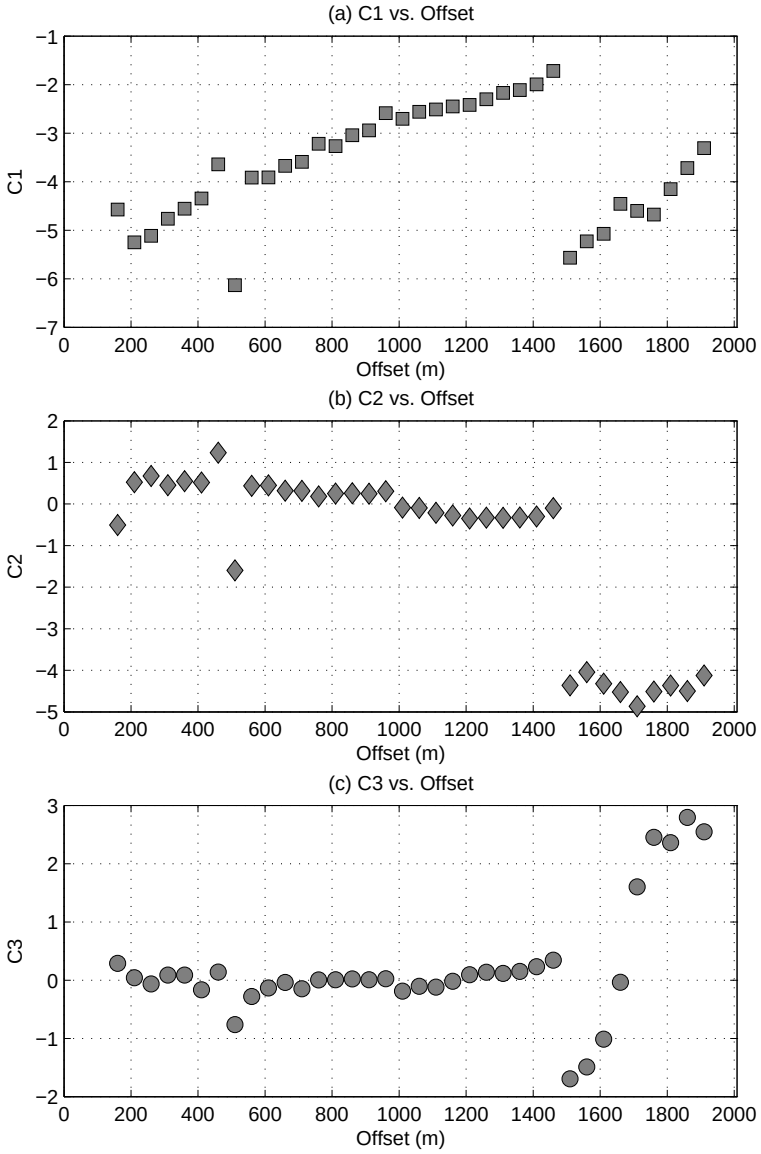

Figure 6.27: Inverted $C1$, $C2$ and $C3$ for Model A.

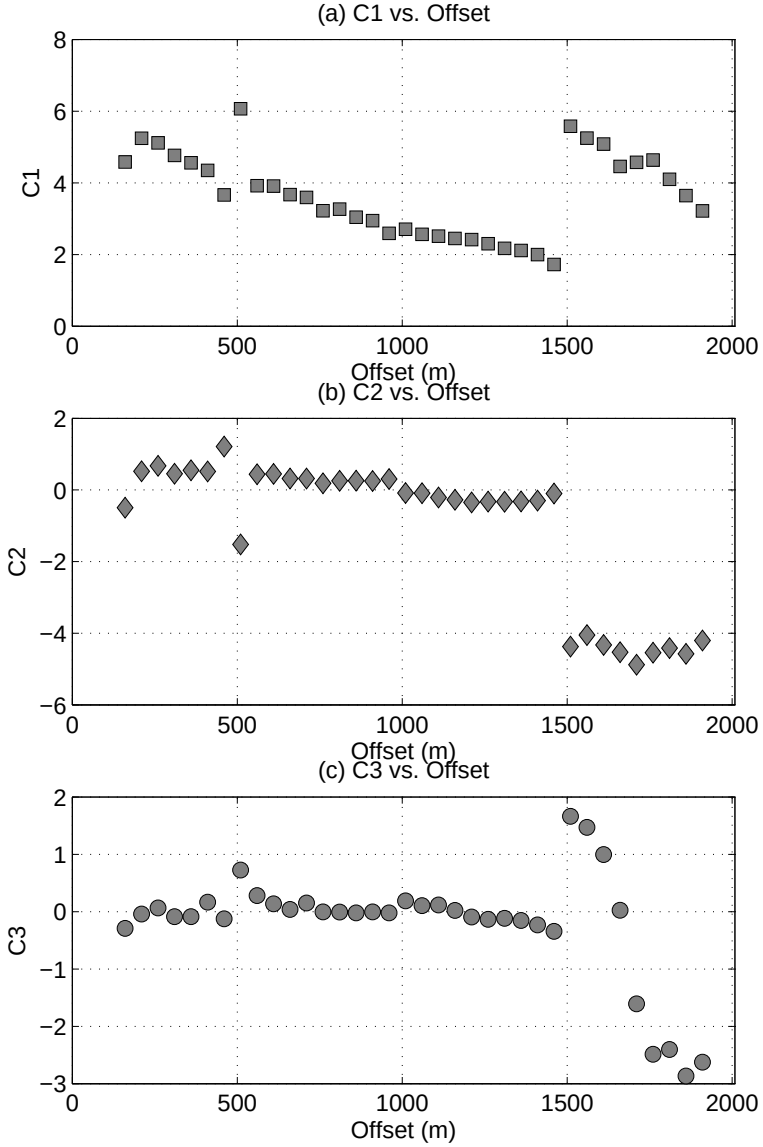

Figure 6.28: Inverted $C1$, $C2$ and $C3$ for Model B.

6.5.2 Approach II: basis functions vary with incidence angle

In addition to the methodology developed in Chapter 5 and applied above, I rotate the matrix of reflection coefficients R such that every row has a different incidence angle and every column a different realization. This results in basis functions that vary with incidence angle and coefficients that vary with azimuthal angle as shown in equation 5.16 replicated here,

$$R(\theta, \phi) = C_1(\phi)F_1(\theta) + C_2(\phi)F_2(\theta) + C_3(\phi)F_3(\theta) + \dots \tag{6.10}$$

The same modelled realizations from the previous section are shown in Figure 6.29 in a direction perpendicular and parallel to the fracture strike, see panels (a) and (b) respectively. The first three basis functions using the new decomposition are shown in panel (c), and the following three basis functions are shown in panel (d). An overview of the first nine basis functions is further displayed in panel (e). Panel (f) shows the first nine singular values of the decomposition.

6.6 Fracture density inversion

6.6.1 Using basis functions from Approach I

Correlation coefficients

In order to invert for fracture density from the inverted coefficients, we first find the coefficient (C_1, C_2 or C_3) from the models with the highest correlation to the fracture density modelled. Given the discussion above on the validity of the fit for the different ranges of offsets/angles of incidence, I calculate the correlation coefficient for each of the ranges as well as for all angles of incidence as shown in Table 6.5. I find that for all the ranges of angles of incidence considered, C_1

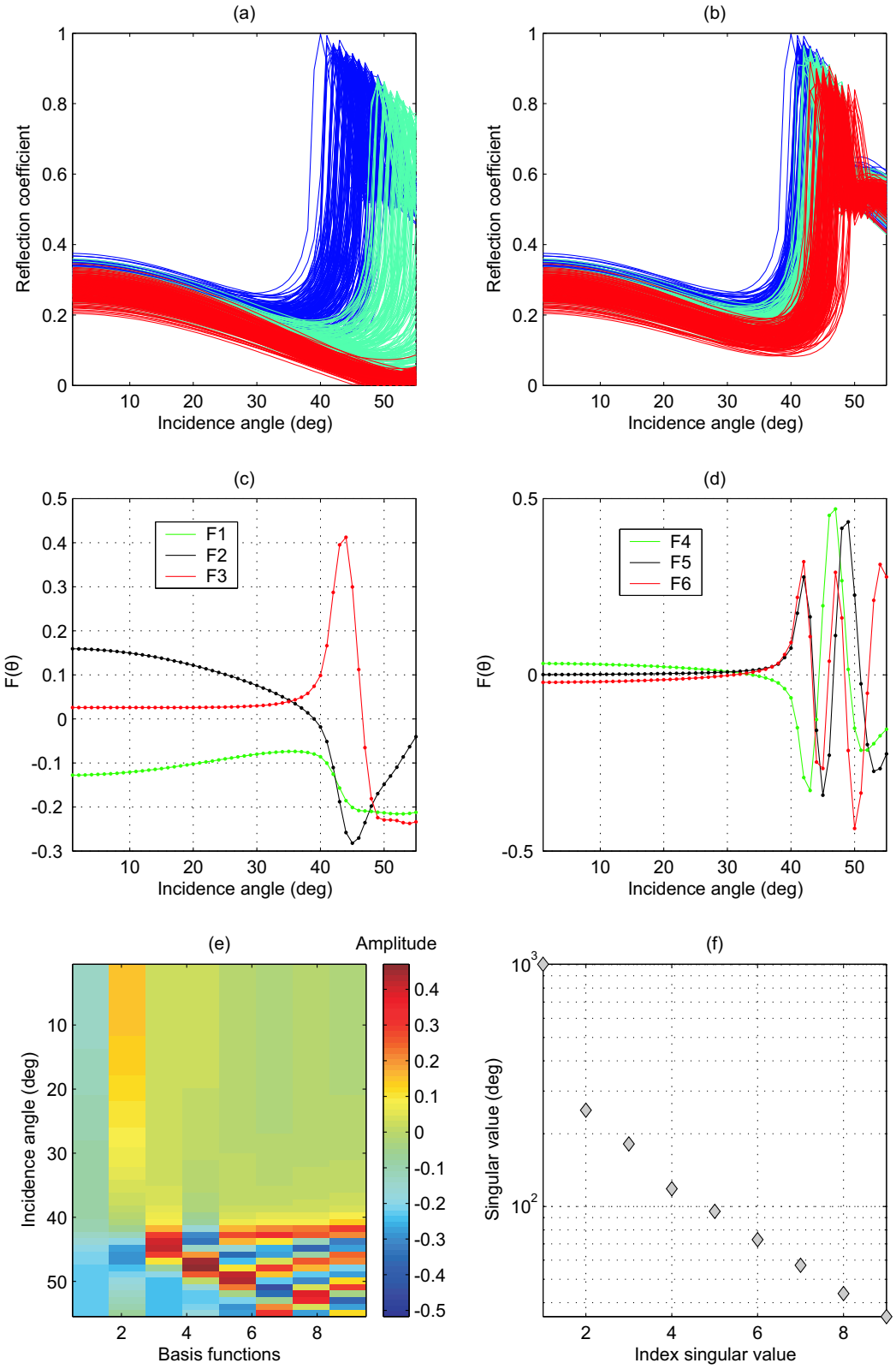

Figure 6.29: Realizations and basis functions varying with angle of incidence for Model A. a) Realizations of the reflection coefficient perpendicular to the fracture plane, b) same as a) but parallel to the fracture plane, c)first three basis functions, d) basis functions 4 to 6, e) basis functions up to nine, f) first nine singular values. In a) and b) red is low fracture density (< 0.1), blue is high fracture density (> 0.2) and cyan is intermediate (between 0.1 and 0.2)

is the coefficient with the highest correlation to fracture density. Furthermore, for the range of angles of incidence of interest ($33 < \theta < 45$) the correlation coefficient between C_1 and the modelled fracture density has a high value of 0.59 for Model A, and -0.6326 for Model B. Thus, I base the inversion from the inverted coefficients to fracture density entirely on C_1.

	Model A			Model B		
Range θ	cc_1	cc_2	cc_3	cc_1	cc_2	cc_3
all	0.435	-0.2897	-0.0718	-0.458	-0.293	0.0757
$\theta < 33^o$	0.299	-0.218	-0.0296	-0.3809	-0.275	-0.0494
$33^o < \theta < 45^o$	0.598	-0.0762	-0.0509	-0.6326	-0.047	0.0139
$\theta < 45^o$	0.896	-0.7962	-0.1355	-0.9154	-0.8160	0.1574

Table 6.5: Correlation coefficient between modelled C_i's and modelled fracture density for models A and B.

Multiple regression coefficients

I also calculate a multiple regression of the coefficients from models A and B to the modelled fracture density using the following general equation.

$$FD = a_1 C_1 + a_2 C_2 + a_3 C_3 \tag{6.11}$$

where a_1, a_2 and a_3 are the multiple regression coefficients between the modelled C_i coefficients and the modelled fracture density FD. Expanding on the model number we get the following set of linear equations,

$$\begin{bmatrix} FD^1 \\ FD^2 \\ FD^3 \\ \vdots \\ FD^n \end{bmatrix} = \begin{bmatrix} C_1^1 & C_2^1 & C_3^1 \\ C_1^2 & C_2^2 & C_3^2 \\ C_1^3 & C_2^3 & C_3^3 \\ \vdots & \vdots & \vdots \\ C_1^n & C_2^n & C_3^n \end{bmatrix} \begin{bmatrix} a_1 \\ a_2 \\ a_3 \end{bmatrix} \tag{6.12}$$

where the superscripts refer to the model number. Using a least squares approach, I solve for the multiple regression coefficients for the different ranges, and list them in Table 6.6. Some of the values of the multiple regression coefficients are strikingly high for C_2 and C_3. However, the inverted values of c_2 and c_3 fall outside the range of those resulting from models A and B. Therefore, I use the coefficient with the highest correlation to fracture density using a single regression, which as shown in Table 6.5 is C_1.

	Model A			Model B		
Range θ	a_1	a_2	a_3	a_1	a_2	a_3
all	-0.0199	-0.0244	-0.0292	0.0197	-0.0244	0.0302
$\theta < 33^o$	0.1484	0.4648	-12.7681	-0.1986	0.7350	14.2424
$33^o < \theta < 45^o$	-0.0149	-0.0140	-0.0624	0.0142	-0.0129	0.0686
$\theta < 45^o$	-0.0104	-0.0397	-0.0182	0.0104	-0.0398	0.0190

Table 6.6: Multiple regression coefficient between modelled C_i's and modelled fracture density for models A and B.

Inversion based on C_1

Figures 6.30 and 6.31 show the inversion for fracture density from C_1 for offsets 760m to 1860m every 100m for models A and B accordingly. The dashed lines on both sides of the trend are the standard deviation for C_1 at that location (offset, angle of incidence and fracture density) from the models. The fact that the standard deviations of the distributions of rock properties is greater for Group A than Group B is reflected in the standard deviations of C_1 versus fracture density in figures 6.30 and 6.31.

Figures 6.32-6.35 show the maps of C_1, C_2 and C_3 versus angle of incidence and fracture density (left) and the inverted fracture density calculated for each angle of incidence from C_1. The right side of figures 6.32-6.35 shows the standard deviation that is attached to each coefficient. Note the drastic change in both the

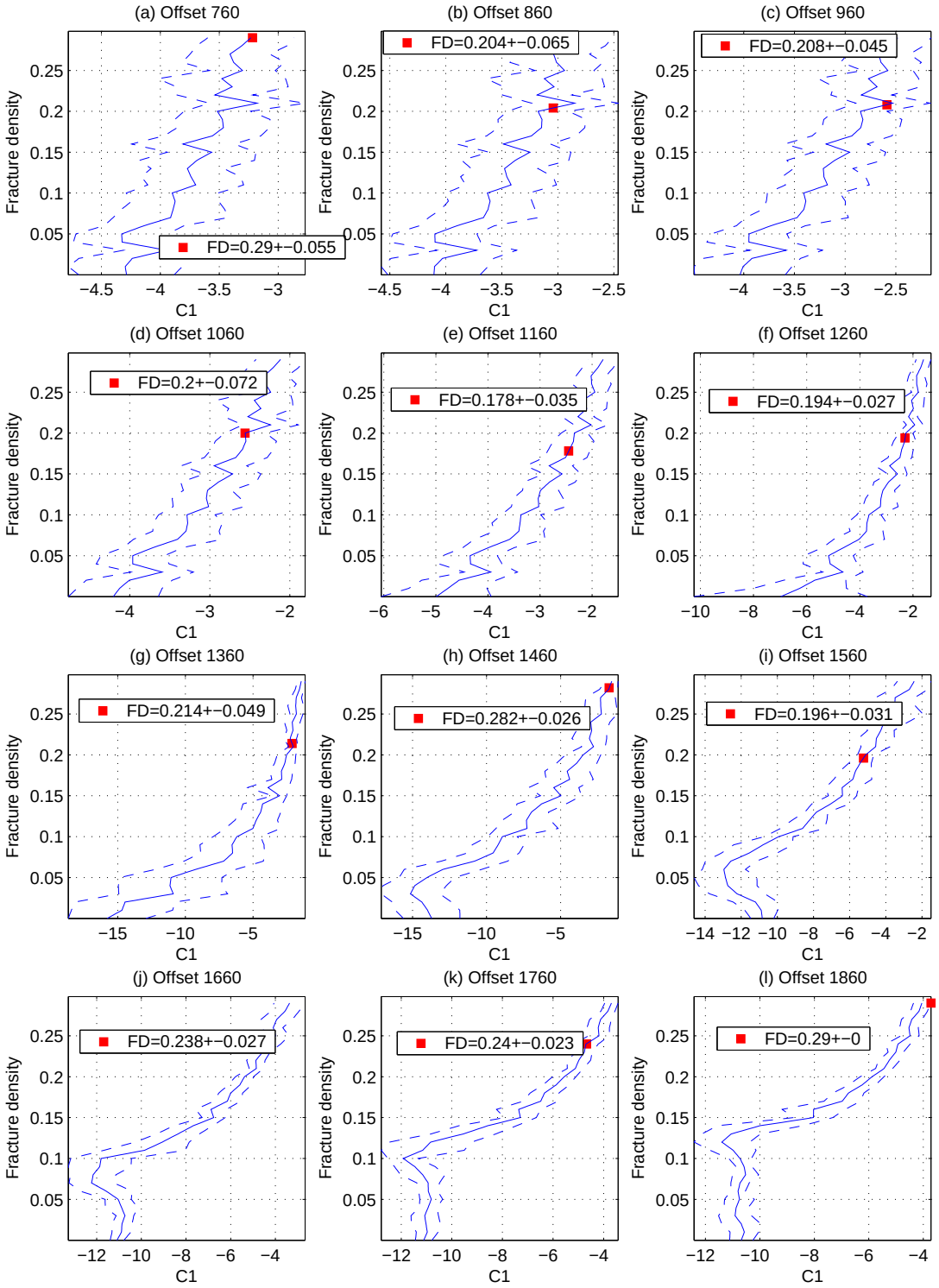

Figure 6.30: Inverted fracture density from C1 for selected common offset gathers for Model A.

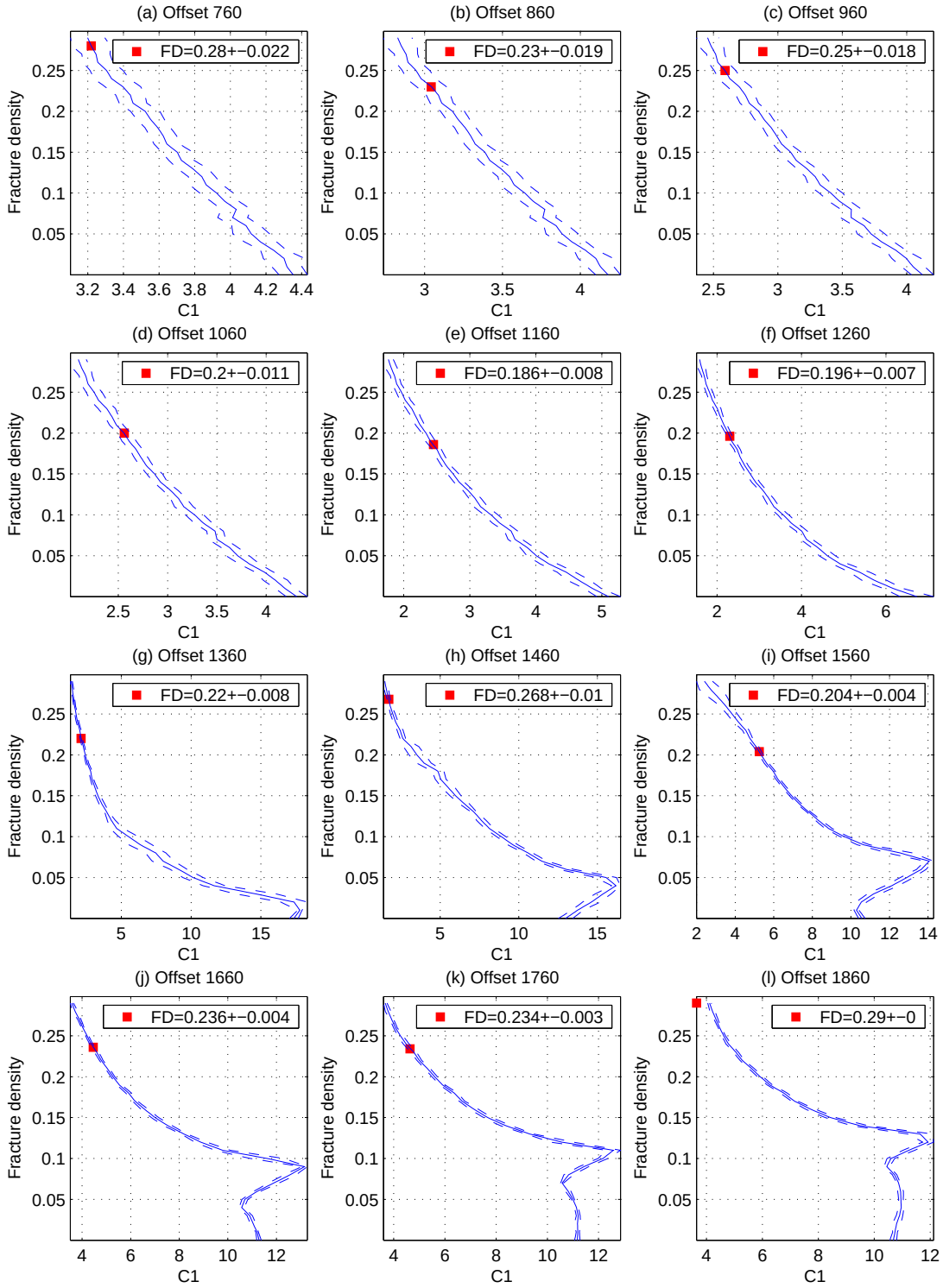

Figure 6.31: Inverted fracture density from C1 for selected common offset gathers for Model B.

coefficients and standard deviations for angles of incidence greater than $\approx 40^o$, see figures 6.33 and 6.35. For comparison, the inverted fracture density is also plotted (grey squares) on figures 6.32-6.35.

The inverted fracture density with their corresponding error per common offset gather is shown in figures 6.36a and 6.37a. The error bars are calculated from the standard deviations (dashed lines) shown in figures 6.30 and 6.31. For both models the error bars become smaller as the offset increases. For the range of angles of incidence of interest, the mean of the inverted fracture density becomes stable around 0.2. However, as the offsets get closer to 1500m (close to the critical angle) the inverted fracture density starts increasing.

For the range of offsets greater than 1500m, the error bars of the inverted fracture density are smaller for both models. However, the errors of the fit of the measured amplitudes with the optimal basis functions and inverted coefficients increase significantly, as shown in figures 6.36b and c, and 6.37b and c. Notice that, as expected, the error of the fit decreases as the number of functions used increases. This effect can be seen in figures 6.36b and c and 6.37b and c where the errors in the fits using two, three, five and nine functions are shown.

6.6.2 Using basis functions from Approach II

The modelled coefficients versus azimuth and fracture density using approach II are shown in Figure 6.38. Notice that in a direction perpendicular to the fracture strike (azimuths $-180°$, $0°$ and $180°$), both C_1 and C_2 vary in an almost linear way with the fracture density. On the other hand, C_3 shows a non-linear behaviour with respect to fracture density for all azimuths.

The RMS error between the measured and estimated reflection coefficients using two, three, five and nine basis functions are shown in Figure 6.39, where the error decreases as the number of basis functions used increases.

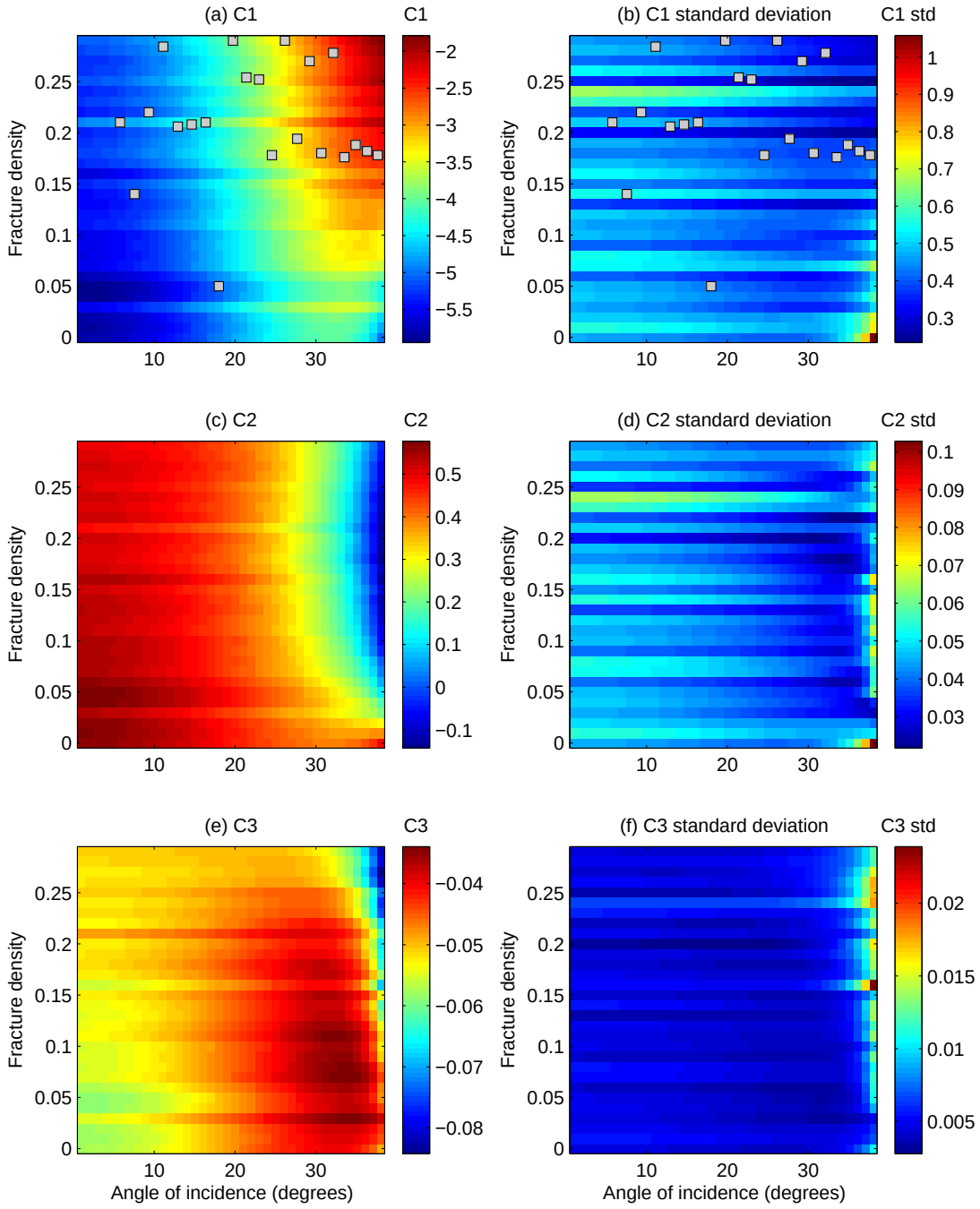

Figure 6.32: Mean and standard deviation for C1, C2 and C3 versus fracture density and angle of incidence for Model A. The standard deviation could be taken as a measure of the uncertainty in the inversion response. For angles of incidence 1^o to 38^o.

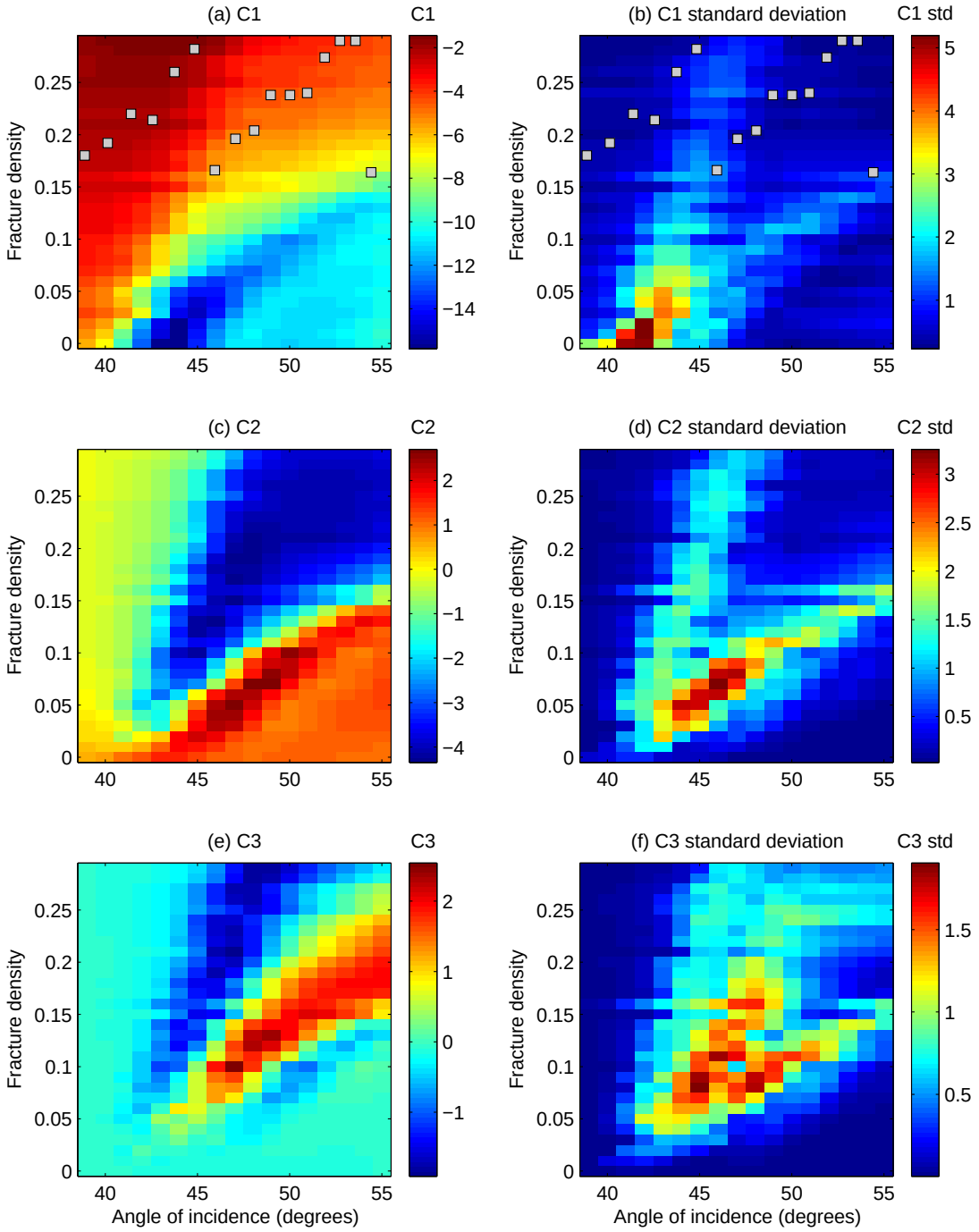

Figure 6.33: Mean and standard deviation for C1, C2 and C3 versus fracture density and angle of incidence for Model A. The standard deviation could be taken as a measure of the uncertainty in the inversion response. The grey squares show the inverted fracture density values. For angles of incidence 39^o to 55^o.

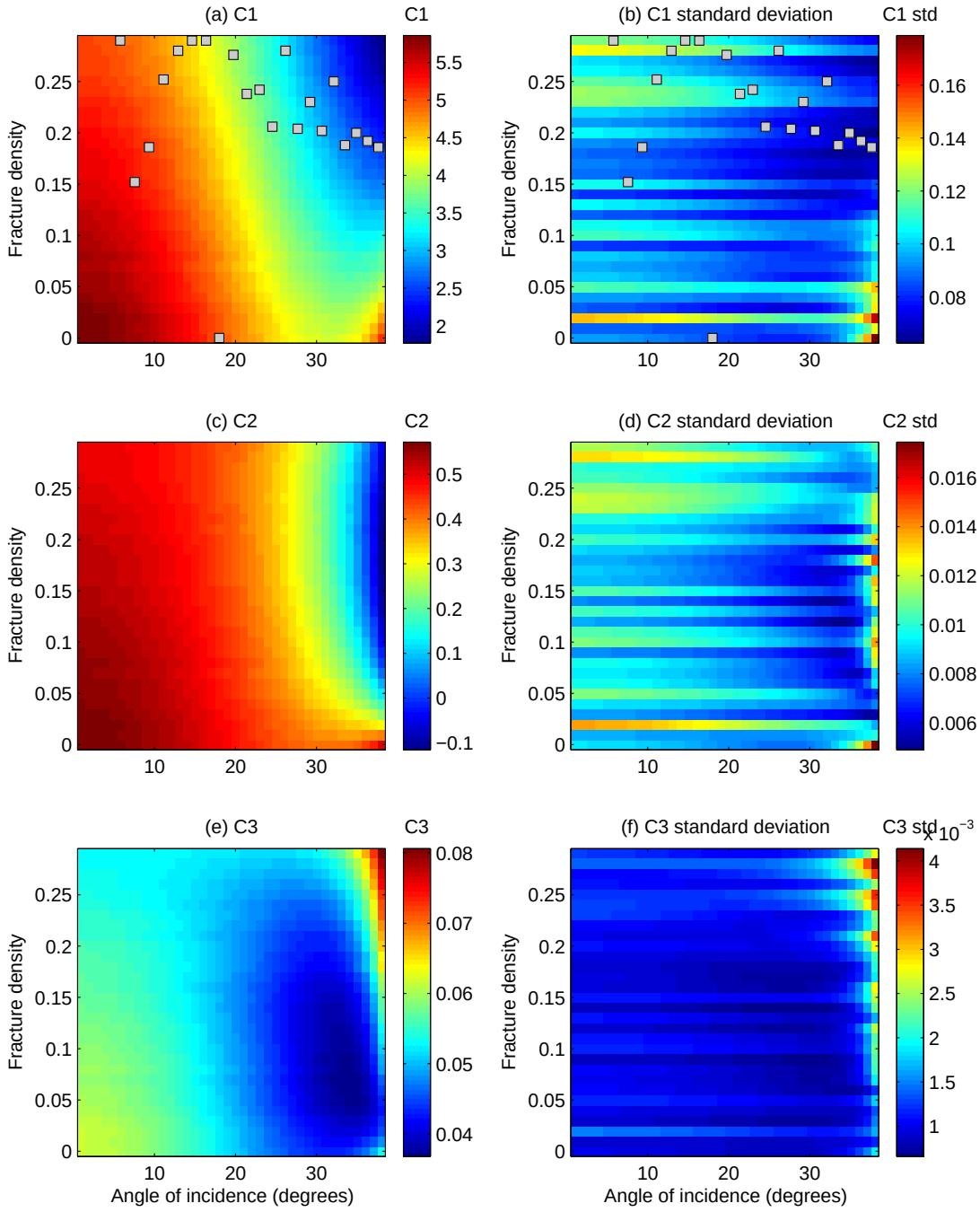

Figure 6.34: Mean and standard deviation for C1, C2 and C3 versus fracture density and angle of incidence for Model B for angles of incidence 1^o to 38^o. The standard deviation could be taken as a measure of the uncertainty in the inversion response. The grey squares show the inverted fracture density values. For angles of incidence 1^o to 38^o.

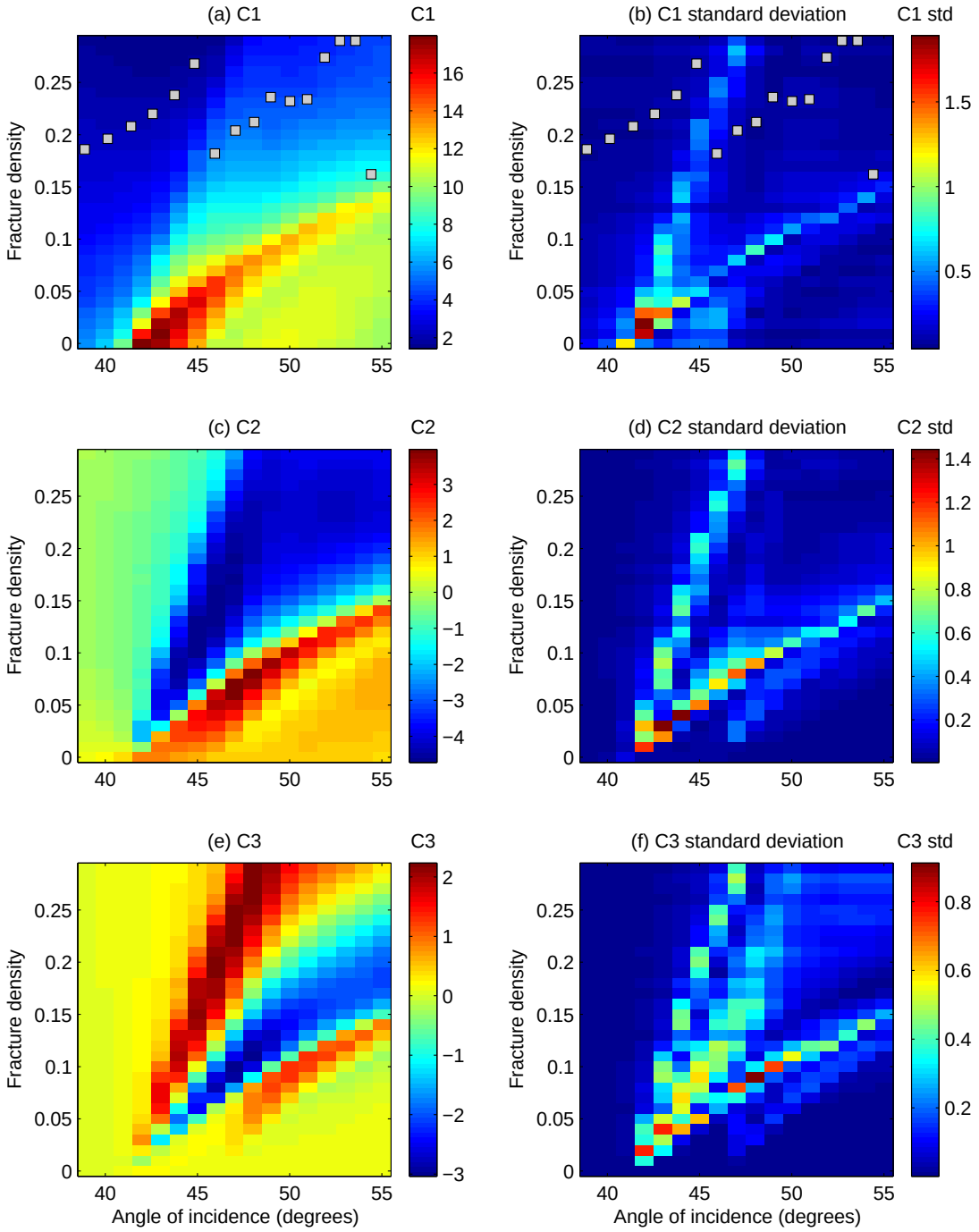

Figure 6.35: Mean and standard deviation for C1, C2 and C3 versus fracture density and angle of incidence for Model B. The standard deviation could be taken as a measure of the uncertainty in the inversion response. The grey squares show the inverted fracture density values. For angles of incidence 39^o to 55^o.

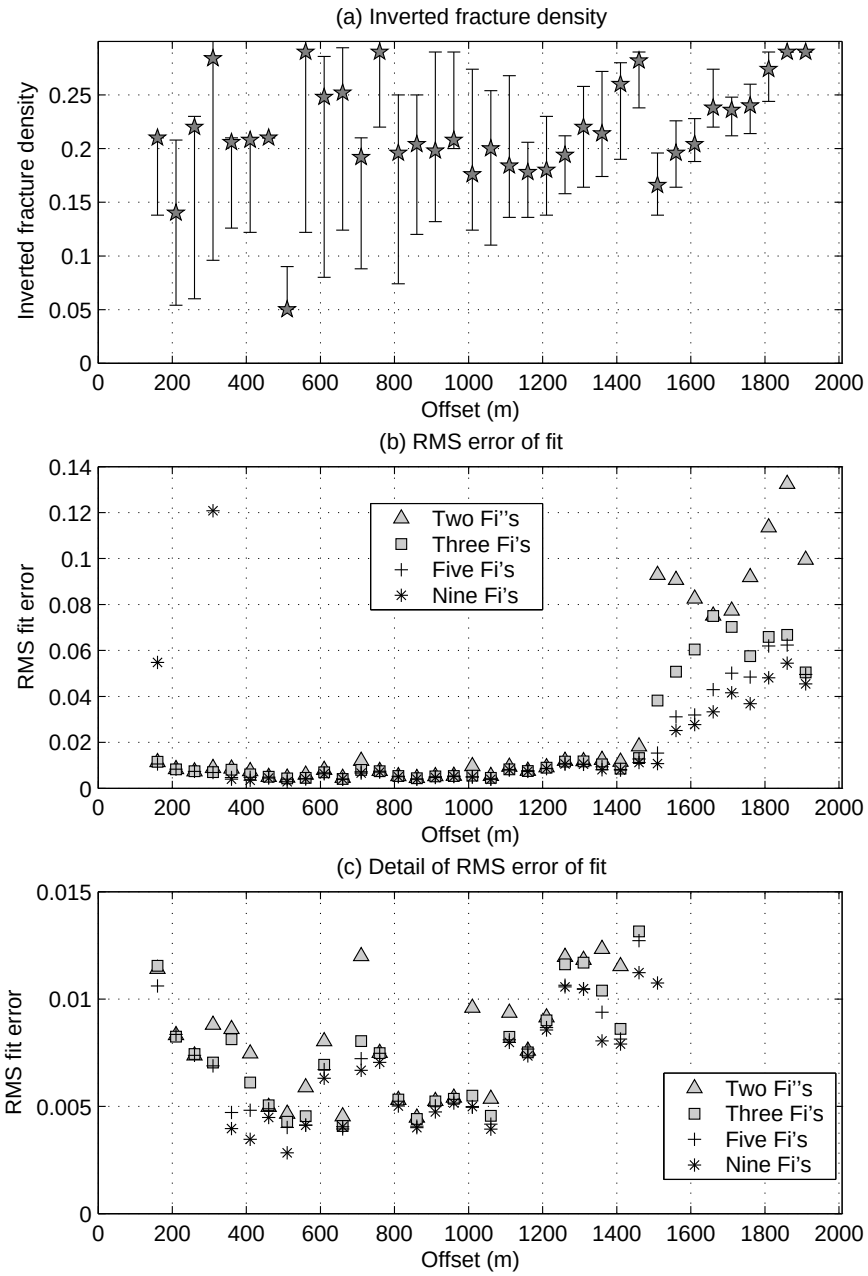

Figure 6.36: a) Inverted fracture density for all offsets for Model A. Top of fractured layer. b) RMS errors between measured and estimated reflection coefficients using two, three, five and nine basis functions. c) an expanded detail of b). The data are plotted for all measured offsets.

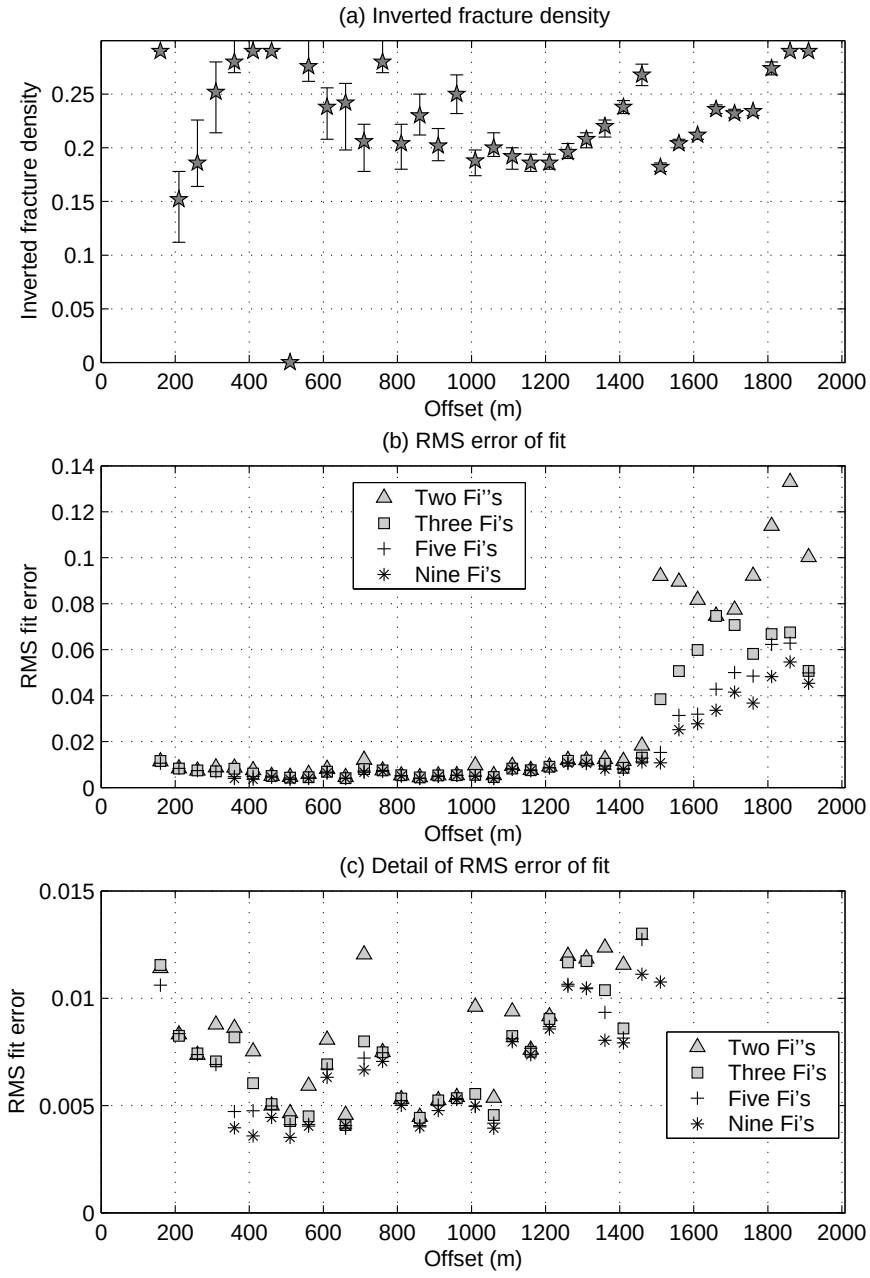

Figure 6.37: Similar to Figure 6.36 but for Model B.

The inverted fracture density using just one coefficient at a time is shown in Figure 6.40. It is clear from this figure that C_1 is the coefficient that provides the best inversion results in this example. Alternately, Figure 6.41 shows the inverted fracture density using a multiple regression with the first three and first two coefficients. When using a multiple regression, the inversion results are usually closer to the desired answer when more coefficients are used. Furthermore, when in a direction perpendicular to the fracture plane, the fracture density inverted using the multiple regression provides a more accurate answer than that obtained using only C_1. Nevertheless, in a direction parallel to the fracture plane, the multiple regression fails to provide a reasonable result, giving an answer less accurate than that obtained when using only C_1 (see figures 6.40 and 6.41).

An important observation resulting from the comparison of approaches I and II is that the difference in magnitude between the coefficients C_1, C_2 and C_3 is smaller for approach II than for approach I. Furthermore, in approach I the magnitude of all three coefficients increases significantly at larger offsets (due to the inclusion in the modelling of reflection coefficients with a non-zero imaginary part). From this point of view it can be said that approach II provides overall more stable coefficients when reflection coefficients with non-zero imaginary parts are included.

In terms of the fracture inversion results, both approaches lead to comparable outcomes. Both have a range of offsets (for approach I) and azimuths (for approach II) where the inversion is valid and leads to accurate results. Similarly, due to the nature of the methodology, both have ranges of offsets and azimuths where the information value given by the inversion process is diminished.

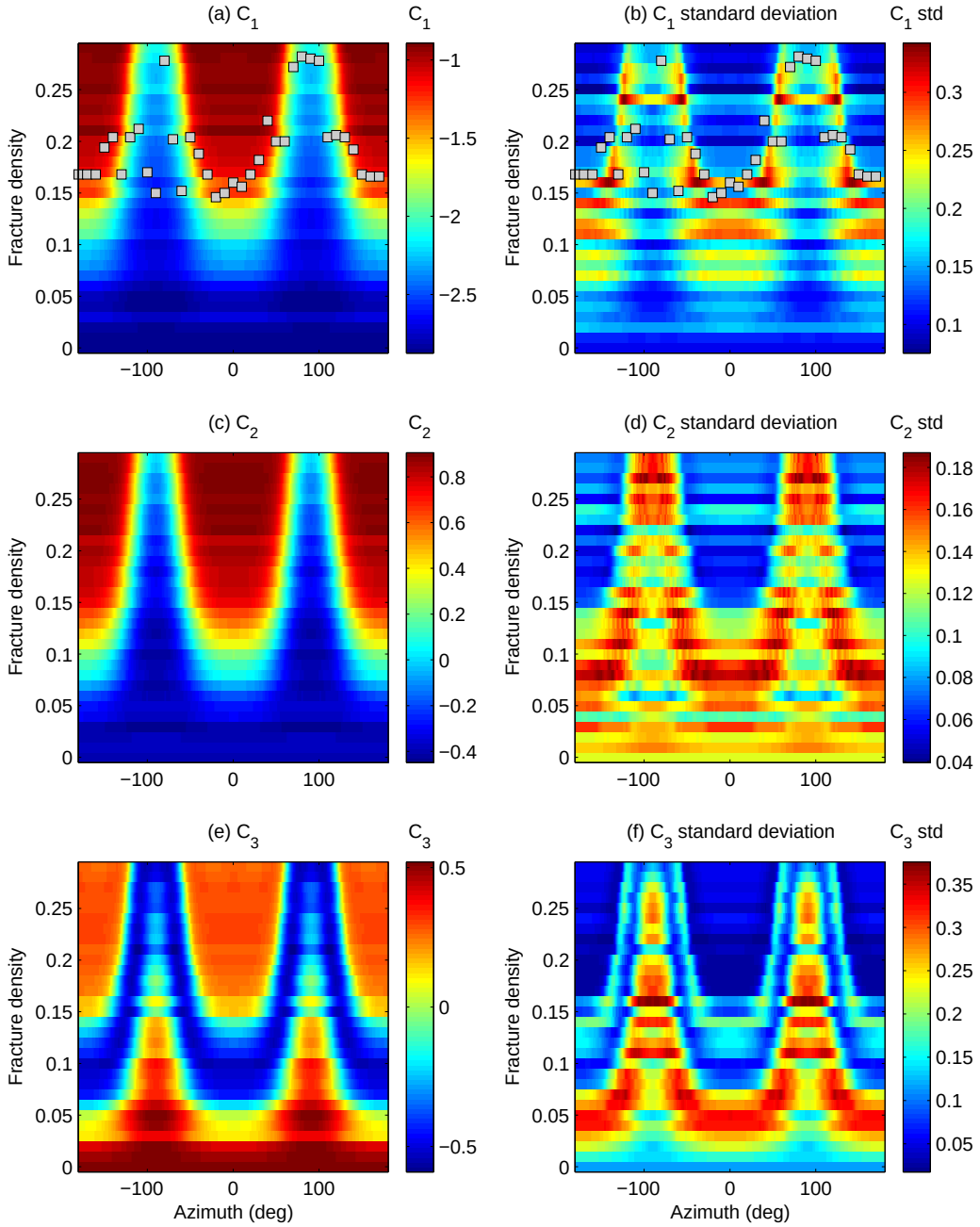

Figure 6.38: Maps of coefficients versus fracture density with basis functions varying with incidence angle.

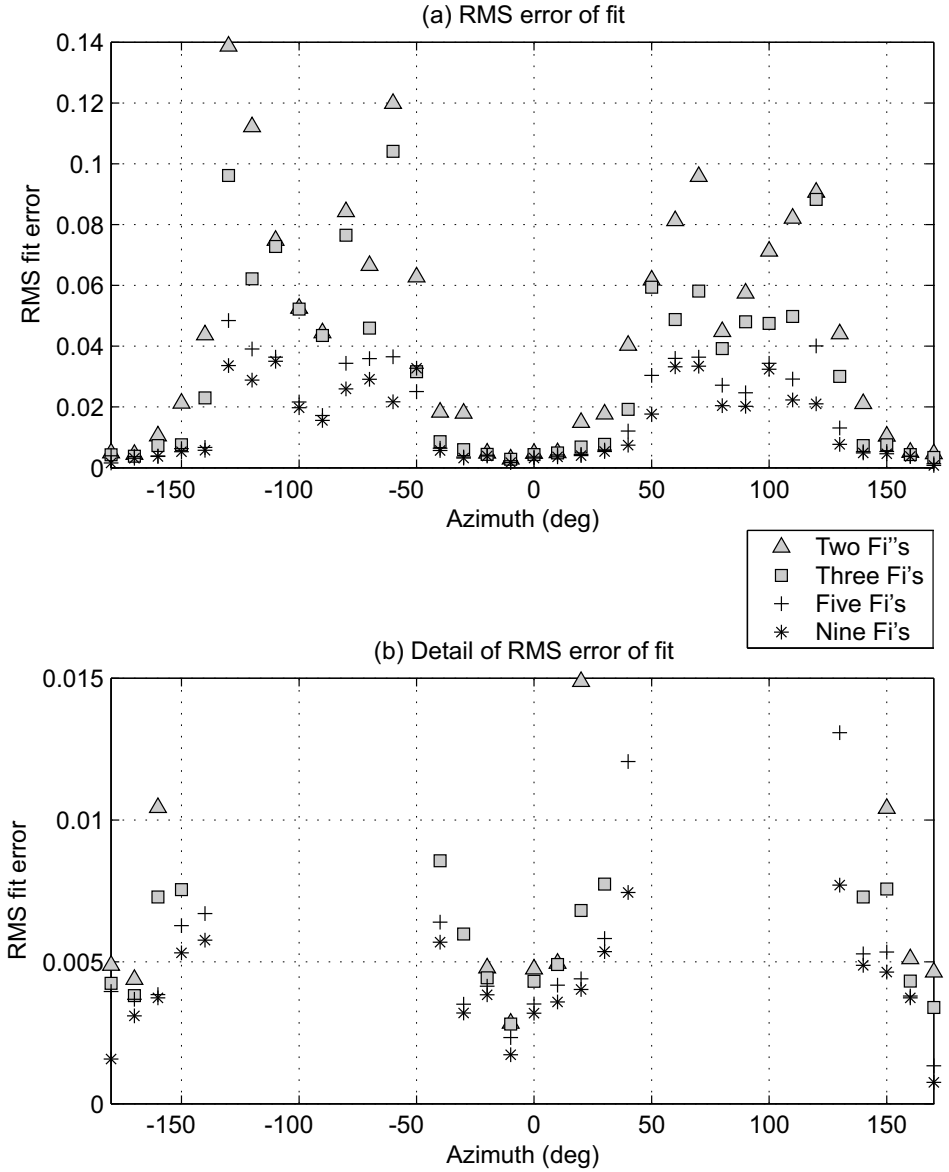

Figure 6.39: RMS error of fit from basis functions varying with incidence angle.

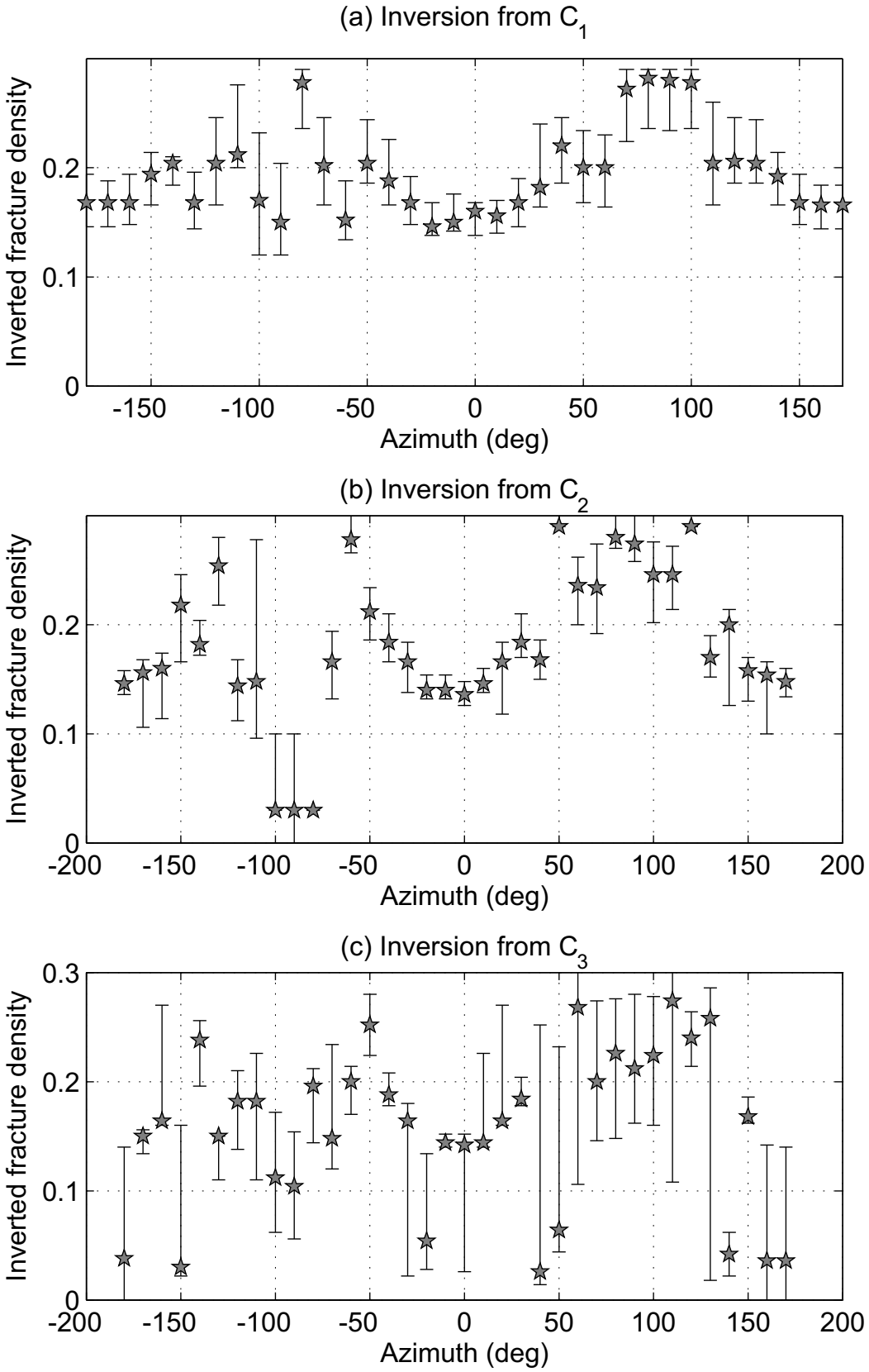

Figure 6.40: Inverted fracture density from coefficients C_1, C_2 and C_3 separately.

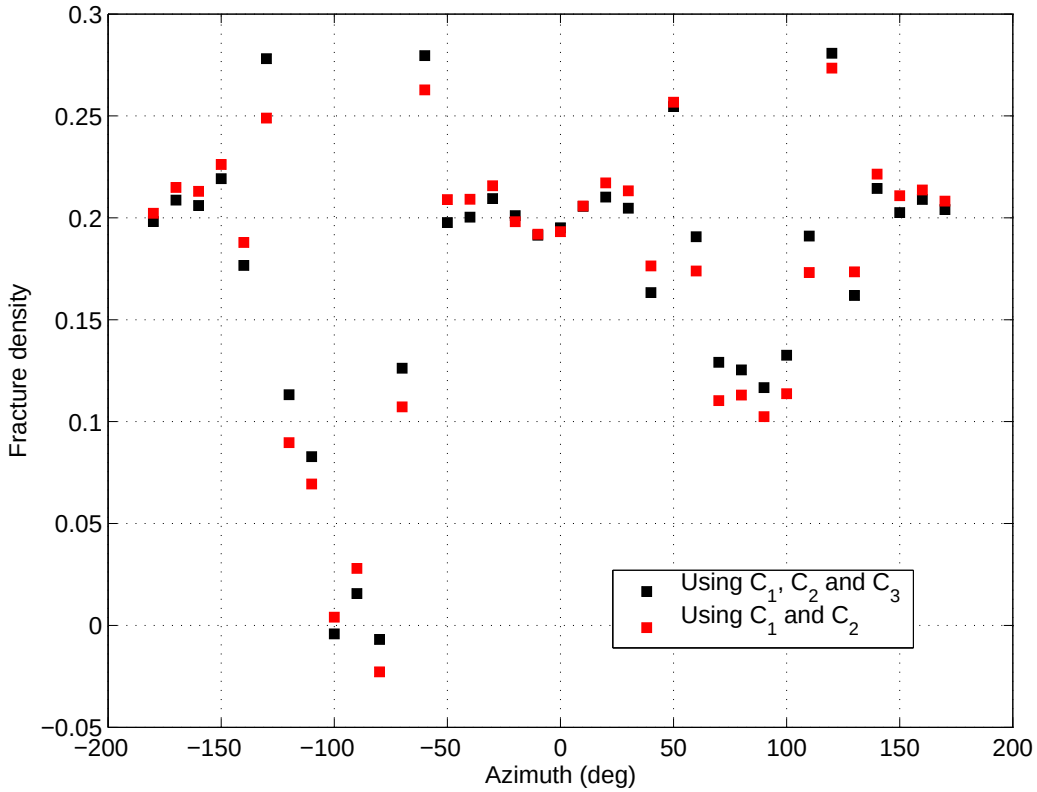

Figure 6.41: Inverted fracture density using a multiple regression between coefficients C_1, C_2 and C_3 and the modelled fracture density.

6.7 Conclusions

Discussion

At the beginning of this chapter I discuss the scaling from amplitudes to reflection coefficients. I justify the scaling by shot-point on three points: 1) There is a marked difference in the amplitudes at short offsets for different azimuths generating two distinct trends that separate as the offsets get smaller, 2) Each of these trends is caused by different sources, 3) There is no physical explanation for this effect as this is a laboratory-scale geological model where the structure and physical properties of the setting are known, and we expect that as the offsets get smaller and converge to zero-offset the amplitudes in all directions should converge. I argue then that the difference in amplitudes at short offsets is due to an acquisition artefact, (perhaps a transducer was changed during the acquisition process). This justifies the transformation from amplitudes to reflection coefficients using a scaling factor by shot-point. Furthermore the objective of this chapter is to prove the applicability of the method in seismic acquired from a laboratory-scale geological model, and not analysis of the seismic data itself.

The second approximation made in this chapter is using HTI symmetry to approximate the orthorhombic elastic constants of the fractured layer. Through construction of the laboratory model the anisotropy in the fractured medium is due to the presence of vertical fibre sheets, which in theory should result in an HTI medium. Wang et al. (2007) measure the elastic constants which are only weakly orthorhombic, but give no explanation as to why they are orthorhombic (instead of HTI). My assumption is that during the construction perhaps the effect of gravity made the medium weakly orthorhombic. In any case I find a reasonable set of parameters that, using the Chapman model, allow for calculation of HTI elastic constants that approximate the orthorhombic symmetry to an acceptable degree. This approximation is useful as it is possible then to model the HTI elastic constants for a constrained set of rock properties and a wide range

of fracture densities.

Conclusions

The method for inverting fracture density from azimuthal AVO using a set of optimal basis functions is applicable to seismic data provided we have prior knowledge of the velocities and densities of the medium. In the data used the overburden is isotropic, however an anisotropic overburden could complicate the AVOZ signal at the interface. As Sayers and Rickett (1997) show, an anisotropic overburden can be misinterpreted as due to the presence of fractures in the layer of interest.

I compare the inversion for two different levels of uncertainty (standard deviations) in the velocities and densities of the modelled reflection coefficients. The inversion results are more precise and accurate when lower uncertainty is used in the rock properties of the modelled reflection coefficients.

The inversion for fracture density of the physical geological model comes entirely from the coefficient that accompanies the function with the $cos(2\phi)$ behaviour. This contrasts with Varela et al. (2007) where the inversion is based on all three functions, but mainly on the coefficient that corresponds to the function that has a behaviour similar to a $cos(4\phi)$. This shows the versatility of the method, as in each application the inversion will be based on the coefficient or coefficients that have the highest correlation with the modelled fracture density.

The data present distinct behaviour in three different offset/angle of incidence ranges. At short offsets ($\theta < 33^o$) the azimuthal variations are very small such that the fit and inversion become meaningless. For very large offsets ($\theta > 45^o$) where the data reaches the critical angle, the modelled amplitudes increase strongly, unlike the measured ones. This might be due to the given physical properties of the model not being exactly right. Perhaps the non-fractured layers were only *assumed* to be isotropic (as it is not clear that Wang et al. (2007)

measured their rock properties[5]) and they might have a built-in gravity effect. Regardless of the speculative reason for this mismatch, the fact that we observe such differences between the modelled reflection coefficients and measured amplitudes also diminishes the information value from the inverted fracture density in this range.

For the middle range of offsets ($33^o < \theta < 45^o$) there are clear azimuthal changes in the measured amplitudes before and after the scaling, a good fit of the amplitudes with the orthogonal basis functions, and inverted fracture density values that can be validated from the geological model. In fact, the inverted values for both groups of modelled reflection coefficients are very close to the fracture density of the laboratory geological model, with better results obtained when the standard deviation in the distribution of rock properties is smaller. Nevertheless, for both models the inverted fracture density increases in this range as the angle of incidence approaches the critical angle ($\approx 45^o$). This is the range for which, on this data set, the inversion is optimal.

In general, due to the data behaviour in these three ranges, the final inverted fracture density values should be related to the offset/angle of incidence range they correspond to.

Finally, I compare two different approaches to the methodology. The first approach (I) is based on finding basis functions that vary with azimuth, whereas in the second (II) they vary with incidence angle. I find that for approach I the inversion results are valid for a given offset range. Similarly, for approach II the inversion is valid for a range of azimuths, namely those perpendicular to the fracture strike. An advantage of approach II is that the difference in magnitude between the three coefficients used is much smaller compared to approach I, which makes the inversion more stable when including the smallest coefficient

[5]Wang et al. (2007) mention that they measure the elastic constants of the fractured layer. However they provide the physical properties of all the isotropic layers without mentioning whether these properties were also measured.

(C_3) in the inversion process.

Chapter 7

Discussion and conclusions

7.1 Discussion

Seismic anisotropy is widely used in fracture characterisation as it has the potential to provide useful information on fracture properties such as the main orientations and the fracture density. However, independent measurements to verify the studies are rare, and questions have been raised about the reliability of these studies and how to calibrate them.

Azimuthal studies of seismic travel time, amplitude and attenuation give useful information on the anisotropy of subsurface rocks (Tsvankin and Lynn, 1999, Marrett et al., 2007). This anisotropy can be due to the presence of fractures, lateral heterogeneities or dipping layers (Tsvankin and Lynn, 1999). At reservoir depths we expect to find mainly vertical fractures, as at such depths the vertical effective stress is much larger than the horizontal stresses, causing any non-vertical fractures to close (Worthington, 2008, Tsvankin and Lynn, 1999).

Although shear wave splitting (birefringence of S-waves) has proven to be a useful tool in seismic fracture characterisation (Mueller, 1992, Crampin, 1985) there are various reasons for the continuous use of P-wave data for this purpose. Tsvankin and Lynn (1999) list the following advantages for using P-wave data: 1) lower cost of P-wave acquisition compared to surveys for acquiring S-waves; 2) usually higher data quality of P-waves compared to S-waves; 3) development of

recent azimuthal techniques on P-wave data for obtaining principal directions and magnitude of anisotropy. To this list I add that the industry has a large history of acquiring P-wave seismic data (Corrigan et al., 1996) and thus the availability of P-wave data for research purposes is higher than that of S-wave surveys, as illustrated by the data sets used in this thesis.

On azimuthal VSP studies

I began my research by performing azimuthal analyses of travel time, amplitude and attenuation or frequency content on VSP data sets, including time-lapse data, from two different fields in the search for azimuthal variations that can be related to the present fracture networks. More precisely, I searched for the azimuthal orientations showing the directions of minimum travel time, maximum amplitude and minimum attenuation or maximum frequency content. Based on rock physics models, these orientations provide the main fracture network of the section under study if the medium presents an HTI symmetry due to vertical fractures. According to effective medium theories, should two or more sets of vertical fractures with different orientations be present, the azimuthal analysis will provide an average of the orientations weighted by their respective fracture densities (Liu et al., 2000). However, at the starting point we may not know whether fractures are present in the area, or whether they are detectable through the acquired seismic. The assumptions behind the analysis of both VSP field studies are that there are no artefacts from the wavefield separation, that the layers are horizontal and that the subsurface fractures are aligned in vertical sets.

In the first study, I calculated relative instantaneous frequency for walk-around VSP's around three wells from a carbonate field in Oman (with one well including two time-lapse surveys), and analysed the results in conjunction with amplitudes and travel time. I chose to use a relative measure of the instantaneous frequency (with respect to a given direction) for a specific event due to the difficulty in measuring absolute attenuation (Liu et al., 2007), whereas for azimuthal stud-

ies a relative measure of attenuation is practical and sufficient (Liu et al., 2007, Maultzsch et al., 2007). Scattering of waves will occur if the size of the heterogeneities (fractures) are of the order of the wavelength of the propagating wave or less (Burns et al., 2007). Even though we would like to discriminate the effect from both phenomena, intrinsic attenuation (due to the physical properties of the porous rock and its fluids), and the attenuation due to scattering of waves, this separation is difficult and may not be possible (Liu et al., 2007). Note that scattered energy from clustering of large fractures (fracture corridors) has also been used in the literature for inverting for fracture properties (Willis et al., 2006, Burns et al., 2007, Willis et al., 2007).

I analysed the responses of these attributes for four seismic events, which included the direct arriving P-wave, an upgoing P-wave in the R-component, and two downgoing PS converted waves in the N-component. I found that when all the data analysed from the three wells and the three different attributes are compiled together, no dominant azimuthal orientation prevails. This shows that there is no single dominating fracture network for the whole depth section and lateral area (the wells are ≈500m, 500m and 300m away from each other). Yet, when separating the data into different depth sections, with the shallow section containing the Fiqa shales and the fractured carbonates from the Natih Formation, azimuthal variations are observed for different attributes in different wells. From these observations, I deduced two different principal orientations for the deeper and shallow sections.

In the shallow section dominant orientations were found at N40E and N70E, and secondary orientations at N40W and NS. The NE orientation is persistent throughout the different attributes in this section, and could be interpreted as the main orientation of the fracture plane for the shallow receiver levels. Furthermore, the maximum horizontal stress for the region where the Omani field is located has a N40E orientation (Heidbach et al., 2008). Additionally, in the Natih field (located 150Km NNW of the field under study), Van der Kolk et al.

(2001) find that the Natih fractured carbonates present one set of open fractures with a NE-SW orientation, which coincides with the main orientation I find in the shallow section. Yet, the large distance between the fields would allow for independent mechanisms causing fracturing in each field, which means that the fracture networks are not required to exhibit the same behaviour. It is common practice to interpret the direction of open fractures to be aligned with that of the maximum horizontal stress as it is expected that in other directions the cracks or fractures will close (Sayers, 2007, Lynn et al., 1996). However, as Marrett et al. (2007) point out, open fractures are not necessarily oriented in the direction of maximum horizontal stress as is commonly assumed. Precipitations within the fractures can cause closed fractures to open or formerly open fractures to close; measurements of fractures from well log data are thus essential to assess this phenomenon. Nevertheless, with the two soft arguments mentioned above supporting our interpretation, it appears that the fracture network of the Natih formation in our field of study exhibits the same main orientation as that in the Natih field and the regional maximum horizontal stress in our field of study. However no hard measurements are available to verify this.

For the deeper section dominant orientations were found at N40W and N80W, with a secondary orientation at N30E. The general NW orientation could be interpreted as the primary fracture orientation for the deeper receiver levels. Even though there may be some persistent orientations in each section, it is often observed that different attributes at the same well and depth section show different dominant orientations. A clear example is given by event A, where for the three different surveys there is a dominant NE-SW orientation for the travel time and amplitude, whereas the frequency attribute shows a NW-SE orientation. I put forward two scenarios that could explain the above observations. In the first one I suggest that a fracture network with more than one set of aligned cracks in different directions is present. These sets of cracks can vary in size, fluid content, connectivity and aperture (they can be open or closed), making some attributes more sensitive to one particular set which could explain the effect de-

scribed above. Liu et al. (2007) show through field examples and a modelling study that azimuthal variations in travel time or velocity and attenuation do not always coincide, and if such a difference is observed these differences could provide additional information on the fracture properties. In a modelling study Liu et al. (2007) show that for a fracture network consisting of two sets of fractures, one set filled with brine, and one set dry, the azimuthal variations will be different for travel time and velocity compared to attenuation, as attenuation will be influenced by the presence of fluids, whereas the velocity will be affected by the presence of dry cracks or fractures. Based on this argument, in the first scenario I interpret the paradox in directions seen for the deeper section to be due to the presence of more than one fracture set with different fluid content in each set.

A second scenario would have noise and land acquisition artefacts lowering the signal to noise ratio of the data and influencing the seismic signal in a random way - or worse in a systematic way. In fact, seismic noise reduction required that for the surveys acquired in 2002 every trace used comes from averaging three shots in the same location. For the surveys acquired in 2004 and 2005 the number of shots per shot location was increased to 10 in an attempt to increase the signal to noise ratio. However, even the presence of noise, is unlikely to affect the data as a function of source-receiver azimuth. Because azimuthal anisotropy is observed throughout the different attributes, even if they do not always exhibit the same symmetry planes (in addition to the discussed explanation for this paradox), I argue in favour of the first scenario.

In my second study, of the Weyburn field in Canada, I performed multi-attribute azimuthal analysis on 3D time-lapse VSP data. The various independent attributes include travel time, peak frequency, angle of incidence and amplitudes. In contrast to the study on the Omani data, I only analysed the direct arriving P-waves. I created rose diagrams for each attribute for different offsets in the base and monitor surveys. In general, the dominant direction in the rose diagrams of the different attributes trends in a NE-SW direction, which coincides

with that described by independent studies of the region as the orientation of the primary fracture network (Li, 2002, Li, 2003, Terrell et al., 2002). Three other less dominant orientations are recognised, one of which has the orientation of the secondary fracture network which has also been described independently to be in a NW-SE direction (Li, 2002, Terrell et al., 2002). Compared to the study on the Omani field, the Weyburn field has various independent studies on surface seismic and VSP data that allow the validation of my analysis.

I find that in terms of the orientations extracted from the attributes, the time-lapse changes in both VSP data sets (Omani and Weyburn) are of second order compared to the changes in orientation between two different wells in the Omani field or two different offsets in the Weyburn field. This means that to first order any changes in the reservoir due to replacement of fluids are not detected in terms of directional changes of the attributes. It remains to examine changes in the strength of the attributes through the time-lapse data.

Although I identify correlations between independent fracture studies or geological structures and stresses in the area with the findings from the VSP data, the usefulness of these correlations is arguable, as no independent hard measurements at the well location (from core or FMI logs) are available to calibrate our results. A more robust inversion of fracture properties would require further knowledge of the physical properties of the medium and forward modelling of the seismic response. A rock physics theory would be required to model the elastic response of the fractured rock. In the second part of this thesis I developed and tested a method for fracture density inversion, which is an attempt to provide a more quantitative basis for the characterisation of fractures.

On the inversion method

Due to the complex non-linear relationship between rock properties and the seismic response, general linearised approximations are commonly used for AVO

analysis. However, these approximations perform poorly at large angles of incidence where the effect of fractures is more significant. I established a linearised relationship between the rock properties and fracture density with the azimuthal AVO response for a specific model based on prior information of the rock properties. A rock physics theory was used for the modelling of the fractured rock elastic constants. It is worth stating that the choice of the rock physics theory used here does not alter the conceptual basis of the method.

I tested the method on synthetic surface seismic CMP gathers acquired above a two-layer model of an isotropic layer over an anisotropic HTI halfspace for values of high and low fracture densities. I found that for the model used, there is a robust relationship between fracture density and the weights obtained from the singular value decomposition of the reference curves, as is desired. Furthermore, from the application of the method to seismic data from a laboratory-scale physical geological model, I showed that the method for inverting fracture density from azimuthal AVO using a set of optimal basis functions is applicable to seismic data provided we have prior knowledge of the velocities and densities of the medium. Additionally, I compared the inversion of the modelled reflection coefficients for two different levels of uncertainty (standard deviations) in the velocities and densities, and showed that the inversion results are more precise and accurate when less uncertainty is used in the rock properties of the modelled reflection coefficients, as expected. Note that in the application of the method to the physical modelling study, an approximation was made to describe the weakly orthorhombic symmetry of the fractured layer with an HTI symmetry. I justify this approximation by the fact that the fractured layer in the physical model is composed of vertically aligned fibre sheets (Wang et al., 2007) and by definition should exhibit an HTI symmetry (Tsvankin, 2001, Mavko et al., 1999).

I compare two different approaches to the methodology in the application to the physical modelling data. The first approach (I) is based on finding basis functions that vary with azimuth, whereas in the second (II) they vary with incidence angle.

I find that for approach I the inversion results are valid for a given offset range. Similarly, for approach II the inversion is valid for a range of azimuths, namely those perpendicular to the fracture strike. An advantage of approach II (for this data set) is that the magnitude of the smallest coefficient is larger compared to approach I, which makes the inversion more stable when including the smallest coefficient (C_3) in the inversion process.

Through the synthetic and physical modelling studies I argue that the coefficient on which the inversion will be based must be determined on a case by case basis, as it will change depending on the contrast between the elastic constants across the boundary of interest. In the synthetic study I showed that the coefficient having the highest correlation with fracture density is C_3, whereas in the physical modelling study C_1 presents a higher correlation. This shows the versatility of the method in different situations and emphasises the argument that prior to inversion the behaviour of the coefficients must be analysed. Furthermore, the inversion will only be possible if a unique (one-to-one) relationship between the fracture density and the coefficients exists. If all coefficients present a non-unique relationship with fracture density, I recommend reducing the variability in the input rock properties, as a larger standard deviation in their distributions can have an effect on the dependence of the coefficients on fracture density.

In both the synthetic and physical model I find that the inversion is optimal for a certain range of offsets/angles of incidence. Additionally, within these ranges the inverted values of fracture density match those of the model (synthetic or physical) within the error. There are several factors that may limit the range of offsets for an optimal inversion. For example, at short offsets the data may not present a strong enough azimuthal anisotropy effect for the inversion, as is the case in the physical modelling data set. Another potential factor is that the relationship between fracture density and the coefficient chosen for inversion may not be linear for a certain offset range, as is shown in the synthetic study. This implies that the optimal range for inversion must also be studied on a case by

case basis, depending on the behaviour of the data.

Limitations of method

A characteristic aspect of the method presented is that, as the inversion relies on the input modelled azimuthal AVO curves, a careful choice of the model parameters (rock properties and their standard deviations) is essential for the inversion process. This is a limitation, or constraint of the method, as the inverted fracture density values will only be valid if the rock properties of the field data fall within the range of the modelled ones. Often in exploration geophysics such information is not available. Thus, the method proposed here is ideally suited to a mature field with scattered hard measurements of V_p, V_s, density and fracture density from well and FMI logs, where an analysis of the fracture network between the wells is desired. Such a study was carried out by Chao et al. (2009) with promising results on the applicability of the method for field seismic data. Possible complications in the application of the method to field seismic data will be in the calibration process from the amplitudes picked on the gathers to the reflection coefficients. A robust calibration is possible when well log or core measurements and VSP or check-shot data are available.

It is worth mentioning that some of the assumptions common to effective medium theories, on which our method relies, may not be exhibited by naturally occurring fractures. Common assumptions are that fractures in the subsurface are vertically aligned, equally spaced, are shaped like disks and exhibit the same size. Marrett et al. (2007) discuss these assumptions and problems found in studies of fractures using geophysical methods. They emphasise that fractures in the subsurface are not equally spaced, but tend to be distributed in clusters, especially for the case of large fractures. A few large interconnected fractures will then increase the permeability of the rock significantly compared to the same number of large but isolated fractures. In addition they demonstrate that the size of fractures varies following a power law distribution, so the assumption of

a single size of fractures is unrealistic. Marrett et al. (2007) also elaborate on the common assumption of a single set of aligned fractures. They mention that rocks may have many sets of open fractures, and within each set fractures are not always parallel. They explain this by isotropic loading which may lead to the generation of randomly orthogonal fracture sets, or by the perturbation of the stress field due to the presence of large faults. Furthermore, in the presence of an orthogonal set of fractures the resulting anisotropy may be less than that from each individual fracture set (Marrett et al., 2007). The method proposed in this thesis relies on the forward modeling of the fracture response based on effective medium theories. Any limitations imposed by the choice of effective medium model used must then be considered in the application of the method.

Implications of work

In terms of the issues to be addressed, the method presented in this work has been developed for the simple case of one layer over a halfspace, which means that no effects from shallower layers are present. In addition, the overburden was modelled as being isotropic, yet an anisotropic overburden could complicate the AVOZ signal at the interface. Sayers and Rickett (1997) show that an anisotropic overburden can lead to misinterpretation; wrongly implying the presence of fractures in a deeper layer. Hence, in the application of the method at an interface below multiple layers, the potential effect of the overburden should be considered.

I have argued that the coefficient that has the highest correlation with fracture density must be determined on a case by case basis. It would be useful to further examine the nature of this correlation; for example, does it vary depending on the AVO class, impedance contrast, and/or the spread in the impedance ranges modelled? If any such correlations exist, this would provide a more structured methodology for the inversion.

The conceptual basis of the method is not restricted to any rock property in

particular, and has no special structural molding to fracture density. It thus has the potential to be modified to estimate other desirable and unknown rock properties. For example, it could be applied to density inversion for a layer of rocks with little or no significant fracturing. Moreover, it would be worthwhile to implement the inversion for attenuation from seismic data, as attenuation is highly correlated with fracture density and fluid content.

Likewise, the method is not solely confined to use with reflected waves; theoretically, it can equally be applied to transmitted waves. Consequently, if deployed in conjunction with analysis of VSP data it could benefit the interpretation of the azimuthal research in a more integrated study.

A prospective continuation of this research would lie in finding possible connections between the model-based approach of my work and an empirical relationship between fracture size and fracture compliance suggested by Worthington (2007). Worthington (2007) discusses the potential benefits of finding a relationship between measurements of fracture compliance at different scales. Currently there are very few field measurements of fracture compliances and most forward modelling of the fractured rock is based only on theoretical estimates (Worthington, 2007). Assuming that the inversion method I present is modified to invert for fracture size, I suggest two outcomes, 1)assuming we know an empirical scaling relationship between fracture size and fracture compliance, the application of our method could then serve as a platform to obtain more field measurements of fracture compliance, 2)assume the inversion method for fracture size is undertaken with a very good knowledge of the rock properties, furthermore, assume the field site has measurements of fracture compliance at two different scales (such as that reported by Lubbe and Worthington (2006)). In this scenario, I argue that our inversion results could then be used to build an empirical scaling relationship, or to accept or reject any existing one.

7.2 Conclusions

In this thesis I researched the problem of fracture analysis using surface seismic and VSP data. I performed multi-attribute analysis, including frequency studies on field VSP data from two different carbonate fields. I compared the findings to independent data available in the region and found that the interpreted fracture orientations from the attribute analyses correlated with either independent fracture studies in the area, the principal axis of major faults surrounding the field, or the maximum horizontal stress of the area studied. However, a need for more quantitative fracture characterisation was evident. Thus, I developed a model-based method for fracture properties inversion from seismic and rock physics data. The method is based on establishing a linear relationship between fracture properties and the seismic signal on a case by case basis with the use of prior information on the rock properties. The relationship is established by developing a new set of basis functions for the AVOZ response of the fractured layer. I tested the method using synthetic seismic data and seismic data acquired from a physical geological model in a laboratory.

This thesis shows that for a reliable interpretation of seismic data in terms of fracture properties, independent measurements used for calibrating the findings are necessary. I expose through the present work the imperative need for using effective medium theories that model the elastic properties of the fractured rock for a quantitative study. This thesis demonstrates that a quantitative inversion method for fracture characterisation can work successfully on seismic data given prior knowledge of the rock properties. Furthermore, I show that a model-based linear relationship between fracture properties and the seismic signal can be established on a case by case basis and be used for a quantitative inversion.

The main steps of the method for fracture density inversion from a two layer model of an isotropic media over an HTI medium containing vertical fractures are as follows:

a) Set rock property ranges and distributions for both layers using available petrophysical data.

b) Model the elastic constants of the fractured layer for different fracture densities using a rock physics theory.

c) Create reference AVOZ curves with varying fracture density and incidence angle using the range of elastic properties set in step a). Store these AVOZ curves in matrix R such that every row has a different azimuthal angle and every column a different angle of incidence and rock properties.

d) Calculate the singular value decomposition of matrix R and obtain the new set of orthogonal AVOZ basis functions and weighting coefficients.

e) Find a suitable relationship between the coefficients resulting from the SVD and the fracture density of the modelled reference AVOZ curves.

f) Fit the measured reflection coefficients to the new basis functions and solve for the corresponding weights.

g) Invert for fracture density using the inverted coefficients and map them into the relationship (established in e) between the coefficients of the modelled AVOZ curves and fracture density.

Inversion methods attempt to quantify the information and uncertainties of the rock properties extracted from the seismic data. This thesis highlights the importance of *a priori* information and the use of rock physics theories for a reliable quantitative inversion and demonstrates the potential of their use in conjunction.

References

Adam, L., Batzle, M., and Brevik, I., 2006, Gassmann's fluid substitution and shear modulus variability in carbonates at laboratory seismic and ultrasonic frequencies: Geophysics, **71**, F173–F183.

Aki, R., and Richards, P. G., 1980, Quantitative seismology - theory and methods:, volume 1, W. H. Freeman and Company.

Alhussain, M., Liu, E., Gurevich, B., Urosevic, M., and Ur Rehman, S., 2007, AVOaz response of a fractured medium: Laboratory measurements versus numerical simulations: 77th Annual Internat. Mtg., Soc. Expl. Geophys., Expanded Abstracts, **26**, no. 1, 254–258.

Arfken, G., 1985, Mathematical methods for physicists: Academic Press, New York.

Barnes, A. E., 1991, Instantaneous frequency and amplitude at the envelope peak of a constant-phase wavelet: Geophysics, **56**, 1058.

Barnes, A., 1993, When the concepts of spectral frequency and instantaneous frequency converge: The Leading Edge, **12**, no. 10, 1020–1023.

Barton, N., 2006, Rock Quality, Seismic Velocity, Attenuation And Anisotropy: Taylor & Francis Group.

Belsley, D., Kuh, E., and Welsch, R., 2005, Regression diagnostics: Identifying influential data and sources of collinearity: Wiley-Interscience.

Berryman, J., 1980, Long-wavelength propagation in composite elastic media: The Journal of the Acoustical Society of America, **68**, 1809–1831.

Berryman, J. G., 1999, Origin of Gassmann's equations: Geophysics, **64**, no. 5, 1627–1629.

Biot, M. A., 1956, Theory of Propagation of Elastic Waves in a Fluid-Saturated Porous Solid. I. Low-Frequency Range: Journal of the Acoustical Society of America, **28**, 168.

Blacquire, G., and van Veldhuizen, E., 2003, Physical modeling versus numerical modeling: SEG, Expanded Abstracts, **22**, no. 1, 2429–2430.

Brown, R., and Korringa, J., 1975, On the dependence of the elastic properties of a porous rock on the compressibility of the pore fluid: Geophysics, **40**, 608.

Burns, D., Willis, M., Toksoz, M., and Vetri, L., 2007, Fracture properties from seismic scattering: The Leading Edge, **26**, no. 9, 1186–1197.

Burrowes, G., and Gilboy, C., 2000, Investigating Sequestration Potential of Carbonate Rocks during Tertiary Recovery from a Billion Barrel Oil Field, Weyburn, Saskatchewan: the Geoscience Framework (IEA Weyburn CO 2 Monitoring and Storage Project): The Geoscience Framework. IEA Weyburn CO2 Monitoring and Storage Project Report.

Castagna, J., and Backus, M., 1993, Offset-dependent reflectivity: Theory and practice of AVO analysis: Society of Exploration Geophysicists.

Castagna, J., Sun, S., and Siegfried, R., 2003, Instantaneous spectral analysis: Detection of low-frequency shadows associated with hydrocarbons: The Leading Edge, **22**, no. 2, 120–127.

Causse, E., and Hokstad, K., 2005, Seismic processing with general non-hyperbolic travel-time corrections: US Patent 6,839,658 B2.

Causse, E., Riede, M., Van Wijngaarden, A., Buland, A., Dutzer, J., and Fillon, R., 2007a, Amplitude analysis with an optimal model-based linear AVO approximation: Part I - Theory: Geophysics, **72**, C59–C69.

——— 2007b, Amplitude analysis with an optimal model-based linear AVO approximation: Part II - Field data example: Geophysics, **72**, C71.

Chao, G., Maultzsch, S., Cadoret, T., Deplante, C., and Varela, I., 2009, Fracture characterization of a tight gas reservoir using seismic attributes derived from singular value decomposition of azimuthal AVO data: International Petroleum Technology Conference, Doha, Qatar.

Chapman, M., Zatsepin, S., and Crampin, S., 2002, Derivation of a microstructural poroelastic model: Geophysical Journal International, **151**, no. 2, 427–451.

Chapman, M., 2003, Frequency dependent anisotropy due to meso-scale fractures in the presence of equant porosity: Geophysical Prospecting, **51**, 369–379.

Cheadle, S., Brown, R., and Lawton, D., 1991, Orthorhombic anisotropy: A physical seismic modeling study: Geophysics, **56**, no. 10, 1603–1613.

Chichinina, T., Sabinin, V., and Ronquillo-Jarillo, G., 2006, QVOA analysis: P-wave attenuation anisotropy for fracture characterization: Geophysics, **71**, C37–C48.

Chopra, S., Alexeev, V., and Lanteigne, J., 2004, New VSP wavefield separation methods: CSEG National Convention.

Coates, R., and Schoenberg, M., 1995, Finite-difference modeling of faults and fractures: Geophysics, **60**, 1514.

Corrigan, D., Withers, R., Darnall, J., and Skopinski, T., 1996, Fracture mapping from azimuthal velocity analysis using 3D surface seismic data: 66th Annual Internat. Mtg., Soc. Expl. Geophys., Expanded Abstracts.

Crampin, S., McGonigle, R., and Bamford, D., 1980, Estimating crack parameters from observations of P-wave velocity anisotropy: Geophysics, **45**, 345.

Crampin, S., 1985, Evaluation of anisotropy by shear-wave splitting: Geophysics, **50**, 142–152.

Dasgupta, R., and Clark, R., 1998, Estimation of Q from surface seismic reflection data: Geophysics, **63**, 2120.

Dasios, A., Astin, T., and McCann, C., 2001, Compressional-wave Q estimation from full waveform sonic data: Geophysical Prospecting, **49**, 353–373.

de Franco, R., and Musacchio, G., 2001, Polarization filter with singular value decomposition: Geophysics, **66**, 932.

Dvorkin, J., Mavko, G., and Nur, A., 1995, Squirt flow in fully saturated rocks: Geophysics, **60**, no. 1, 97–107.

Endres, A., and Knight, R., 1997, Incorporating pore geometry and fluid pressure communication into modeling the elastic behavior of porous rocks: Geophysics, **62**, no. 1, 106–117.

Evans, B., McDonald, J., and French, W., 2007, Seismic physical modelling of reservoirs, its past, present and future: ASEG Extended Abstracts.

Fatkhan, M., and McDonald, J. A., 2001, Numerical and physical modelling of P-wave AVO response for fractured media: Exploration Geophysics, **32**, 279–283.

Freire, S., and Ulrych, T., 1988, Application of singular value decomposition to vertical seismic profiling: Geophysics, **53**, no. 6, 778–785.

Galikeev, T., and Davis, T., 2003, Reservoir modeling of a thin carbonate reservoir using geostatistics and 4-D seismic attributes, Weyburn field, Saskatchewan, Canada: 73th Annual Internat. Mtg., Soc. Expl. Geophys., Expanded Abstracts, **22**, no. 1, 1354–1357.

Gassmann, F., 1951, Uber die elastizitat poroser medien: Vierteljahrsschrift der Naturforschenden Gesellschaft in Zurich, **96**, 1–23.

Geertsma, J., and Smit, D., 1961, Some aspects of elastic wave propagation in fluid-saturated porous solids: Geophysics, **26**, no. 2, 169–181.

Gibson, R. L., Theophanis, S., and Toksöz, N. M., 2000, Physical and numerical modeling of tuning and diffraction in azimuthally anisotropic media: Geophysics, **65**, no. 5, 1613–1621.

Grechka, V., and Tsvankin, I., 1998, 3-D description of normal moveout in anisotropic inhomogeneous media: Geophysics, **63**, no. 3, 1079–1092.

Hadi, A., 1996, Matrix algebra as a tool: Duxbury Press Belmont, Ca.

Haugen, G., and Ursin, B., 1996, AVO-A analysis of a vertically fractured reservoir underlying shale: 66th Annual Internat. Mtg., Soc. Expl. Geophys., Expanded Abstracts, pages 1826–1829.

Heidbach, O., Tingay, M., Barth, A., Reinecker, J., Kurfeß, D., and Müller, B., 2008, The World Stress Map database release 2008: doi:10.1594/GFZ.WSM.Rel2008.

Hendrick, N., and Hearn, S., 1999, Polarisation analysis: What is it? Why do you need it? How do you do it?: Exploration Geophysics, **30**, 177–190.

Herawati, I., and Davis, T. L., 2003, The use of time-lapse P-wave impedance inversion to monitor CO2 flood at Weyburn Field, Saskatchewan, Canada: 73th Annual Internat. Mtg., Soc. Expl. Geophys., Expanded Abstracts, **22**, no. 1, 1350–1353.

Hilterman, F., 1989, Is AVO the seismic signature of rock properties?: 59th Annual Internat. Mtg., Soc. Expl. Geophys., Expanded Abstracts.

Hudson, J., Liu, E., and Crampin, S., 1996, The mechanical properties of materials with interconnected cracks and pores: Geophysical Journal International, **124**, no. 1, 105–112.

Hudson, J. A., 1980, Overall properties of a cracked solid: Math. Proc. Camb. Phil. Soc, **88**, 371–384.

Hudson, J. A., 1981, Wave speeds and attenuation of elastic waves in material containing cracks: Geophysical Journal International, **64**, no. 1, 133–150.

Hudson, J. A., 1988, Seismic wave propagation through material containing partially saturated cracks: Geophysical Journal International, **92**, no. 1, 33–37.

Johnston, D., and Toksöz, M., 1981, Definitions and terminology *in* Toksöz, M., and Johnston, D., Eds., Seismic Wave attenuation, Geophysics reprint series:: Society of Exploration Geophysicists, 1–5.

Kalman, D., 1996, A singularly valuable decomposition: The SVD of a matrix: College Mathematics Journal, pages 2–23.

Kendall, R. R., Winarsky, R., Davis, T. L., and Benson, R. B., 2003, 9C, 4D seismic processing for the weyburn co2 flood, saskatchewan, canada: SEG, Expanded Abstracts, **22**, no. 1, 750–752.

Klimentos, T., 1995, Attenuation of P-and S-waves as a method of distinguishing gas and condensate from oil and water: Geophysics, **60**, no. 2, 447–458.

Kuster, G., and Toksöz, M., 1974, Velocity and attenuation of seismic waves in two phase media: Geophysics, **39**, 587–618.

Landrø, M., and Tsvankin, I., 2007, Seismic critical-angle reflectometry: A method to characterize azimuthal anisotropy?: Geophysics, **72**, no. 3, D41–D50.

Leary, P. C., Crampin, S., and McEvilly, T. V., 1990, Seismic fracture anisotropy in the Earth's crust: An overview: Journal of Geophysical Research, **95**, no. B7.

Lefeuvre, F., 2005, Fracture related anisotropy detection and analysis: and if the P-waves were enough?: 64th Annual Internat. Mtg., Soc. Expl. Geophys., Expanded Abstracts, **13**, 942–945.

Li, X., 1999, Fracture detection using azimuthal variation of P-wave moveout from orthogonal seismic survey lines: Geophysics, **64**, no. 4, 1193–1201.

Li, G., 2002, Time-Lapse (4-D) Seismic Monitoring of Massive CO2 Flood at Weyburn Field, S.E. Saskatchewan: EnCana Corporation Report.

Li, G., 2003, 4D seismic monitoring of CO2 flood in a thin fractured carbonate reservoir: The Leading Edge, **22**, no. 7, 690–695.

Liu, E., Hudson, J., and Pointer, T., 2000, Equivalent medium representation of fractured rock: Journal of Geophysical Research-Solid Earth, **105**, no. B2, 2981–3000.

Liu, E., Chapman, M., Varela, I., Li, X. Y., Queen, J. H., and Lynn, H., 2007, Velocity and attenuation anisotropy: Implication of seismic fracture characterizations: The Leading Edge, **26**, 1170–1175.

Loosveld, R., Bell, A., and Terken, J., 1996, The tectonic evolution of interior Oman: Geo Arabia, **1**, 28–50.

Lubbe, R., and Worthington, M., 2006, A field investigation of fracture compliance: Geophysical Prospecting, **54**, no. 3, 319–331.

Lubbe, R., Sothcott, J., Worthington, M., and McCann, C., 2008, Laboratory estimates of normal and shear fracture compliance: Geophysical Prospecting, **56**, no. 2, 239–247.

Lynn, H., Simon, K., and Bates, C., 1996, Correlation between P-wave AVOA and S-wave traveltime anisotropy in a naturally fractured gas reservoir: The Leading Edge, **15**, no. 8, 931–935.

MacBeth, C., and Li, X. Y., 1999, AVD an emerging new marine technology for reservoir characterization: acquisition and application: Geophysics, **64**, no. 4, 1153–1159.

MacBeth, C., 1999, Azimuthal variation in P-wave signatures due to fluid flow: Geophysics, **64**, no. 4, 1181–1192.

Macbeth, C., 2002, Multi-component VSP analysis for applied seismic anisotropy:, volume 1 Pergamon.

Mari, J., 2006, Seismic wave separation by SVD and (F-K) combined filters: Second International Symposium on Communications, Control and Signal Processing, Proceedings.

Marrett, R., Laubach, S., and Olson, J., 2007, Anisotropy and beyond: Geologic perspectives on geophysical prospecting for natural fractures: The Leading Edge, **26**, no. 9, 1106–1111.

Maultzsch, S., Chapman, M., Liu, E., and Li, X. Y., 2003, Modeling frequency dependent seismic anisotropy in saturated rock with aligned fractures: implications for fracture size estimation from anisotropic measurements: Geophysical Prospecting, **51**, no. 5, 381–392.

Maultzsch, S., Chapman, M., Liu, E., and Li, X., 2007, Modelling and analysis of attenuation anisotropy in multi-azimuth VSP data from the Clair field: Geophysical Prospecting, **55**, no. 5, 627–642.

Maultzsch, S., 2005, Analysis of frequency-dependant anisotropy in VSP data: University of Edinburgh, PhD Thesis.

Mavko, G., and Jizba, D., 1991, Estimating grain-scale fluid effects on velocity dispersion in rocks: Geophysics, **56**, 1940.

Mavko, G., Mukerji, T., and Dvorkin, J., 1999, The rock physics handbook: Tools for seismic analysis in porous media: Cambridge University Press.

Mueller, M., 1992, Using shear waves to predict lateral variability in vertical fracture intensity: The Leading Edge, **11**, no. 2, 29–35.

Nur, A., 1991, Critical porosity, elastic bounds, and seismic velocities in rocks: EAGE 53rd Conference and Technical Exhibition, Florence, Italy 1991, Extended Abstracts.

Ostrander, W., 1984, Plane-wave reflection coefficients for gas sands at nonnormal angles of incidence: Geophysics, **49**, no. 10, 1637–1648.

Perelberg, A. I., and Hornbostel, S. C., 1994, Applications of seismic polarization analysis: Geophysics, **59**, 119–130.

Pollastro, R. M., 1999, Ghaba Salt Basin Province and Fahud Salt Basin Province: Oman Geological overview and total petroleum systems: US Geological Society Open-File, pages 99–50.

Potter, M., 1978, Author Mathematical methods in the physical sciences/Merle C. Potter.: Prentice-Hall.

Rathore, J. S., Fjaer, E., Holt, R. M., and Renlie, L., 1994, P-and S-wave anisotropy of a synthetic sandstone with controlled crack geometry: Geophysical Prospecting, **43**, no. 6, 711–728.

Reid, F. J. L., Bertrand, A., McInally, M. T., and MacBeth, C., 2003, 4D signal enhancement using singular value decomposition, application to mapping OWC movement across the Nelson field: SEG, Expanded Abstracts, **22**, no. 1, 1398–1401.

Riede, M., Causse, E., Van Wijngaarden, A., Buland, A., Dutzer, J., and Fillon, R., 2005, Optimized AVO analysis by using optimal linear approximation: 75th Annual Internat. Mtg., Soc. Expl. Geophys., Expanded Abstracts, pages 222–225.

Rüger, A., 1995, P-wave reflection coefficients for transversely isotropic media with a vertical and horizontal axis of symmetry: SEG, Expanded Abstracts, **65**, 278–281.

Rüger, A., 1996, Reflection coefficients and azimuthal AVO analysis in anisotropic media: Doctoral thesis: Colorado School of Mines.

Rüger, A., 2001, Reflection coefficients and azimuthal AVO analysis in anisotropic media: SEG: Society of Exploration Geophysics.

Saleh, S., and de Bruin, J., 2000, AVO attribute extraction via principal component analysis: 70th Annual Internat. Mtg., Soc. Expl. Geophys., Expanded Abstracts, pages 126–129.

Sayers, C. M., and Rickett, J. E., 1997, Azimuthal variation in AVO response for fractured gas sands: Geophysical Prospecting, **45**, 165–182.

Sayers, C., 2007, Introduction to this special section: Fractures: The Leading Edge, **26**, no. 9, 1102–1105.

Schoenberg, M., 1980, Elastic wave behavior across linear slip interfaces: The Journal of the Acoustical Society of America, **68**, 1516.

Schön, J., 1998, Physical properties of rocks: fundamentals and principles of petrophysics: Pergamon Pr.

Sheriff, R., 2002, Encyclopedic Dictionary of Applied Geophysics: Society of Exploration Geophysicists Tulsa, OK.

Shlens, J., 2005, A tutorial on principal component analysis: Systems Neurobiology Laboratory, University of California at San Diego, December.

Shuey, R. T., 1985, A simplification of the zoeppritz equations: Geophysics, **50**, 609–614.

Smith, G., and Gidlow, P., 1987, Weighted stacking for rock property estimation and detection of gas: Geophysical Prospecting, **35**, no. 9, 993–1014.

Smith, T., Sondergeld, C., and Rai, C., 2003, Gassmann fluid substitutions: A tutorial: Geophysics, **68**, 430.

Stewart, R., 1985, Median filtering: review and a new F/K analogue design: Journal of the Canadian Society of Exploration Geophysicists, **21**, 54–63.

Strang, G., 2006, Linear algebra and its applications: Brooks/Cole Pub Co.

Taner, M. T., Koehler, F., and Sherriff, R. E., 1979, Complex seismic trace analysis: Geophysics, **44**, 1041–1063.

Teakle, G., Cao, S., and Greenhalgh, S., 1995, Tube wave suppression in high frequency mine seismic data by singular value decomposition: Exploration Geophysics, **26**, no. 3, 512–517.

Teng, L., and Mavko, G., 1996, Fracture signatures on P-wave AVOZ: 66th Annual Internat. Mtg., Soc. Expl. Geophys., Expanded Abstracts, pages 1818–1821.

Terrell, M., Davis, T., Brown, L., and Fuck, R., 2002, Seismic monitoring of a CO_2 flood at Weyburn field, Saskatchewan, Canada: demonstrating the robustness of time-lapse seismology: 72th Annual Internat. Mtg., Soc. Expl. Geophys., Expanded Abstracts.

Thomsen, L., 1986, Weak elastic anisotropy: Geophysics, **51**, 1954.

Thomsen, L., 1990, Poisson was not a geophysicist!: The Leading Edge, **9**, no. 12, 27–29.

Tonn, R., 1991, The determination of the seismic quality factor Q from VSP data: A comparison of different computational methods: Geophysical Prospecting, **39**, no. 1, 1–27.

Tsvankin, I., and Lynn, H. B., 1999, Special section on azimuthal dependence of P-wave seismic signatures-Introduction: Geophysics, **64**, no. 4, 1139–1142.

Tsvankin, I., 2001, Seismic signatures and analysis of reflection data in anisotropic media: Pergamon.

van der Baan, M., 2006, PP/PS Wavefield separation by independent component analysis: Geophysical Journal International, **166**, no. 1, 339–348.

Van der Kolk, C., Guest, W., and Potters, J., 2001, The 3D shear experiment over the Natih field in Oman: the effect of fracture-filling fluids on shear propagation: Geophysics, **49**, 179–197.

Varela, I., Nasser, M., Chapman, M., and Liu, E., 2006, Anisotropic azimuthal attenuation as an indicator of fracture properties, a studey on walkaround VSP data: EAGE 68th Conference and Technical Exhibition, Vienna, Austria, 12-15 June 2006, Extended Abstracts, **68**.

Varela, I., Maultzsch, S., Li, X., and Chapman, M., 2007, Fracture-properties inversion from azimuthal AVO using singular value decomposition: 77th Annual Internat. Mtg., Soc. Expl. Geophys., Expanded Abstracts, pages 259–263.

Vavryčuk, V., and Pšenčík, I., 1998, PP-wave reflection coefficients in weakly anisotropic elastic media: Geophysics, **63**, 2129–2141.

Vrabie, V. D., Mars, J. I., and Lacoume, J. L., 2004, Modified singular value decomposition by means of independent component analysis: Signal Processing, **84**, no. 3, 645 – 652.

Wandler, A., Evans, B., and Link, C., 2007, AVO as a fluid indicator: A physical modeling study: Geophysics, **72**, C9–C17.

Wang, S., Li, X., Qian, Z., Di, B., and Wei, J., 2007, Physical modeling studies of 3-D P-wave seismic for fracture detection: Geophys. J. Int., **168**, 745–756.

Wang, Z., 2000, The Gassmann equation revisited: comparing laboratory data with Gassmann's predictions *in* Wang, Z., and Nur, A., Eds., Seismic and acoustic velocities in reservoir rocks, recent developments:: SEG, 8–23.

Wang, Z., 2001, Fundamentals of seismic rock physics: Geophysics, **66**, 398.

Willis, M., Burns, D., Rao, R., Minsley, B., Toksöz, M., and Vetri, L., 2006, Spatial orientation and distribution of reservoir fractures from scattered seismic energy: Geophysics, **71**, O43.

Willis, M., Burns, D., Lu, R., Toksoz, M., and House, N., 2007, Fracture quality from integrating time-lapse VSP and microseismic data: The Leading Edge, **26**, no. 9, 1198.

Wilson, A., Chapman, M., and Li, X. Y., 2009, Frequency-dependent AVO inversion: 79th Annual Internat. Mtg., Soc. Expl. Geophys., Expanded Abstracts, **79**.

Worthington, M., 2007, The compliance of macrofractures: The Leading Edge, **26**, no. 9, 1118.

Worthington, M. H., 2008, Interpreting seismic anisotropy in fractured reservoirs: First Break, **26**, 57–63.

Yilmaz, O., 1999, Seismic data processing, investigations in geophysics 2:, volume 2, Society of Exploration Geophysicists.

Zoeppritz, K., 1919, Erdbebenwellen, On the reflection and penetration of seismic waves through unstable layers: Göttinger Nachrichten, **1**, 66–84.

Appendix A

Trigonometric fit

Throughout this thesis the data points y(x) are often fitted to a function of the form,

$$\tilde{y}(x) = a_1 + a_2 \cos 2(x - \phi_{sym}) \tag{A.1}$$

where $\tilde{y}(x)$ are the estimated data points at location x using the trigonometric fit. a_2 is the amplitude of the trigonometric fit, ϕ_{sym} provides the symmetry plane and a_1 is the mean or average of the fit. a_1, a_2 and ϕ_{sym} are constants that can be found as explained below.

$$\begin{aligned} \tilde{y}(x) &= a_1 + a_2 \cos 2(x - \phi_{sym}) \\ &= a_1 + a_2 \cos(2x - 2\phi_{sym}) \end{aligned} \tag{A.2}$$

using the trigonometric identity $\cos(x \pm y) = \cos x \cos y \mp \sin x \sin y$ in equation A.2, we have,

$$\tilde{y}(x) = a_1 + a_2 \left[\cos(2x)\cos(2\phi_{sym}) + \sin(2x)\sin(2\phi_{sym})\right] \tag{A.3}$$

$$= \underbrace{a_1}_{c_1} + \underbrace{a_2 \sin(2\phi_{sym})}_{c_3} \sin(2x) + \underbrace{a_2 \cos(2\phi_{sym})}_{c_2} \cos(2x) \tag{A.4}$$

$$\tilde{y}(x) = c_1 + c_2 \sin(2x) + c_3 \cos(2x) \tag{A.5}$$

with,

$$a_1 = c_1 \tag{A.6}$$

$$a_2 = \frac{c_2}{\sin(2\phi_{sym})} = \frac{c_3}{\cos(2\phi_{sym})} \tag{A.7}$$

$$\phi = \frac{1}{2}\tan^{-1}\left(\frac{c_2}{c_3}\right) \tag{A.8}$$

We can then find the coefficients c_1, c_2 and c_3, and in turn the coefficients a_1, a_2 and ϕ_{sym}, by using the above relationships and finding the least squares solution to the following equations,

$$\begin{bmatrix} \tilde{y}(x_1) \\ \tilde{y}(x_2) \\ \vdots \\ \tilde{y}(x_n) \end{bmatrix} = \begin{bmatrix} 1 & \sin(2x_1) & \cos(2x_1) \\ 1 & \sin(2x_2) & \cos(2x_2) \\ \vdots & & \vdots \\ 1 & \sin(2x_n) & \cos(2x_n) \end{bmatrix} \begin{bmatrix} c_1 \\ c_2 \\ c_3 \end{bmatrix} \tag{A.9}$$

or in matrix form,

$$\tilde{Y} = AC \tag{A.10}$$

The coefficients c_1, c_2 and c_3 and then be calculated by finding the least squares solution to equation A.10 as follows,

$$C \approx (A^T A)^{-1} A^T Y \tag{A.11}$$

Appendix B

Geophone Rotations

3C geophone rotation

The three component, 3C, geophone rotation is geometrically described as the change in relative orientation of two orthogonal coordinate systems by two rotations. These rotations are described by two Euler angles (Arfken, 1985). The Euler angles used are θ and ϕ. The first rotation is in a clockwise direction around axis Z on the XY plane, where θ is the angle between X and X', and Y and Y'. The triplets $X'Y'Z'$ and $X''Y''Z''$ are the axis orientations after rotations 1 and 2 respectively.

The second rotation is on the $Y'Z'$ plane around axis X' of the newly generated coordinate system. ϕ is the angle between Y' and Y'', and Z' and Z''.

From Euler's theorem the relative change in orientation from the coordinate system XYZ to $X''Y''Z''$ can be represented by one rotation matrix A, where A is defined as,

$$A = BC,$$

where C and B are the rotation matrices corresponding to the first and second

rotations respectively, and are written as,

$$B = \begin{bmatrix} \cos\phi & 0 & -\sin\phi \\ 0 & 1 & 0 \\ \sin\phi & 0 & \cos\phi \end{bmatrix}, C = \begin{bmatrix} \cos\theta & \sin\theta & 0 \\ -\sin\theta & \cos\theta & 0 \\ 0 & 0 & 1 \end{bmatrix}$$

which results in the final rotation matrix A as,

$$\begin{bmatrix} X'' \\ Y'' \\ Z'' \end{bmatrix} = \underbrace{\begin{bmatrix} \cos\theta\cos\phi & \sin\theta\cos\phi & -\sin\phi \\ -\sin\theta & \cos\theta & 0 \\ \cos\theta\sin\phi & \sin\theta\sin\phi & \cos\phi \end{bmatrix}}_{\text{A}} \begin{bmatrix} X \\ Y \\ Z \end{bmatrix}$$

The naming convention used is $Y' = Rh$, for horizontaly radial component, $X' = T$ for transverse component, $Z' = Z$. After the second rotation around axis X'', $Z'' = R$, which is the radial component pointing from the source to the receiver, $Y'' = N$ or normal component lies in the vertical plane through the source and receiver (also known as sagital plane), and $X'' = T$ which lies in the horizontal plane. The T, transverse component is perpendicular to the direct P-wave and should thus contain S-wave energy. Note that A satisfies the orthogonality condition $A^T A = I$, and $\det(A) = 1$.

Rotation types

The three types of geophone rotations performed are:

1. 3C maximum energy ϕ: As explained above in section B, this consists of two rotations around axis Z and followed by a rotation around axis X'. ϕ is estimated to provide the maximum energy to component R.

2. 3C geometric ϕ: Same as rotation 1 except ϕ is the geometric phi assuming straight ray paths from source to receiver.

3. 2C maximum energy θ: Geophone rotation only around axis Z, the angle θ is estimated such that Y' has maximum energy and X' minimum, these in turn will be the radial and transverse components on the XY plane.

4. 2C geometric θ: Similar to rotation 3, with the difference that θ points in a straight line from receiver to source location.

Appendix C

Publications list

Parts of this work have been published or presented at conferences as follows:

1. **Varela, I.**, Chapman, M. and Li, X. Y., 2009, Fracture density inversion from a physical geological model using azimuthal AVO with optimal basis functions. 79th Ann. Internat. Mtg.: Soc. of Expl. Geophys. Houston, TX, SEG Expanded Abstracts, Volume 28.

2. Chao, G., Maultzsch, S., Cadoret, T., Deplante, C. and **Varela, I.**, 2009, Fracture characterization of a tight gas reservoir using seismic attributes derived from singular value decomposition of azimuthal AVO data. International Petroleum Technology Conference, Doha, Qatar.

3. Liu, E., Chapman, M., **Varela, I.**, Li, X., Queen, J. and Lynn, H., 2007, Velocity and attenuation anisotropy: Implication of seismic fracture characterizations. The Leading Edge, Volume 26, Issue 9, pp. 1170-1174.

4. **Varela, I.**, Maultzsch, S., Li, X.Y., and Chapman, M., 2007, Fracture Properties Inversion from Azimuthal AVO Using Singular Values Decomposition, 77th Ann. Internat. Mtg.: Soc. of Expl. Geophys. San Antonio, TX, SEG Expanded Abstracts, Volume 26, pp. 259 - 263.

5. **Varela, I.** and Maultzsch, S., 2007, Azimuthal AVO Inversion for Fracture Characterization: A new technique using Singular Value Decomposition., 70th EAGE Conference and Exhibition, London.

6. **Varela, I.**, Liu, E. and Chapman, M., 2006, Azimuthal multi-attribute analysis for fracture properties in time-lapse VSP data, 76th Ann. Internat. Mtg.: Soc. of Expl. Geophys. New Orleans, LA. SEG Expanded Abstracts, Volume 25, pp. 3432 - 3436.

7. **Varela, I.**, Nasser, M., Chapman, M. and Liu, E., 2006, Anisotropic azimuthal attenuation as an indicator of fracture properties, a study on walkaround VSP data, 68th EAGE Conference and Exhibition, Vienna, Austria. **(Recipient of the Louis Cagnaird Award)**. Vienna.

8. Chapman, M., Liu, E., **Varela, I.** and Li, X.-Y., 2006, Use of P-Wave Attenuation Anisotropy to Improve Fracture Characterisation, Seismic Anisotropy Workshop, 68th EAGE Conference and Exhibition, Vienna, Austria.